COHESIVE ZONE MODELING OF DYNAMIC FAILURE IN HOMOGENEOUS AND FUNCTIONALLY GRADED MATERIALS

BY

ZHENGYU ZHANG

B.E., Tong Ji University, 1995

THESIS

Submitted in partial fulfillment of the requirements
for the degree of Master of Science in Civil and Environmental Engineering
in the Graduate College of the
University of Illinois at Urbana-Champaign, 2003

Urbana, Illinois

Abstract

COHESIVE ZONE MODELING OF DYNAMIC FAILURE IN
HOMOGENEOUS AND FUNCTIONALLY GRADED MATERIALS

Zhengyu Zhang

Department of Civil and Environmental Engineering
University of Illinois at Urbana-Champaign

Glaucio H. Paulino, Advisor

The dynamic failure of homogeneous and Functionally Graded Materials (FGMs) can be simulated by incorporating a Cohesive Zone Model (CZM) into the numerical scheme. The failure criterion is incorporated by the CZM using both a finite cohesive strength and work to fracture in the material description. In this study, first the general dynamic behavior of FGMs (without initial crack) is investigated considering bulk material modeled with graded elements, *i.e.* elements possessing a spatially varying material property field, such as Young's modulus, Poisson's ratio, mass density, etc. The results reveal some interesting features of dynamic behavior of FGMs compared to that of homogeneous materials. Next, two CZMs developed for FGMs are described and the numerical implementation scheme is discussed. Finally, the influence of material property variation on the crack propagation pattern for FGM structures under impact loading is investigated with a number of examples. The powerful features of CZMs in simulating branching and spontaneous crack initiation behaviors are also presented. The present finite element code is named I-CD (Illinois Cohesive Dynamic).

To my loving family

Acknowledgments

I take this opportunity to express my profound gratitude towards my advisor Prof. Glaucio H. Paulino. This work would have been impossible without his constant guidance, invaluable suggestions and warm encouragement. His rich knowledge and experience, with his enthusiasm and dedication to research, have been a source of motivation and constant inspiration during my study. Moreover, I deeply appreciate the time and effort Prof. Paulino spent on reading and correcting my thesis. His comments and suggestions constitute an indispensable ingredient of this thesis.

I would also like to thank many of my friends at the U of I for their warm friendship and support. I benefited tremendously from the vibrant and friendly discussions with my group members—Matthew Carl Walters, Alok Sutradhar, Jeong-Ho Kim, Seong-Hyeok Song and Zhaoxu Dong. Thanks to their company, my study and life at the U of I are more enjoyable and fulfilling. I would also like to thank my friends, Rui Zhao and Mu Gao, for their care, listening and help.

I would also like to thank Prof. Zhang Ruo Jing and and Prof. Ji Xing in Tong Ji University, China, for their kind guidance and encouragement during my study there. Their trust and encouragement led to my advanced study at the U of I.

I am grateful to my family, for their abiding love and care. Every step I make in my life witnesses their support. Last but not the least, I would like to thank my husband, Chijie Lin. He is most patient and helpful when I have a question to ask, and he is most understanding and supportive of my busy study.

Table of Contents

List of Tables

List of Figures

List of Figures continued

List of Figures continued

List of Figures continued

List of Figures continued

List of Figures continued

List of Figures continued

Chapter 1

Introduction

Cohesive Zone Models (CZMs) are of growing interest for fracture modeling and are currently widely used in simulations for both homogenous and inhomogeneous material systems. Various models have been proposed, their advantages, disadvantages and limitations being debated. This Chapter introduces and motivates the topic of CZMs by providing a comprehensive review of the history of these models, presenting and discussing several representative models. After that, the concept of functionally graded material (FGM) is introduced briefly. Then the outline of the finite element framework incorporating CZMs is described. In addition, the organization of the overall work is presented at the end of the Chapter.

1.1 Background

A realistic fracture model which is physics-based and, at the same time, can easily adapt itself to experimental calibration and numerical implementation remains elusive. A schematic drawing is shown in Figure 1.1 to describe three regions at the crack tip where different classes of material responses are dominant. The outer-ring represents the so-called *K-field* and relies on the classical approach based on linear elastic fracture mechanics (LEFM), where the material behavior is linear and stress and strain fields can be determined with a single parameter, typically the stress intensity factor (SIF) or energy release rate. The intermediate ring is the *Hutchinson-Rice-Rosengren (HRR) field* [17, 37], where the elastic-plastic response is incorporated. For the inner ring which is very close to the crack tip, the microstructure of material, *e.g.*, distribution of microcracks and voids, will significantly influence the material response due to effects like void nucleation. In continuum mechanics, the Gurson model [14] successfully incorporated these effects into the constitutive model for ductile materials, however, the large number of parameters that need to be calibrated poses

a strong challenge for the model to be used widely.

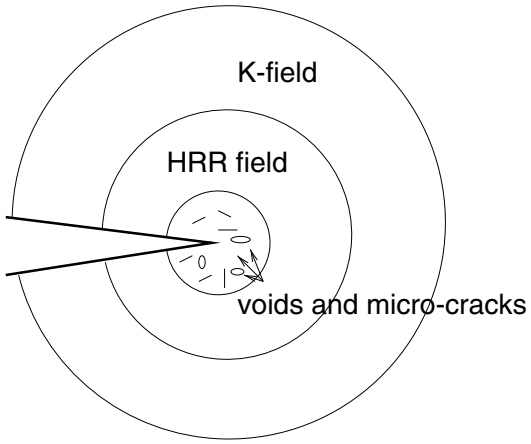

Figure 1.1: Crack tip zones with different material response characteristics.

There are a few shortcomings with the aforesaid approaches. First, whether only LEFM model is used to describe crack tip field or more complicated phenomena incorporated, an external criterion is required for the crack to propagate, and the crack propagation direction is also imposed. Second, phenomena such as fracture instability (which has not been thoroughly understood yet), cannot be simulated with a purely phenomenological model. Third, crack branching and fragmentation that usually occur in impact loading events cannot be properly simulated. Finally, the classical approaches require pre-existing, crack-like flaws. The nucleation of voids can be treated in Gurson model, however as explained above, the wide usage of this model remains problematic.

An alternative way to describe the near-tip behavior and propagate the crack is by means of the CZM, which incorporates a cohesive strength and finite work to fracture in the description of material behavior. The concept of "cohesive failure" is illustrated in Figure 1.2 for tensile (mode I) case. It is assumed that a *cohesive zone*, along the plane of potential crack propagation, is present in front of the crack tip. Within the extent of the cohesive zone, the material points which were identical when the materials was intact, separate to a distance of Δ due to the influence of high stress at the crack tip vicinity. The cohesive zone surface sustains a distribution of tractions T which are functions of the displacement jump across the surface Δ, and the relationship between the traction T and separation Δ is defined as the constitutive law for the cohesive zone surface. In general, the constitutive law indicates that with increasing interfacial separation Δ, the traction T across the cohesive interface first increases, reaches a maximum value at critical separation value δ, then decreases, and finally vanishes at a characteristic separation value, here denoted as Δ^c, where complete decohesion is assumed to occur and the material is considered to have

completely failed. The subscript n (normal) is attached to the parameters in Figure 1.2 to denote the tensile (Mode I) fracture case, and in Mode-II or mixed-mode case the tangential traction-separation should be included.

The aforementioned approach has the promise of simulating fracture process where fracture occurs spontaneously. The fracture path and speed become natural outcome of the simulation rather than being specified *ad hoc*.

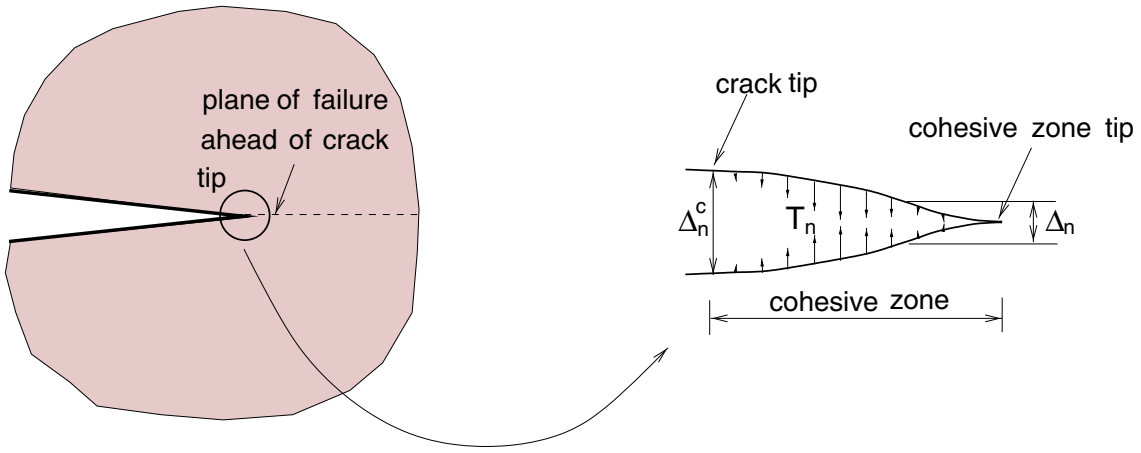

Figure 1.2: Schematic representation of (a) the cohesive zone concept and (b) the cohesive tractions along a cohesive surface at the crack tip vicinity.

1.2 Cohesive Zone Models

The concept of CZM dates back to 1933, when in Prandtl's [35] work a cohesive traction relation is used to predict the length of a debonded zone between two slender beams. In 1959, Barenblatt [1, 2] proposed the CZM for perfectly brittle materials that accounted for the interaction between atoms near a crack tip. Around the same time frame Dugdale [10] extended the concept to perfectly plastic material by postulating the existence of a process zone at the crack tip. Later on, a computational method called "nodal release" [39] which models fracture by splitting nodes along the fracture path within a finite element setting was proposed. During recent years, the CZM became an active research field and many models have been proposed that consider increasing physical complexity, *e.g.* the rate-dependent behavior, damage, and viscoelasticity [26, 48, 9, 29]. However, here, the discussion will focus on the basic characteristics of a few representative CZMs: the potential-based model by Xu and Needleman [46], the initial-rigid model by Camacho and Ortiz [6], the bilinear

model by Geubelle and Baylor [12], and the Virtual Internal Bond model by Klein, Gao and co-workers [27, 28]. The cohesive zone model for FGMs will be discussed in Chapter 3.

1.2.1 Xu and Needleman's Model

The model proposed by Xu and Needleman [46] assumes a scalar decohesion potential ϕ in the form

$$\phi(\mathbf{\Delta}) = \phi_n + \phi_n \exp\left(-\frac{\Delta_n}{\delta_n}\right)\left\{\left[1 - r + \frac{\Delta_n}{\delta_n}\right]\frac{(1-q)}{(r-1)} - \left[q + \frac{(r-q)}{(r-1)}\frac{\Delta_n}{\delta_n}\right]\exp(-\Delta_t^2)\right\} \quad (1.1)$$

from which the cohesive traction force can be obtained as

$$\mathbf{T} = -\frac{\partial \phi}{\partial \mathbf{\Delta}} \quad (1.2)$$

where $\mathbf{T} = [T_n, T_t]$ is the traction force vector — in the two dimensional case it comprises traction in normal and tangential directions. The displacement jump vector $\mathbf{\Delta} = [\Delta_n, \Delta_t]$ denotes the displacement discontinuity across the cohesive surface in the normal and tangential directions. The parameters ϕ_n and ϕ_t are the energies required for pure normal and tangential separation, respectively. The parameters δ_n and δ_t are the critical opening and sliding displacements for normal and tangential separation, respectively, which are related to the cohesive normal strength $\sigma_{\max}$ and the tangential strength $\tau_{\max}$ as

$$\phi_n = e\sigma_{\max}\delta_n\,, \qquad \phi_t = \sqrt{e/2}\tau_{\max}\delta_t\,. \quad (1.3)$$

Moreover,

$$q = \phi_t/\phi_n \quad (1.4)$$

is the energy ratio and r is defined as the value of Δ_n/δ_n after complete shear separation with $T_n = 0$. The resulting normal and shear traction components are derived from (1.2):

$$T_n = -\frac{\phi_n}{\phi_t}\exp\left(-\frac{\Delta_n}{\delta_n}\right)\left\{\frac{\Delta_n}{\delta_n}\exp\left(-\frac{\Delta_t^2}{\delta_t^2}\right) + \frac{(1-q)}{(r-1)}\left[1 - \exp\left(-\frac{\Delta_t^2}{\delta_t^2}\right)\right]\left[r - \frac{\Delta_n}{\delta_n}\right]\right\} \quad (1.5)$$

$$T_t = -\frac{\phi_n}{\phi_t}\left(2\frac{\delta_n}{\delta_t}\right)\frac{\Delta_t}{\delta_t}\left\{q + \frac{(r-q)}{(r-1)}\frac{\Delta_n}{\delta_n}\right\}\exp\left(-\frac{\Delta_n}{\delta_n}\right)\exp\left(-\frac{\Delta_t^2}{\delta_t^2}\right) \quad (1.6)$$

Figure 1.3 (a) shows the normal traction across the surface, T_n, as a function of Δ_n with $\Delta_t = 0$. The maximum value of T_n is σ_n and occurs when $\Delta_n = \delta_n$. The variation of T_t with Δ_t is shown in Figure 1.3 (b). The maximum value of $|T_t| = \tau_{max}$ is attained when $\Delta_t = \sqrt{2}\delta_t/2$.

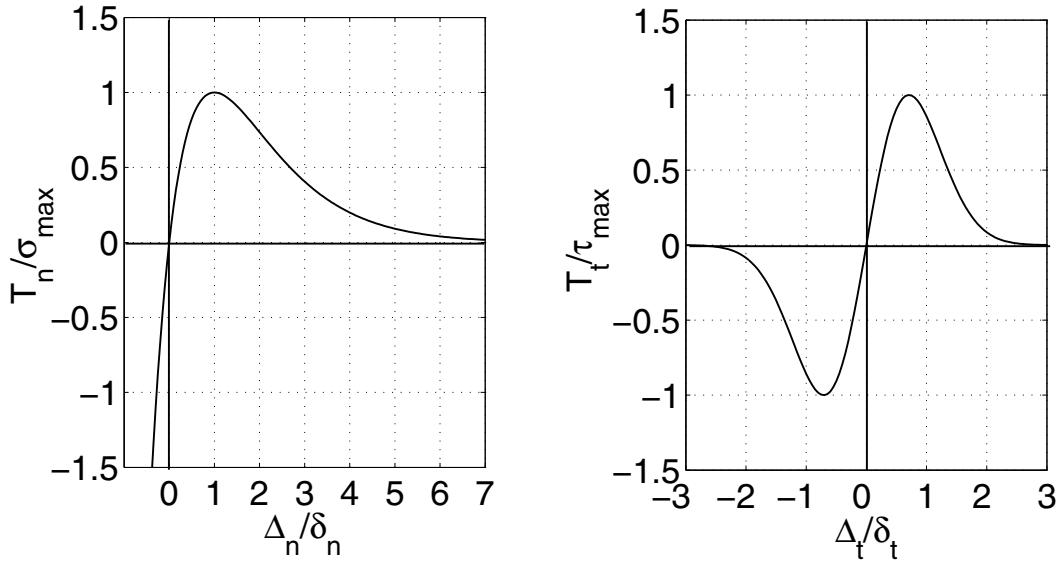

Figure 1.3: The *intrinsic* potential-based exponential cohesive model in (a) pure tension and (b) pure shear.

With the model described above, Xu and Needleman [46] investigated dynamic behavior of fast crack growth in brittle solids and demonstrated that the model is capable of simulating many dynamic fracture phenomena such as crack branching, dependence of crack speed on impact velocity, and abrupt crack arrest.

The above intrinsic model, sometimes referred to as "cohesive surface network" [28], requires the existence of cohesive elements in the structure before the simulation begins. This renders certain simplicity to the numerical implementation, however this approach adds fictitious compliance to the structure (the detailed mechanism will be discussed in Chapter 3), and hence affect adversely the accuracy of numerical simulation. To mitigate the influence of this artifact, a large initial stiffness *i.e.* steep initial slope of T_n versus Δ_n and T_t versus Δ_t curves in Figure 1.3 is desired. Since neither cohesive energy nor cohesive strength had been experimentally determined with high degree of certainty [28], certain latitude is permitted for the choice of cohesive strength. Orowan [32] estimated $E/\sigma_{max} = 30$, and in the work by Xu and Needleman [46], $\sigma_{max} = E/10$ is generally used. However, a consequent drawback with higher initial stiffness is that smaller elements and smaller time step are required to produce stable results .

The distinct features of Xu and Needleman's model [46] are summarized as follows:

- It is an *intrinsic* model, in the sense that the cohesive surface elements are embedded in the structure, so the mesh is unchanged during the entire computation time. No

extrinsic criterion is needed for crack nucleation or propagation.

- The normal and tangential traction-separation relationships are derived from one cohesive energy potential expression, in which 4 parameters need to be determined, *i.e.* ϕ_n, ϕ_t, σ_{max}, τ_{max}. Usually it is assumed that $\phi_n = \phi_t$, and $r = \Delta_n/\delta_n = 0$, which means that under pure shear deformation, the normal displacement jump remains zero after complete separation.

- The formulation generates a healing effect so that the closing fracture surfaces do not take permanent damage into account.

- The elastic response of the cohesive elements prior to crack propagation introduces artificial compliance to the computation model and reduces accuracy.

1.2.2 Camacho and Ortiz's Model

This model minimizes the artificial softening effect due to elastic deformation of cohesive interface present in Xu and Needleman's model [46]. Ideally the initial interface stiffness should be infinity, *i.e.* prior to crack propagation, the cohesive interface should not generate any deformation. Figure 1.4 illustrates the model by Camacho and Ortiz [6] which possesses this characteristic. In the implementation stage, the cohesive elements are adaptively inserted into the mesh, *i.e.* the initial topology of the mesh does not have any cohesive elements. When a certain fracture criterion is met, a cohesive element is inserted in the proper location of the mesh which allows the crack to propagate. Since this model requires a failure criterion which is external to the cohesive law, this kind of CZMs is referred to as "*extrinsic*". The failure criterion may be chosen in terms of a critical fracture stress σ_{fr} determined from the critical mode I stress intensity factors K_{Ic} and the initial flaw size a_0 of the material

$$\sigma_{fr} = \frac{K_{IC}}{\sqrt{\pi a_0}} \tag{1.7}$$

This model is based on *effective quantities.* The *effective stress* σ_{eff} is defined as

$$\sigma_{eff} = \sqrt{T_n^2 + \beta_\tau T_t^2} \qquad \text{for } T_n \geq 0 \tag{1.8a}$$

$$\sigma_{eff} = \sqrt{\beta_\tau}\left(|T_t| - \mu |T_n|\right) \qquad \text{for } T_n < 0 \tag{1.8b}$$

where T_n and T_t are the cohesive tractions in normal and tangential direction, respectively; β_τ is the shear stress factor, which represents the mode mixity effect, and μ is the friction coefficient. When the fracture condition $\sigma_{eff} \geq \sigma_{fr}$ is met, a new surface is introduced into

the mesh by doubling nodes and creating the cohesive zone elements. The cohesive force that resists the opening and sliding of the new surface is assumed to weaken irreversibly with increasing crack opening. Permanence of damage is retained by keeping track of the maximum displacement in the simulation history and using it as the indicator for loading or unloading, as shown in Figure 1.4. The cohesive traction and separation relationship is described as follows:

- $T_n \geq 0$**, tensile case.** Under loading condition, when the current displacement is larger than that in history, the cohesive traction ramp down linearly as displacement jump increases and reduces to zero as opening reaches critical opening displacement $\Delta_n = \delta_n$. The decohesion is complete at this point and cohesive force vanishes thereafter.

$$\begin{aligned} T_n &= \sigma_{\max}\left(1 - \frac{\Delta_n}{\delta_n}\right) \\ & \qquad\qquad \text{for } \Delta_n \geq \Delta_{n_{(max)}} \\ T_t &= \tau_{\max}\left(\frac{\Delta_n}{\delta_n}\right) sgn(\Delta_t) \end{aligned} \tag{1.9}$$

  where $\Delta_{n_{(max)}}$ is the maximum normal opening displacement recorded in history, and $sgn(x) = x/|x|$ is the signum function. If unloading occurs, the crack begins to close, and the traction obeys the linear unloading relation

$$\begin{aligned} T_n &= \sigma_{max}\left(1 - \frac{\Delta_{n_{(max)}}}{\delta_n}\right)\frac{\Delta_n}{\Delta_{n_{(max)}}} \\ & \qquad\qquad \text{for } \Delta_n < \Delta_{n_{(max)}} \\ T_t &= \tau_{max}\left(1 - \frac{\Delta_{n_{(max)}}}{\delta_n}\right)\frac{\Delta_n}{\Delta_{n_{(max)}}} sgn(\Delta_t) \end{aligned} \tag{1.10}$$

  as shown in Figure 1.4(a). If the crack reopens, the reloading path follows the unloading path in reverse direction till $\Delta_{n_{(max)}}$ and then follows the original ramp-down relation (1.9).

- $T_n < 0$**, compression case.** In Ortiz and Camacho's study [6], when normal compression occurs, a contact algorithm is employed to treat the normal displacement penetration, while the tangential traction-separation relations follow

$$T_t = \tau_{\max}\left(1 - \frac{\Delta_{t_{(max)}}}{\delta_t}\right) sgn(\Delta_t) \qquad \text{for } \Delta_t \geq \Delta_{t_{(max)}} \tag{1.11}$$

$$T_t = \tau_{\max}\left(1 - \frac{\Delta_{t_{(max)}}}{\delta_t}\right)\frac{\Delta_t}{\Delta_{t_{(max)}}} \qquad \text{for } \Delta_t < \Delta_{t_{\max}} \tag{1.12}$$

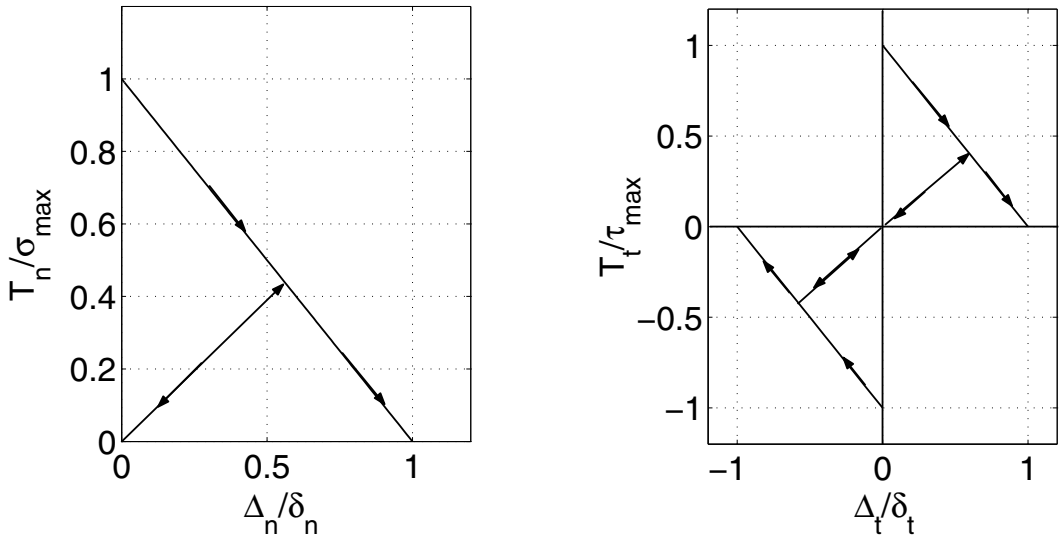

(a) (b)

Figure 1.4: The extrinsic initial-rigid cohesive model in (a) pure tension and (b) pure shear.

for loading and unloading cases, respectively, where $\Delta_{t_{(max)}}$ is the maximum tangential opening displacement in the simulation history.

With the model above, Camacho and Ortiz [6] investigated impact damage in brittle materials. Simulation of severe fragmentation under high velocity impact loading was carried out, in which thermal effects and rate dependence were also considered.

The features of Camacho and Ortiz' model [6] are summarized as follows:

- It is an *extrinsic* model, in that the cohesive elements are adaptively inserted into the mesh. It avoids the artificial softening effect present in *intrinsic* models, however at the price of extra work consisting of adaptively updating the mesh by renumbering nodes and elements. Moreover, an extrinsic failure criterion is required.

- The critical fracture stress is determined by linear elastic fracture mechanics formula, and is much lower than used in Xu and Needleman's [46] model. In their work, Camacho and Ortiz [6] used a value around $E/\sigma_{max} = 600$.

- Permanent damage is considered.

- It is based on *effective quantities*, which can be considered a drawback of the model.

- Explicit contact/friction algorithm is employed to treat normal displacement penetration case.

- The relations between normal and tangential components of the traction and displacement jump are not coupled. Effect of mode mixity is represented by the arbitrary parameter β_τ, whose value can vary within a large range due to lack of experimental evidence.

1.2.3 Bilinear Model

The bilinear model was presented by Geubelle and Baylor [12, 4] and it is illustrated in Figure 1.5. A scalar "residual strength parameter" S is defined as

$$S = 1 - \sqrt{(\Delta_n/\delta_n)^2 + (\Delta_t/\delta_t)^2} \tag{1.13}$$

which takes a value close to unity initially and vanishes when complete failure is achieved. This parameter is forced to be monotonically decreasing, which ensures permanence of damage. To this end, its historic minimum value S_{min} is stored and S is determined as

$$S = \min\left(S_{\min},\ \max\left(0, 1 - \sqrt{(\Delta_n/\delta_n)^2 + (\Delta_t/\delta_t)^2}\right)\right) \tag{1.14}$$

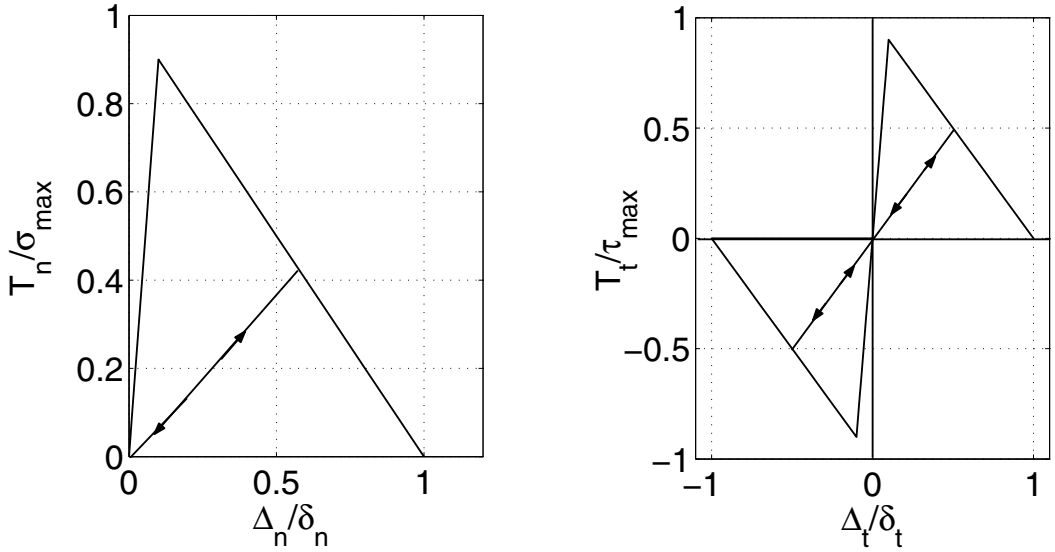

Figure 1.5: The bilinear cohesive model in (a) pure tension and (b) pure shear.

The traction-separation relation follows

$$T_n = \frac{S}{1-S}\frac{\Delta_n}{\delta_n}\sigma_{\max} \tag{1.15a}$$

$$T_t = \frac{S}{1-S}\frac{\Delta_t}{\delta_t}\tau_{\max} \tag{1.15b}$$

where

$$\delta_n = \frac{2G_{Ic}}{\sigma_{\max}S_{initial}} \tag{1.15c}$$

$$\delta_t = \frac{2G_{IIc}}{\tau_{\max}S_{initial}} \tag{1.15d}$$

in which G_{Ic} and G_{IIc} are the critical energy release rates for mode I and mode II respectively. $S_{initial}$ is the initial value for S.

In Geubelle and Baylor's work [12], the model is employed to investigate fracture nucleation and propagation in composite materials under impact loading, and delamination between distinct material layers. The general features of this model are summarized here:

- It is an *intrinsic* model, the cohesive elements are embedded in the discretized structure.
- Permanent damage effect is incorporated with the introduction of parameter S. The loading and unloading paths are analogous to those of Camacho and Ortiz's [6] model.
- By choosing the initial strength parameter $S_{initial}$, the accuracy with intrinsic model can be controlled, however accuracy and computational stability are always at odds.

1.2.4 Virtual Internal Bond Model

The Virtual Internal Bond (VIB) model is different from the previous three models discussed above in that it does not differentiate the *bulk material* and *cohesive surface*, but rather incorporates the cohesive surface effect into the continuum constitutive relationship. In essence, it is an elasticity model. In the previous models described above, the bulk response is accounted for by means by bulk elements, for which the constitutive relationship is described with the continuum Hooke's law, while the fracture behavior is captured by explicit cohesive elements, which follows a cohesive traction-separation relationship. In contrast, there is no "cohesive element" in the VIB model, and the behavior of the bulk material depends on the local strain status. The increasing strain localization softens the material and when a certain "fracture" criterion is satisfied, the crack is initiated or propagated.

The VIB model assumes cohesive interactions between material particles from an atomistic view, and the network of cohesive bonds is statistically incorporated into the constitutive law of the material via the Cauchy-Born rule, *i.e.* by equating the strain energy density on the continuum level to the potential energy stored in the cohesive bonds due to an imposed deformation. With this approach, fracture is directly introduced into the continuum constitutive behavior.

For a homogeneous, hyperelastic solid, internal cohesive bonds are assumed to exist between material particles at the microstructure level. Each bond is described by a potential energy function $U(\ell)$ where ℓ denotes the deformed bond length, which can be expressed in terms of right Cauchy-Green tensor as

$$\ell = \ell_0 \sqrt{\xi_I C_{IJ} \xi_J}, \tag{1.16}$$

where ξ_I denotes the bond orientation in Lagrangian configuration, ℓ_0 denotes the length of the unstretched bond, and (C_{IJ}) is the IJ component of the Cauchy-Green tensor $\mathbf{C}$. The important idea in this model is to link the discrete microstructure cohesive description and the macroscopic continuum model by the Cauchy-Born rule as

$$\Phi(C_{IJ}) = \langle U(\ell) \rangle = \left\langle \ell_0 \sqrt{\xi_I C_{IJ} \xi_J} \right\rangle \tag{1.17}$$

where Φ denotes the strain energy density. The position of each bond is characterized by a spherical coordinate system (ℓ_0, θ, ϕ), and the notation $< \cdots >$ is defined as the volumetric average

$$\langle \cdots \rangle \equiv \int \int \int (\cdots)\, D(\ell_0, \theta, \phi) \sin\theta d\ell_0 d\theta d\phi \tag{1.18}$$

where $D(\ell_0, \theta, \phi)$ is the bond density function, which characterizes the spatial distribution of internal bonds.

By employing a finite deformation formulation, the symmetric second Piola-Kirchhoff stress tensor $\mathbf{S}$ and material tangent moduli tensor $\mathbf{C}$ can be represented in component form as

$$S_{IJ} = 2\frac{\partial \Phi}{\partial C_{IJ}} = \left\langle \frac{\ell_0 U'(\ell)}{\ell} \xi_I \xi_J \right\rangle \tag{1.19}$$

$$C_{IJKL} = 4\frac{\partial^2 \Phi}{\partial C_{IJ} C_{KL}} = \left\langle \ell_0^4 \left(\frac{U'(\ell)}{\ell^2} - \frac{U''(\ell)}{\ell^3} \right) \xi_I \xi_J \xi_K \xi_L \right\rangle \tag{1.20}$$

Notice that now the "material parameters" in $\mathbf{C}$ are no longer *constant*; rather, they become function of the cohesive bond distribution $D(\ell_0, \theta, \phi)$, bond cohesive potential $U(\ell)$, as well as local deformation $\ell(C_{IJ})$.

Several special bond cases are proposed [27], *e.g.*, for plane stress, isotropic solid,

$$D(\ell_0, \theta, \phi) = D_0 \delta_D(\ell_0 - \ell_0^*)\delta_D(\theta - \pi/2) \tag{1.21}$$

where δ_D denotes the Dirac delta function, and ℓ_0^* is the characteristic bond length.

By Taylor expansion of strain energy density expression (1.17) within small strain case, the linear elasticity case is produced, and the elastic modulus takes the form

$$c_{ijkl} = \mu(\delta_{ij}\delta_{kl} + \delta_{ik}\delta_{jl} + \delta_{il}\delta_{kj}) \tag{1.22}$$

where μ is defined as the shear modulus

$$\mu = \frac{\pi}{4}\left\langle \ell_0^2 U''(\ell_0)\right\rangle \tag{1.23}$$

with other parameters taking the following forms

$$\lambda = \mu, \qquad \nu = 1/3, \qquad E = \frac{2\pi}{3}\left\langle \ell_0^2 U''(\ell_0)\right\rangle \tag{1.24}$$

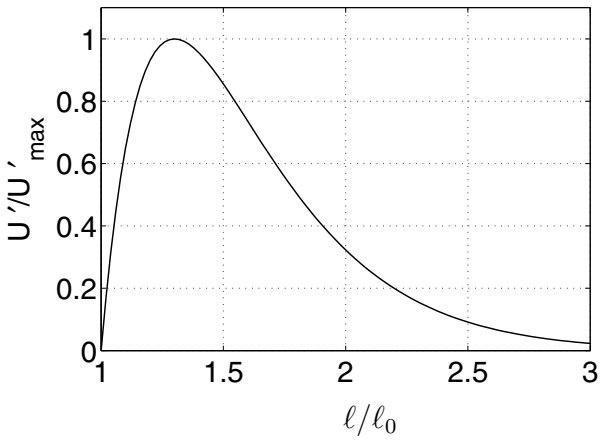

Figure 1.6: A general cohesive force law for an isotropic VIB derived considering equibiaxial stretching.

With the above form, once the potential $U(\ell)$ is defined, the constitutive model is set. A phenomenological cohesive force law is introduced (Figure 1.6)

$$U'(\ell) = A(\ell - \ell_0)\exp\left(-\frac{\ell - \ell_0}{B}\right) \tag{1.25}$$

in which the parameters A and B need to be calibrated from experiments. The constant A represents the material "stiffness" at the unstretched state $U''(\ell_0) = A$, and B denotes a

characteristic length. With the D_0 distribution for isotropic plane stress case (Eq. (1.21)), the cohesive strength under equibiaxial stretching is given by

$$\sigma_c = \frac{D_0 \ell_0^4}{\Omega_0} \frac{AB\pi}{e(\ell_0 + B)} \tag{1.26}$$

where Ω_0 denotes representative volume. In the work by Klein *et al.* [27, 28], the VIB model has been used to simulate failure detection, crack propagation, and fracture toughening.

The features of VIB model are hereby summarized:

- It links the cohesive traction between material particles at the microstructural level and the material constitutive law at the macroscopic level, by equating the strain energy density and average value of cohesive bond potential. No cohesive surface is explicitly generated in the numerical simulation.
- The elastic parameters, *e.g.* Young's modulus E and Poisson's ratio ν, are no longer constant, but depend on the cohesive bond behavior, which in turn depends on local deformation. With accumulated strain localization, material becomes weaker.

1.3 Functionally Graded Material (FGM)

Functionally graded materials or FGMs are a new generation of engineered composites characterized by spatially varied microstructures accomplished through nonuniform distribution of the reinforcement phase with different properties, sizes and shapes, as well as by interchanging the roles of reinforcement and matrix (base) materials in a continuous manner. This new concept of engineering the material microstructure and recent advances in material processing science allows one to fully integrate material and structural design considerations [34].

The initial emphasis for FGMs focused on the synthesis of thermal barrier coatings for space applications, however, subsequent investigations have addressed a wide variety of applications [38]. Many of these applications involve dynamic events such as blast protection for critical structures and armors for ballistic protection. For example, a functionally graded armor composite with a tailored ceramic to metal through-thickness gradient combines the beneficial effects of ceramics (e.g. hardness) and metals (e.g. toughness) in the same material system while suppressing adverse strength reduction that would occur with discrete interfaces [7]. Gooch et al. [13] have reported on an investigation of functionally graded TiB/Ti armors. Other applications of FGMs include bone and dental implants, piezoelectric and thermoelectric devices, optical materials with graded refractive indices, and spaceflight structures [38, 34]. New applications are continuously being discovered.

Fracture mechanics of FGMs have been an active area of research [11]. For instance, Kim and Paulino [19-25] have provided techniques for evaluating mixed-mode stress intensity factors, J-integrals, interaction integrals, T-stress, and crack initiation angles under static and quasi-static conditions for both isotropic and anisotropic materials. Some of the experimental work will be referred to in Chapter 5, where numerical simulation is performed and compared with experimental results.

1.4 Finite Element Formulation

To incorporate a cohesive zone model into the numerical approach of dynamic fracture investigation, the *cohesive element* is developed and implemented as part of the finite element scheme, which follows the cohesive *traction-separation* relationship, *e.g.*, the models discussed above. In contrast, the conventional finite element, which is now called "*bulk* element" or "*volumetric* element", follows the conventional *stress-strain* relationship.

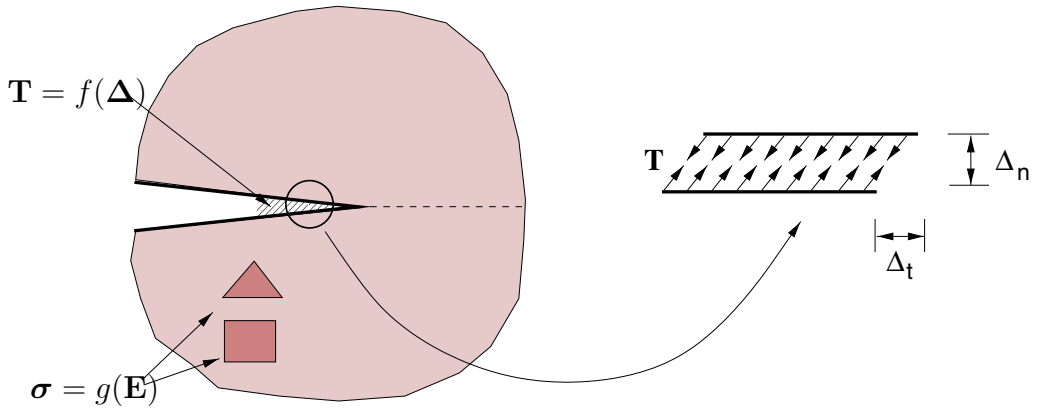

Figure 1.7: Schematic representation of *bulk* elements and *cohesive* elements in the finite element formulation.

Figure 1.7 illustrates the concept of the two classes of elements. The bulk behavior of the material is counted for by the conventional volumetric elements, whose constitutive relationship is usually defined by Hooke's Law. To model fracture initiation and propagation, cohesive elements are positioned along the possible path of crack propagation, attached to the volumetric elements, and are capable of performing decohesion, depending on whether the decohesion force the element experiences has exceeded the cohesive strength. The constitutive law of cohesive elements is inherently embedded in the finite element model, so that the presence of cohesive elements would allow spontaneous crack propagation, and thus it is

very promising in the investigation of bifurcation and/or impact dynamic loading problem, where multiple crack paths are possible.

The FEM formulation with cohesive elements can be derived from the principle of virtual work, as described in the following. The principle of virtual work of the 2D dynamic finite element formulation can be expressed as ([46]):

$$\int_{\Omega} (\mathrm{div}\boldsymbol{\sigma} - \rho\ddot{\mathbf{u}})\, \delta\mathbf{u} d\Omega - \int_{\Gamma} (\mathbf{T} - \boldsymbol{\sigma}\mathbf{n}) \delta\mathbf{u}\, d\Gamma = 0 \tag{1.27}$$

where Ω represents domain area, Γ denotes boundary line with normal vector $\mathbf{n}$, $\mathbf{u}$ is the displacement vector, $\mathbf{T}$ is the traction at boundary, and $\boldsymbol{\sigma}$ is the Cauchy stress tensor. The superposed dot in $\ddot{\mathbf{u}}$ denotes differentiation with respect to time, and ρ is the material density. If cohesive surface is *not* considered, by applying divergence theorem and integral by parts to the general expression in (1.27), the following conventional expression can be obtained:

$$\int_{\Omega} (\boldsymbol{\sigma} : \delta\mathbf{E} + \rho\ddot{\mathbf{u}} \cdot \delta\mathbf{u})\, d\Omega - \int_{\Gamma_{ext}} \mathbf{T}_{ext} \cdot \delta\mathbf{u}\, d\Gamma_{ext} = 0 \tag{1.28}$$

where Γ_{ext} represents the boundary line on which external traction $\mathbf{T}_{ext}$ is applied, and $\mathbf{E}$ is the Green strain tensor. When the cohesive surface is considered, the contribution of cohesive traction-separation work emerges when the integral by parts technique is applied to (1.27), and one more term appears in the resultant expression:

$$\int_{\Omega} (\boldsymbol{\sigma} : \delta\mathbf{E} + \rho\ddot{\mathbf{u}} \cdot \delta\mathbf{u})\, d\Omega - \int_{\Gamma_{ext}} \mathbf{T}_{ext} \cdot \delta\mathbf{u}\, d\Gamma_{ext} - \int_{\Gamma_{coh}} \mathbf{T}_{coh} \cdot \delta\Delta\mathbf{u}\, d\Gamma_{coh} = 0 \tag{1.29}$$

where Γ_{coh} represents the internal cohesive surfaces Γ_{coh} on which the cohesive tractions $\mathbf{T}_{coh}$ and displacement jumps $\Delta\mathbf{u}$ are present. Notice that in FGMs the mass density is no longer constant, but depends on position.

The integrals in Eqs. (1.27-1.29) are carried out in the deformed configuration. If infinitesimal deformation is assumed, the undeformed configuration can be used instead. However, when using finite deformation formulation, it is preferable to convert the integral from deformed configuration to original configuration, and work conjugates other than $\boldsymbol{\sigma}$ and $\mathbf{E}$ are used instead. The large deformation formulation scheme is briefly described in the following.

In finite deformation domain, we define the displacement vector $\mathbf{u}$ as

$$\mathbf{u} = \mathbf{x} - \mathbf{X} \tag{1.30}$$

where $\mathbf{x}$ and $\mathbf{X}$ denote the location of material point in the undeformed and deformed

configurations, respectively. The deformation gradient tensor $\mathbf{F}$ and the Lagrangian strain tensor $\mathbf{E}$ are defined as

$$\mathbf{F} = \frac{\partial \mathbf{x}}{\partial \mathbf{X}}, \tag{1.31}$$

$$\mathbf{E} = \frac{1}{2}(\mathbf{F}^T\mathbf{F} - \mathbf{I}), \tag{1.32}$$

respectively, where $\mathbf{I}$ is a fourth-order identity tensor.

The principle of virtual work (1.27), with all quantities referred to undeformed configuration, can be re-written as

$$\int_\Omega (\mathrm{div}\mathbf{P} - \rho\ddot{\mathbf{u}})\,\delta\mathbf{u} d\Omega - \int_\Gamma (\mathbf{T} - \mathbf{P}\mathbf{n})\delta\mathbf{u}\, d\Gamma = 0 \tag{1.33}$$

where Ω represents domain area, Γ denotes boundary line with normal vector $\mathbf{n}$ and $\mathbf{T}$ is the traction at boundary. The first Piola-Kirchhoff stress tensor $\mathbf{P}$ is related to the Cauchy stress tensor $\boldsymbol{\sigma}$ as

$$\mathbf{P} = J\boldsymbol{\sigma}\mathbf{F}^{-T}, \quad \text{where } J = det\mathbf{F} \tag{1.34}$$

At the boundary, the following relationship holds: $\mathbf{T} = \mathbf{P}\mathbf{n}$. By applying the divergence theorem and integral by parts to the general expression in (1.33), if cohesive surface is *not* considered, the following conventional expression can be obtained (in the absence of cohesive surface):

$$\int_\Omega (\mathbf{P} : \delta\mathbf{F} + \rho\ddot{\mathbf{u}} \cdot \delta\mathbf{u})\, d\Omega - \int_{\Gamma_{ext}} \mathbf{T}_{ext} \cdot \delta\mathbf{u}\, d\Gamma_{ext} = 0 \tag{1.35}$$

When the cohesive surface is considered, one more term appears in the resultant expression:

$$\int_\Omega (\mathbf{P} : \delta\mathbf{F} + \rho\ddot{\mathbf{u}} \cdot \delta\mathbf{u})\, d\Omega - \int_{\Gamma_{ext}} \mathbf{T}_{ext} \cdot \delta\mathbf{u}\, d\Gamma_{ext} - \int_{\Gamma_{coh}} \mathbf{T}_{coh} \cdot \delta\Delta\mathbf{u}\, d\Gamma_{coh} = 0 \tag{1.36}$$

By means of the following relationship for the second Piola-Kirchhoff stress tensor $\mathbf{S}$

$$\mathbf{S} = \mathbf{F}^{-1}\mathbf{P} = J\mathbf{F}^{-1}\boldsymbol{\sigma}\mathbf{F}^{-T} \tag{1.37}$$

the alternative expression of Eqn. (1.36) becomes

$$\int_\Omega (\mathbf{S} : \delta\mathbf{E} + \rho\ddot{\mathbf{u}} \cdot \delta\mathbf{u})\, d\Omega - \int_{\Gamma_{ext}} \mathbf{T}_{ext} \cdot \delta\mathbf{u}\, d\Gamma_{ext} - \int_{\Gamma_{coh}} \mathbf{T}_{coh} \cdot \delta\Delta\mathbf{u}\, d\Gamma_{coh} = 0 \tag{1.38}$$

In the present work the explicit central difference time stepping scheme [5] is used, and

the updating scheme for nodal displacements, accelerations and velocities from time step n to $n+1$ is:

$$\mathbf{u}_{n+1} = \mathbf{u}_n + \Delta t \dot{\mathbf{u}}_n + \frac{1}{2}\Delta t \ddot{\mathbf{u}}_n \tag{1.39}$$

$$\ddot{\mathbf{u}}_{n+1} = \mathbf{M}^{-1}(\mathbf{F} + \mathbf{R}_{int_{n+1}} - \mathbf{R}_{coh_{n+1}}) \tag{1.40}$$

$$\dot{\mathbf{u}}_{n+1} = \dot{\mathbf{u}}_n + \frac{\Delta t}{2}(\ddot{\mathbf{u}}_n + \ddot{\mathbf{u}}_{n+1}) \tag{1.41}$$

where Δt denotes the time step, $\mathbf{M}$ is the mass matrix, $\mathbf{F}$ is the external force vector, $\mathbf{R}_{int}$ and $\mathbf{R}_{coh}$ are the global internal and cohesive force vectors, which are obtained from the contribution of *bulk* and *cohesive* elements, respectively.

The formulation described above applies to both homogeneous and FGM problems. By introducing the generalized isoparametric element formulation in the numerical scheme, the material gradient is treated appropriately at element level. The discussion of the generalized isoparametric element will be carried out in Chapter 2. The detailed FEM formulation of the internal force vector $\mathbf{R}_{int}$ and cohesive force vector $\mathbf{R}_{coh}$ can be found in the appendix.

1.5 Thesis Organization

The contents of the remaining Chapters of this thesis are outlined as follows. The dynamic behavior of FGMs (without crack) is investigated in Chapter 2. Section 2.1 presents the explicit dynamic scheme for the FEM without cohesive element. Section 2.2 introduces the concept of *generalized isoparametric formulation*, which is employed to treat material gradation. Section 2.3 discusses wave speed in FGMs and the time step used for the explicit updating scheme. Section 2.4 provides simulations for two example problems to validate the code and to investigate the influence of material gradation on the dynamic behavior of FGMs. Chapter 3 presents two cohesive zone models for FGMs and energy terms involved in the CZM approach. Section 3.1 describes a CZM which uses effective quantities (for calculation of displacement jump and traction) to deal with mode mixity. Section 3.2 describes the extension of an existing CZM for FGMs, which employs actual displacement jump and traction quantities instead of effective quantities. A critical discussion on the features and potential drawbacks of these two models are presented in Section 3.3. Energy terms in the CZM simulation are described in Section 3.4 along with a simple example. Chapter 4 focuses on the general issues of the cohesive elements implementation. Section 4.1 provides detailed procedures of mesh generation with cohesive elements and includes a few examples. Section 4.2 studies the stability and accuracy of the numerical scheme, which are influenced by the

various parameters of the cohesive model adopted, as well as the geometry discretization employed. Chapter 5 provides three problems which focus on various capabilities of the CZM approach in modelling dynamic fracture propagation in FGMs, and demonstrates the influence of material gradation on the fracture behavior. Section 5.1 presents the simulation of spontaneous crack growth in an elastic strip, combined with mesh convergence study, as well as evidence of spontaneous *crack nucleation* (without initial crack) capability of the CZM. Section 5.2 presents the the simulation of crack growth in a 3-point-bending FGM specimen and the results are compared to experimental results. Section 5.3 demonstrates the capacity of crack branching with CZM approach by simulating a plate subjected to impact loading with cohesive elements in a large region. The simulation results presented in the thesis are obtained from the small deformation formulation except for the branching problem presented in Section 5.3. Finally, a summary of the current work and some suggestions for future work are presented in Chapter 6.

Chapter 2

Dynamic Behavior of Bulk Material

The dynamic behavior of FGM material is investigated with only bulk elements and no cohesive elements involved, so that the influence of bulk and cohesive elements on the stability and accuracy of the FEM analysis can be differentiated. In this Chapter, first the explicit updating scheme tailored for the framework without cohesive elements is given, then the graded element formulation of FGM bulk material is presented, and finally results for two classes of problems are presented. A cantilever beam subjected to transient point load is simulated to validate the code by comparing the results to those from analytical solution and modal analysis. The stress evolution history for a three-point bending beam subjected to impact loading is studied, which provides valuable insight on the prediction of crack initiation time sequence for different material gradient cases.

2.1 Explicit Dynamic Scheme

The dynamic updating scheme in bulk material is given by the following equations

$$\mathbf{u}_{n+1} = \mathbf{u}_n + \Delta t \dot{\mathbf{u}}_n + \frac{1}{2}\Delta t \ddot{\mathbf{u}}_n \tag{2.1}$$

$$\ddot{\mathbf{u}}_{n+1} = \mathbf{M}^{-1}(\mathbf{F} + \mathbf{R}_{int_{n+1}}) \tag{2.2}$$

$$\dot{\mathbf{u}}_{n+1} = \dot{\mathbf{u}}_n + \frac{\Delta t}{2}(\ddot{\mathbf{u}}_n + \ddot{\mathbf{u}}_{n+1}) \tag{2.3}$$

which can be obtained from Eqs. (1.39–1.41) by eliminating cohesive terms.

2.2 Generalized Isoparametric Element Formulation for FGM

To treat the material nonhomogeneity inherent in the problem, we can use either homogeneous elements with constant material properties at the element level, which are evaluated at the centroid of each element (Figure 2.1), or graded elements, which incorporate the material property gradient at the size scale of the element (Figure 2.2). The latter scheme (Kim and Paulino, [18]) was demonstrated to result in smoother and more accurate results than the homogeneous elements. In this scheme, the same shape functions are used to interpolate the unknown displacements, the geometry, and the material parameters, and hence earned the name *Generalized Isoparametric Element Formulation*. The interpolations for spatial coordinates (x, y), displacements (u, v) and material properties (E, ν, ρ) are given by

$$x = \sum_{i=1}^{m} N_i \; x_i, \qquad y = \sum_{i=1}^{m} N_i \; y_i \tag{2.4}$$

$$u = \sum_{i=1}^{m} N_i \; u_i, \qquad v = \sum_{i=1}^{m} N_i \; v_i \tag{2.5}$$

$$E = \sum_{i=1}^{m} N_i \; E_i, \qquad \nu = \sum_{i=1}^{m} N_i \; \nu_i, \qquad \rho = \sum_{i=1}^{m} N_i \; \rho_i \tag{2.6}$$

respectively, where N_i are the shape functions. The variations of material property, *e.g.*, Young's Modulus E, for graded and homogeneous elements are illustrated in Figure 2.2.

Both homogeneous and graded elements are implemented in the code, however, for the reasons given above, we prefer to use the graded elements. It is evident from Figure 2.1 and Figure 2.2 that the graded elements can approximate the material gradation much better, with a smooth transition at element boundaries (though not perfectly smooth, we naturally expect), while the homogeneous elements give a staircase-like profile. Using graded elements will be particularly beneficial within regions with coarse mesh or with high stress gradient. Therefore, the volumetric elements employed to address problems presented in the thesis are T6/T3 elements, with 3/4 Gauss points for T6 elements and 1 Gauss point for T3 element (Figure 2.3). The choice of triangular elements in favor of quadrilateral elements is because the former element allows crack to grow in more arbitrary directions. For example, the triangular elements of 45° orientation allow crack to grow along either 0°, ±45° or ±90°, while the quadrilateral elements only allow crack to grow along horizontal or vertical directions.

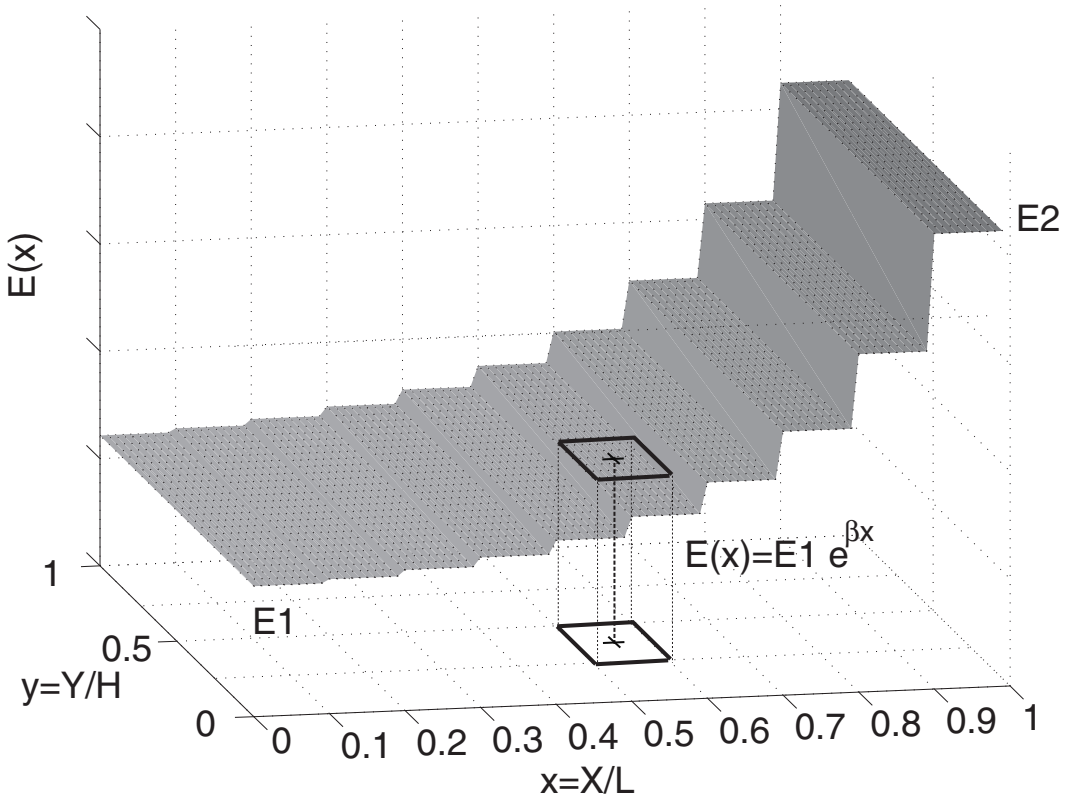

Figure 2.1: Material properties evaluated at the centroid of homogeneous elements, and used for whole element. Exponential gradation in x direction for Young's modulus E is provided as example

2.3 Wave Speed in FGM and Time Step Control

The stability of conventional explicit finite element schemes is usually governed by the Courant condition [3], which provides an upper limit for the size of the time step Δt:

$$\Delta t \leq \frac{\ell_e}{C_d} \tag{2.7}$$

where ℓ_e is the mesh equivalent length of the shortest distance between two nodes, and the dilatational wave speed C_d is expressed in terms of the material elastic constants $E = E(\mathbf{x})$, $\nu = \nu(\mathbf{x})$, and density $\rho = \rho(\mathbf{x})$ as

$$C_d(\mathbf{x}) = \sqrt{\frac{E(\mathbf{x})(1-\nu(\mathbf{x}))}{(1+\nu(\mathbf{x}))(1-2\nu(\mathbf{x}))\rho(\mathbf{x})}}: \quad \text{plane strain} \tag{2.8}$$

$$C_d(\mathbf{x}) = \sqrt{\frac{E(\mathbf{x})}{(1+\nu(\mathbf{x}))(1-\nu(\mathbf{x}))\rho(\mathbf{x})}}: \quad \text{plane stress} \tag{2.9}$$

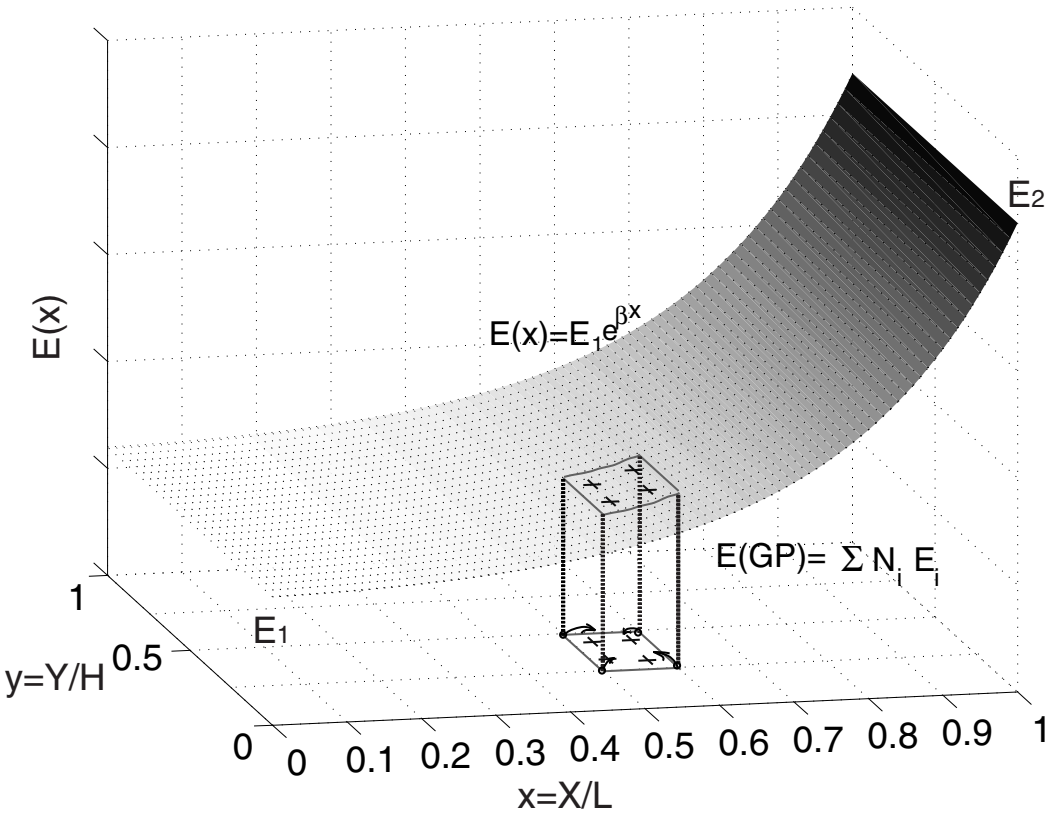

Figure 2.2: Material property first evaluated at element nodes and interpolated to Gauss points using shape functions (2.6). Exponential gradation in x direction for Young's modulus E is provided as example.

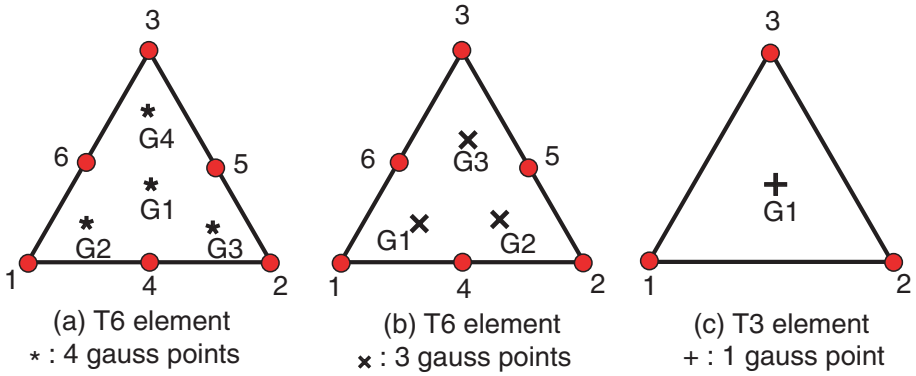

Figure 2.3: T6 and T3 elements and Gauss points

This expression of dilatational wave speed assumes linear elasticity, and since our problem is restricted to linear elasticity, this expression applies for the explicit FEM formulation. However, since for FGM all material properties could vary in space, C_d is no longer a constant. To simplify the implementation, the maximum wave speed is calculated depending on the

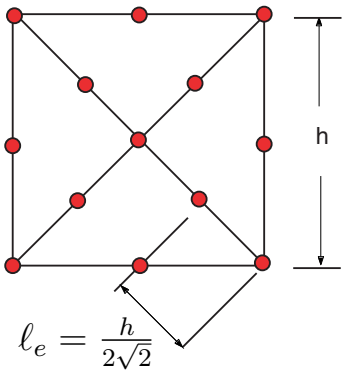

Figure 2.4: Shortest distance between nodes for computing Δ_t.

profile of the material property, and a uniform maximum time step is applied to the whole structure.

Table 2.1 provides wave speeds for a few materials, in which C_S and C_R denote the shear wave speed and Rayleigh wave speed, respectively. This table gives an idea about the range of materials used in this work.

Table 2.1: Wave speeds for a few materials

Material	$C_d\,(m/s)$	$C_S\,(m/s)$	$C_R\,(m/s)$
Air	345	/	/
PMMA	2090	1004	939
Steel	6001	3208	2975
Zirconia	6882	3611	3355

2.4 Homogeneous and Functionally Graded Beams

The dynamic behavior of bulk FGM structures is of significant importance due to various engineering applications (*e.g.*vibration problems, impact loading). We perform a thorough check of stability and accuracy before we proceed to cohesive elements formulation and fracture analysis. Two classes of problems are addressed here, one is an FGM cantilever beam under tip point load, with material gradation in either length or height direction; the other is an FGM beam under prescribed point velocity load, where the results are compared to those of Rousseau and Tippur's [40].

2.4.1 Transient Point Loading

The response of a cantilever beam under transient point load is a classical dynamics problem with well-established solution. Investigating a problem that is simple, yet involves rich

dynamics, serves as a good starting point that can reveal many important dynamics characteristics particular to FGMs, as well as providing a strong foothold for more complex problems. First the analytical solution for a homogeneous beam under transient point load is given, next the Rayleigh-Ritz method is employed to evaluate the influence of material gradation profile on the natural frequencies and modes of the structure. This result is further verified with FEM modal analysis, which revealed some interesting features that had been neglected by the Rayleigh-Ritz method. Finally, the responses of FGM beams of different material gradation profile are compared for two loading cases, which are in agreement with the prediction of the Rayleigh-Ritz method.

Transient Point Loading. Consider the cantilever beam illustrated by Figure 2.5. The beam is of length $L = 2mm$, Height $H = 0.1mm$ (Figure 2.5), loading (Figure 2.6) is uniformly distributed along the free end of the beam, and consists of a sine pulse of duration T chosen as the period of the fundamental vibration mode of the cantilever beam, *i.e.*,

$$T = \frac{2\pi}{\omega_1} \tag{2.10}$$

where ω_1 is the fundamental frequency of the beam. The natural frequencies ω_i of the cantilever beam are given by

$$\omega_i^2 = \lambda_i^4 \frac{EI}{\rho A} \tag{2.11}$$

where A, E, ρ and I denote the beam cross-sectional area, stiffness, density and moment of the inertia, respectively, and [8]

$$\lambda_1 = 1.875/L, \quad \lambda_2 = 4.694/L, \quad \lambda_3 = 7.855/L, ... \tag{2.12}$$

The tip deflection is given by Warburton (1976, [47]) as

$$\begin{aligned} w(L,t) &= 4\frac{P}{m}\sum_{i=1}^{n}\left[\frac{1}{\omega_i}\int_0^l \sin\frac{\pi\tau}{T}\sin\omega_i(t-\tau)d\tau\right] \qquad for\ 0 \le t \le T \\ &= 4\frac{PL^3}{EI}\sum_{i=1}^{n}\left[\frac{\pi/\left(\omega_i T\right)}{\left(\lambda_i L\right)^4\left(\left(\omega_i T\right)^2-1\right)}\left\{\begin{array}{c}\left(\cos\omega_i T+1\right)\sin\omega_i(t-T)\\ +\sin\omega_i T\cos\omega_i(t-T)\end{array}\right\}\right] for\ t \ge T \end{aligned} \tag{2.13}$$

The T6 elements, with mesh discretization shown in Figure 2.5, produced very good results compared with the analytical solution expressed in Eq. (2.13), as demonstrated in Figure 2.7. which shows that both results agree with plotting accuracy. We next investigate the influence of material gradation.

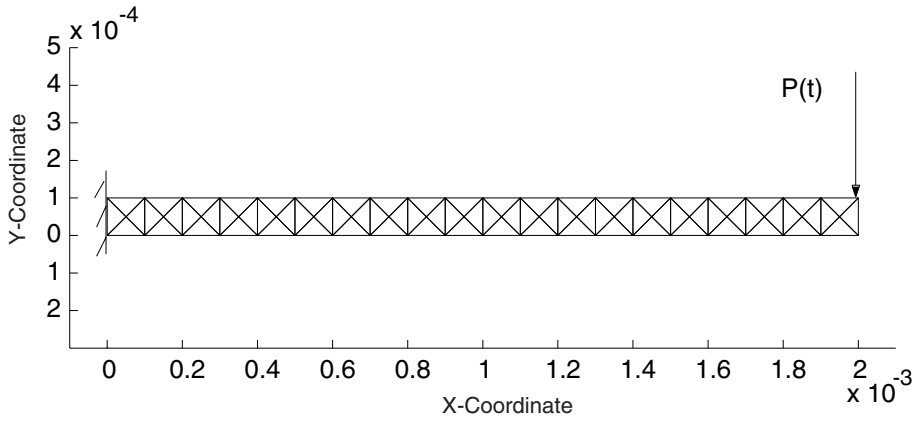

Figure 2.5: Geometry and discretization (203 nodes, 80 T6 elements) of cantilever beam

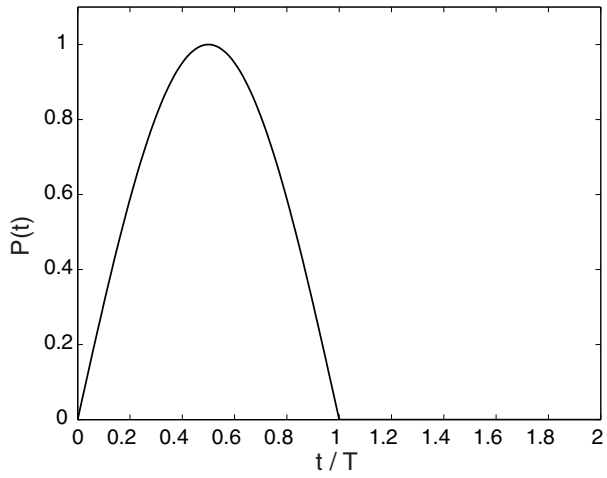

Figure 2.6: Normalized load history

Material Gradation Profiles. For the FGM cantilever beam under consideration, material gradation can be in either x or y direction (Figure 2.8). For each direction, three material gradation profiles were considered: exponential, linear, and equivalent homogeneous beam, which can be expressed as follows (assume material properties vary in x direction).

For exponential material gradation

$$E(x) = E_1 e^{\alpha x}$$
$$\rho(x) = \rho_1 e^{\beta x}$$
$$\nu(x) = \nu_1 e^{\gamma x}$$

where α, β and γ are the material gradation parameters for E, ρ and ν, respectively.

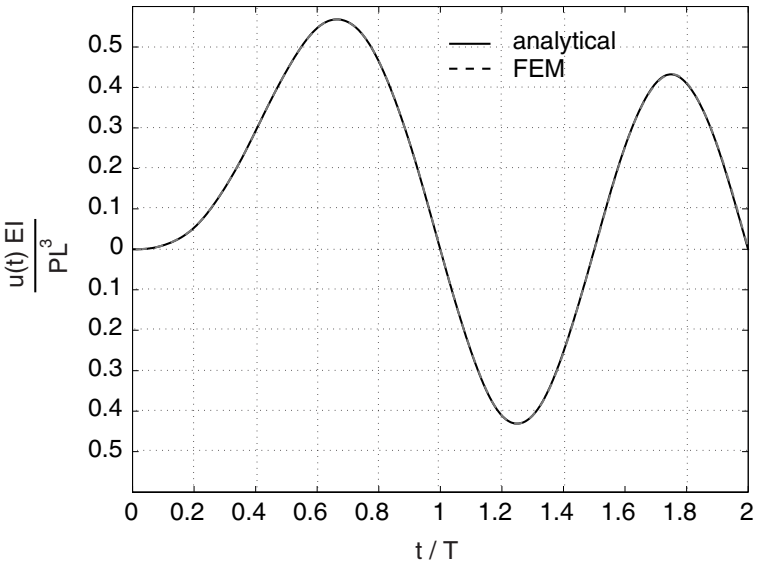

Figure 2.7: Normalized displacement of homogeneous cantilever beam

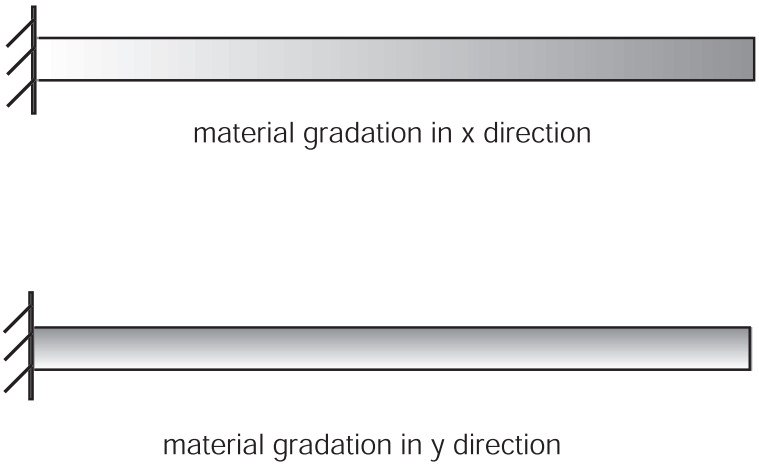

Figure 2.8: beam material gradation direction

For linear material variation

$$\begin{aligned} E(x) &= E_1 + (E_2 - E_1)x/L \\ \rho(x) &= \rho_1 + (\rho_2 - \rho_1)x/L \\ \nu(x) &= \nu_1 + (\nu_2 - \nu_1)x/L \end{aligned} \tag{2.14}$$

For equivalent homogeneous beam

$$\begin{aligned}\overline{E} &= \frac{1}{A}\int E(x)dA \\ \overline{\rho} &= \frac{1}{A}\int \rho(x)dA \\ \overline{\nu} &= \frac{1}{A}\int \nu(x)dA\end{aligned} \tag{2.15}$$

which are defined as the equivalent material constants.

Modal Analysis using Rayleigh-Ritz method. The governing equation for the cantilever beam problem under consideration is

$$\frac{\partial^2}{\partial x^2}\left[E(x)I\frac{\partial^2}{\partial x^2}q(x,t)\right] + \rho(x)A\frac{\partial^2}{\partial t^2}q(x,t) = f(x,t) \tag{2.16}$$

where $q(x,t)$ is the beam response under load $f(x,t)$. To solve the eigenvalue problem, we set $f(x,t) = 0$, and $q(x,t)$ harmonic in time, *i.e.*,

$$q(x,t) = u\,(x)\,e^{i\omega t} \tag{2.17}$$

where ω is frequency and $u(x)$ is the corresponding mode shape, and there are infinite solutions sets for a continuum problem. The kinetic energy of the system can be written as

$$\begin{aligned}T(t) &= \tfrac{1}{2}\int_0^L \rho(x)A\left(\frac{\partial q(x,t)}{\partial t}\right)^2 dx \\ &= \tfrac{1}{2}\omega^2 e^{2i\omega t}\int_0^L \rho(x)A\left(u(x)\right)^2 dx\end{aligned} \tag{2.18}$$

and the potential energy has the form

$$\begin{aligned}V(t) &= \tfrac{1}{2}\int_0^L \left[E(x)I\left(\frac{\partial q^2(x,t)}{\partial x^2}\right)\right]\left(\frac{\partial q^2(x,t)}{\partial x^2}\right)dx \\ &= \tfrac{1}{2}e^{2i\omega t}\int_0^L E(x)I\left(\frac{\partial u^2(x)}{\partial x}\right)^2 dx\end{aligned} \tag{2.19}$$

For a conservative system the total energy E is constant, i.e.

$$E = 0 + T_{\max} = V_{\max} + 0 \tag{2.20}$$

from which it follows that

$$T_{\max} = V_{\max} \tag{2.21}$$

Define reference kinetic energy

$$T^* = \tfrac{1}{2} \int_0^L \rho(x) A \left(u(x)\right)^2 dx \tag{2.22}$$

and introduce Eqs. (2.19) and (2.22) into (2.21), we obtain the Rayleigh's quotient

$$R(u) = \omega^2 = \frac{V_{\max}}{T^*} = \frac{\int_0^L E(x) I \left[u''(x)\right]^2 dx}{\int_0^L \rho(x) A \left(u(x)\right)^2 dx} = \frac{N(u)}{D(u)} \tag{2.23}$$

where

$$\begin{aligned} N(u) &= \int_0^L E(x) I \left[u''(x)\right]^2 dx \\ D(u) &= \int_0^L \rho(x) A \left(u(x)\right)^2 dx \end{aligned} \tag{2.24}$$

in which the prime denote $\partial/\partial x$. If u chosen for the (2.23) happens to be a true mode function, the ω solved will be the corresponding frequency. The stationarity of Rayleigh quotient states that "The frequency of vibration of a conservative system vibrating about an equilibrium position has a stationary value in the neighborhood of a natural mode".([31]), hence we can construct trial modes functions and try to minimize the Rayleigh's quotient. A trial mode function can be constructed as

$$u_n(x) = \sum_{i=1}^{n} a_i \phi_i(x)$$

where a_i are coefficients to be determined and ϕ_i are admissible functions that satisfy all the essential boundary conditions

$$\begin{aligned} \phi(0) &= 0 \\ \phi'(0) &= 0 \end{aligned} \tag{2.25}$$

The necessary conditions for the minimum of Rayleigh's quotient are

$$\frac{\partial R(u)}{\partial a_j} = \frac{D(u)\left[\partial N(u)/\partial a_j\right] - N(u)\left[\partial D(u)/\partial a_j\right]}{D^2(u)} = 0, \qquad j = 1, 2..., n \tag{2.26}$$

from which it follows

$$\frac{\partial N(u)}{\partial a_j} - \lambda \frac{\partial D(u)}{\partial a_j} = 0, \qquad j = 1, 2..., n \tag{2.27}$$

where λ is defined as the minimum estimated value of Rayleigh's quotient

$$\min(R(u)) = \lambda$$

Now we define

$$\begin{aligned} \mathbf{K}_{ij} &= \int_0^l E\,(x)\, I \frac{\partial \phi_i(x)}{\partial x} \frac{\partial \phi_j(x)}{\partial x} dx \\ \mathbf{M}_{ij} &= \int_0^l \rho\,(x)\, A \phi_i(x) \phi_j(x) dx \end{aligned} \tag{2.28}$$

The symmetry of matrices $\mathbf{K}$ and $\mathbf{M}$ can be confirmed by proving that the eigenvalue problem under consideration is self-adjoint:

For any two arbitrary comparison functions u and v which satisfy all boundary conditions, *i.e.* essential boundary conditions

$$\begin{aligned} u(0) &= 0, \qquad v(0) = 0 \\ u'(0) &= 0, \qquad v'(0) = 0 \end{aligned} \tag{2.29}$$

as well as natural boundary conditions

$$\begin{aligned} EIu''|_{x=L} &= 0 \\ \left(EIu''\right)'|_{x=L} &= 0 \end{aligned} \tag{2.30}$$

then the system is self-adjoint provided the following statements hold true

$$\begin{aligned} \int_0^l uL(v)dx &= \int_0^l vL(u)dx \\ \int_0^l uM(v)dx &= \int_0^l vM(u)dx \end{aligned} \tag{2.31}$$

where the linear operators L and M for the current problem are

$$\begin{aligned} L &= \frac{\partial^2}{\partial x^2}\left(E(x)I\frac{\partial^2}{\partial x^2}\right) \\ M &= \rho(x)A \end{aligned} \tag{2.32}$$

By means of integrations by part we can easily prove (2.31):

$$\begin{aligned} \int_0^l uL(v)dx &= \int_0^l u\frac{\partial^2}{\partial x^2}\left(E(x)I\frac{\partial^2 v}{\partial x^2}\right)dx \\ &= \left[uE(x)Iv'\right]|_0^L - \int_0^l \frac{\partial u}{\partial x}\frac{\partial}{\partial x}\left(E(x)I\frac{\partial^2 v(x)}{\partial x^2}\right)dx \\ &= 0 - \left[u'E(x)Iv'\right]|_0^L + \int_0^l \frac{\partial^2 u}{\partial x^2}\left(E(x)I\frac{\partial^2 v(x)}{\partial x^2}\right)dx \\ &= 0 - 0 + \left[u''E(x)Iv\right]|_0^L - \int_0^l \frac{\partial}{\partial x}\left(\frac{\partial^2 u}{\partial x^2}E(x)I\right)\frac{\partial v}{\partial x}dx \\ &= 0 - 0 + 0 - \left[\left[u''E(x)I\right]v\right]|_0^L - \int_0^l \frac{\partial^2}{\partial x^2}\left(E(x)I\frac{\partial^2 u}{\partial x^2}\right)vdx \\ &= \int_0^l vL(u)dx \end{aligned} \tag{2.33}$$

and the same to

$$\int_0^l uM(v)dx = \int_0^l vM(u)dx \tag{2.34}$$

since the system is self-adjoint, we have

$$\mathbf{K}_{ij} = \mathbf{K}_{ji,} \qquad \mathbf{M}_{ij} = \mathbf{M}_{ji} \tag{2.35}$$

Now $N(u)$ can be written in terms of $\mathbf{K}_{ij}$ as

$$\begin{aligned} N(u) &= \int_0^L E(x)I\left[u''(x)\right]^2 dx \\ &= \int_0^L E(x)I\left[\sum_{i=1}^n a_i\phi_i''(x)\right]\left[\sum_{j=1}^n a_j\phi_j''(x)\right]dx \\ &= \sum_{i=1}^n\sum_{j=1}^n a_i a_j \int_0^L E(x)I\phi_i''(x)\phi_j''(x)dx \\ &= \sum_{i=1}^n\sum_{j=1}^n \mathbf{K}_{ij}a_i a_j \end{aligned} \tag{2.36}$$

and similarly $D(u)$ as

$$N(u) = \sum_{i=1}^{n}\sum_{j=1}^{n} \mathbf{M}_{ij} a_i a_j \tag{2.37}$$

Taking the partial derivatives with respect to a_r and recalling the symmetry of the coefficients $\mathbf{K}_{ij}$, we write

$$\begin{aligned}
\frac{\partial N}{\partial a_r} &= \sum_{i=1}^{n}\sum_{j=1}^{n} \left(\mathbf{K}_{ij} \frac{\partial a_i}{\partial a_r} a_j + \mathbf{K}_{ij} a_i \frac{\partial a_j}{\partial a_r} \right) \\
&= \sum_{i=1}^{n}\sum_{j=1}^{n} \left(\mathbf{K}_{ij} \delta_{ir} a_j + \mathbf{K}_{ij} a_i \delta_{jr} \right) \\
&= \sum_{j=1}^{n} \mathbf{K}_{rj} a_j + \sum_{i=1}^{n} \mathbf{K}_{ir} a_i \\
&= 2\sum_{j=1}^{n} \mathbf{K}_{rj} a_j, \qquad r = 1, 2, ..., n.
\end{aligned} \tag{2.38}$$

and similarly,

$$\frac{\partial D}{\partial a_r} = 2\sum_{j=1}^{n} \mathbf{M}_{rj} a_j, \qquad r = 1, 2, ..., n. \tag{2.39}$$

Introducing (2.38–2.39) into (2.27) we obtain

$$\sum_{j=1}^{n} (\mathbf{K}_{rj} - \lambda \mathbf{M}_{rj}) a_j = 0, \qquad r = 1, 2, ..., n. \tag{2.40}$$

which represent a set of n homogeneous algebraic equations in the unknowns a_j, and $\mathbf{K}$ is the stiffness matrix and $\mathbf{M}$ is the mass matrix. Note that $\lambda = \omega^2$, render the linear Eqs. (2.40) into matrix form

$$\mathbf{K} = \omega^2 \mathbf{M} \tag{2.41}$$

we can solve for the natural frequencies and corresponding modes, and the frequencies ω provide upper bounds for the true frequencies ω^* ([31]):,

$$\omega \geq \omega^* \qquad r = 1, 2, ..., n. \tag{2.42}$$

The base functions chosen for the FGM cantilever beams under consideration are the polynomial series:

$$\phi_1(x) = x^2, \quad \phi_2(x) = x^3, \quad \phi_3(x) = x^4, \quad \phi_4(x) = x^5 \tag{2.43}$$

and *etc.* By incorporating more and more terms in the formulation, the Rayleigh-Ritz method guarantees that, with a complete set of base functions, the solution approaches the exact value asymptotically. The results listed in table 2.2–2.4 are obtained for material properties

$$\begin{aligned} E_1 &= 1GPa, & E_2 &= 5GPa \\ \rho_1 &= 0.5g/cm^3, & \rho_2 &= 1.5g/cm^3 \end{aligned} \tag{2.44}$$

where subscript 1 denotes side where material elastic constants are lower, and 2 where it is larger.

Table 2.2: Natural frequency ω_1 for FGM beam and equivalent homogeneous beam, considering gradation in x direction, obtained from Rayleigh-Ritz method

num. of base functions	$\omega_1(\times 10^4)$					
	Exponential Variation			Linear Variation		
	SoftLHS	StiffLHS	Equiv.	SoftLHS	StiffLHS	Equiv.
2	2.7934	6.0983	4.2128	3.0405	6.2166	4.4159
3	2.6516	6.0705	4.1942	2.8388	6.2153	4.3963
4	2.6477	6.0673	4.1929	2.8183	6.2138	4.3950
5	2.2425	6.0666	4.1929	2.3823	6.2137	4.3950
6	2.2423	6.0655	4.1929	2.3816	6.2137	4.3950
Analytical			4.1929			4.3950

Table 2.3: ω_2 for FGM beam and equivalent homogeneous beam, considering gradation in x direction, obtained from Rayleigh-Ritz method

num. of base functions	$\omega_2(\times 10^4)$					
	Exponential Variation			Linear Variation		
	SoftLHS	StiffLHS	Equiv.	SoftLHS	StiffLHS	Equiv.
2	46.479	36.856	41.508	47.063	38.972	43.509
3	23.842	29.600	26.514	25.332	30.936	27.792
4	22.428	29.140	26.424	23.837	30.785	27.697
5	22.425	29.000	26.277	23.823	30.685	27.544
6	22.423	28.971	26.277	23.816	30.675	27.543
Analytical			26.277			27.543

In table 2.2–table 2.4, *SoftLHS*, *StiffLHS* and *Equiv.* denote the cases where the beam is softer at the clamped end, stiffer at the clamped end, and equivalent homogeneous beam as defined in (2.15). It is apparent that the beam which is softer at the clamped end has smaller natural frequency, thus the whole structure is more compliant than the case where the beam is stiffer at the clamped end. The equivalent homogeneous result is in between the other two, however it is not simply the average of the two.

Table 2.4: ω_3 for FGM beam and equivalent homogeneous beam, considering gradation in x direction, obtained from Rayleigh-Ritz method

num. of base functions	$\omega_2(\times 10^4)$					
	Exponential Variation			Linear Variation		
	SoftLHS	StiffLHS	Equiv.	SoftLHS	StiffLHS	Equiv.
3	168.62	114.65	140.89	167.70	118.71	147.68
4	73.990	79.009	75.542	77.142	82.066	79.183
5	69.346	76.547	75.414	72.671	80.779	79.050
6	68.793	75.224	73.598	72.428	79.645	77.145
7	68.680	74.948	73.596	72.415	79.521	77.144
8	68.676	74.945	73.575	72.407	79.519	77.122
Analytical			73.580			77.126

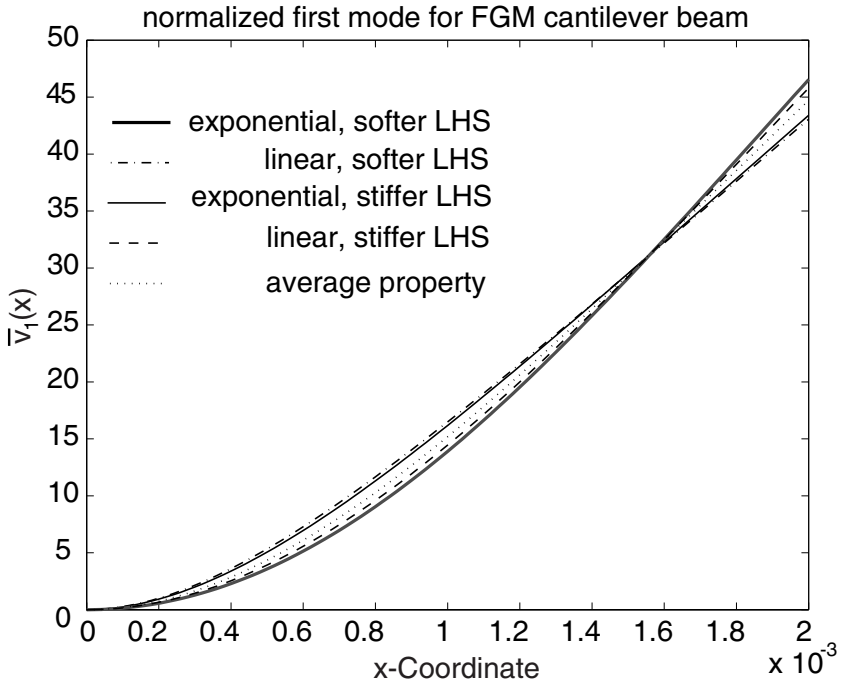

Figure 2.9: 1st mode shapes of FGM cantilever beams, Rayleigh-Ritz method

The analytical solution for the equivalent homogeneous beams in table 2.2-2.4 are obtained by substituting averaged material properties (2.15) into (2.11) and (2.12). Clearly the Rayleigh-Ritz method gives excellent estimation of lower frequencies at only a few base functions for this case, and for FGM beams the frequencies also converge pretty fast. However for higher modes we would expect that more terms are needed. Since Rayleigh-Ritz method is usually used to obtain lower frequencies, the study stopped at 3rd mode.

The first three mode shapes of the structure are plotted. It can be observed that for the

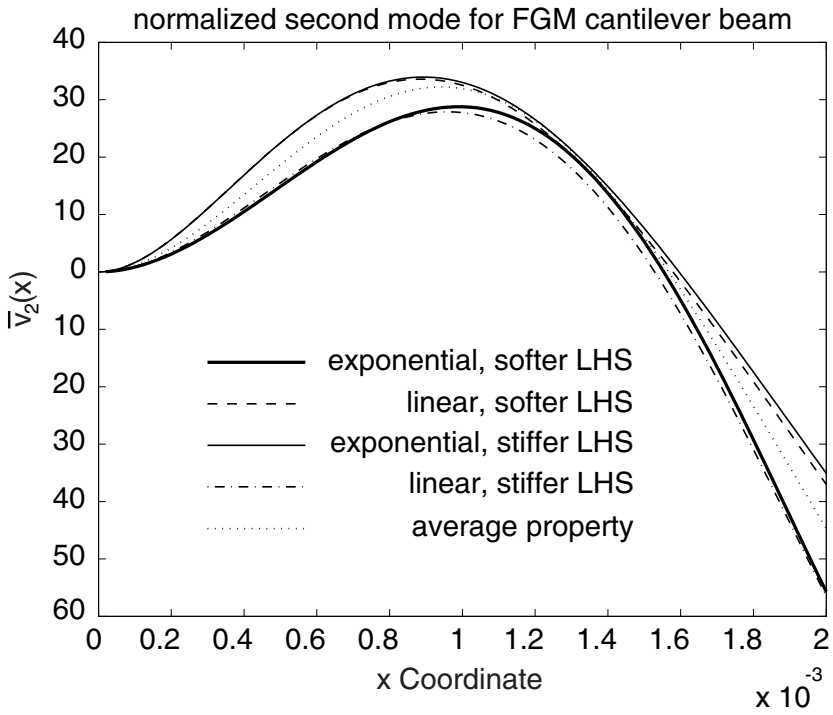

Figure 2.10: 2nd mode shape of FGM cantilever beams, Rayleigh-Ritz method

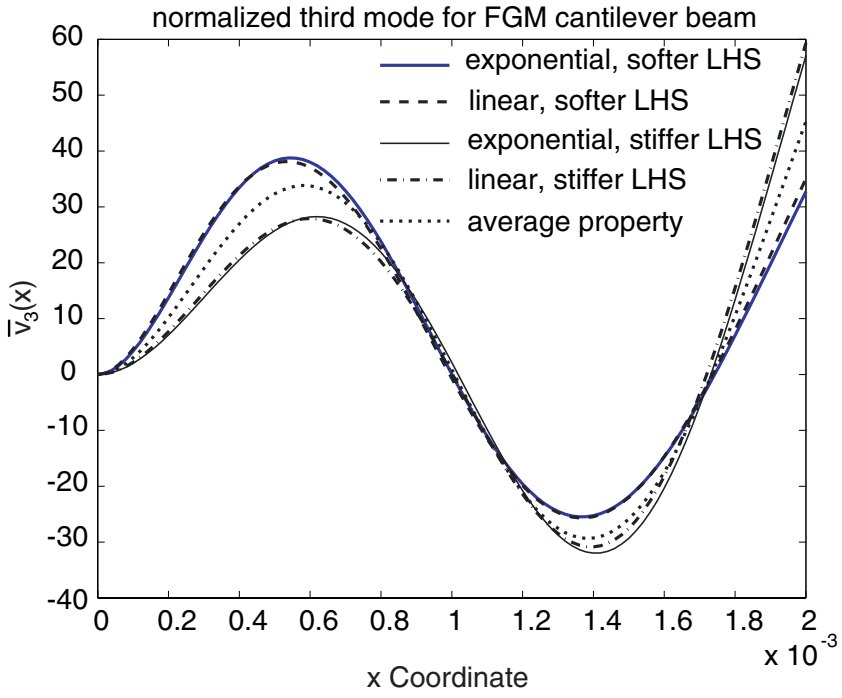

Figure 2.11: 3rd mode shapes of FGM cantilever beams, Rayleigh-Ritz method

normalized mode shape, which is defined as

$$\overline{v}_i(x) = \frac{v_i(x)}{\sqrt{\int_0^L v_i^2(x)dx}} \tag{2.45}$$

where $v_i(x)$ is the ith mode shape before normalization. The first mode is quite similar for all material gradation cases (Figure 2.9), while for higher mode the difference is more noticeable (Figure 2.10 and 2.11). However, Rayleigh-Ritz method provides better estimation of frequencies rather than mode shapes, so the results of mode shapes here can not be taken as seriously as the frequencies, and we will reexamine the results in light of its comparison with FEM results in the next section.

Modal Analysis using FEM. As an alternative approach to obtain the natural frequencies and modes, modal analysis by FEM is performed. The global stiffness matrix $\mathbf{K}$ and mass matrix $\mathbf{M}$ are assembled, and boundary conditions are introduced. Then we solve for

$$\mathbf{Ku} - \omega^2\mathbf{Mu} = \mathbf{0} \tag{2.46}$$

Table 2.5: Natural frequencies (w) for FGM beam and equivalent homogeneous beam from FEM modal analysis

	Exponential Variation				Linear Variation			
w ($\times 10^4$)	SofLHS	StiffLHS	Y_grad	Equiv.	SoftLHS	StiffLHS	Y_grad	Equiv.
ω_1	2.649	6.055	3.882	4.190	2.816	6.204	4.055	4.392
ω_2	22.15	28.63	24.08	25.97	23.52	30.31	25.16	27.22
ω_3	66.70	72.83	66.38	71.51	70.31	77.25	69.39	74.96
ω_4	93.86	136.36	127.19	129.89	100.20	144.48	133.13	136.15
ω_5	130.27	162.41	130.00	136.94	137.29	169.56	136.21	143.54
ω_6	211.04	217.14	205.04	220.16	222.47	229.82	214.70	230.77

Up to six natural frequencies are tabulated in table 2.5 for FGM beams and equivalent homogeneous beams, each with different material gradation profiles. Some conclusions can be drawn from table 2.5:

- Comparison of table 2.5 and table 2.2-2.4 reveals that the results from the two methods are in good agreement, while the values of FEM results are consistently a little lower than their counterparts from Rayleigh-Ritz method. This is one of the consequences of modeling the 2-D structure in 1-D model with Rayleigh-Ritz method employed in the previous section, where the Poisson ratio effect is overlooked, thus the structure stiffness is artificially increased, which results in slightly larger frequency values. Recall that by discretization in FEM the structural stiffness is larger than real structure, we

conclude that the frequencies obtained from Rayleigh-Ritz method and FEM are both larger than than that of real structure.

- The trend of influence of material gradation on frequency is consistent with the conclusion of Rayleigh-Ritz method, *i.e.* beams softer at clamped end are more compliant than beams stiffer at clamped end, thus producing smaller frequencies compared to the latter. For material gradation in Y direction, the results are close to that of equivalent homogeneous beams, yet a bit more compliant.

- At lower modes, the influence of different material gradation on frequencies are more pronounced than at higher modes *e.g.*, for exponential material gradation, at mode 1 the frequency for *SoftLHS* is 2.3 times of that for *StiffLHS* (6.055/2.649 = 2.29), while at mode 6, the ratio is merely 1.029 (217.14/211.04).

- Usually we expect the frequencies of consecutive modes to be at somewhat regular intervals, yet it is not always the case *e.g.*, for linear gradation in Y direction case, frequencies of $4th$ and $5th$ modes are 133.13 and 136.21, respectively, which are pretty close compared to the other frequency intervals (*e.g.*, $\omega_3 = 69.39$, $\omega_6 = 214.70$). This should not be surprising, though, since actually it results from the 2-D nature of the problem, *i.e.* the strange mode 5 (Figure 2.14) is the vibration mode in longitudinal (x) direction, while other frequencies correspond to vibration mode in vertical (y) direction. This can be further confirmed with the mode shapes plots (Figures 2.12–2.14).

Should the beam act like a 1-D string, it would have $n-1$ *nodes* for nth mode. However, beam is a 2D structure, hence it can move like a string as well as a *rod*, *i.e.* it can make elongation-compression movement in x direction also. This is exactly what happened in $4th$ mode of Figure 2.12 and $5th$ mode of Figure 2.13. A comparison of mode shapes for different material gradation profiles reveals that this mode occurs as $4th$ mode for both beams softer at clamped end and equivalent homogeneous beams (as in Figure 2.12), while occurs as $5th$ mode for beams stiffer at clamped end (Figure 2.13). It is of interest to notice that a similar mode shape occurs for beams graded in Y direction at $5th$ mode (Figure 2.14), yet it is not purely elongation-compression in x direction, but rather accompanied with warping in Y direction. Reason for this is that the upper and lower half of the beam cross section are nonsymmetric, thus preventing it from displaying a deformation pattern purely in x direction.

Reflection on the formulation of Rayleigh-Ritz method reveals that the Rayleigh-Ritz method performed in previous section will not be able to catch the *"rod-like"* mode shape, since the polynomial base functions can only give deformation in y direction. This is inherent

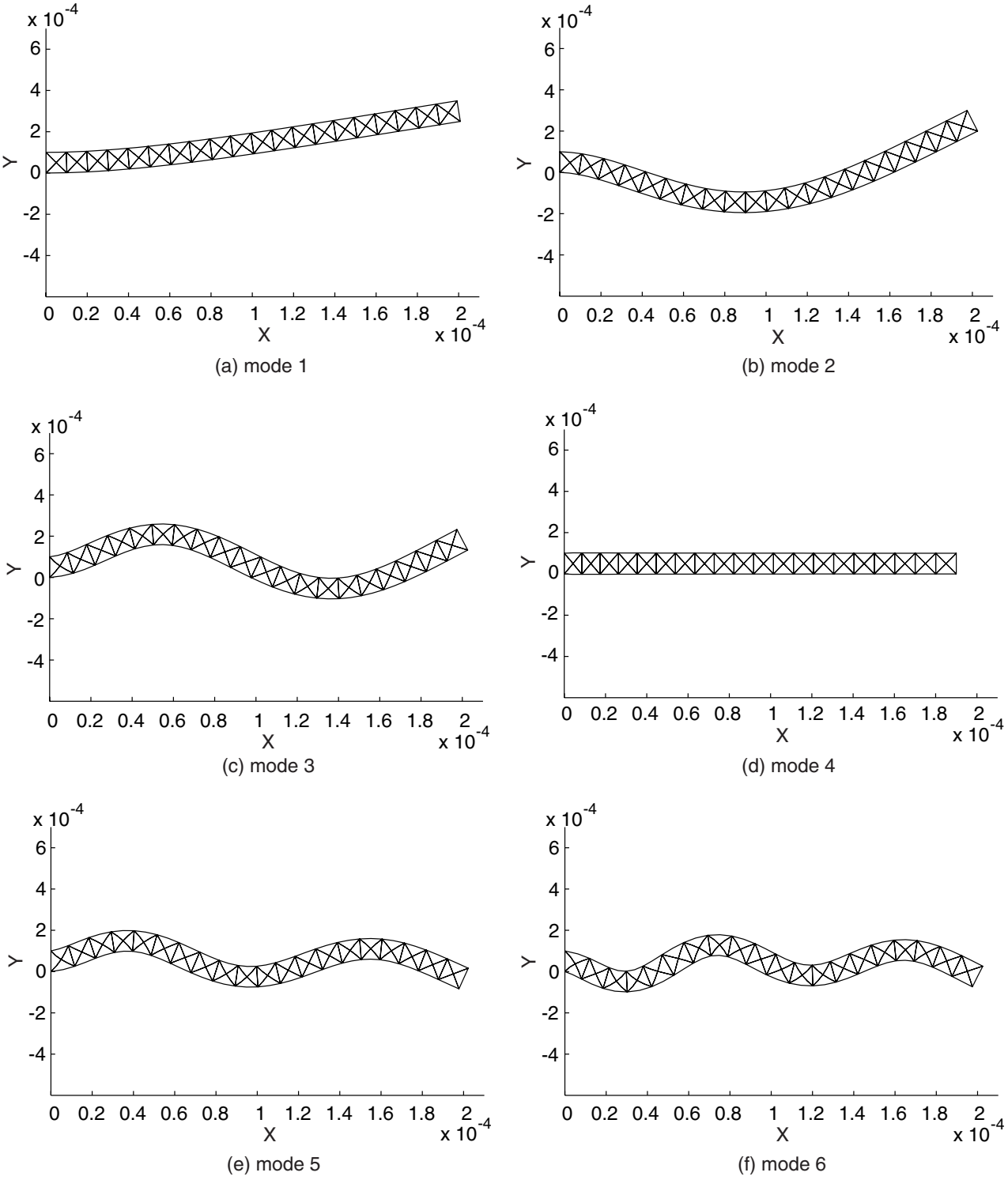

(a) mode 1 (b) mode 2

(c) mode 3 (d) mode 4

(e) mode 5 (f) mode 6

Figure 2.12: Six mode shapes of FGM cantilever beam, linear gradation, softer at clamped end, $E_2/E_1 = 5$, $\rho_2/\rho_1 = 3$.

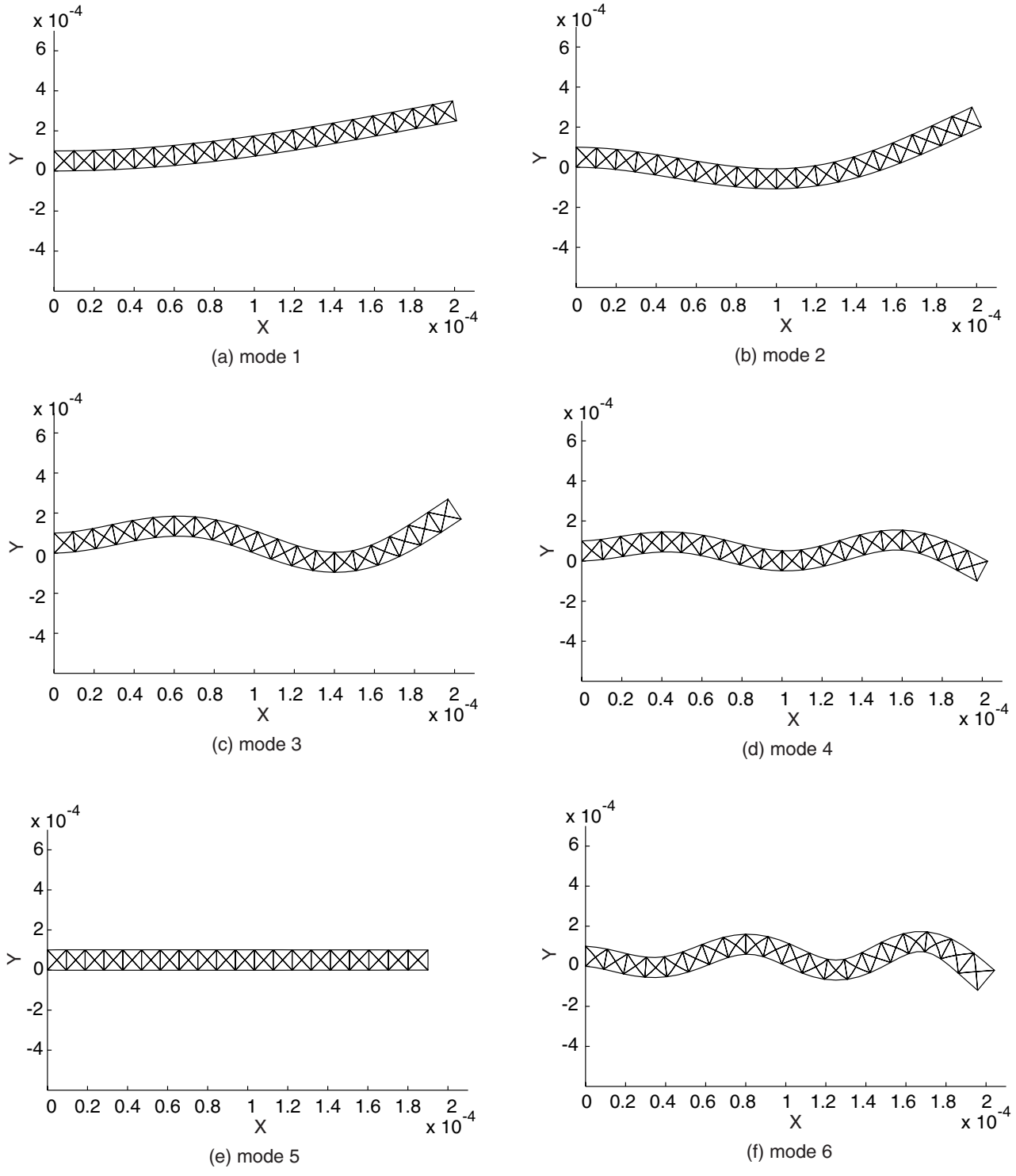

Figure 2.13: Six mode shapes of FGM cantilever beam, linear gradation, stiffer at clamped end, $E_2/E_1 = 5$, $\rho_2/\rho_1 = 3$.

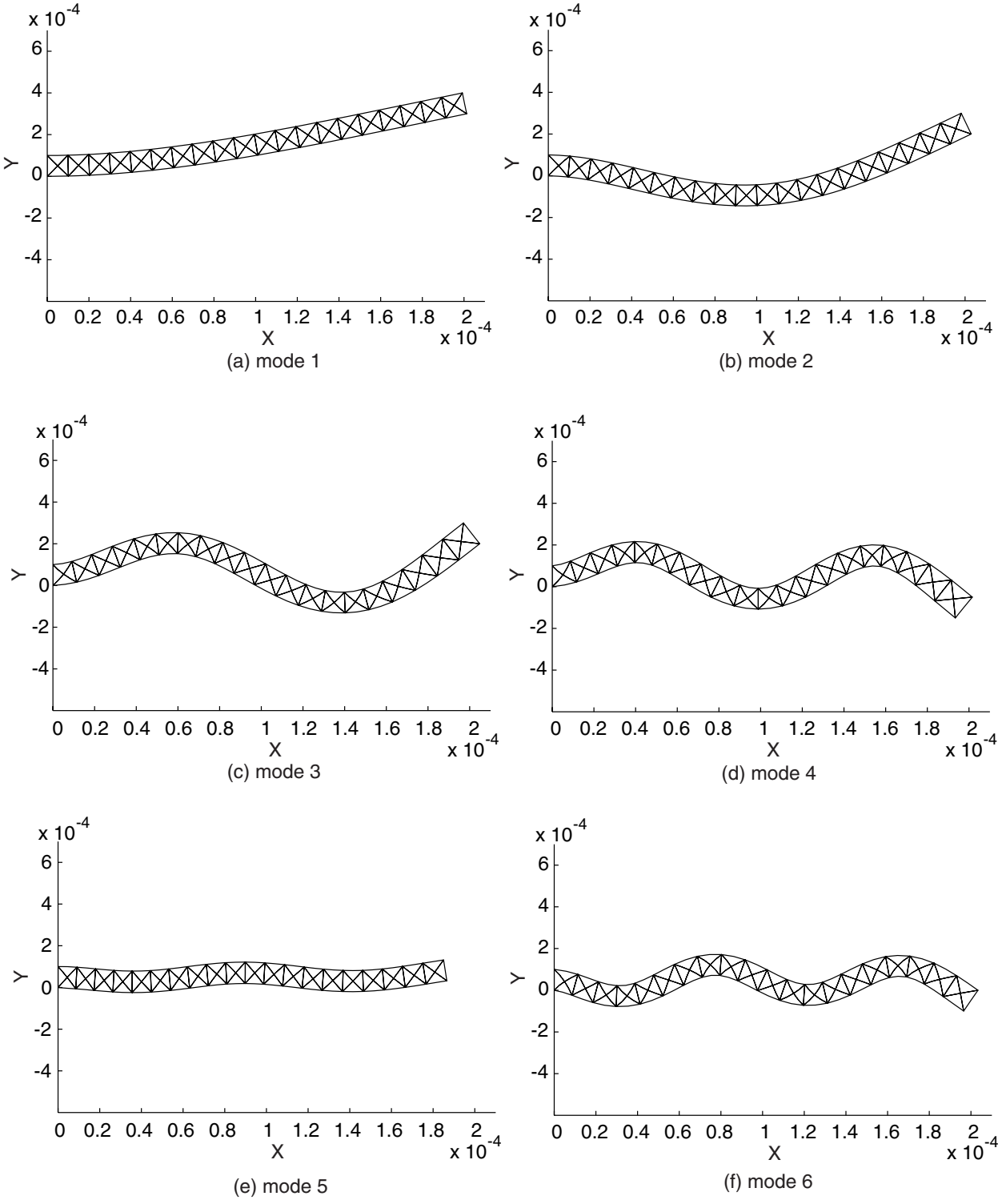

Figure 2.14: Six mode shapes of FGM cantilever beam, linear gradation Y direction, $E_2/E_1 = 5$, $\rho_2/\rho_1 = 3$.

to base functions we choose, however, and Rayleigh-Ritz method still proves to be very efficient and accurate for obtaining the lower frequency and mode shape.

For comparison purpose, mode shape results of Rayleigh-Ritz method and FEM, for two cases where material stiffer and softer at clamped end, respectively, are plotted in Figure 2.15 and 2.16. It can be observed that they are in agreement at large, especially for the fundamental mode, but some difference for $2nd$ and $3rd$ modes are apparent.

Results. Under the tip point load (Figure 2.6), where the period T is the fundamental period of each FGM beam, the response of the cantilever beam is dominated by the first mode behavior. This can be clearly observed from Figure 2.17, where all beams responses match the $1st$ natural frequency. At $t > T$, when transient force disappeared, the free vibration of each beam follows its own fundamental period, and its amplitude is scaled with respect to the amplitude at $t < T$ in the same pattern as the analytical solution in Figure 2.7. The deflection amplitude of beams with different material gradations are exactly as having been indicated in the previous section, *i.e.*, beam softer at clamped end has largest deflection; beam stiffer at clamped end smallest deflection; beam graded in Y direction and equivalent beam are in between the other two, while beam graded in Y direction is more compliant than equivalent beam.

Since both displacement and time are normalized in Figure 2.17, details of frequencies for each case are more or less concealed. It would be more intuitive to illustrate the response of each beam under the same loading without normalization, thus further computation was carried out for the same group of FGM beams subjected to the an impulse loading (Figure 2.18), and results are plotted in Figure 2.19.

Again, beams softer at clamped end gives largest displacement, and vibrates at a much slower speed than that of beams stiffer at clamped end, just as we have expected. Besides, FEM analysis for material gradation in Y direction case with more refined mesh (Figure 2.20) was also performed, and the result plotted in figure 2.19, notice that the results of coarser and refiner mesh agree with plotting accuracy.

With these results obtained and code proved to give accurate results, a more complicated problem is addressed in next section.

2.4.2 Homogeneous and FGM Beams Subjected to Impact Load

This section investigates the influence of material gradation profile on the evolution of stress state, via simulation of a 3-point-bending specimen under impact loading, as illustrated in Figure 2.21. The motivation for choosing this particular problem is because this simulation is based on a *real* material system. The experiments on material properties and dynamic

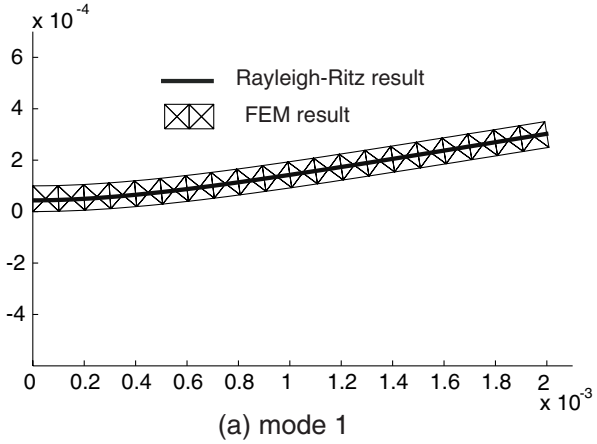

(a) mode 1

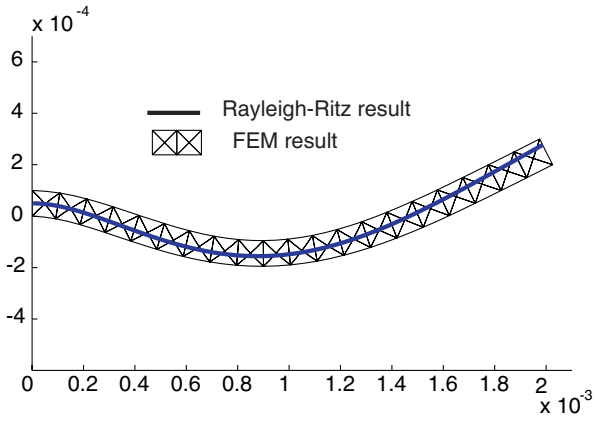

(b) mode 2

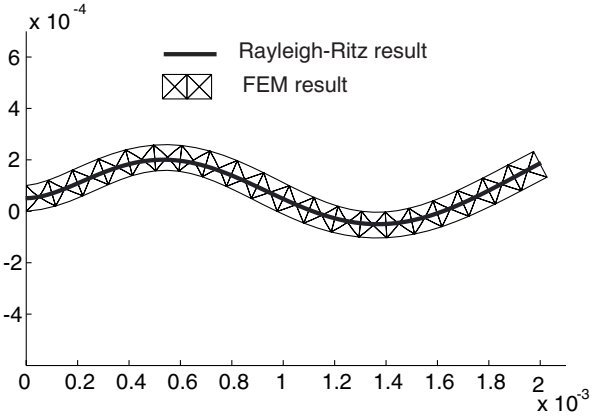

(c) mode 3

Figure 2.15: Comparison of mode shape results of Rayleigh-Ritz method and FEM, material gradation in x direction, softer at clamped end (LHS). (a) mode 1; (b) mode 2; (c) mode 3.

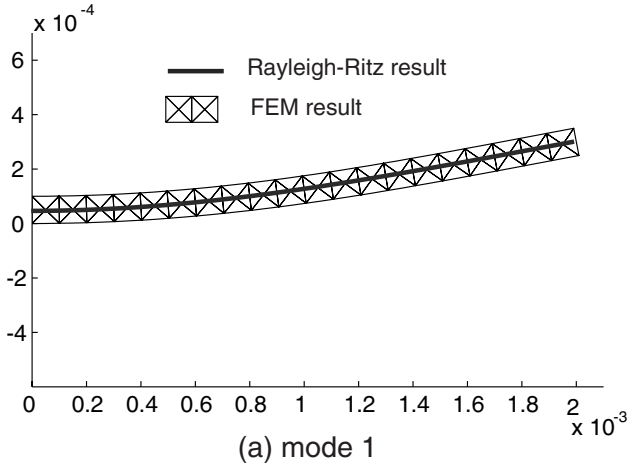

(a) mode 1

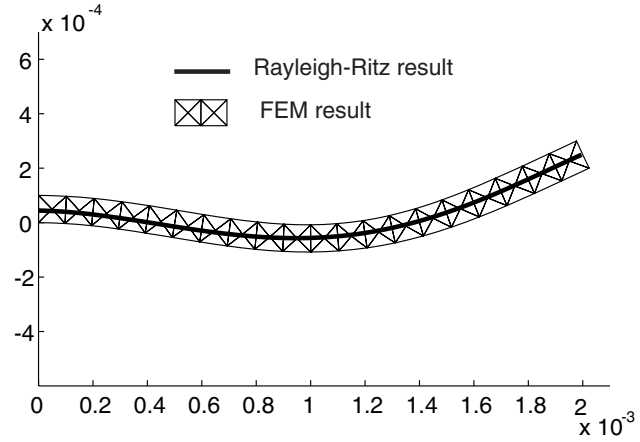

(b) mode 2

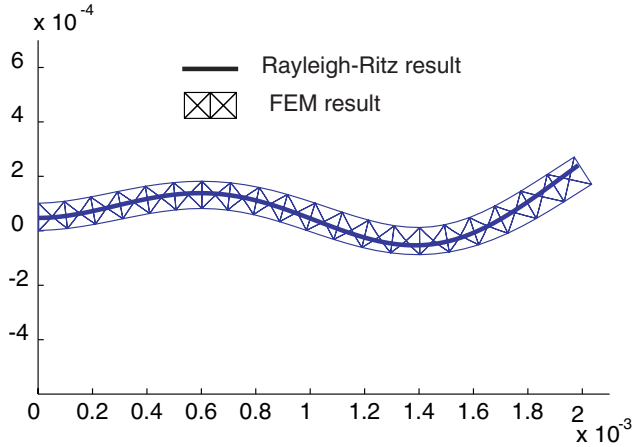

(c) mode 3

Figure 2.16: Comparison of mode shape results of Rayleigh-Ritz method and FEM, material gradation in x direction, stiffer at clamped end (LHS). (a) mode 1; (b) mode 2; (c) mode 3.

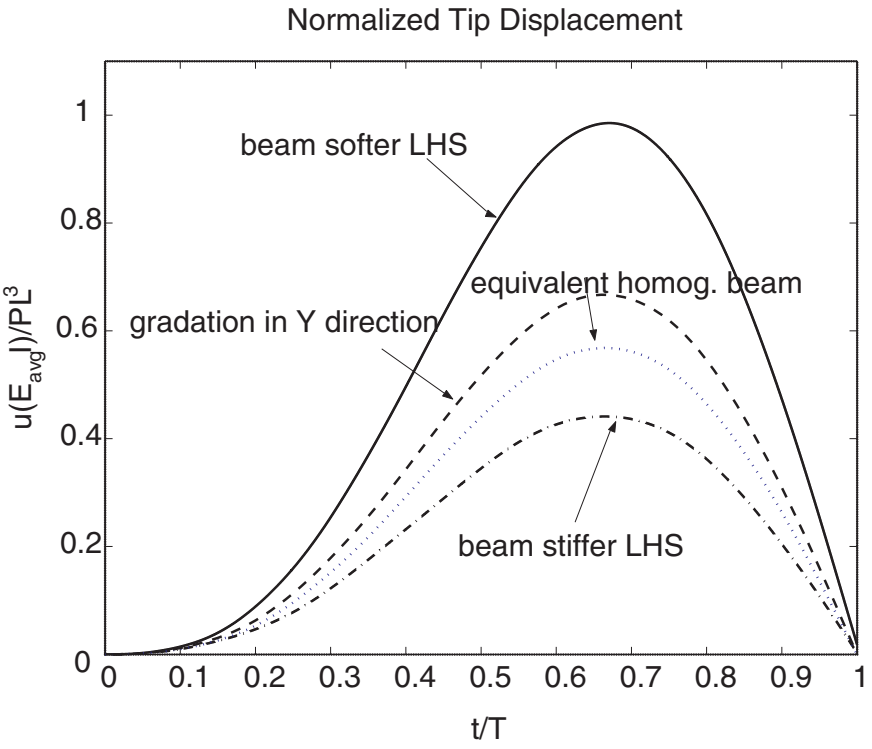

Figure 2.17: Normalized tip displacement of FGM cantilever beams under transient sine curve load (Figure 2.6), linear material gradation, $E_2/E_1 = 5$, $\rho_2/\rho_1 = 3$

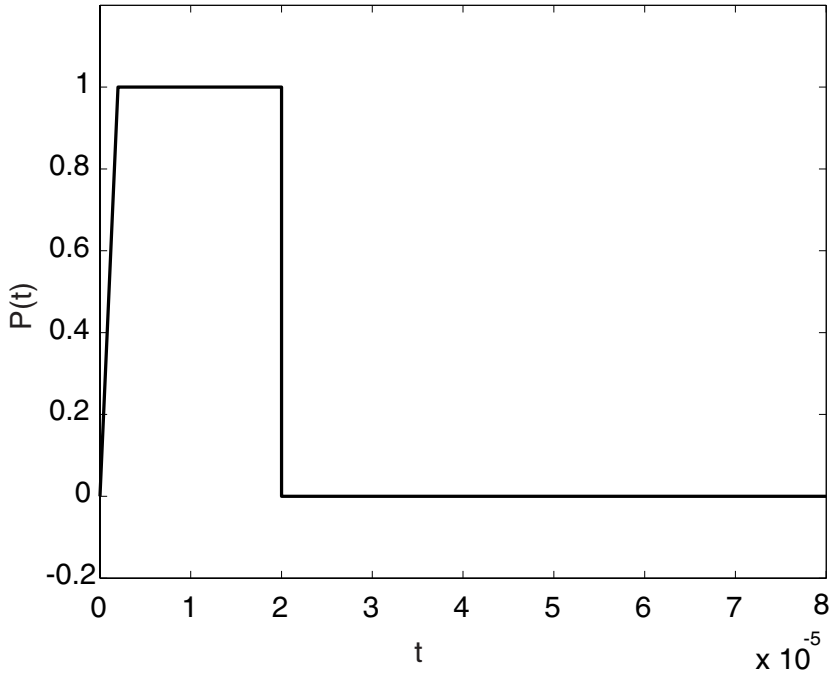

Figure 2.18: Step impulse loading at cantilever beam tip

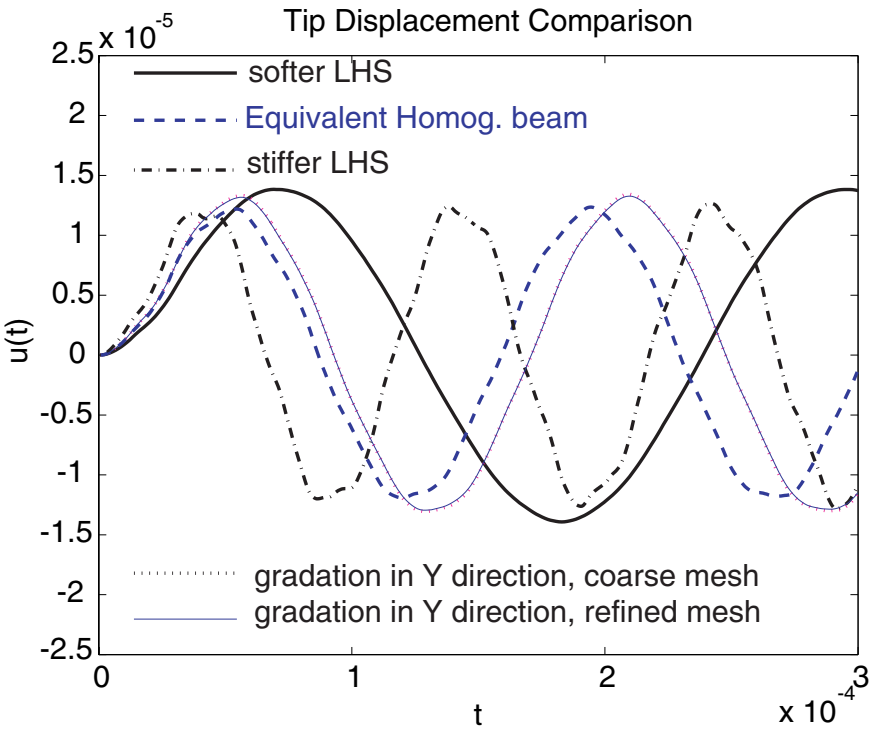

Figure 2.19: Tip deflection of FGM cantilever beam under step impulse load (Figure 2.18), linear material gradation, $E_2/E_1 = 5$, $\rho_2/\rho_1 = 3$.

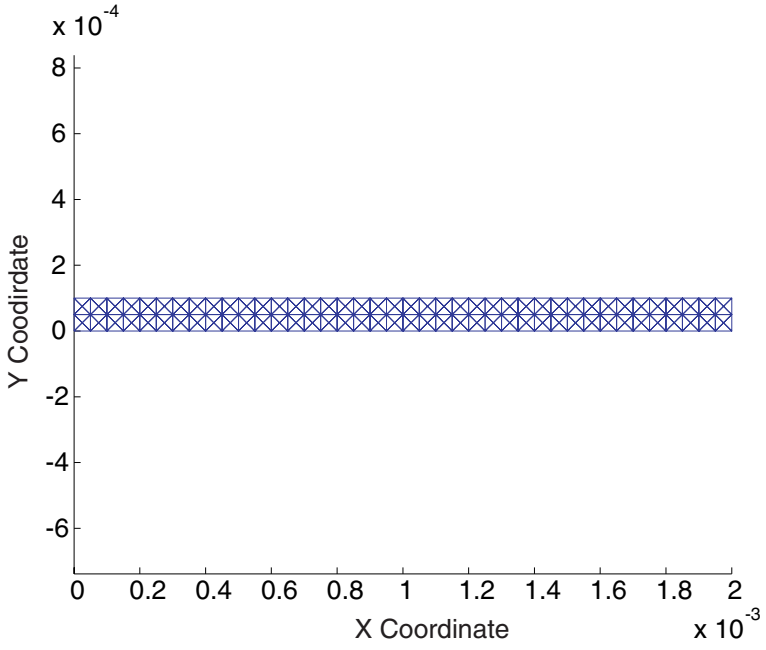

Figure 2.20: Refined mesh (725 nodes, 320 T6 elements) of cantilever beam.

fracture behavior of this graded glass/epoxy specimen have been conducted by Rousseau and Tippur [40, 41, 42, 43]. The numerical simulation of crack propagation and its comparison with experimental data will be described later in Section 3.2. However, before addressing the fracture problem, it is helpful to study the problem of same geometry and loading, but without an initial crack. This study offers background knowledge of the dynamic behavior of this material system, as well as a better understanding of the stress field inside homogeneous and graded materials, which helps to predict the fracture initiation time in specimens of various material gradients.

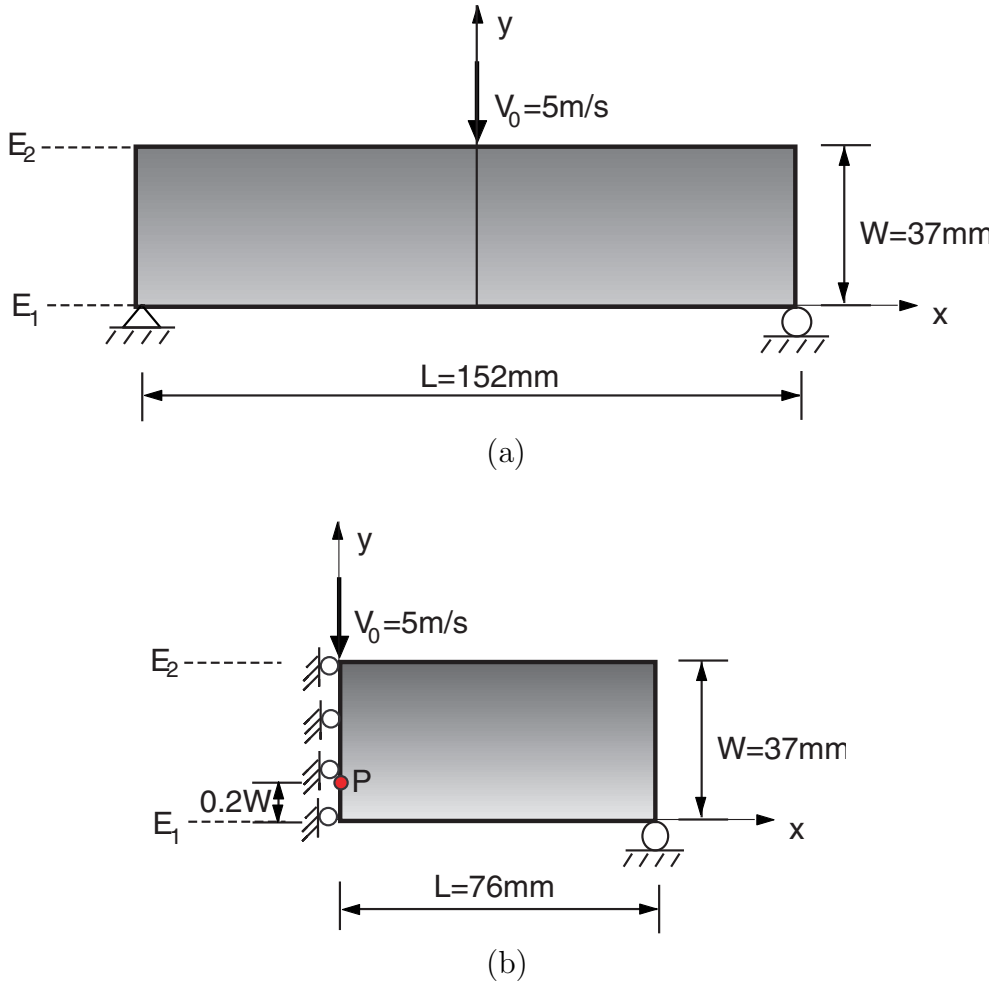

Figure 2.21: Uncracked FGM beam subjected to point impact loading; (a) 3-point-bending specimen; (b) numerical simulation using half model, with symmetric boundary conditions prescribed. Stress values are retrieved at point P ($(x, y) = (0, 0.2W)$).

The mesh of the uncracked beam problem is plotted in Figure 2.22. Notice that only half of the geometry needs to be modelled for the numerical simulation by taking advantage of the symmetry in geometry, material property, loading and boundary conditions. The mesh

is refined at the center line with uniform element size $h = 92.5\mu m$, and the stress variation versus time is retrieved at the location $(x, y) = (0, 0.2W)$, where W is the height of the beam. For the numerical simulation of crack propagation in the beam, the initial crack extends from $(x, y) = (0, 0)$ to $(x, y) = (0, 0.2W)$, which follows the experiments [43]. Hence, the location of interest in this study corresponds to the crack tip location when the crack is present.

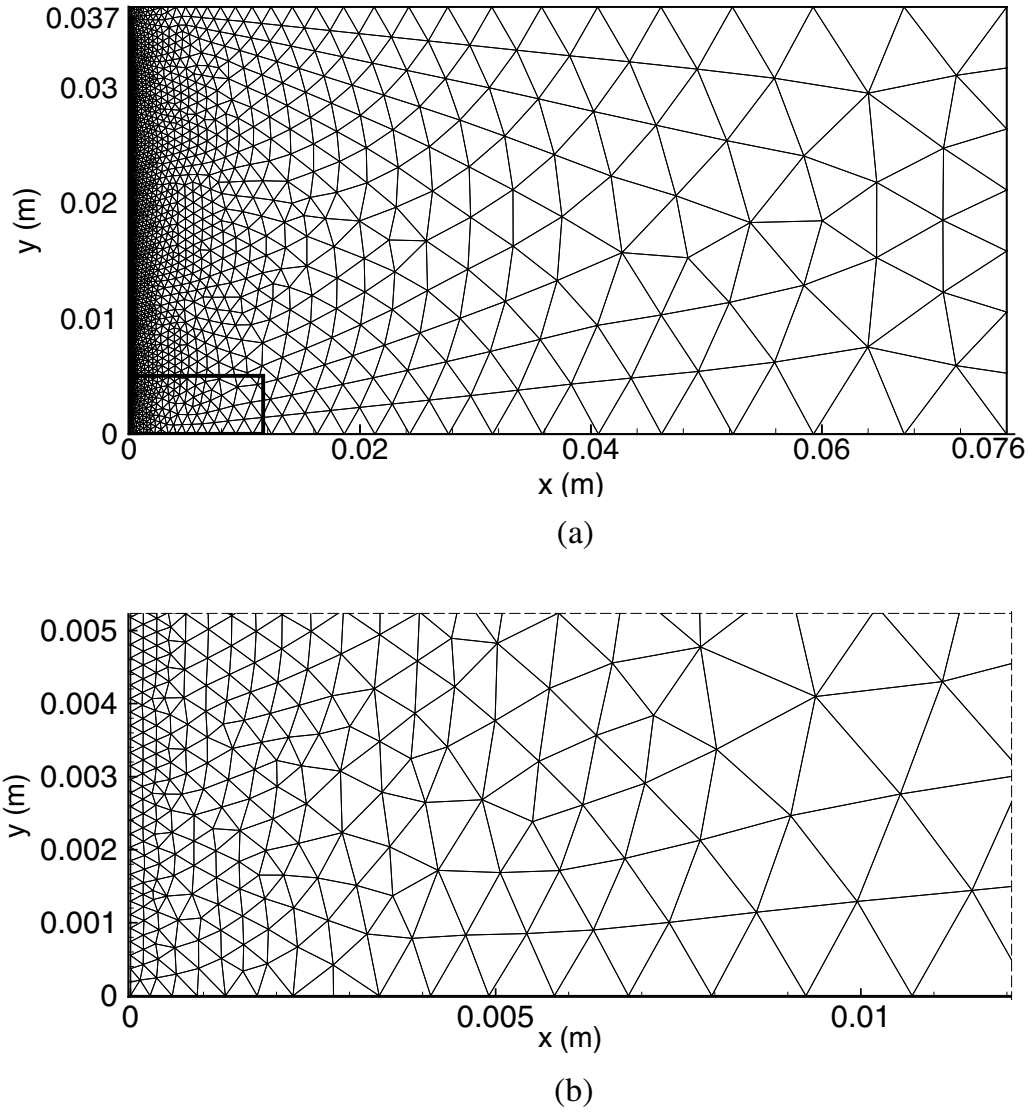

Figure 2.22: Discretization of half of the 3-point-bending beam model. Mesh contains 7562 nodes and 3647 T6 elements; (a) global mesh; (b) zoom of box region in (a).

Three simulations are performed, for these beam configurations:

- homogeneous beam ($E_2 = E_1$)
- FGM beam stiffer at the impacted surface ($E_2 > E_1$)

- FGM beam more compliant at the impacted surface ($E_2 < E_1$)

where subscript 1 and 2 denote bottom and top surface, respectively. Plane stress condition is used. Figure 2.23 shows the linear variation of Young's modulus E and mass density ρ for the above three cases. The range of variation is between $4GPa$ to $12GPa$ for E, and $1000kg/m^3$ to $2000kg/m^3$ for ρ, which approximates the range of real FGM material [43, 44]. For the homogeneous beam, the mass density is taken as the mean value of the FGM counterpart, *i.e.* $1500kg/m^3$, and the Young's modulus is calculated such that the equivalent E/ρ value equals that of the FGM case:

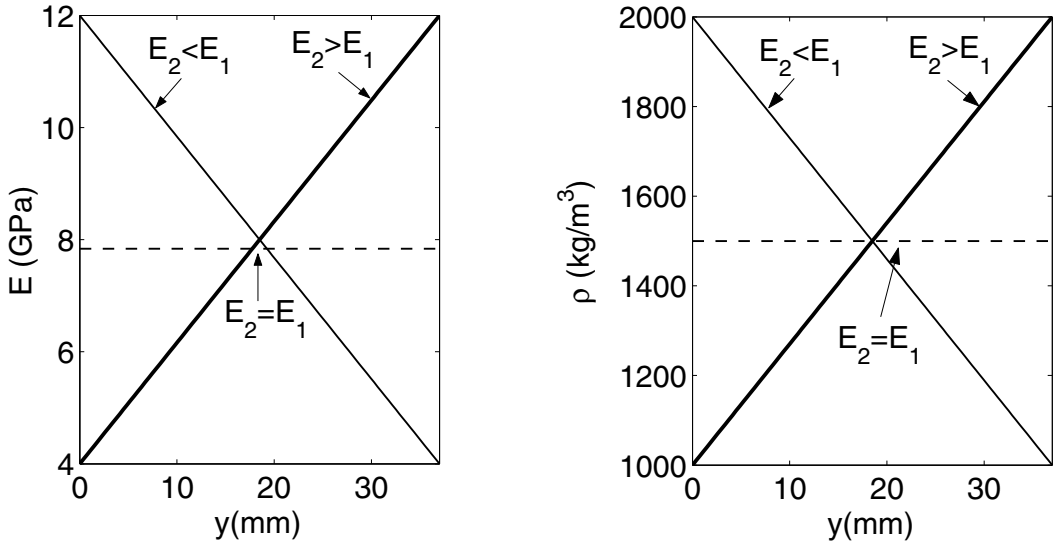

(a) (b)

Figure 2.23: Variation of (a) Young's modulus E and (b) mass density ρ in homogeneous and FGM beams along y direction. The variation of ρ and E are approximated from those provided in Figures 1 and 2, respectively, of reference [44].

$$\left(\frac{E}{\rho}\right)_{equiv} = \frac{1}{W}\int_0^W \frac{E(y)}{\rho(y)}dy, \tag{2.47}$$

as shown in Figure 2.24(a). Thus the approach from Eq. (2.47) explains the offset observed in Figure 2.23(a) for the homogeneous material modulus ($E_1 = E_2$). Notice that although E and ρ are linear functions of y, the ratio E/ρ is not. Poisson's ratio is taken as 0.33 in all cases. The difference of the average wave speeds, defined as (*e.g.*, dilatational wave speed C_d)

$$(C_d)_{avg} = \frac{1}{W}\int_0^W C_d(y)dy,$$

for each case are marginal ($2421.5m/s$ for homogeneous beam, $2418.4m/s$ for FGM beam,

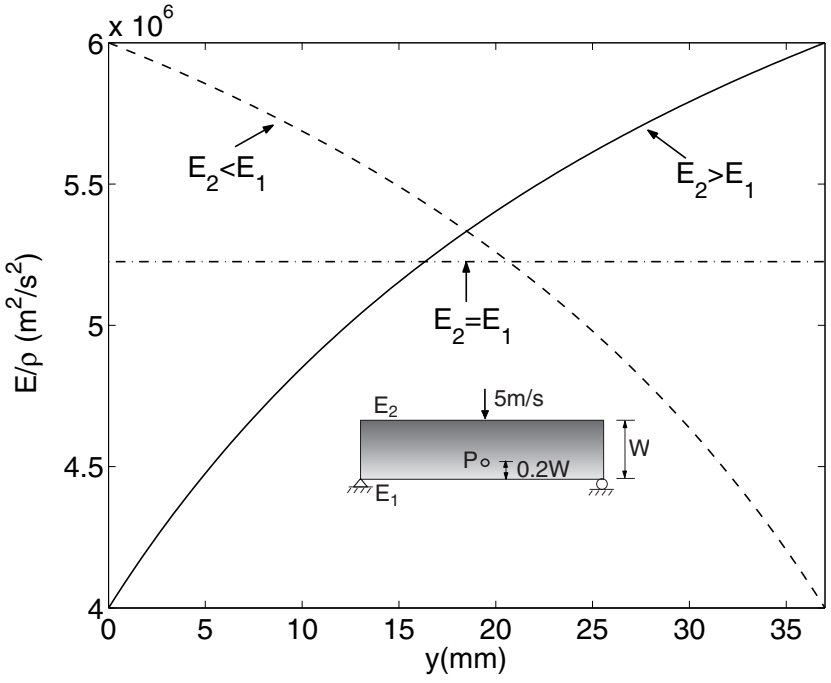

(a)

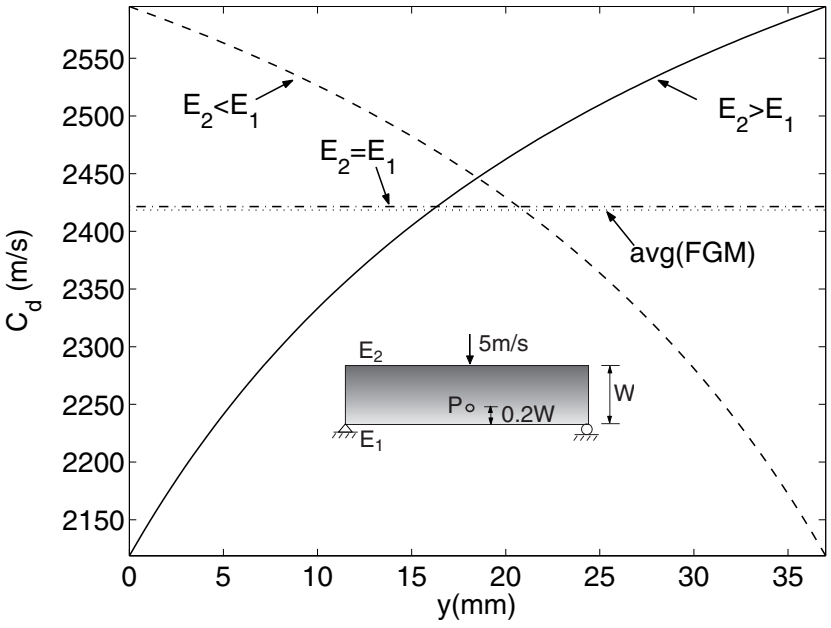

(b)

Figure 2.24: Variation of (a) E/ρ versus y and (b) dilatational wave speed C_d versus y in homogeneous and FGM beams.

plotted in Figure 2.24(b)). Thereby the influence of the elastic gradients is isolated. The results are plotted in Figures 2.25, 2.26 and 2.27 for variation of σ_x, σ_y and $(\sigma_x + \sigma_y)$ versus normalized time, respectively.

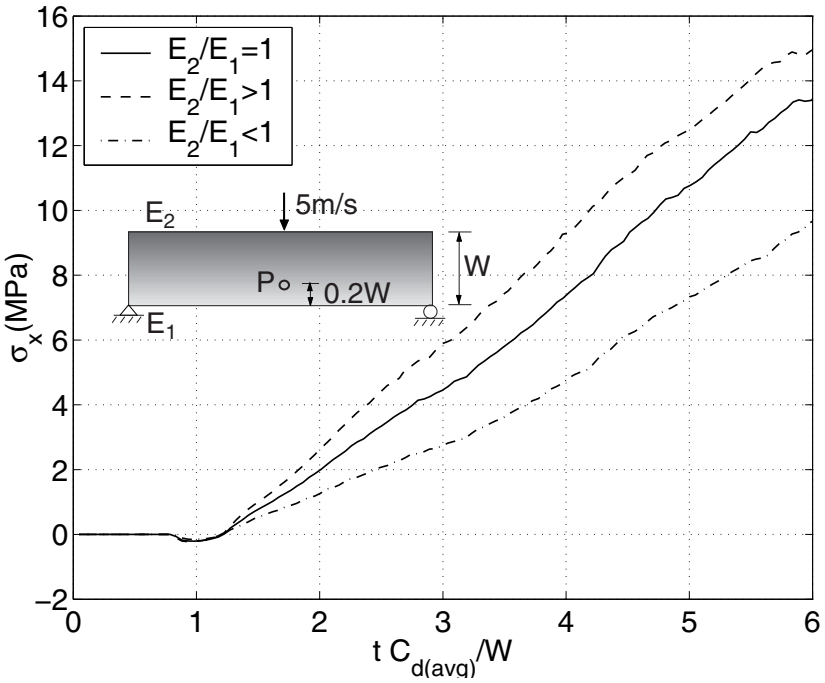

Figure 2.25: Stress σ_x at location $x = 0, y = 0.2W$ in uncracked homogeneous and FGM beams, with linearly varying elastic moduli, subjected to one point impact by a rigid projectile.

The location of interest (point P in Figure 2.21(b)) first experiences stress wave at normalized time 0.8 because the time needed for the first wave front to reach this point is $0.8W/C_d$. This value is exact for homogeneous beam, while for the graded beam, the normalized time is slightly less than 0.8 for $E_2 > E_1$ case and slightly larger than 0.8 for $E_2 < E_1$ case. This is due to the effect of material gradation within the span of top surface to the location of interest. The difference, though moderate, can be discerned in stress plots.

First, let us consider the overall stress evolution trend versus time. Figure 2.25 indicates that stress component σ_x is primarily dominated by the bending effect. When the first tide of compressive wave reaches the point of interest, σ_x become negative (during normalized time period 0.8-1.3) due to Poisson ratio effect, however, this is quickly counterbalanced by the bending effect, and afterwards the stress value increases monotonically with respect to time.

On the other hand, the stress component σ_y in Figure 2.26 shows strong influence of waves traveling in y direction. The initial stages of this plot can be explained by the dominance of

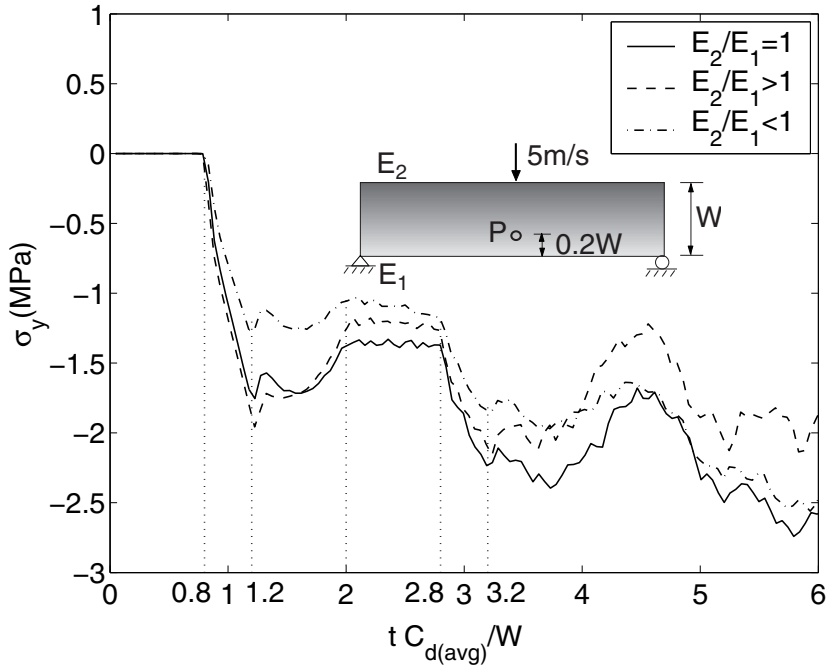

Figure 2.26: Stress σ_y at location $x = 0, y = 0.2W$ in uncracked homogeneous and FGM beams, with linearly varying elastic moduli, subjected to one point impact by a rigid projectile.

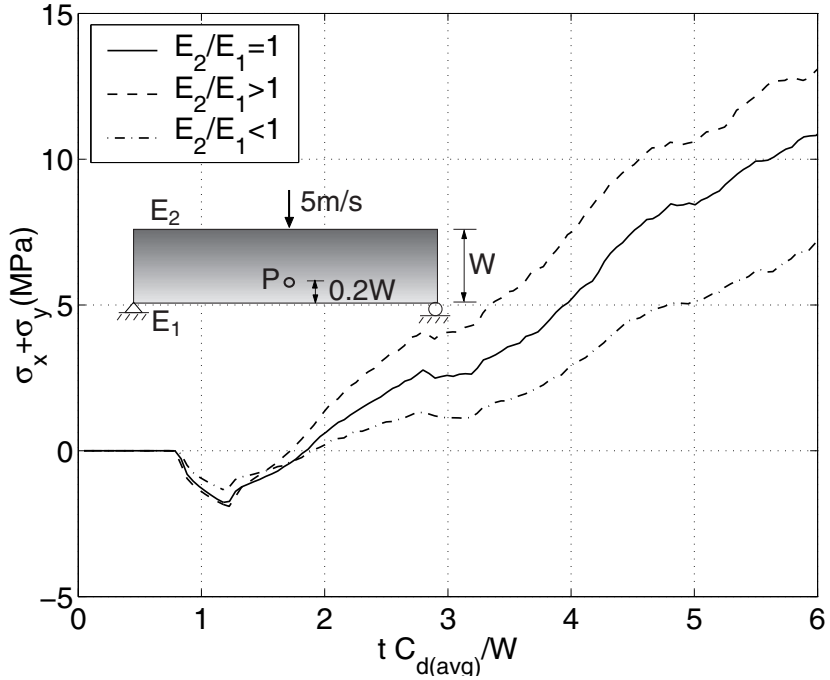

Figure 2.27: Combined stress $(\sigma_x + \sigma_y)$ at location $x = 0, y = 0.2W$ in uncracked beams, with linearly varying elastic moduli, subjected to one point impact by a rigid projectile.

the first batch of propagating waves. At normalized time 0.8, the first tide of compressive wave brings a sharp increase of σ_y in magnitude, as compressive stress. The magnitude of σ_y increases as the subsequent tide of compressive waves pass through point P, till the first compressive wave passes this point again, as tensile wave, after being reflected from the bottom surface at normalized time 1.0. The arrival of the tensile wave at this location, at normalized time 1.2, brings a sharp change of the stress profile towards the opposite direction (absolute value decreases). This trend is sustained for a while till normalized time 2.0, after which the combined effect of subsequent tensile waves that bounced back from the bottom surface, and the compressive waves emanated from the velocity loading, reaches certain balance level at this location, and a "plateau" can be observed from normalized time 2.0 to 2.8. At normalized time 2.8, the very first tide of stress wave, after being reflected from top surface, again passes through point P, and another cycle of *increase–decrease* in magnitude of σ_y can be observed during normalized time period $2.8 - 3.2$, which is similar to that of time interval $0.8 - 1.2$. Afterwards, the combined effect of the numerous wave tides clouds the influence of any isolated wave, and thus it is difficult to detect the precise time when σ_y curve changes its trend. Furthermore, waves that traveled to the lateral boundaries also bounce back, adding more complexity to the stress state.

The first stress invariant $(\sigma_x + \sigma_y)$ is plotted in Figure 2.27. At the inception of wave impact, this value is dominated by the compressive stress σ_y, giving a negative value; then it is soon neutralized by the tensile wave and the bending effect is dominant at later stages. The "flat" part of $(\sigma_x + \sigma_y)$ curve (*e.g.*, during time interval $2.8 - 3.2$) manifests influence of the sharp change in σ_y value.

To gain some insight on crack initiation sequence for the three beams described above, the effect of material gradation on stress levels is examined next. For the problem with an initial crack, the crack tip is situated at $(x, y) = (0, 0.2W)$. The region close to the impact loading experiences negative σ_x, and the central bottom part of the beam experiences positive σ_x, as shown in Figure 2.28. However, the stress contour patterns are distinctively different for various material gradient cases. First, we notice that close to the top surface, region of negative σ_x value is larger and spans much wider in x direction for beam with $E_2 > E1$, compared to homogeneous beam (*cf.* Figures 2.28(c) and 2.28(b)), and is mostly constricted for beam with $E_2 < E1$ (Figures 2.28(a)). This is due to the difference in material stiffness at location under point load. For beam with $E_2 < E1$, the material is soft under the point load, thus the beam deforms locally and the severe deformation is constricted within a relatively small region. Consequently, the negative stress region is constricted. For beam with $E_2 > E1$, the material is relatively rigid under the point load, hence the deformation is sustained by nearby region also. Therefore, a larger negative stress region is developed for

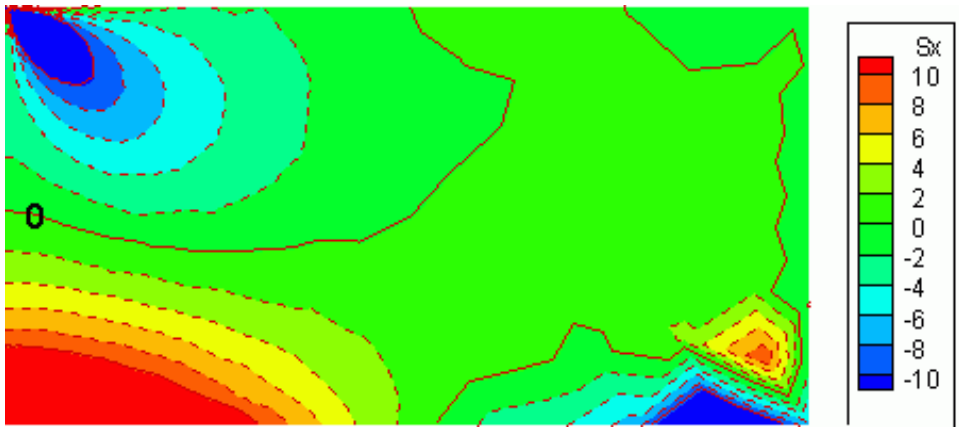

(a)

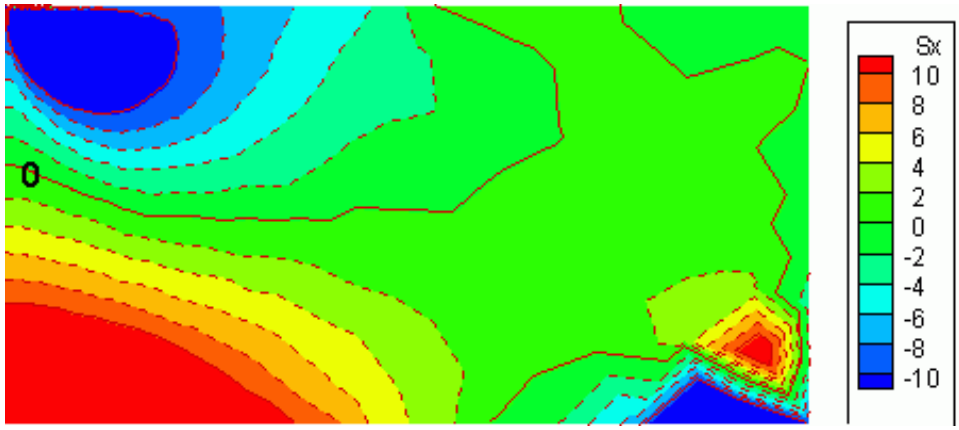

(b)

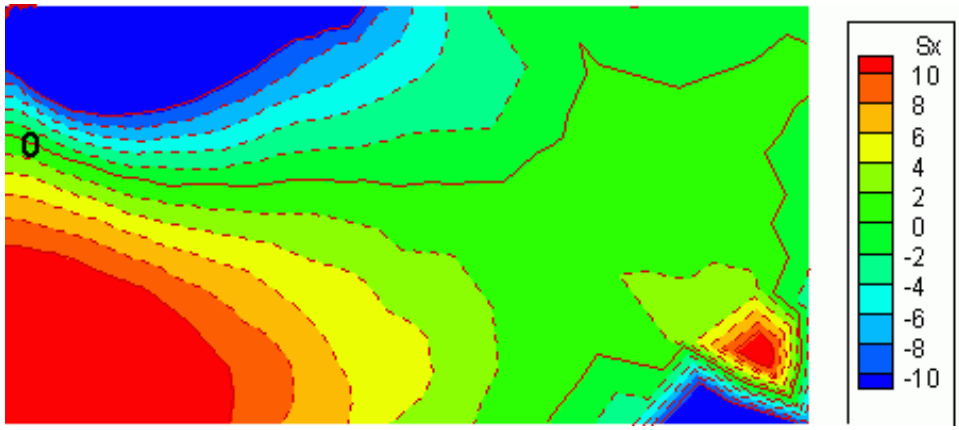

(c)

Figure 2.28: Effect of material gradient on the contour plot of stress field σ_x. Data obtained at time $t = 90\mu s$. legend shows σ_x value in MPa. (a) FGM beam with $E_2 < E_1$; (b) homogeneous beam; (c) FGM beam with $E_2 > E_1$.

beam with $E_2 > E1$ than that for beam with $E_2 < E_1$.

One may speculate that the opposite trend should occur in the positive stress region near the central bottom surface, *i.e.* the region of positive σ_x is larger for beam with $E_2 < E_1$ and smaller for beam with $E_2 > E_1$. However, this is not the case. The σ_x value at the central bottom region, being far from the point loading, is dominated by the bending effect. To understand the difference in tensile σ_x distribution patterns in the three beams, we resort to first examine a simpler and well-understood problem–a beam subjected to static uniform bending, *e.g.*, the central region of 4-point-bending beam.

Consider the stress distribution along y direction in the static case. By enforcing the equilibrium conditions, *i.e.*,

$$\begin{aligned} N &= \int_0^W \sigma_x(y)dy = 0, \\ M &= \int_0^W \sigma_x(y)ydy, \end{aligned}$$

location of neutral axis can be obtained. In above expression, N denotes the summation of normal traction along height, and M is the bending moment acting on the cross section of beam. For uniform bending problem, M is constant. For the homogeneous beam, the neutral axis is located at half height of the beam. For the beam with $E_2 < E_1$, the material is stiffer at bottom part, thus the neutral axis shifts towards bottom. The opposite situation applies to beam with $E_2 > E_1$. This instinctive observation can be confirmed by mathematical derivation. A simple calculation reveals that the neutral axis is located at

$$\begin{aligned} y &= 0.415W, \qquad \text{for } E_2 < E_1 \\ y &= 0.585W, \qquad \text{for } E_2 > E_1 \end{aligned}$$

for the material gradient considered (Figure 2.23). Hence, a larger tensile stress region develops in beam with softer material at bottom ($E_2 > E_1$). At the location of interest, the tensile stress is higher for beam with $E_2 < E_1$ than that for beam with $E_2 > E_1$. A simple calculation is carried out here. Assume strain

$$\epsilon_2 = 0.01$$

at top surface. In linear elastic beam with $E_2 > E_1$, corresponding strain at bottom surface is

$$\epsilon_1 = \frac{0.585W}{0.415W} \times 0.01 = 0.014097.$$

At location P ($x = 0, y = 0.2W$), σ_x can be obtained as

$$\sigma_x(P) = E(P)\epsilon(P) = (5.6 \times 10^9)\left(0.014097 \times \frac{0.585 - 0.2}{0.585}\right) = 51.96MPa$$

while for beam with $E_2 < E_1$, with the same assumption of $\epsilon_2 = 0.01$ at top surface,

$$\epsilon_1 = \frac{0.415W}{0.585W} \times 0.01 = 0.007094$$

at bottom surface. At location P ($x = 0, y = 0.2W$), σ_x is obtained as

$$\sigma_x(P) = E(P)\epsilon(P) = (10.4 \times 10^9)\left(0.007094 \times \frac{0.415 - 0.2}{0.415}\right) = 38.22MPa$$

The above argument, though made for *static* analysis of linear elastic beam subjected to *uniform bending*, provides an useful analogy for understanding the *dynamic* problem for beam under *point loading*. For a beam subjected to point load, the compressive strain at the top surface is localized under the point load, while the tensile strain develops in a relatively larger region at bottom. The localization of compressive region shifts the neutral axis towards the top surface, as shown in the homogeneous case in Figure 2.28(b). Compared to the homogeneous beam, the neutral axis further shifts towards the top surface for FGM beam with $E_2 > E_1$, and shifts towards the bottom surface for FGM beam with $E_2 < E_1$ (*cf.* Figure 2.28(a) and (c) with (b)) This observation is consistent with that made for the static uniform bending beam problem. The dynamic nature of the problem adds more difficulty to a precise prediction of the stress distribution at certain time, as the neutral axis shifts with respect to time. However, at any specified time, the overall stress distributions in the three beams are similar to what was shown in Figure 2.28. The above observation implies that the location of interest in the FGM beam with $E_2 > E_1$ is consistently subjected to higher tensile stress than its counterparts. Since the crack initiation is primarily dominated by σ_x, consequently crack initiation would be expected to occur earlier for beam with $E_2 > E_1$. This is confirmed by both the experiment [43] and the simulation carried out in Section 5.1. However, this conclusion assumes identical fracture toughness at the crack tip for the three specimens, which is not true. Fracture toughness depends on local material compositions, which are clearly different for the three cases. This mechanism will be discussed in further detail in Section 5.1 and will be considered in the simulation.

Chapter 3

Cohesive Model for FGMs

Four widely used cohesive zone models have been discussed in Chapter 1. However, an appropriate CZM for modeling fracture in FGMs poses more challenge due to the complexity of FGM microstructure. For instance, consider a typical metal/ceramic FGM, both the metal-rich and ceramic-rich regions can be regarded as matrix/inclusion composites, and the failure models for conventional composites may be adopted. However, the dominant failure mechanism at the interconnecting region, which has no distinct matrix and inclusion phases, remains elusive. To circumvent this problem, Jin *et al.* [30] have proposed a volume-fraction based, phenomenological cohesive fracture model and successfully implemented it to treat quasi-static crack growth in FGMs. In this study, this model is extended to the dynamic case. Further, the underlying concept in this model that accounts for the interaction between different material constituents is also adopted to extend the Xu and Needleman [46] model to FGM case.

In this chapter, the aforesaid two FGM cohesive models are first introduced, followed by a detailed discussion on the advantages and limitations of each. Finally, the energy balance check that incorporates cohesive element contribution is described, with expressions of each energy term given. An example problem is provided to demonstrate the computation of each term, and the precise calculation of external energy is discussed.

3.1 Model Based on Effective Quantities

For this FGM cohesive zone model proposed by Jin *et al.* [30], the material system under discussion is metal/ceramic. Extension of other material systems will be discussed later in Section 3.3. The notation in the formulas below follows the paper by Jin *et al.* [30], except for the substitution of the subscripts "met" and "cer", which originally denote metal and ceramic phases, to "1" and "2", so that the notation is more general and consistent with those

presented in the extended Xu and Needleman's [46] model, which is discussed in Section 3.2.

Mode-I fracture.

The normal traction force across the cohesive surface, σ_{fgm}, which depends on the position $\mathbf{x}$, is approximated by the volume-fraction based formula

$$\sigma_{fgm}(\mathbf{x}) = \frac{V_1(\mathbf{x})}{V_1(\mathbf{x}) + \beta_1[1 - V_1(\mathbf{x})]}\sigma_1 + \frac{1 - V_1(\mathbf{x})}{1 - V_1(\mathbf{x}) + \beta_2 V_1(\mathbf{x})}\sigma_2 \tag{3.1}$$

where σ_1 and σ_2 are cohesive traction of material phase 1 and 2, respectively, and each phase assumes an exponential form of cohesive model, *i.e.*

$$\sigma_1 = \frac{\partial \phi_1}{\partial \delta} \tag{3.2}$$

$$\phi_1 = e\sigma_1^c \delta_1^c \left[1 - \left(1 + \frac{\delta}{\delta_1^c}\right) \exp\left(-\frac{\delta}{\delta_1^c}\right)\right] \tag{3.3}$$

$$\sigma_1 = e\sigma_1^c \left(\frac{\delta}{\delta_1^c}\right) \exp\left(-\frac{\delta}{\delta_1^c}\right) \tag{3.4}$$

where ϕ_1 represents cohesive energy of material phase 1, σ_1^c denotes the maximum cohesive traction of material phase 1, and δ_1^c is the value of δ at $\sigma_1 = \sigma_1^c$. Similarly, for the material phase 2, the cohesive model is given by

$$\phi_2 = e\sigma_2^c \delta_2^c \left[1 - \left(1 + \frac{\delta}{\delta_2^c}\right) \exp\left(-\frac{\delta}{\delta_2^c}\right)\right] \tag{3.5}$$

and

$$\sigma_2 = e\sigma_2^c \left(\frac{\delta}{\delta_2^c}\right) \exp\left(-\frac{\delta}{\delta_2^c}\right) \tag{3.6}$$

where ϕ_2 represents cohesive energy of material phase 2, σ_2^c denotes the maximum cohesive traction of material phase 2 and δ_2^c the value of δ at $\sigma_2 = \sigma_2^c$. The cohesive force-displacement relationships of material phases 1 and 2 are illustrated in Figure 3.1, where it is obvious that the cohesive energy (the area under cohesive curve) for material phase 2 (ceramic phase for the model under discussion [30]), is only a small portion of that for material phase 1 (metal phase in discussion [30]). The energy potential ϕ, as function of cohesive surface displacement δ, is plotted in Figure 3.2. Since this plot uses normalized quantities, it may refer to either the two material phases (Eq. (3.3) or (3.5)).

In Eq. (3.1), $V_1(\mathbf{x})$ denotes volume fraction of the material phase 1, β_1 and β_2 are two cohesive gradation parameters that describe the transition of the failure mechanism from

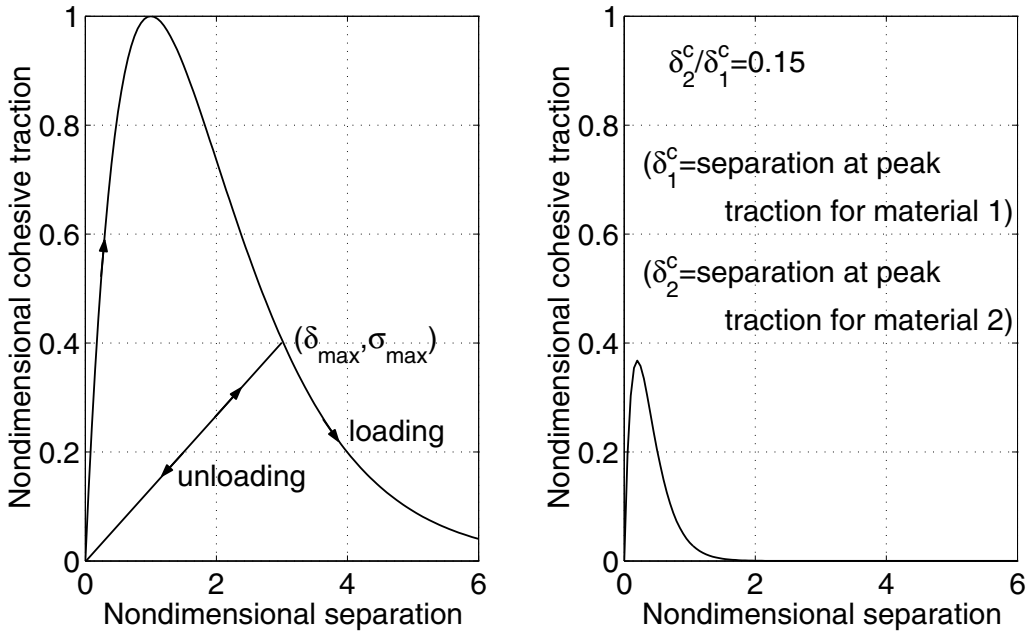

Figure 3.1: Normalized cohesive traction versus nondimensional separation displacement, strength ratio of the two material phases, σ_2^c/σ_1^c, is taken as 0.35; (a) for material phase 1, σ_1/σ_1^c vs. δ/δ_1^c; (b) for material phase 2, σ_2/σ_1^c vs. δ/δ_1^c.

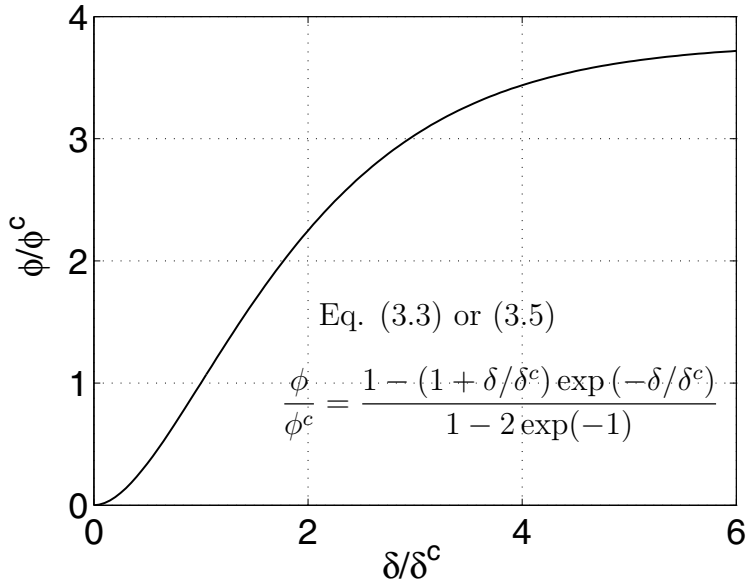

Figure 3.2: Normalized energy potential versus nondimensional separation displacement for Mode-I problem. The parameter ϕ^c is defined as the value of ϕ evaluated at $\delta = \delta^c$.

pure material phase 1 to pure material phase 2. With the above formulation, the cohesive traction σ_{fgm} reduces to that of the material 1 when $V_1 = 1$ and to that of the material 2 when $V_1 = 0$. The two additional parameters, β_1 and β_2, which are material dependent, should be calibrated by experiments. For instance, by conducting fracture test of FGMs using standard specimen geometries, *e.g.*, Compact Tension (CT) test, fracture behavior of the material can be measured, *e.g.*, load-crack extension length relationship, and compared with numerical simulation using different β_1 and β_2 values. For instance, the Compact Tension tests of TiB/Ti FGM specimen with parameters $\beta_2 = 1$ and β_1=1,3,5 respectively, were simulated, and load-crack extension responses in [30]. The results presented in [30] indicates that the fracture resistance reduces with increasing β_1 value. Hence, once the same test is performed on real TiB/Ti specimen, by matching the experimental results and computational ones, the value of parameters β_1 and β_2 can be determined.

By substituting Eqs. (3.4) and (3.6) into Eq. (3.1), the cohesive traction of FGM under loading condition is obtained:

$$\begin{aligned} \sigma_{fgm}(\mathbf{x}) &= \frac{V_1(\mathbf{x})}{V_1(\mathbf{x}) + \beta_1[1 - V_1(\mathbf{x})]} e\sigma_1^c \left(\frac{\delta}{\delta_1^c}\right) \exp\left(-\frac{\delta}{\delta_1^c}\right) + \\ &\quad \frac{1 - V_1(\mathbf{x})}{1 - V_1(\mathbf{x}) + \beta_2 V_1(\mathbf{x})} e\sigma_2^c \left(\frac{\delta}{\delta_2^c}\right) \exp\left(-\frac{\delta}{\delta_2^c}\right) \end{aligned} \tag{3.7}$$

and the corresponding free energy density function is

$$\begin{aligned} \phi_{fgm}(\mathbf{x}, \delta) &= \frac{V_1(\mathbf{x})}{V_1(\mathbf{x}) + \beta_1[1 - V_1(\mathbf{x})]} e\sigma_1^c \delta_1^c \left[1 - \left(1 + \frac{\delta}{\delta_1^c}\right) \exp\left(-\frac{\delta}{\delta_1^c}\right)\right] \\ &\quad + \frac{1 - V_1(\mathbf{x})}{1 - V_1(\mathbf{x}) + \beta_2 V_1(\mathbf{x})} e\sigma_2^c \delta_2^c \left[1 - \left(1 + \frac{\delta}{\delta_2^c}\right) \exp\left(-\frac{\delta}{\delta_2^c}\right)\right] \end{aligned} \tag{3.8}$$

To retain the irreversibility of fracture path, the following updating scheme is prescribed. The traction σ_{fgm} takes the form of Eq. 3.8 under loading condition, *i.e.*

$$\delta = \delta_{\max}, \quad \text{and} \quad \dot{\delta} \geq 0 \qquad \text{loading.} \tag{3.9}$$

Moreover, the traction follows the linear relationship

$$\sigma_{fgm} = \left(\frac{\sigma_{\max}}{\delta_{\max}}\right) \delta \tag{3.10}$$

under unloading condition, *i.e.*

$$\delta < \delta_{\max}, \quad \text{or} \quad \dot{\delta} < 0 \qquad\qquad \text{unloading}, \tag{3.11}$$

where δ_{max} is the maximum opening displacement attained, and $\dot{\delta}$ denotes the rate of δ.

Mixed Mode fracture

In 2-D mixed mode fracture problem, an effective opening displacement jump δ_{eff} is defined as

$$\delta_{eff} = \sqrt{\delta_n^2 + \eta^2 \delta_t^2} \tag{3.12}$$

where δ_n and δ_t denote the normal and tangential displacement jumps across the cohesive surface. The parameter η assigns different weights to the opening and sliding displacements and is usually taken as $\sqrt{2}$ for homogeneous materials. For such material, the energy potential ϕ, as function of both δ_n and δ_t, is plotted in Figure 3.3, for $\eta = 1$ and $\eta = 2$, respectively. With increasing value of η, certain energy potential is reached at smaller value of δ_t. For instance, sample values of δ_n and δ_t corresponding to ϕ/ϕ^c are given in Figure 3.3 (a) and (b), where ϕ^c is defined as value of ϕ evaluated at $\delta_n = \delta_n^c$, $\delta_t = 0$. When $\eta = 1$, normal and tangential opening displacement jumps δ_n and δ_t are assigned equal weights in computing the effective displacement jump, and energy potential is symmetric with respect to the two variables δ_n and δ_t. In this case, for example, and $\phi/\phi^c = 3$ occurs at symmetric displacement value pairs $\delta_n/\delta_n^c = 2.95$, $\delta_t/\delta_t^c = 0$ and $\delta_n/\delta_n^c = 0$, $\delta_t/\delta_t^c = 2.95$. On the other hand, for $\eta = 2$, $\phi/\phi_c = 3$ value occurs at a much smaller tangential displacement jump value (equals half of the value for $\eta = 1$ case) of $\delta_t/\delta_t^c = 1.48$ when $\delta_n/\delta_n^c = 0$. Therefore, with an η value larger than 1, the tangential direction is assigned a weaker fracture resistance property.

Analogous to the effective displacement, the effective cohesive traction can be defined as

$$\sigma_{eff} = \sqrt{\sigma_n^2 + \eta^{-2} \sigma_t^2} \tag{3.13}$$

where σ_n and σ_t denote the normal and shear tractions across the cohesive surfaces. With these two effective quantities introduced, the energy potential in 2-D case takes the same

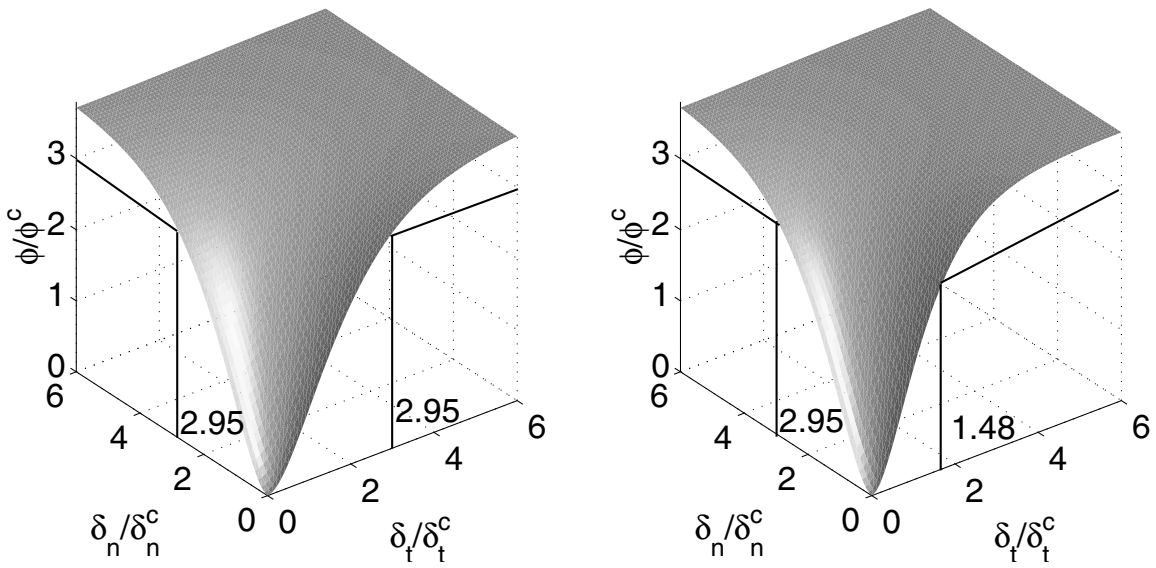

Figure 3.3: Normalized energy potential versus nondimensional separation displacement in mixed mode problem. The parameter ϕ^c is defined as the value of ϕ evaluated at $\delta_n = \delta_n^c$, $\delta_t = 0$; (a) $\eta = 1$; (b) $\eta = 2$.

form as that for Mode-I case, Eq. (3.8), *i.e.*,

$$\begin{aligned}\phi_{fgm}(\mathbf{x},&\delta_{eff}, \delta_{eff}^{\max}) = \\ &\frac{V_1(\mathbf{x})}{V_1(\mathbf{x}) + \beta_1[1 - V_1(\mathbf{x})]} e\sigma_1^c\delta_1^c \left[1 - \left(1 + \frac{\delta_{eff}}{\delta_1^c}\right) \exp\left(-\frac{\delta_{eff}}{\delta_1^c}\right)\right] \\ &+ \frac{1 - V_1(\mathbf{x})}{1 - V_1(\mathbf{x}) + \beta_2 V_1(\mathbf{x})} e\sigma_2^c\delta_2^c \left[1 - \left(1 + \frac{\delta_{eff}}{\delta_2^c}\right) \exp\left(-\frac{\delta_{eff}}{\delta_2^c}\right)\right]\end{aligned} \tag{3.14}$$

The normal and tangential cohesive traction thus follows

$$\sigma_n = \frac{\partial \phi_{fgm}}{\partial \delta_n} = \frac{\partial \phi_{fgm}}{\partial \delta_{eff}} \frac{\partial \delta_{eff}}{\partial \delta_n} = \left(\frac{\sigma_{eff}}{\delta_{eff}}\right) \delta_n \tag{3.15}$$

$$\sigma_t = \frac{\partial \phi_{fgm}}{\partial \delta_t} = \frac{\partial \phi_{fgm}}{\partial \delta_{eff}} \frac{\partial \delta_{eff}}{\partial \delta_t} = \eta^2 \left(\frac{\sigma_{eff}}{\delta_{eff}}\right) \delta_t \tag{3.16}$$

where

$$\begin{aligned}
\sigma_{eff} &= \frac{\partial \phi_{fgm}}{\partial \delta_{eff}} \\
&= \frac{V_1(\mathbf{x})}{V_1(\mathbf{x}) + \beta_1[1 - V_1(\mathbf{x})]} e\sigma_1^c \left(\frac{\delta}{\delta_1^c}\right) \exp\left(-\frac{\delta}{\delta_1^c}\right) + \\
&\quad \frac{1 - V_1(\mathbf{x})}{1 - V_1(\mathbf{x}) + \beta_2 V_1(\mathbf{x})} e\sigma_2^c \left(\frac{\delta}{\delta_2^c}\right) \exp\left(-\frac{\delta}{\delta_2^c}\right), \qquad (3.17) \\
\text{if } \delta_{eff} &= \delta_{eff}^{\max}, \text{ and } \dot{\delta}_{eff} \geq 0: \qquad \text{loading}, \qquad (3.18)
\end{aligned}$$

where δ_{eff}^{max} is the maximum value of δ_{eff} attained, and

$$\begin{aligned}
&\sigma_{eff}(x) = \left(\frac{\sigma_{eff}^{\max}}{\delta_{eff}^{\max}}\right) \delta_{eff}, \qquad (3.19) \\
&\text{if } \delta_{eff} < \delta_{eff}^{\max}, \text{ or } \dot{\delta}_{eff} < 0: \qquad \text{unloading}.
\end{aligned}$$

Notice that σ_{eff}^{max} is the value of σ_{eff} at $\delta_{eff} = \delta_{eff}^{max}$ computed from Eq. (3.19).

3.2 Model Based on Actual Quantities

The FGM cohesive zone model introduced in Section 3.1 uses effective quantities (δ_{eff} and σ_{eff} in Eqs. 3.12 and 3.12) when dealing with mixed mode fracture. Alternatively, the actual quantities can be used to describe the traction-separation relationship along normal and tangential directions, respectively. To this end, A new FGM cohesive zone model is proposed, which extends the Xu and Needleman's model [46] FGM case, and introduces the similar material parameters as in the previous model to account for material interaction.

Let

$$\boldsymbol{\sigma}_{fgm} = \left[\sigma_n^{fgm}, \sigma_t^{fgm}\right]$$

denote the traction force vector across the cohesive surfaces of a two-phase FGM, which comprises normal and tangential traction force component. We propose that the cohesive traction $\boldsymbol{\sigma}_{fgm}$ can be approximated by the following volume-based formula

$$\boldsymbol{\sigma}_{fgm}(\mathbf{x}) = \frac{V^1(\mathbf{x})}{V^1(\mathbf{x}) + \beta_1[1 - V^1(\mathbf{x})]} \boldsymbol{\sigma}^1 + \frac{1 - V^1(\mathbf{x})}{1 - V^1(\mathbf{x}) + \beta_2 V^1(\mathbf{x})} \boldsymbol{\sigma}^2 \qquad (3.20)$$

where superscript 1 and 2 denotes the two individual material phases (*e.g.*, metal and ceramic respectively). The parameters β_1 and β_2 are newly introduced material parameter that count

for the reduction of fracture toughness due to interaction of material phases, and should be calibrated with experimental data. The traction force vectors

$$\boldsymbol{\sigma^1} = \left[\sigma_n^1, \sigma_t^1\right], \quad \boldsymbol{\sigma^2} = \left[\sigma_n^2, \sigma_t^2\right]$$

are associated with material phases 1 and 2 respectively, and in 2D case comprises traction in normal and tangential direction. Assume for individual material phase the cohesive traction-separation relationship follows Xu and Needleman's model:

$$\boldsymbol{\sigma}^1 = -\frac{\partial \phi^1}{\partial \boldsymbol{\delta}}, \quad \boldsymbol{\sigma}^2 = -\frac{\partial \phi^2}{\partial \boldsymbol{\delta}} \tag{3.21}$$

in which parameters $\boldsymbol{\delta} = [\delta_n, \delta_t]$ denotes the displacement jump across cohesive surface in normal and tangential direction, and ϕ^1 and ϕ^2 are the energy potential of the two material phases, which assume exponential form

$$\phi^1(\delta) = \phi_n^1 + \phi_n^1 \exp\left(-\frac{\delta_n}{\delta_n^{c1}}\right)\left\{\left[1 - r^1 + \frac{\delta_n}{\delta_n^{c1}}\right]\frac{(1-q^1)}{(r^1-1)} - \left[q^1 + \frac{(r^1-q^1)}{(r^1-1)}\frac{\delta_n}{\delta_n^{c1}}\right]\exp(-\frac{\delta_t}{\delta_t^{c1}}^2)\right\} \tag{3.22}$$

$$\phi^2(\delta) = \phi_n^2 + \phi_n^2 \exp\left(-\frac{\delta_n}{\delta_n^{c2}}\right)\left\{\left[1 - r^2 + \frac{\delta_n}{\delta_n^{c2}}\right]\frac{(1-q^2)}{(r^2-1)} - \left[q^2 + \frac{(r^2-q^2)}{(r^2-1)}\frac{\delta_n}{\delta_n^{c2}}\right]\exp(-\frac{\delta_t}{\delta_t^{c2}}^2)\right\} \tag{3.23}$$

respectively. Other parameters in the expression that respectively refer to material phase 1 and 2, are explained hereby without superscript 1 or 2 notation: parameters ϕ_n and ϕ_t are the energies required for pure normal and tangential separation, respectively, δ_n^c and δ_t^c are the critical opening displacement for normal and tangential separation, which are related to the cohesive normal strength $\sigma_n^{\max}$ and tangential strength $\sigma_t^{\max}$ as

$$\phi_n = e\sigma_n^{\max}\delta_n^c, \qquad \phi_t = \sqrt{e/2}\sigma_t^{\max}\delta_t^c \tag{3.24}$$

$q = \phi_t/\phi_n$, and r is defined as the value of δ_n/δ_n^c after complete shear separation with $\sigma_n = 0$. The resulting normal and shear traction components can be obtained

$$\sigma_n = -\frac{\phi_n}{\delta_n}\exp\left(-\frac{\delta_n}{\delta_n^c}\right)\left\{\frac{\delta_n}{\delta_n^c}\exp\left(-\frac{\delta_t^2}{\delta_t^{n2}}\right) + \frac{(1-q)}{(r-1)}\left[1 - \exp\left(-\frac{\delta_t^2}{\delta_t^{c2}}\right)\right]\left[r - \frac{\delta_n}{\delta_n^c}\right]\right\} \tag{3.25}$$

$$\sigma_t = -\frac{\phi_n}{\delta_n}\left(2\frac{\delta_n^c}{\delta_t^c}\right)\frac{\delta_t}{\delta_t^c}\left\{q + \frac{(r-q)}{(r-1)}\frac{\delta_n}{\delta_n^c}\right\}\exp\left(-\frac{\delta_n}{\delta_n^c}\right)\exp\left(-\frac{\delta_t^2}{\delta_t^{c2}}\right) \tag{3.26}$$

for each material phase.

When both material have the same material properties, then by setting both the two material parameters β_1 and β_2 to unity, the above formulation reduces to that of Xu and Needleman's model. This model avoids the effective quantities like effective separation δ_{eff}, which is dubious for FGM problem due to the complicated microstructure fracture mechanism. The main drawback is that two more material parameters used for the tangential cohesive strength σ_t^{max} and energy ϕ_t are needed compared to the model by [30]. However, in the future investigation, most problems employing this model are homogeneous material, and the parameters are provided by works of other researchers, *e.g.* [46].

3.3 Discussion on Above Models

The cohesive zone models described in the previous sections are phenomenological model, and they do not incorporate a physical description of the FGM microstructure. The fracture property that these models describe is captured by the two newly introduced parameters β_1 and β_2, which are calibrated with experiments. The first model, with its neat expression, convenient implementation and effectiveness in treating some specific problems [30], is appealing and has some advantages. The second model is newly proposed and its effectiveness is under investigation. Here, a detailed discussion is provided on the features and possible drawbacks of the two models.

3.3.1 Shape of Traction-Separation Curve

Tvergaard and Hutchinson [45] have reported that for metals, the shape of traction-separation curve is not very important when compared to the cohesive energy (area below cohesive relation curve) and cohesive strength σ^c. However, for brittle materials like ceramics, Guinea *et al.* [15] have shown that the shape of the curve also plays a significant role in determining the peak load. In the model described above, however, it is assumed that the failure mechanism is dominated by the metal phase (material phase 1), thus for simplicity the ceramic phase (material phase 2) also adopts an exponential form.

3.3.2 Influence of Material Parameters on Cohesive Energy Density

The cohesive energy density for FGMs, Γ^c_{fgm}, is defined by

$$\Gamma^c_{fgm} = \int_0^\infty \sigma\left(\delta_{eff}\right) d\delta_{eff} \tag{3.27}$$

By substituting expression of σ_{eff} into the above equation, we obtain

$$\begin{aligned}\Gamma^c_{fgm}(x) &= \frac{V_1(x)}{V_1(x)+\beta_1[1-V_1(x)]}\Gamma^c_1 \\ &\quad + \frac{1-V_1(x)}{1-V_1(x)+\beta_{cer}V_1(x)}\Gamma^c_2\end{aligned} \tag{3.28}$$

where Γ^c_1 and Γ^c_2 are the cohesive energy densities of the material phases 1 and 2:

$$\Gamma^c_1 = e\sigma^c_1\delta^c_1, \quad \Gamma^c_2 = e\sigma^c_2\delta^c_2, \tag{3.29}$$

respectively.

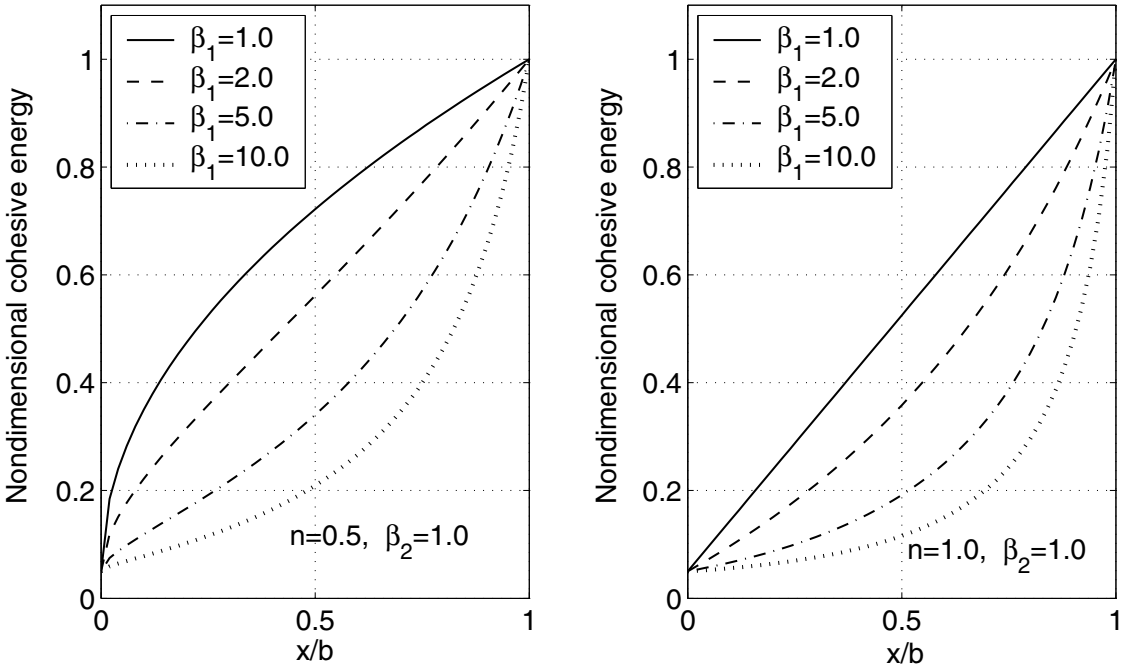

Figure 3.4: Normalized cohesive energy density $\Gamma^c_{fgm}/\Gamma^c_1$ considering $\Gamma^c_2/\Gamma^c_1 = 0.05$ and $V_1(x) = (x/b)^n$); (a) $n = 0.5$; (b) $n = 1.0$.

The transition between the fracture mechanism of the two material phases is represented by the two parameters β_1 and β_2 in this model. The values of both parameters must be larger or equal to 1, so that they result in a reduced cohesive traction σ^c_{eff}, as compared to that predicted by conventional mixture rule. The influence of the two parameters is illustrated in Figure 3.4, which shows the normalized cohesive energy density $\Gamma^c_{fgm}/\Gamma^c_1$ versus nondimensional coordinate x/b, with metal volume fraction $V_1(x) = (x/b)^n$, where b is the thickness of FGM specimen in gradation direction. In the above plot, the cohesive gradation

parameter for the material phase 2 is taken as unity, *i.e.*, $\beta_2 = 1.0$. Notice that the largest cohesive energy always occurs at material phase 1, and with increasing value of β_1, the cohesive energy for FGM reduces remarkably. The straight line in Figure 3.4(b) represents the standard mixture rule with $\beta_1 = 1$, $\beta_2 = 1$.

3.3.3 Energy Variation Versus Composition

The cohesive energy density variation (Figure 3.4) described above is conceivably true for metal/ceramic FGMs, and has produced reasonably good results [30]. However this may not hold for FGMs of different materials. For instance, the experimental data for epoxy/glass FGM, presented by Rousseau and Tippur [40], shows that the cohesive energy curve attains maximum value at volume fraction of glass inclusion at around 22 percent, rather than at the maximum glass inclusion volume fraction of 50 percent. A comparison of above model (see Figure 3.4) with that by Rousseau and Tippur [40] reveals that in the former, the energy grows monotonically as volume fraction of metal phase increases, while in the latter it increases at small volume fraction of glass inclusion, and then decreases gradually when volume fraction of inclusion exceeds 22 percent. This issue is further addressed in Section 5.2.2.

Rousseau and Tippur [40] argued that the underlying mechanism for this interesting phenomena is due to the fact that the strength of glass is much higher than that of epoxy, and thus the crack develops along the interfaces between the two phases rather than penetrating the glass particles. Therefore, the presence of glass inclusion makes the crack path tortuous, and results in greater crack surface area, hence larger fracture resistance. On the other hand, however, at higher volume fraction, the glass particles tend to concentrate and form local defects. Thus the toughness becomes a competition of the two mechanisms, and as glass volume fraction increses, the toughness first increases, attains its maximum value, and then it drops gradually.

3.3.4 Mode Mixity

As illustrated in Figure 3.3, in the cohesive zone model discussed in the Section 3.1, the mode mixity is accounted by using effective quantities with different weights assigned to the normal and tangential direction. However, whether this feature works effectively remains untested, especially for FGMs. The problem under investigation in [30] was a mode-I problem, and cohesive elements are prescribed along the fracture plane that is subject to pure mode-I loading. Care needs to be taken when using this model to deal with mixed-mode problem.

When mode-II fracture is involved, even for homogeneous material, the local fracture behavior becomes complicated and highly depends on the microstructure of the material, since the property of grain size, shape, surface roughness, *etc.* are all going to affect the friction when sliding occurs. For homogeneous material, the effective quantities with different weights introduced by a simple parameter η may be acceptable, however for FGMs, the complicated interaction of material constituents at microstructure level can hardly be captured by this simple scheme. Consider a typical ceramic/metal FGM, the ceramic grain size is of a much smaller scale compared to metal phase, and the ceramic is more brittle, thus at ceramic-rich region the crack is more likely to propagate between the ceramic grain surfaces, while in the region where ceramic and metal phase are not distinctive, the crack may penetrate the metal phase. The friction effect of ceramic-ceramic, ceramic-metal and metal-metal phases need to be distinguished. Moreover, with different material constituents, the grain shape will also affect the fracture behavior. For example, for some ceramic grain with spherical shape, crack propagation is more likely to meander along the grain boundary, while for some ceramic grains with cylindrical shape, the crack may penetrate through the particle. With the above arguments, caution needs to be taken when the method of effective quantities is adopted to deal with mixed-mode problem, especially in FGMs. To further elaborate, the traction force in normal and tangential direction (σ_n and σ_t) that correspond to several sets of separation values (δ_n and δ_t), are compared for effective quantities model (see Section 3.1) and actual quantities model (see Section 3.2), as tabulated in Table 3.1.

Table 3.1: Traction-separation values for effective and actual quantity methods

Fracture Mode	$\frac{\delta_n}{\delta_n^c}$	$\frac{\delta_t}{\delta_t^c}$	Model by Xu & Needleman [46]		Effective quantities model							
					$\eta=\sqrt{2}$				$\eta=2$			
			$\frac{\sigma_n}{\sigma_n^{max}}$	$\frac{\sigma_t}{\sigma_n^{max}}$	$\frac{\delta_{eff}}{\delta_n^c}$	$\frac{\sigma_{eff}}{\sigma_n^{max}}$	$\frac{\sigma_n}{\sigma_n^{max}}$	$\frac{\sigma_t}{\sigma_n^{max}}$	$\frac{\delta_{eff}}{\delta_n^c}$	$\frac{\sigma_{eff}}{\sigma_n^{max}}$	$\frac{\sigma_n}{\sigma_n^{max}}$	$\frac{\sigma_t}{\sigma_n^{max}}$
I	1	0	1	0	1	1	1	0	1	1	1	0
II	0	$\frac{\sqrt{2}}{2}$	0	2.332	1	1	0	1.414	1.414	0.935	0	1.869
Mixed	$\frac{1}{2}$	$\frac{\sqrt{2}}{4}$	0.728	1.543	0.707	0.948	0.670	0.948	0.866	0.990	0.572	1.617
Mixed	$\frac{1}{\sqrt{2}}$	$\frac{1}{2}$	0.738	1.782	1	1	0.707	1.000	1.225	0.978	0.565	1.597
Mixed	1	1	0.368	1.472	1.732	0.833	0.481	0.962	2.236	0.650	0.291	1.162

The model used for above comparison assumes $\delta_n^c = \delta_t^c$, and for actual quantities model the normal work of separation ϕ_n equals tangent work of separation ϕ_t. The material is homogeneous, and for effective quantity method two η values are taken as examples: $\eta = \sqrt{2}$ and $\eta = 2$. Five sets of separation values (δ_n and δ_t) are included, which respectively correspond to:

- Mode-I problem, with tangential separation $\delta_t = 0$ and normal separation $\delta_n = \delta_n^c$

which corresponds to maximum normal cohesive strength σ_n^{max} for Xu and Needleman's model.

- Mode-II problem, with normal separation $\delta_n = 0$ and tangential separation $\delta_t = \sqrt{2}/2\delta_t^c$ which corresponds to maximum tangential cohesive strength σ_t^{max} for Xu and Needleman's model. Recall for this model $\sigma_t = \sigma_t^{max}$ occurs at $\delta_t = \sqrt{2}/2\delta_t^c$ and $\sigma_t^{max} = \sqrt{2e}\sigma_n^{max}$ with $\phi_n = \phi_t$.

- Mixed-mode problem with normal and tangential separation values ($\delta_n = 0.5\delta_n^c$, $\delta_t = \sqrt{2}/4\delta_t^c$), which equal to half of those values ($\delta_n = \delta_n^c$, $\delta_t = \sqrt{2}/2\delta_t^c$) that respectively correspond to maximum normal and tangential cohesive tractions for Xu and Needleman's model.

- Mixed-Mode problem with normal and tangential separation values that result in an effective separation δ_{eff} equals critical separation δ_n^c for $\eta = \sqrt{2}$.

- Mixed-mode problem with normal and tangential separation values equal to critical normal and tangential separation values, respectively.

The comparison of above table reveals that

- The two methods produce the same results for Mode-I problem, irrespective of the η value selected.

- For pure mode-II problem, the selected δ_t value correspond to maximum tangential traction for both Xu and Needleman's model and effective quantity method with $\eta = \sqrt{2}$, however, the peak traction values are quite different: the maximum tangential traction obtained from Xu and Needleman's model is $\sqrt{2e}/\sqrt{2} = 1.65$ times of that from effective quantity method. In effort to approximate tangential strength of effective quantity method to that of Xu and Needleman's method in Mode-II problem, a larger η value is used, taken as $\eta = 2$, which produces a larger traction value in this case, however still less than that from Xu and Needleman's model. Furthermore, notice that the δ_t value corresponds to peak cohesive traction value for both Xu and Needleman's model and effective quantity method with $\eta = \sqrt{2}$, yet for effective quantity method with $\eta = 2$, the effective separation δ_{eff} exceeds the critical value δ_n^c and thus the corresponding cohesive traction is at the declining curve that past the peak value.

- For the three mixed-mode cases, the normal tractions σ_n obtained from effective quantity method are smaller compared to that from Xu and Needleman's method, and

the discrepancies increase with larger η value (percentage difference around 5-20% at $\eta = \sqrt{2}$ and 20-25% at $\eta = 2$). On the other hand, the difference in tangential tractions σ_t results between that obtained from Xu and Needleman's model and effective quantity method is more markedly for $\eta = \sqrt{2}$ (percentage difference around 60-70%) than for $\eta = 2$ (percentage difference around 19-25%).

In the simulations using effective quantity method, generally $\eta = \sqrt{2}$ is used since it represent an equivalent cohesive rule as Xu and Needleman's model in the sense that in both pure Mode-I and mode-II cases, the maximum cohesive force occurs at the same separation values for the two models. However, this also implies that separation in tangential direction would occur at a much lower stress if effective quantity method is used instead of Xu and Needleman's model.

3.3.5 Effective versus Actual Quantities

To avoid using effective quantities, we propose to extend Xu and Needleman's cohesive zone model [46] for the FGM case. This model differs from the previously discussed FGM model in that it allows separate cohesive traction-separation laws for both normal and tangential traction-separation relationships. By retaining the features of Xu and Needleman's model as discussed in Chapter 1 for homogeneous material constituents, and by introducing the same concept of new material parameters (such as β_1 and β_2) to count for the reduction of cohesive traction due to interaction of different material constituents, the cohesive laws for both normal and tangential traction-separation relationships in FGMs are obtained.

3.3.6 Cohesive Model Adopted in This Study

Further investigation needs to be carried out to better capture the cohesive modelling in FGMs, and probably a single model is not suitable for all situations. On occasions when more realistic material properties are available, the actual material property data will be used, *e.g.*, the epoxy/glass FGM data from [40].

3.4 Energy Balance

Energy balance check not only helps to validate the finite element simulation results, but also provides valuable insight for dynamic problems, especially fracture problems, through understanding the conversion between various energetics associated with deformation, kinetics

and fracture process. In this section, the expression of each energy term is given, and then a simple problem is studied to test the energy balance, where some discussion is presented on the computation of external work.

3.4.1 Energy Terms in Dynamic Fracture

In the present study, material behavior is assumed to be elastic, so no energy dissipation occurs for plastic behavior. Therefore, in a dynamic fracture problem with cohesive model approach, external work should balance the sum of strain energy, kinetic energy and dissipated fracture energy. In the finite element framework, these terms are computed as following:

- External work E_{ext}

$$\begin{aligned} E_{ext} &= \int_{\Gamma_{ext}} T_i^{ext} \Delta_i^{res} d\Gamma \qquad \text{for force-control problems} \\ &= \int_{\Gamma_{ext}} T_i^{react} \Delta_i^{ext} d\Gamma \qquad \text{for displacement-control problems} \end{aligned} \tag{3.30}$$

  where Γ denotes the boundary where external force or displacement is applied, T_i^{ext} and Δ_i^{res} are the applied external force and resultant displacement for force-control problems, while Δ_i^{ext} and T_i^{react} are the applied external displacement and resultant reaction force for displacement-control problems.

- Kinetic energy K

$$\begin{aligned} K &= \frac{1}{2} \int_{\Omega} \rho v^2 d\Omega \\ &= \frac{1}{2} m_i v_i^2 \end{aligned} \tag{3.31}$$

  where ρ denotes mass density and v is material point velocity. In finite element scheme, the lumped mass at nodes m_i and nodal velocities v_i are used.

- Strain energy due to elastic deformation of the bulk elements U_{bulk}

$$U_{bulk} = \frac{1}{2} \int_{\Omega} \sigma_{ij} \epsilon_{ij} d\Omega \tag{3.32}$$

  where Ω denotes domain surface area, σ_{ij} and ϵ_{ij} are stress and strain components, respectively.

- Deformation energy due to elastic deformation of the cohesive elements U_{coh}

$$U_{coh} = \frac{1}{2} \int_{\Gamma_{coh}} T_i \Delta_i d\Gamma_{coh} \tag{3.33}$$

where Γ_{coh} include all the cohesive interfaces, T_i and Δ_i cohesive traction and separation across the cohesive interface. This recoverable strain energy is depicted in Figure 3.5, where permanent damage and partial "relaxation" of the interface have occurred.

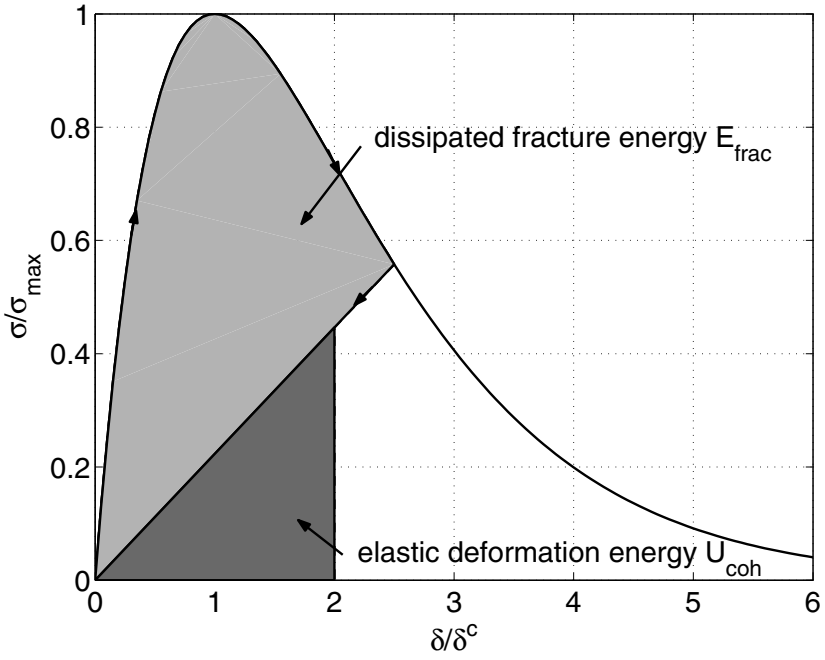

Figure 3.5: Components of the cohesive energy.

- Total elastic deformation energy U

$$U = U_{bulk} + U_{coh} \tag{3.34}$$

- Total cohesive energy E_{coh}

$$E_{coh} = \int_0^t \left(\int_{\Gamma_{coh}} T_i \dot{\Delta}_i d\Gamma_{coh} \right) d\tau \tag{3.35}$$

where $\dot{\Delta}_i$ is the rate of displacement jump across cohesive interface. This term contains integral over time, so in FEM simulation the rate of total energy needs to be computed at short time intervals, if not at every time step, to ensure accuracy.

- Fracture energy E_{frac}

$$E_{frac} = E_{coh} - U_{coh} \tag{3.36}$$

The energy dissipated by fracture given by the difference between the total energy at present time and the recoverable strain energy described above.

3.4.2 A Simple Example and Influence of Boundary Conditions

In this section, energy balance check is performed for a simple plate which consists 8 identical T6 elements and cohesive elements are prescribed at every interface, as depicted in Figure 3.6. Two cases of problems are studies, with *force-control* and *displacement-control* boundary conditions respectively, as shown in Figure 3.6 (a) and (b). It takes a finite time t_0 for the force or velocity to attain the prescribed value, and this creates some problem for external work computation if a simplified scheme is adopted.

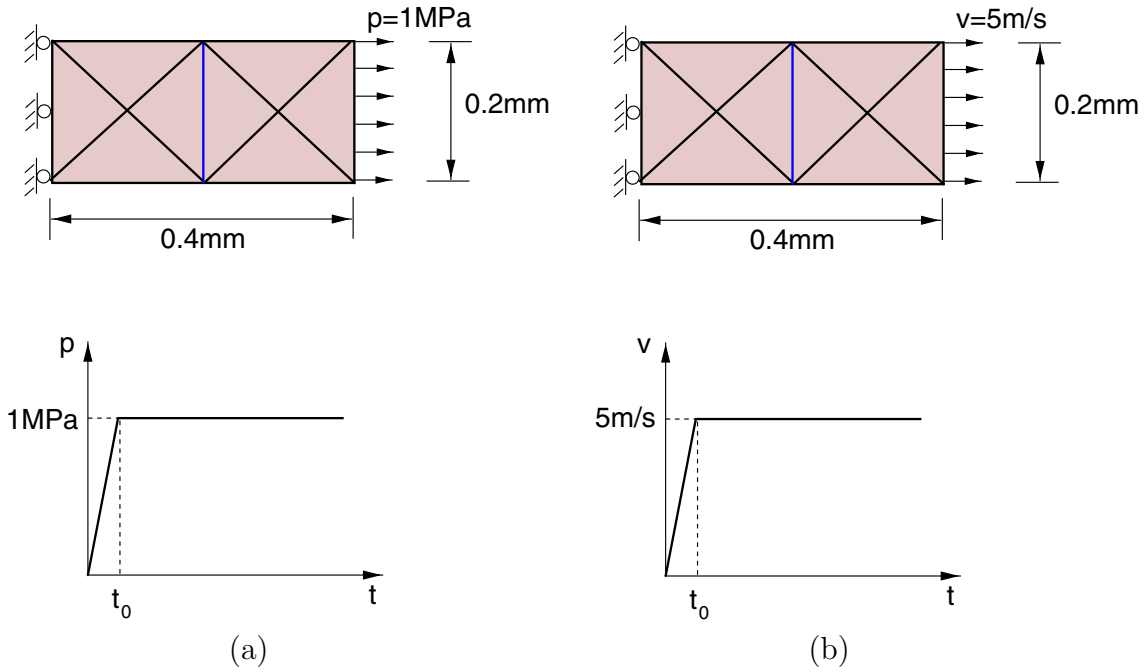

Figure 3.6: Model used for energy balance check, (a) plate subjected to uniform traction, which rises within time $t = [0, t_0]$ from 0 to $1MPa$, then kept constant; (b) plate subjected to uniform displacement, velocity rises within time $t = [0, t_0]$ from 0 to $5m/s$, then kept constant.

In theory, the external work is the accumulation of work done by external force within

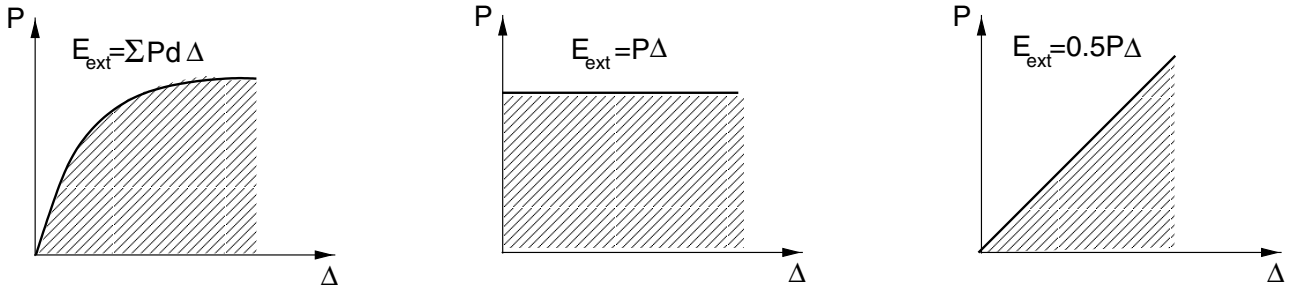

(a) (b) (c)

Figure 3.7: External energy calculation, (a) general $P-\Delta$ relationship; (b) external force P kept constant; (c) linear $P-\Delta$ relationship.

infinitesimal time intervals, as shown in Figure 3.7(a):

$$E_{ext} = \int_0^{\Delta} P(\Delta) d\Delta \tag{3.37}$$

This approach requires computation at each time step, hence more expensive, and it is desirable if the calculation can be simplified so that only the current values of P and Δ are involved, instead of the entire $P-\Delta$ history. If external force is kept constant, the external work can be computed as

$$E_{ext} = \int_0^{\Delta} P d\Delta = P \int_0^{\Delta} d\Delta = P\Delta \tag{3.38}$$

as shown in Figure 3.7(b). If $P-\Delta$ relationship is linear, the external work expression is

$$E_{ext} = \int_0^{\Delta} P(\Delta) d\Delta = \frac{1}{2} P\Delta \tag{3.39}$$

as shown in Figure 3.7(c). The problems described in Figure 3.6 roughly fall into the above two categories, however, in dynamic problem, it always takes finite time for the force or velocity to attain the prescribed value, so the accuracy of employing expression 3.38 and 3.39 to calculate external energy depends on the value of parameter t_0. For example, for the constant traction problem shown in Figure 3.6 (a), the shorter the rising time t_0 is, the closer the $P-\Delta$ relationship approaches the curve in Figure 3.7(b), so the result is better using Eq. 3.38. On the other hand, for the constant velocity boundary condition problem, short rising time t_0 produces oscillating result when expression 3.39 is used. These effects are illustrated in the following discussion.

Constant traction loading. Results comparisons of using precise versus simplified external energy computation are plotted in Figures 3.8, 3.9 and 3.10. When the t_0 value is sufficiently small, *e.g.*, $t_0 = 0.01\mu s$, the two approaches (Eq. 3.37 and 3.38 give indistinguishable results, thus only one data set is plotted, as in Figure 3.8. The balance between external work and internal energy, which is the sum of kinetic energy, bulk strain energy and total fracture energy, is captured. However, for a larger t_0 values, *e.g.*, $t_0 = 0.1\mu s$, using simplified formula (Eq. 3.38) results in unbalanced energy check, as evident in Figure 3.9. By using the precise formulation (Eq. 3.37), the energy balance is obtained, as shown in Figure 3.10.

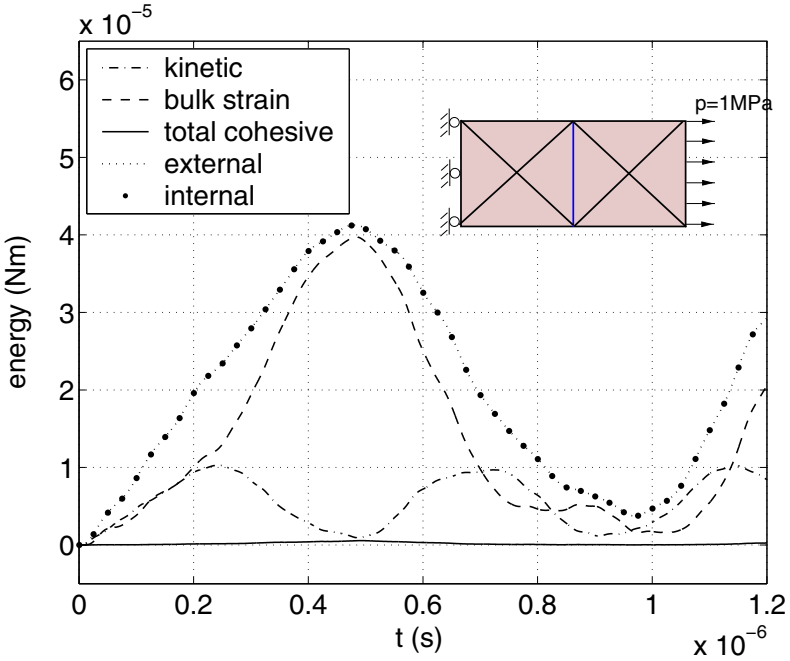

Figure 3.8: Energy balance obtained using either original or simplified external work calculation when rising time for traction is $t_0 = 0.01\mu s$.

Constant velocity loading. Results comparisons of using precise versus simplified external energy computation are plotted in Figures 3.11, 3.12 and 3.13. When the t_0 value is small, *e.g.*, $t_0 = 0.01\mu s$, the simplified approach (Eq. 3.39) gives oscillating external energy curve, as shown in Figure 3.11. This oscillation is spurious, and results in inequality of energy. On the other hand, using accurate formulation (Eq. 3.37) produces smooth external energy curve and captures the balance between external work and internal energy, as shown in Figure 3.12. Using larger value of t_0 will improve the smoothness of external energy curve when using simplified formulation, but energy balance is still lost, as indicated by Figure 3.13.

With the above examples presented, we reach the conclusion that for external energy

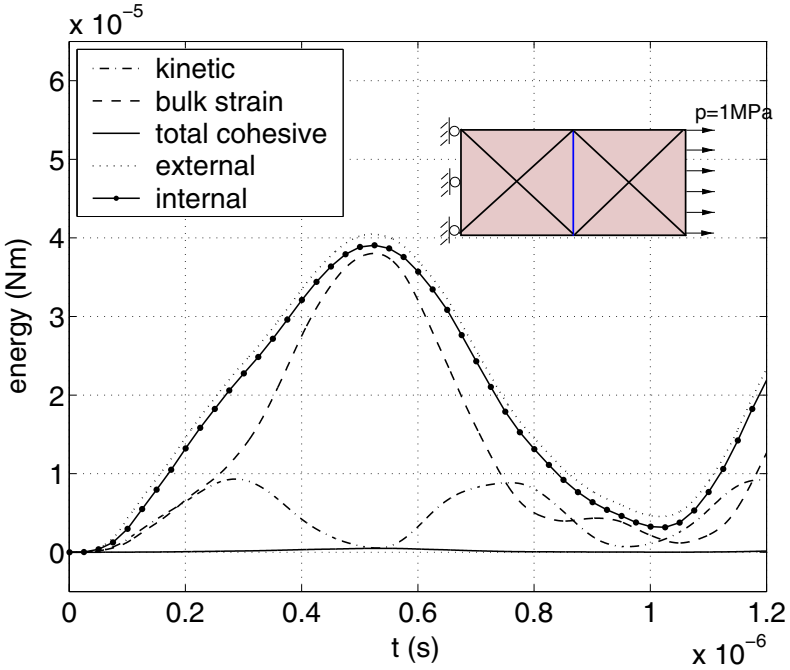

Figure 3.9: Energy balance lost using simplified external work calculation when rising time for traction is $t_0 = 0.1\mu s$.

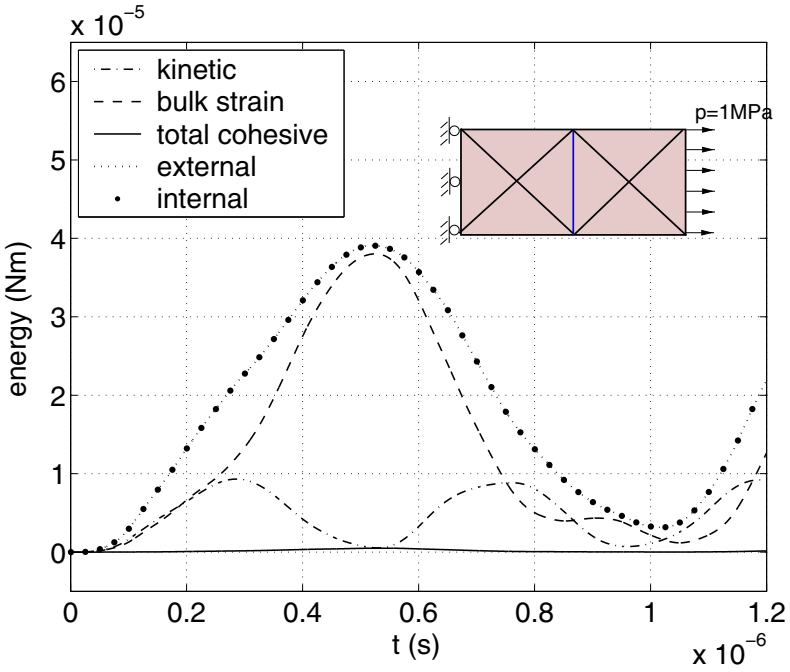

Figure 3.10: Energy balance obtained using original external work calculation when rising time for traction is $t_0 = 0.1\mu s$.

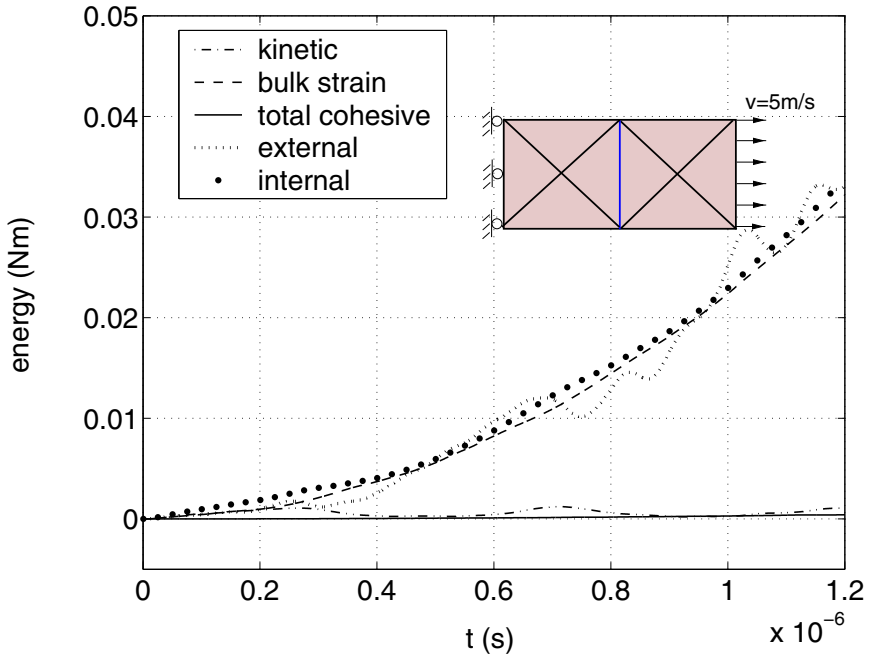

Figure 3.11: External energy curve oscillates, and Energy balance is lost using approximate external work calculation when rising time for velocity is $t_0 = 0.01\mu s$.

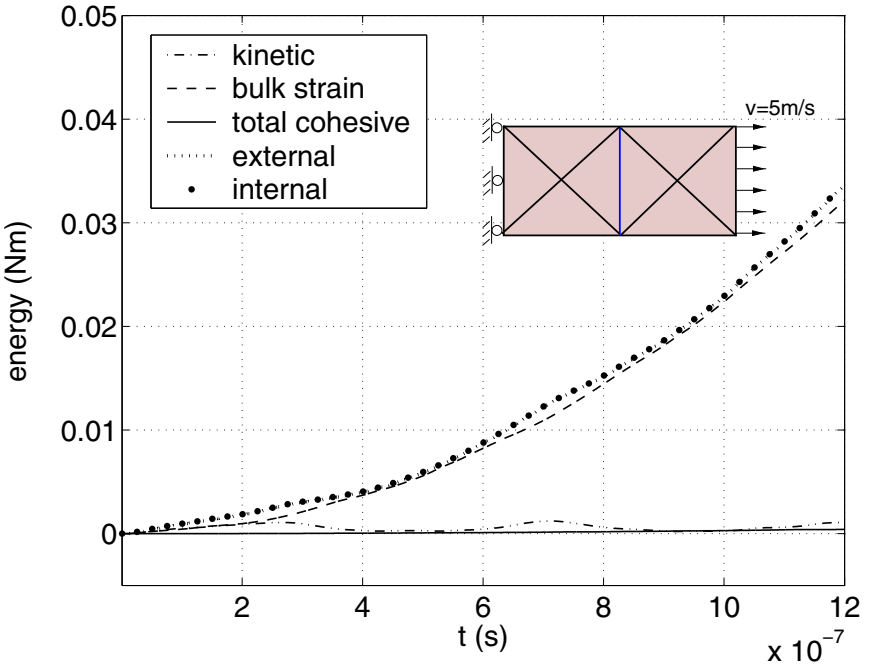

Figure 3.12: Energy balance is obtained using accurate external work calculation when rising time for velocity is $t_0 = 0.01\mu s$.

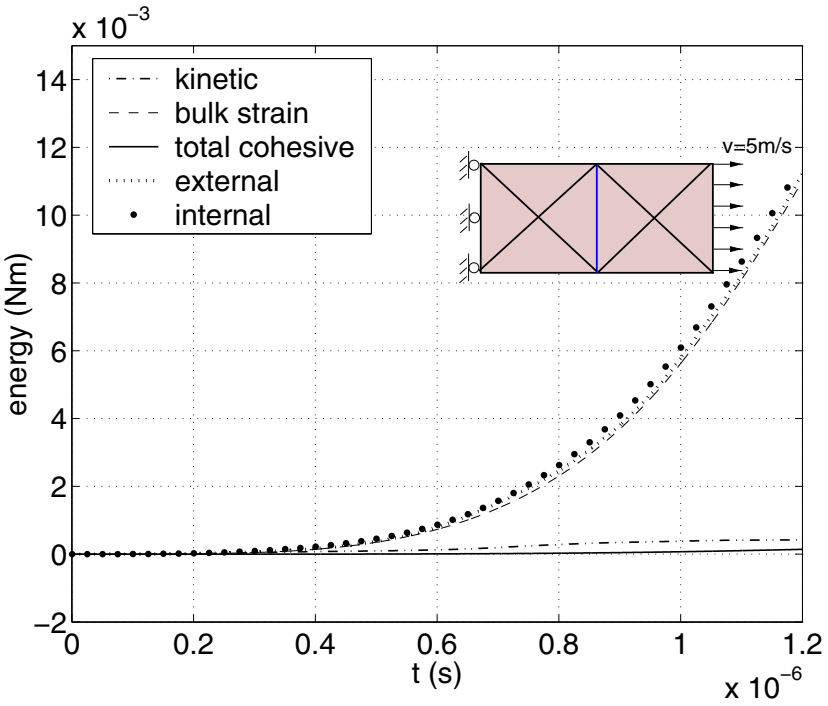

Figure 3.13: External energy curve is smooth, but energy balance is lost using approximate external work calculation when rising time for velocity is $t_0 = 1\mu s$.

calculation, it is better to use the accurate formulation. With this said, the simplified approach can be adopted if the applied force or velocity are constant, so as to save some computation overhead. However this approach may produce slight inequality of energy check. For force-control problem, the approximation overestimates the external work, as shown in Figure 3.8; for displacement-control problem, the approximation underestimates the external work, as shown in Figure 3.13.

Chapter 4

Mesh Generation, Stability and Accuracy

The introduction of cohesive zone model affects various implementation and performance aspects of the numeric scheme. First, cohesive elements need to be generated explicitly. Further, the presence of cohesive elements dictates smaller time step than traditional explicit dynamic scheme to guarantee stability. Moreover, the accuracy decreases with increasing number of cohesive elements as well as decreasing cohesive strength. Cohesive elements also puts an upper limit on the element size, and this will be discussed in Chapter 5 with an example of elastic strip subjected to initial stretch.

4.1 Cohesive Elements Generation

For intrinsic cohesive model as employed in current approach, cohesive elements are predefined in the domain of interest before the dynamic computation starts. The added cohesive elements not only affect stability but also accuracy (see [12, 28], these effects will be discussed in detail in the next section), which requires limiting cohesive elements in a certain region, rather than being present in entire domain. The code is capable of reading in bulk mesh information and generating cohesive elements. Considering the following general situations:

- 1. Cohesive elements along a straight line (Figure 4.1(a)).
- 2. Cohesive elements within a rectangular box region (Figure 4.1(b)).
- 3. Cohesive elements everywhere in the domain.

The procedure of generating one cohesive element between two T6 elements is illustrated in Figure 4.2.

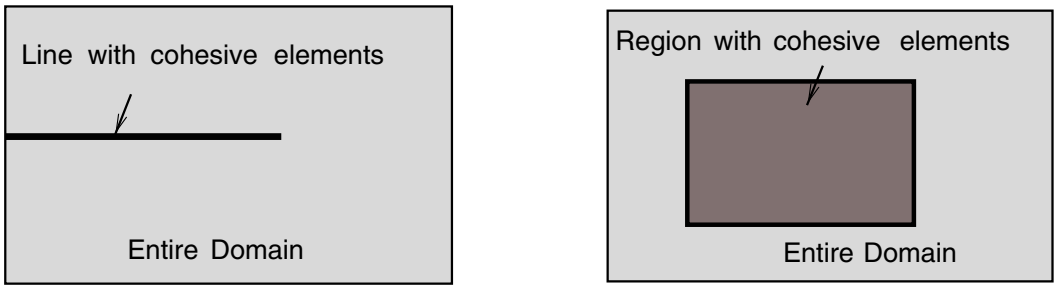

(a) (b)

Figure 4.1: Generation of cohesive elements (a) along a straight line; (b) within a box region

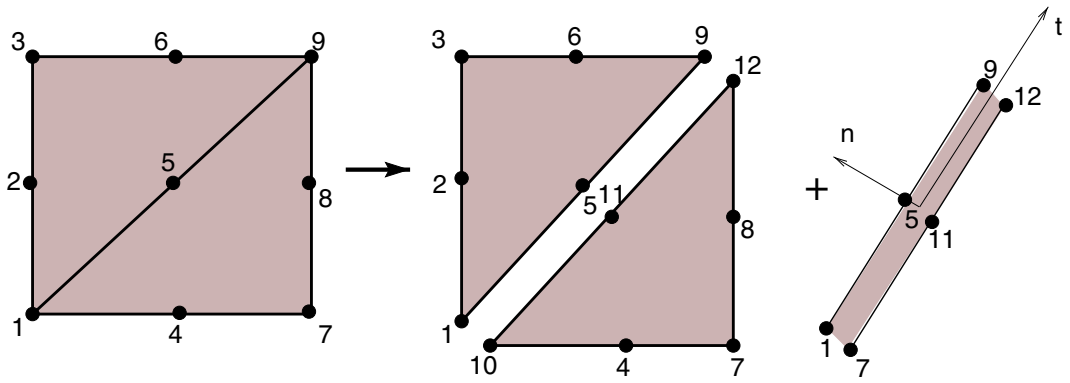

Figure 4.2: Node renumbering in the procedure of generating one cohesive element between two existing bulk elements.

1. *Generate cohesive elements along a straight line specified in the input file.* This is for cases when the crack propagation direction can be predicted.

- First, select all nodes that are along the predefined cohesive path.
- Second, use element connectivity information to count the node connectivity number n (*i.e.* how many elements share the node) for each of the nodes selected.
- Third, duplicate each of the selected nodes an additional copy, which shares the same coordinate, but is numbered uniquely.
- Fourth, for each of the two nodes that have the same coordinates, assign one node to bulk elements at one side of the cohesive path, and the other one to the bulk elements at the other side.
- Finally, pair the nodes that form two edges of different bulk elements but share the same position to form one cohesive element (See Figure 4.2).

2. *Generate cohesive elements inside a rectangular region which is specified a priori.* This feature has been developed for cases when the propagation direction of the crack(s) is uncertain, but the potential region where cracking is possible can be estimated. The procedure to generate cohesive elements in a block region is briefly described as follows, and partly illustrated in Figure 4.3 and 4.4 for a simple mesh with 8 bulk T6 elements. In this simple mesh, cohesive elements are finally generated in entire domain, so the feature of cohesive elements only inside a region is not highlighted, yet the procedure is explained as following.

- First, bulk elements inside the cohesive region are selected and the subsequent generation of cohesive elements is performed within this region. In the simple mesh in Figure 4.3, all elements numbered from 1 through 8 are selected.
- Second, use element connectivity information to count the node connectivity number n (*i.e.* how many elements share the node) for each of those nodes that are inside the region and at the interface between selected and unselected elements. For instance, node 13 is shared by 6 elements ($n = 6$) while node 19 is shared by 2 elements ($n = 2$).
- Third, duplicate each of the nodes additional $n - 1$ copies, where n is the sharing number defined above. At this point there are totally n copies of nodes that share the same coordinates but are numbered uniquely. For example, node 13 in Figure 4.3 is shared by 6 elements, so additional 5 nodes are generated at the same location.
- Fourth, assign each node to each bulk element that shares the original node.
- Finally, pair the nodes that form two edges of different bulk elements but share the same position to form one cohesive element.

3. *Generate cohesive elements everywhere in the problem domain.* This case is similar to case 2, except for that all bulk elements are selected in step 1 so there is no interface nodes between selected and unselected elements. For completeness, the procedure is summarized as follows, and illustrated in Figure 4.3 and 4.4 for a simple mesh with 8 bulk T6 elements.

- First, select all bulk elements in entire region. In the simple mesh in Figure 4.3, all elements numbered from 1 through 8 are selected.
- Second, use element connectivity information to count the node connectivity number n (*i.e.* how many elements share the node) for all the nodes. For instance, node 13 is shared by 6 elements ($n = 6$) while node 19 is shared by 2 elements ($n = 2$).

- Third, duplicate each of the nodes additional $n-1$ copies, where n is the sharing number defined above. At this point there are totally n copies of nodes that share the same coordinates but are numbered uniquely. For example, node 13 in Figure 4.3 is shared by 6 elements, so additional 5 nodes are generated at the same location.
- Fourth, assign each node to each bulk element that shares the original node.
- Finally, pair the nodes that form two edges of different bulk elements but share the same position to form one cohesive element.

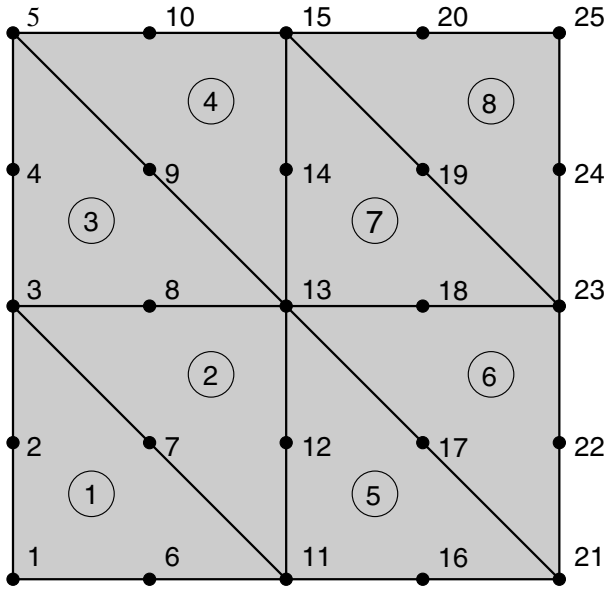

Figure 4.3: A simple mesh containing 8 T6 bulk elements, 25 nodes, and no cohesive elements.

4.2 Stability and Accuracy Issues

Before applying the proposed cohesive zone model to the impact induced fracture problem, validation of the formulation and implementation needs to be carried out. In this section, a number of example problems are tested to validate the code and examine the issues of stability and accuracy, which are essential for obtaining satisfactory computational results. The study starts with an investigation of the stability of the numerical scheme, which turns out to be also dependent upon cohesive zone model parameter, besides the factors present in the conventional explicit dynamic finite element scheme. Next the influence of the maximum cohesive strength and element size on the accuracy of computational results is illustrated

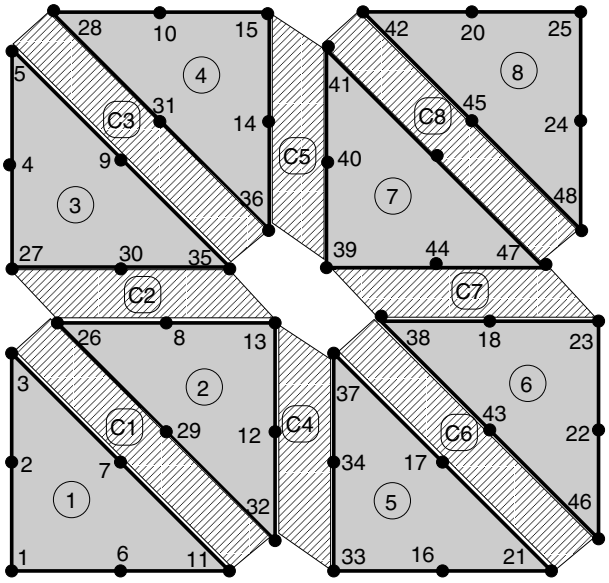

Figure 4.4: Mesh after cohesive elements are generated in entire domain. It contains 48 nodes, 8 T6 elements and 8 cohesive elements (numbered as C1-C8). Notice that the nodes that share the same position are plotted separately for clarity, *e.g.*, the center nodes 13, 35, 36, 37, 38 and 39 are actually at the same location and thus have the same Cartesian coordinates.

by a simple beam example with one cohesive element added. Finally a cantilever beam subjected to transient loading problem is presented to validate the accuracy of the code.

4.2.1 Stability

The stability of conventional explicit schemes is usually governed by the Courant condition (see, for example, reference [3]) which provides an upper limit for the time step size Δt:

$$\Delta t \leq \frac{\ell_e}{C_d} \tag{4.1}$$

where ℓ_e is the equivalent mesh length of the shortest distance between two nodes, and the dilatational wave speed C_d is expressed in terms of the material elastic constants $E = E(\mathbf{x})$, $\nu = \nu(\mathbf{x})$, and density $\rho = \rho(\mathbf{x})$ as

$$C_d(\mathbf{x}) = \sqrt{\frac{E(\mathbf{x})(1-\nu(\mathbf{x}))}{(1+\nu(\mathbf{x}))(1-2\nu(\mathbf{x}))\rho(\mathbf{x})}} \tag{4.2}$$

for *plane-strain* problems, and

$$C_d(\mathbf{x}) = \sqrt{\frac{E(\mathbf{x})}{(1+\nu(\mathbf{x}))(1-\nu(\mathbf{x}))\rho(\mathbf{x})}} \tag{4.3}$$

for *plane-stress* problems.

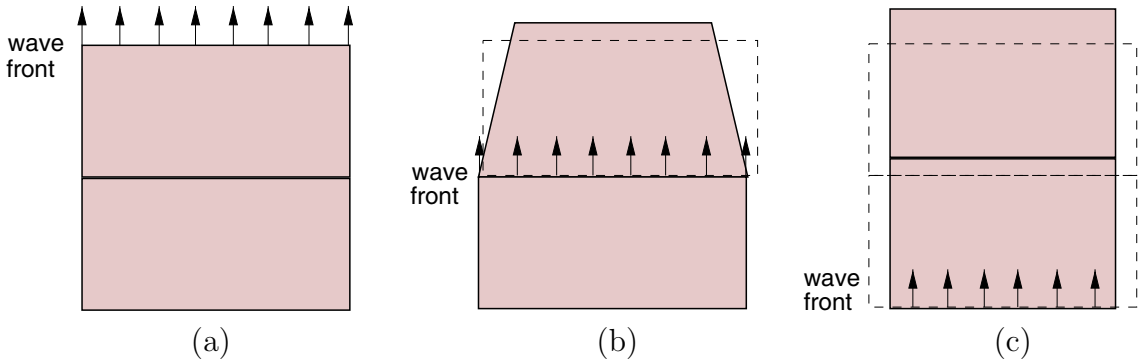

Figure 4.5: Wave transmission across conventional finite element boundary. Wave front (a) at upper surface of upper element; (b) transmits across boundary of two bulk elements; (c) and arrives at lower surface of lower element.

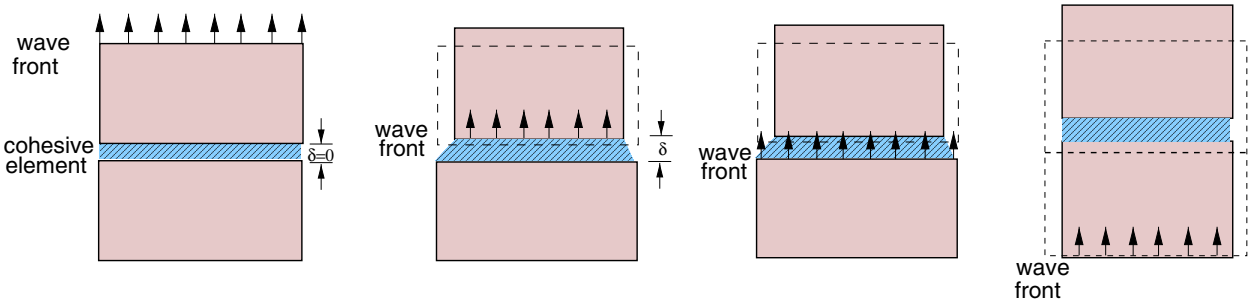

Figure 4.6: Wave transmission across cohesive element interface; (a) wave front at upper surface of upper element; (b) wave front at upper surface of cohesive element interface. Upper element deforms independently; (c) interface separation cause traction developed along cohesive interface, and the wave front transmits across the interface; (d) wave front arrives at lower surface of lower bulk element.

The introduction of cohesive elements affect the stability adversely by requiring smaller time step sizes of the finite element scheme, because of the discontinuous manner the wave is transmitted between the bulk elements through cohesive interfaces. Schematic representation of a tensile wave transmission between two bulk elements, without and with cohesive element respectively, are shown in Figures 4.5 and 4.6. For conventional finite element

scheme (Figure 4.5), the wave front that reached the upper boundary of top element in Figure 4.5(a), is smoothly transmitted across the interface of the two elements (Figure 4.5(b)), and arrived the bottom boundary of lower element (Figure 4.5(c)), deforming the element shape continuously.

Consider now a single cohesive element inserted between the interface of two elements, as illustrated by Figure 4.6(a). When the stress wave reaches the interface (Figure 4.6(b)), there is no immediate resistance developed along the interface at this time step, and the upper element can move independently. Only by the next time step, the separation of the interface δ causes cohesive traction to develop along the interface according to the prescribed cohesive law, and the stress wave is transmitted to the other side of interface (Figure 4.6(c)). If the upper element experienced too large deformation at the previous step, a large cohesive force corresponding to the large δ value will result in a large compensating deformation in the opposite direction (upper element move downward and lower element move upward). Thus, only when the time step Δt is sufficiently small, the interface could approach a steady state value of traction-separation that is consistent with the magnitude of the stress wave; otherwise the results at the interface oscillate and lead to unstable behavior.

In order to investigate stability, dynamic behavior of a simple finite element model (Figure 4.7) consisting of 2 quads each divided into four T6 elements is simulated. It is subjected to uniform traction p at the right end and fixed in x direction at the left end. Note that no constraint is provided along y direction, which would have resulted in singularity of global stiffness matrix in *implicit* scheme, while poses no problem for the *explicit* dynamic scheme. The load $p(t)$ is given by

$$p(t) = \frac{\sigma_{max}}{1000}\frac{C_d t}{h} \tag{4.4}$$

where h is the size of the longest edge of the triangular element, which is equal to

$$h = 2\sqrt{2}\ell_e \tag{4.5}$$

where ℓ_e is the smallest distance between element nodes.

Numerical simulations are performed for the dilatational wave to propagate distance of $10h$, yielding a maximum value of applied load $p = \sigma_{max}/100$, which is well below the maximum cohesive traction σ_{max}. The material properties are those of PMMA [46], which are tabulated in Table 4.1.

The cohesive zone model proposed by Jin *et al.* [30] is used, with identical material properties (Table 4.1) for the two phases, and material parameters β_m and β_c set to unity, so that the actual material properties are achieved. Besides, the η value that counts for mode

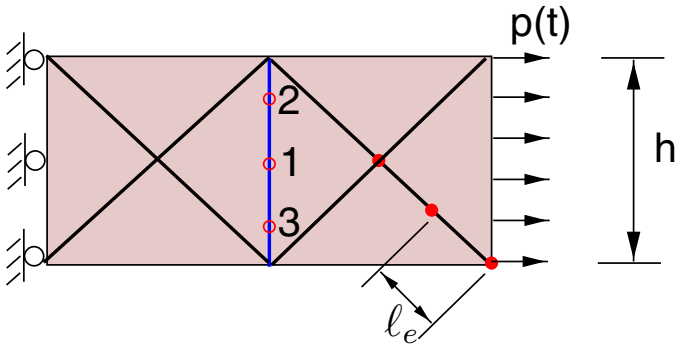

Figure 4.7: Model used for stability investigation. The plate consists of 8 T6 elements.

Table 4.1: PMMA material properties

E (GPa)	ν	ρ (kg/m^3)	G_{Ic} (N/m)	$\sigma_{\max}$ (MPa)	δ_c (μm)
3.24	0.35	1190	351.2	324	0.4

mixity is taken as $\eta = \sqrt{2}$.

The time step criterion given by Eq. (4.1)

$$\begin{aligned} \Delta t &= \frac{\ell_e}{C_d} \\ &= 3.38 \times 10^{-2} \mu s \qquad (\text{plane-strain}, h = 0.2mm, C_d = 2090m/s) \\ &= 4.01 \times 10^{-2} \mu s \qquad (\text{plane-stress}, h = 0.2mm, C_d = 1761m/s) \end{aligned} \tag{4.6}$$

provides an *upper* limit for the conventional explicit scheme, and the minimum value of Δt for stability depends on problem. For the problem described in Figure 4.7, stability is first checked for conventional explicit scheme (without cohesive elements added), by finding a threshold value of maximum Δt that produces stable results, and is obtained as

$$\begin{aligned} \Delta t &= 0.55 \frac{\ell_e}{C_d} \qquad (\text{no cohesive elements}) \\ &= 1.86 \times 10^{-2} \mu s \qquad (h = 0.2mm) \end{aligned} \tag{4.7}$$

for *plane-strain* case, and

$$\begin{aligned} \Delta t &= 0.54 \frac{\ell_e}{C_d} \qquad (\text{no cohesive elements}) \\ &= 2.17 \times 10^{-2} \mu s \qquad (h = 0.2mm) \end{aligned} \tag{4.8}$$

for *plane-stress* case.

When cohesive elements are inserted, the threshold value of Δt for stable result decreases, and also depends on the ratio of mesh size and critical interface separation δ_n^c. First one cohesive element is inserted in the model (Figure 4.7) at the middle of the plate, in vertical direction. The positions of the three Gauss points on the cohesive element are numbered as 1, 2 and 3 in the figure. The normal separation and traction at the three locations are retrieved for different time step Δt values. Stable results can be obtained once a threshold value Δt is reached (see Figure 4.8 and 4.9). For instance, for $h = 500\delta_n^c = 0.2mm$, the threshold occurs at

$$\begin{aligned} \Delta t &= 0.055\frac{h}{C_d} = 0.157\frac{\ell_e}{C_d} \qquad \text{(1 cohesive element)} \\ &= 0.53 \times 10^{-2}\mu s \qquad (h = 0.2mm) \end{aligned} \tag{4.9}$$

for *plane-strain* case, and

$$\begin{aligned} \Delta t &= 0.047\frac{h}{C_d} = 0.133\frac{\ell_e}{C_d} \qquad \text{(1 cohesive element)} \\ &= 0.53 \times 10^{-2}\mu s \qquad (h = 0.2mm) \end{aligned} \tag{4.10}$$

for *plane-stress* case.

Next, similar simulation is performed for the problem in Figure 4.7 with cohesive elements inserted along every interface. The normal separation and traction results are still retrieved from the Gauss points of the vertical cohesive element, and results become stable at certain threshold of Δt (Figure 4.9). This value is noticeably lower compared to the case with only *one* cohesive element inserted in the middle of plate. For instance, For $h = 500\delta_n^c = 0.2mm$ case, the threshold occurs at

$$\begin{aligned} \Delta t &= 0.029\frac{h}{C_d} = 0.082\frac{\ell_e}{C_d} \qquad \text{(9 cohesive elements)} \\ &= 0.28 \times 10^{-2}\mu s \qquad (h = 0.2mm) \end{aligned} \tag{4.11}$$

for *plane-strain* case, and

$$\begin{aligned} \Delta t &= 0.024\frac{h}{C_d} = 0.063\frac{\ell_e}{C_d} \qquad \text{(9 cohesive elements)} \\ &= 0.25 \times 10^{-2}\mu s \qquad (h = 0.2mm) \end{aligned} \tag{4.12}$$

for *plane-stress* case, which are roughly half of the critical Δt value for the problem with *one* cohesive element inserted.

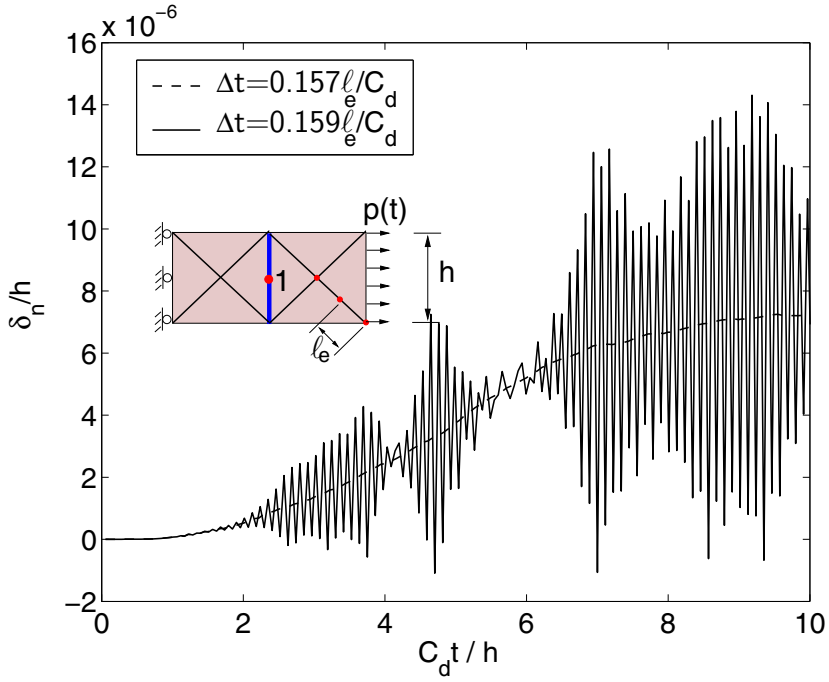

(a)

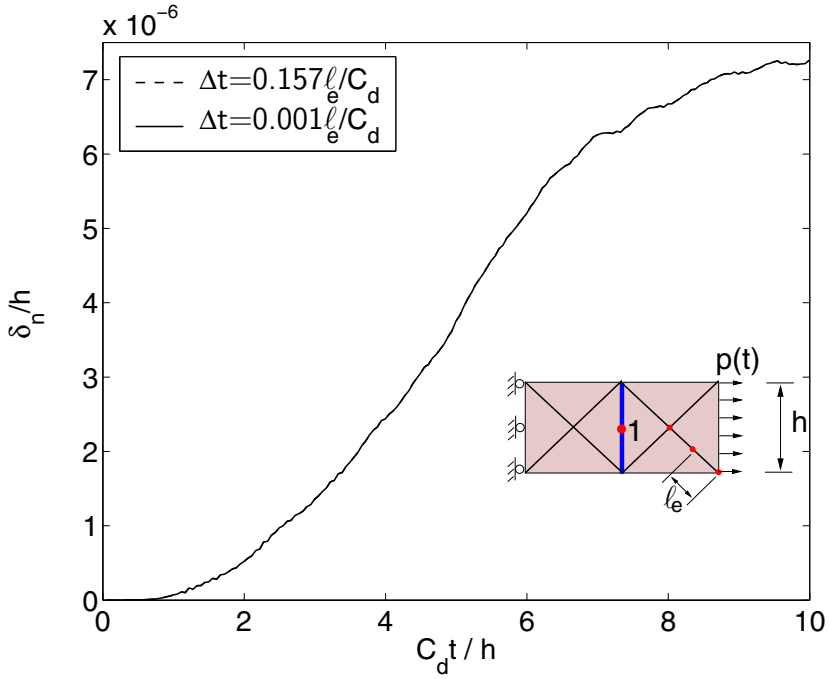

(b)

Figure 4.8: Determination of the stability threshold for problem in Figure 4.7, considering plane strain and 1 cohesive element inserted at middle vertical line. The normal separation δ_n is retrieved at node 1; (a) result is stable at $\Delta t = 0.157\ell_e/C_d$, but oscillates at $\Delta t = 0.159\ell_e/C_d$; (b) once threshold is reached, results don't depend on Δt.

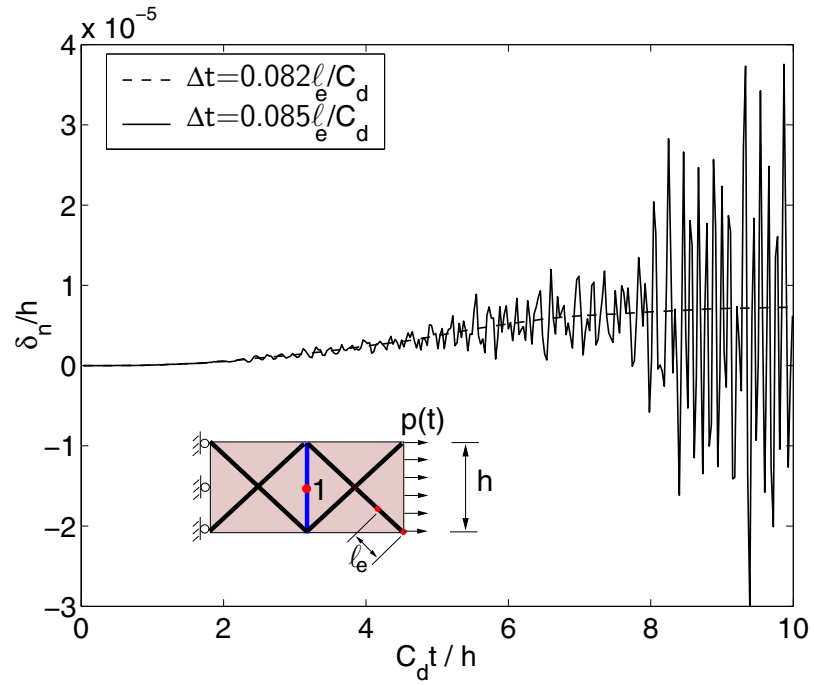

(a)

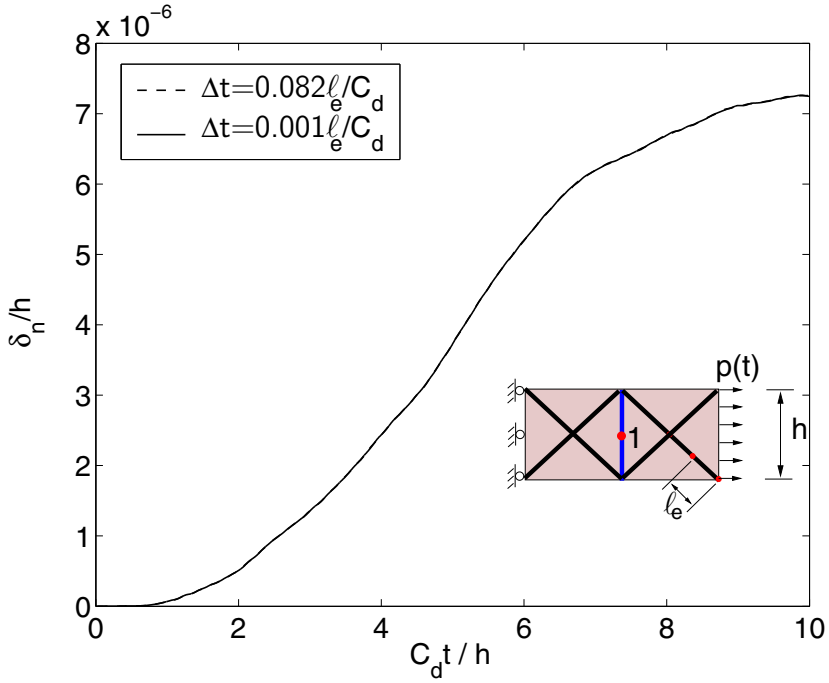

(b)

Figure 4.9: Determination of the stability threshold for problem in Figure 4.7, considering plane strain and cohesive element inserted along all interfaces. The normal separation δ_n is retrieved at node 1; (a) result is stable at $\Delta t = 0.082\ell_e/C_d$, but oscillates at $\Delta t = 0.085\ell_e/C_d$; (b) once threshold is reached, results don't depend on Δt.

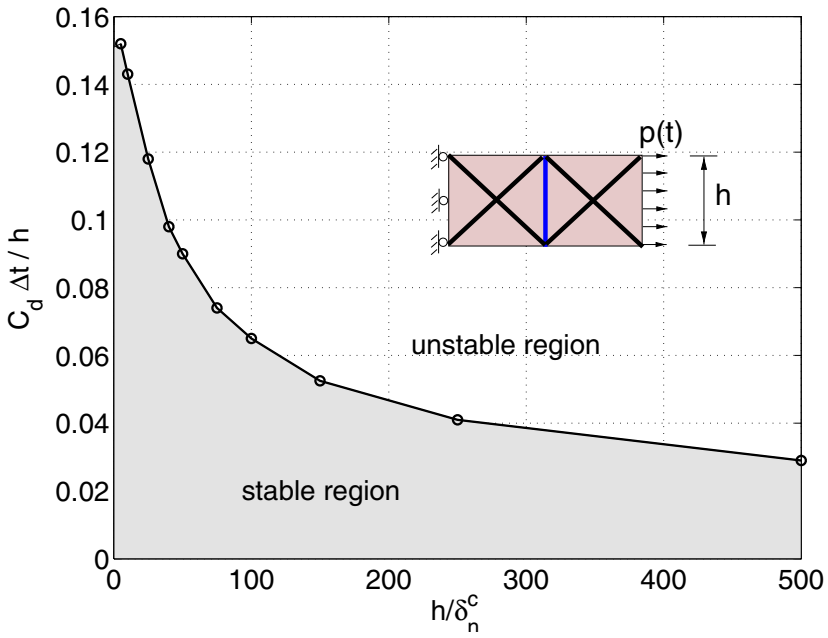

Figure 4.10: Stability threshold for different ratios of mesh size h with respect to critical displacement opening δ_n^c. The cohesive elements are inserted along every interface and plane strain is considered.

That the critical Δ_t value decreases with more cohesive elements is due to the increased complexity of stress wave transmission across the cohesive interfaces. With only one cohesive element, which is aligned normal to the wave propagation direction, the instability is only induced at one cohesive interface, and as long as the time step is small enough to resolve the "communication" of the traction-separation relationship to a steady stage at that interface, the result becomes stable. However with more cohesive interfaces, multiple "communications" are present, and the adjustment of separation at one cohesive element interface will influence that of others, therefore the time step that is good for only one cohesive element case can not satisfy the stable 'communications' of more interfaces, thus a smaller time step is needed.

The above results also indicate that the reduction of time step Δt for the cohesive element approach compared to the conventional FEM approach, is more significant for *plane-stress* than in *plane-strain* case.

The stability highly depends upon the ratio of element size and cohesive zone model parameter δ_n^c. The stability threshold Δt, normalized with dilatational wave speed C_d and element size h, calculated for different h/δ_n^c values, are presented in Figure 4.10 for plane-strain case. The stability decreases with increasing element size. This phenomenon can be understood as follows: when element size is smaller, it takes shorter time for the stress wave

to propagate through one bulk element and come across an interface. With such short time interval, the change of current stress wave profile (intensity, direction, *etc.*) from the last wave front that impact the interface is also smaller, so that it is easier to solve the "balance" of the separation-traction "communication" of the interface. However, with smaller element size, more cohesive elements need to be inserted, and accuracy of the scheme will be reduced, as will be discussed in the following section.

4.2.2 Accuracy

The added cohesive elements affect the accuracy of the FEM result ([12, 28]. Ideally, prior to crack propagation, the FEM simulation with cohesive elements should produce the same result as that without cohesive elements. However, the elastic model as employed in the current study introduces additional compliance to the structure, and thus entails larger deformation. This situation can be understood as described below.

As the previous section explains, to generate cohesive elements, one node shared by two or more bulk elements is duplicated with respect to the number of bulk elements sharing that node. In this case, each element has a node that is numbered separately, yet possesses the same spatial position along with some others. The connection of bulk elements, previously guaranteed by the shared node, is now sustained by cohesive elements, which relates pairs of coincident nodes following the cohesive law. Requiring the same result for FEM with and without cohesive elements implies that the initially coincident nodes do not separate prior to crack propagation, which is, unfortunately, impossible with the intrinsic elastic cohesive model. The cohesive elements can be conceived as nonelastic springs connecting bulk elements; initially with zero loading they do not extend. Under force they extend or shrink, and spring forces (cohesive forces here) are produced, trying to bring the nodes together again, yet the displacement between initially coincident nodes cannot be avoided. Thus, the stiffness of the springs, *i.e.* the cohesive elements will influence the accuracy of the result.

Figure 4.11 presents a cantilever beam with only one cohesive element, which is positioned at half length of the beam, in the vertical direction. The beam is subjected to tip traction and the prescribed force is small enough to keep the deformation within the elastic range. Displacement at three nodes are tracked: one tip node (1), and two nodes which form a pair in the cohesive element (nodes 2 and 3).

In Figure 4.12, it is obvious that the lower the maximum cohesive strength σ_{max}, the larger the tip displacement. By taking the FEM result for the same problem without cohesive element as reference, one notices that the results obtained for the case $\sigma_{max} = E/10$ are very

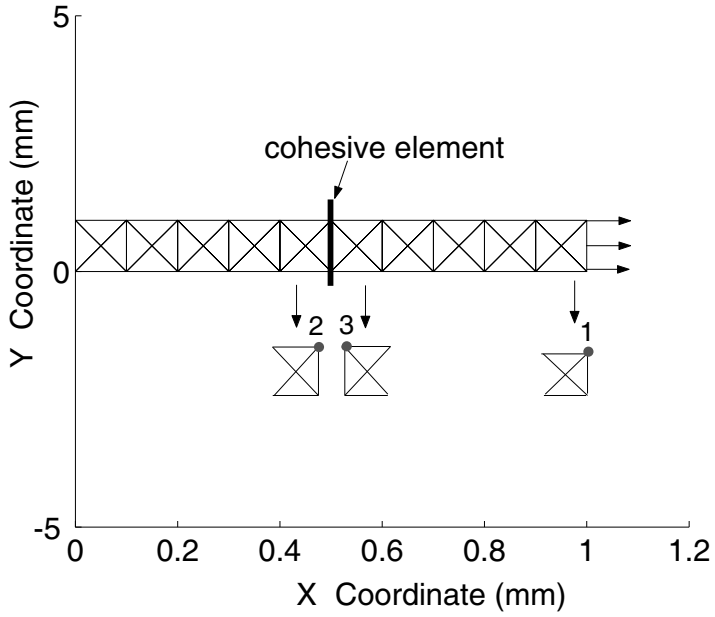

Figure 4.11: One cohesive element in a cantilever beam. Displacement in x-direction at nodes 1 (tip node), 2 and 3 (initially at the same position) are retrieved.

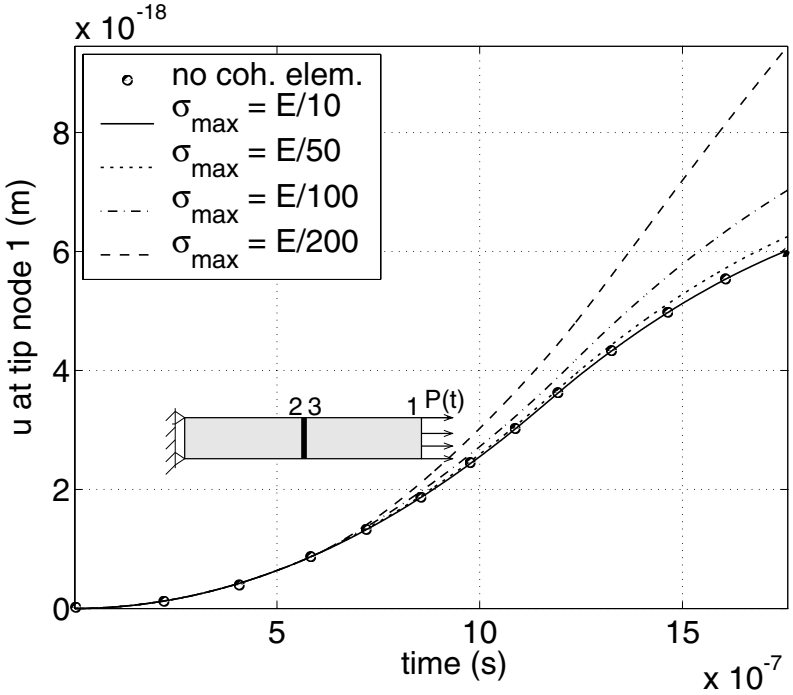

Figure 4.12: Tip-displacement comparison for different cohesive strength cases.

close to the reference solution, while that for $\sigma_{max} = E/200$ represent a more compliant beam.

The difference is due to the cohesive element. Figure 4.13 shows the displacement at the three nodes (1, 2 and 3), plotted for the $\sigma_{max} = E/200$ case. Ideally, the gap between nodes 2 and 3 should be negligible, however, in this plot the two curves for these two nodes are far apart. The ratios of the gap between nodes 2 and 3 ($U_3 - U_2$) to the tip displacement at 1 (U_1 for different cohesive strength cases are plotted in Figure 4.14. For the weak interface, *i.e.*$\sigma_{max} = E/200$, at the end of test time, 40 percent of the maximum displacement at the tip is due to the gap resulting from the cohesive element.

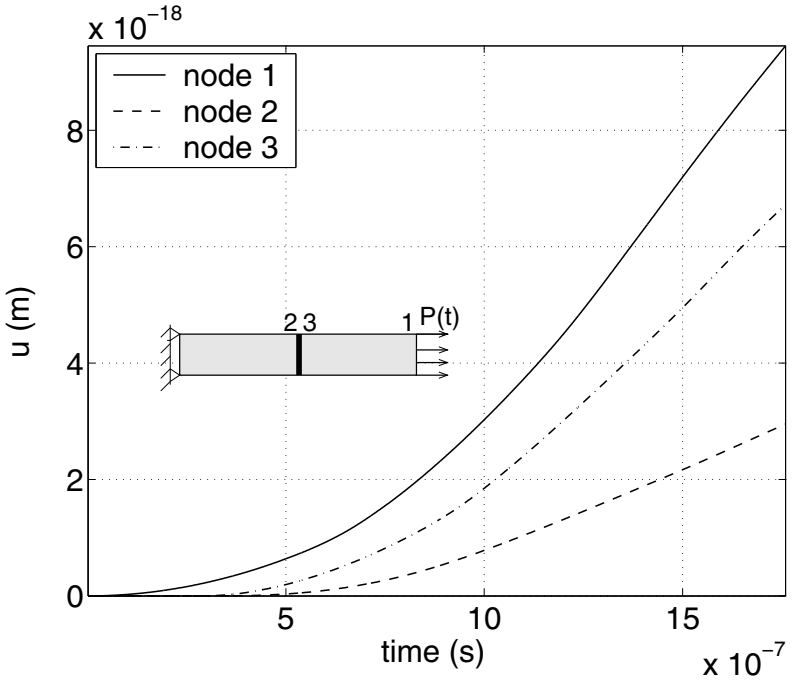

Figure 4.13: Displacement in x-direction at nodes 1 (tip node), 2 and 3 (initially at the same position) are retrieved for $\sigma_{max} = E/200$ case.

Based on above discussion, $\sigma_{max} = E/10$ is taken to test for the validity of the code. It is anticipated that with this strength value, the presence of cohesive elements would have a nominal influence on the dynamic problem under small loading.

Again the cantilever beam (Figure 2.5) subjected to transient half-sine shape impact loading (Figure 2.6) example is considered because reference results without cohesive elements are available (shown in Chapter 3). To observe the influence of cohesive elements on the accuracy of results, results for beam *with* cohesive elements in entire region and *without* cohesive elements are presented in Figure 4.15 for homogeneous beam, and Figure 4.16 for

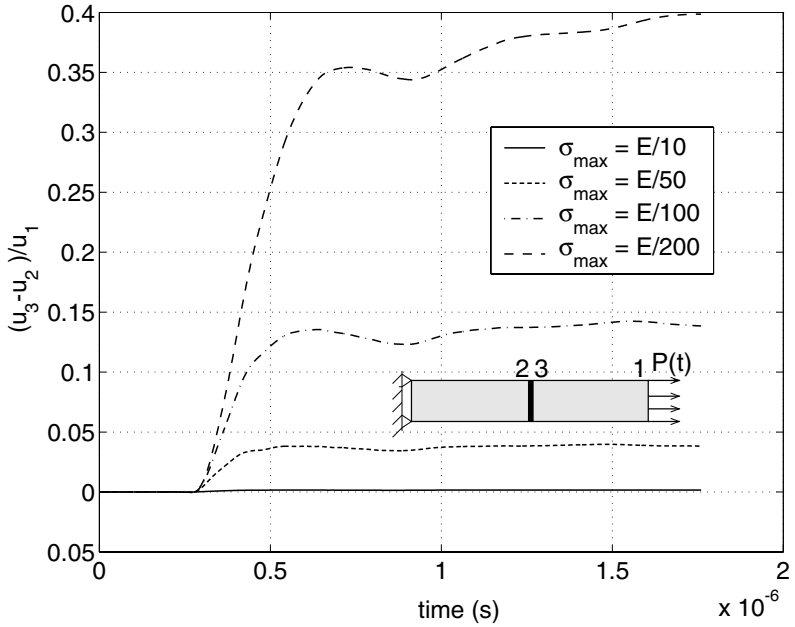

Figure 4.14: Ratio of the displacement gap at cohesive element to the tip displacement for different cohesive strength cases.

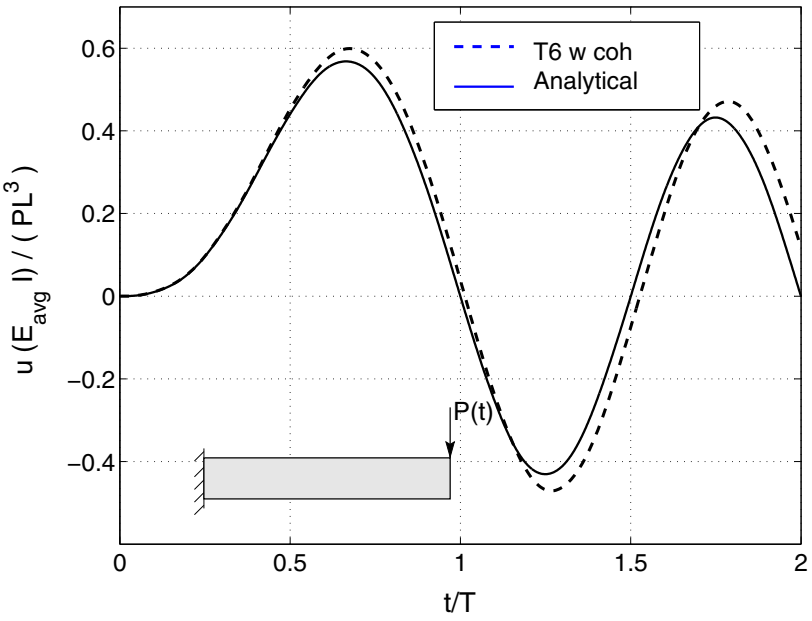

Figure 4.15: Comparison of tip displacement for cantilever beam with cohesive elements in entire domain and without cohesive elements. Homogeneous material, $E = 5GPa$, $\rho = 1g/cm^3$, $\nu = 0.3$, $\sigma_{max} = E/10$.

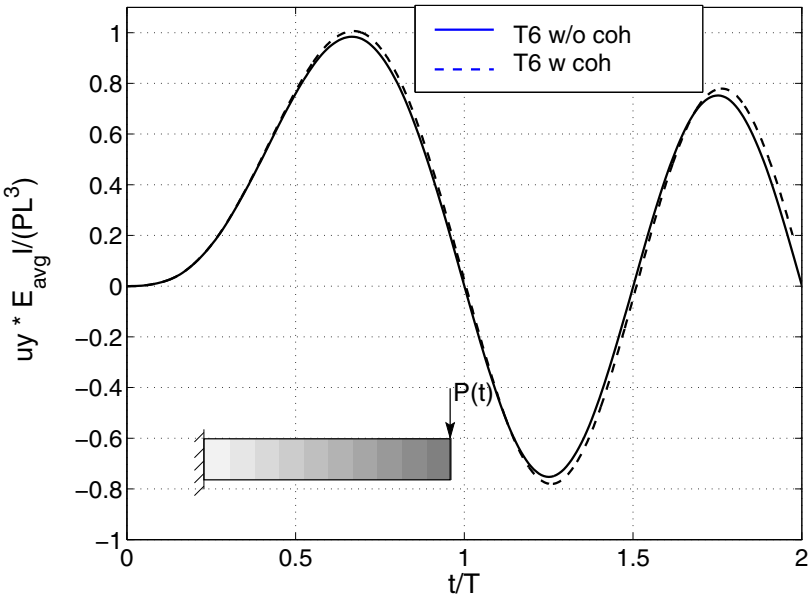

Figure 4.16: Comparison of tip displacement for cantilever beam with (in entire domain) and without cohesive elements. Nonhomogeneous material, $E_1 = 1GPa$, $E_2 = 5GPa$, $\nu_1 = \nu_2 = 0.3$, $\rho_1 = 0.5g/cm^3$, $\rho_2 = 1.5g/cm^3$, $\sigma_{max1} = E1/10$, $\sigma_{max2} = E2/10$.

FGM beam with linear material gradation in x direction. In Figure 4.15, comparison is given between the FEM result and analytical solutions, while in Figure 4.16 comparison is made between FEM results since analytical solution is not attainable. As expected, the presence of cohesive elements results in slightly larger displacement and longer period, yet within acceptable range.

Chapter 5

Dynamic Fracture of Brittle FGMs

With the code validated and numerical stability and accuracy issues discussed and understood, we proceed to apply the CZM approach to investigate fracture problems with richer dynamic features. In this Chapter, three classes of problems are studied:

- Spontaneous rapid crack growth in an elastic homogeneous/FGM strip. This example is to further investigate the influence of mesh refinement, orientation, and capacity of crack nucleation without initial crack for CZM approach. Also, energy balance is checked, which provides valuable insight into the energy exchange in the fracture process.
- Dynamic fracture propagation of FGM beam under impact loading. This example provides a rare opportunity to employ *real* FGM material parameters and compare results with that of experiments.
- Crack branching in homogeneous/FGM plate. A plate subjected to impact loading is simulated to demonstrate the important feature of crack branching capacity of the CZM approach. In this example, cohesive elements are assigned in a large region, and crack evolves in a branched pattern.

5.1 Spontaneous Rapid Crack Growth in an Elastic Homogeneous/FGM Strip

In this section, the rapid propagation of a straight crack along defined path is studied for an elastic strip subjected to initial stretch [4]. First, the mesh convergence of the numerical method is investigated. Result of the crack tip velocity reveals its dependence on mesh

refinement. Next, energy balance issue is investigated in detail, which also provides verification information for the numerical implementation. After that, graded material property is adopted to investigate the influence of material variation. Moreover, to further explore the capability of simulating spontaneous crack nucleation, the elastic strip *with* initial strain problem is extended to FGM case *without* initial crack prescribed. It was found that by manipulating material properties of FGM strip the crack can nucleate at high stress region and propagate thereafter.

5.1.1 Problem Description

The geometry and boundary conditions for the strip problem are illustrated in Figure 5.1. The strip is initially stretched uniformly by imposing an initial displacement field

$$u(x, y; t = 0) = 0, \quad v(x, y; t = 0) = \epsilon_0 y \tag{5.1}$$

The upper and lower surfaces are held fixed and a small crack length a is introduced at the left edge at time $t = 0$. For homogeneous strip case, the material is taken as PMMA, and its properties are tabulated in Table 5.1. For the FGM problem, the detailed material properties are described for each case in later sections.

Table 5.1: Material properties for PMMA strip subjected to initial stretch

E (GPa)	ν	ρ (kg/m^3)	G_{Ic} (N/m)	$\sigma_{\max}$ (MPa)	δ_c (μm)
3.24	0.35	1190	352.3	324	0.4

5.1.2 Mesh Convergence

The domain is discretized uniformly by T6 elements of various element sizes as shown by Figure 5.2. Cohesive elements are inserted along plane y=H in order to constrain the crack path along its original plane and prevent crack branching.

Driven by the strain energy stored in the pre-stretched strip, the crack quickly propagates. As the strain energy put into the system is increased, the fracture speed should approach the Rayleigh speed C_R of PMMA, which is 939m/s.

It is essential to investigate the convergence of the numerical scheme in terms of the relation between the characteristic cohesive length scale δ^c and mesh size h. Here h is defined as the minimum nodal distance of the cohesive elements. Since quadratic elements

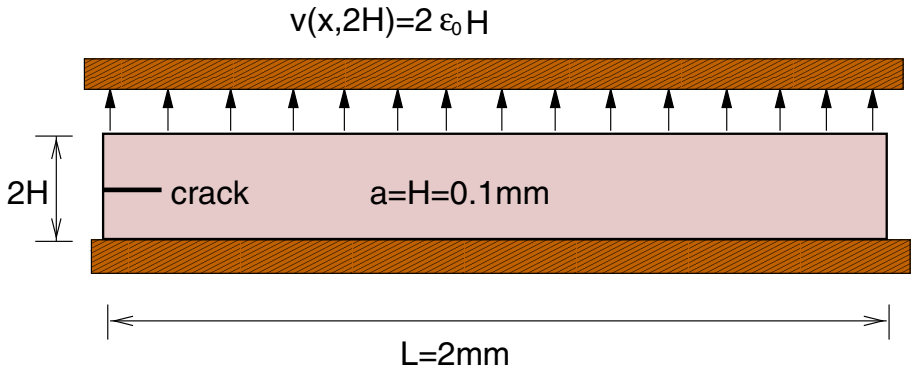

Figure 5.1: Domain and boundary conditions of the strip dynamic fracture test

are used, one element length equals $2h$. A static estimate of the cohesive zone size for a constant traction-separation relation [36] is

$$R = \frac{\pi}{8} \frac{E}{1-\nu^2} \frac{G_{Ic}}{\sigma_{ave}^2} \tag{5.2}$$

where for exponential cohesive law, $\sigma_{ave} = 0.453\sigma_{max}$, as shown in Figure 5.3. For PMMA, Young's modulus $E = 3.24GPa$, Poisson ratio $\nu = 0.35$, mode I critical energy release rate $G_{Ic} = 352.3J/m^2$, thus the cohesive zone size is approximately 23.6 μm.

The influence of mesh size on the evolution of the crack tip position is shown in Figure 5.4 and 5.5, for an initial stretching parameter $\epsilon_0 = 0.035$ and $\epsilon_0 = 0.032$, respectively. Crack tip is defined as the right-most point along the fracture plane for which $\delta > 6\delta^c$, where δ denotes the interface displacement jump.

Evidently, mesh size plays an important role in the spontaneous propagation of fast crack. When the mesh is too coarse (h=50μm), the crack does not propagate at all. As mesh is progressively refined, the solution converges as shown in Figure 5.4 and 5.5. The $C_{crack} = C_R$ curve assumes an ideal case for which the crack starts to propagate at $t = 0$ through the crack path at Rayleigh wave speed. Since it takes a finite time interval for crack to initiate, this curve is shifted from the rest of FEM results. However the crack tip speed of these mesh refinement cases, *i.e.* the slope of the curves, does indicate that with refined mesh, the crack tip speed is asympototically closer to the Rayleigh wave speed for high initial stretch, as shown in Figure 5.4.

The rate of mesh convergence also depends on the initial condition of the problem. To drive the crack propagate through the whole length of strip, the minimum initial stretch can be estimated as $\epsilon_0 = 0.031$. The detailed derivation will be given in the energy balance discussion. Therefore, for both cases ($\epsilon_0 = 0.035, 0.032$) in Figure 5.4 and 5.5, the initial strain energies stored in the elastic strip are high enough to drive the crack to propagate

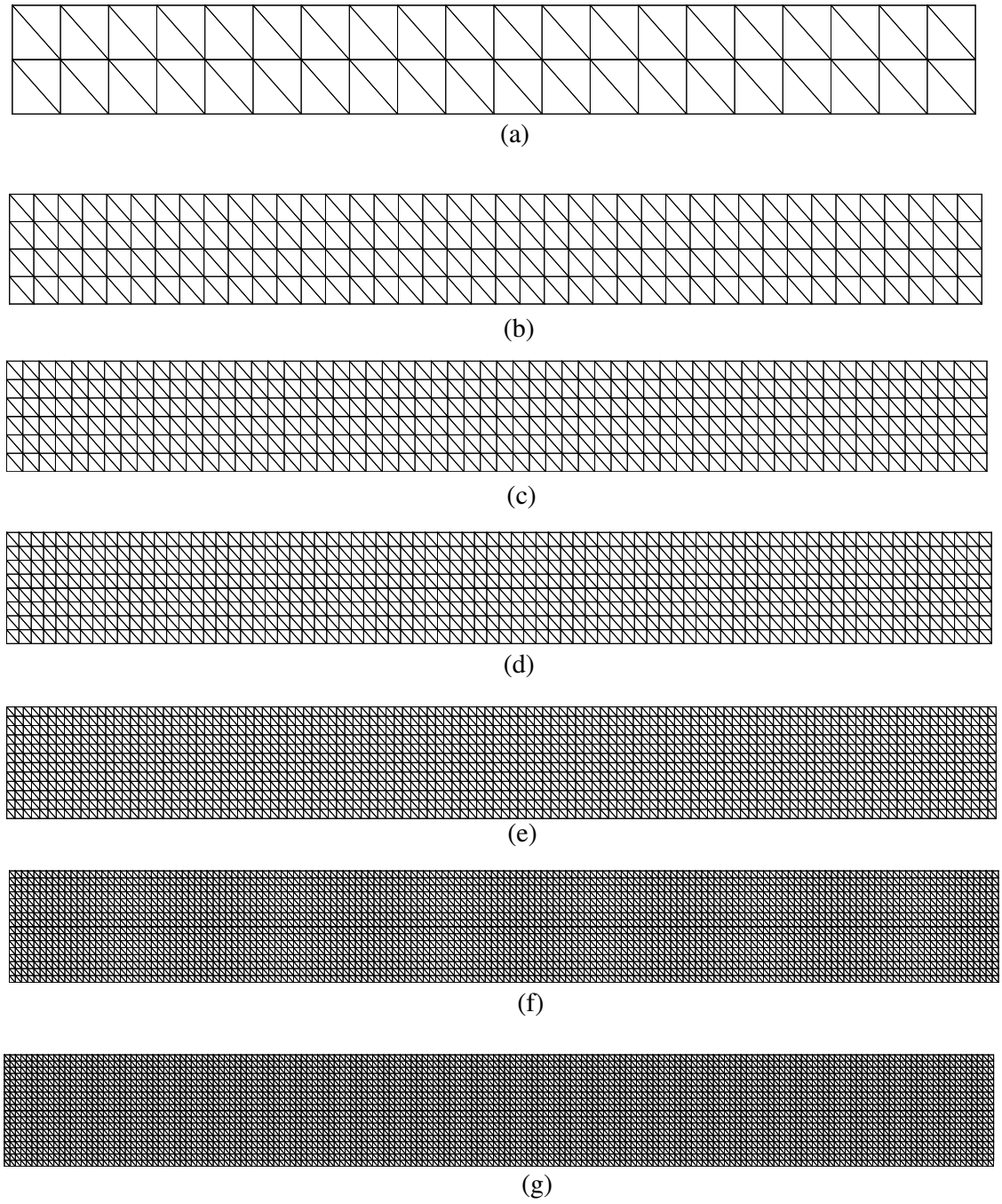

Figure 5.2: Mesh discretization with different T6 element size for elastic strip subjected to initial tension problem. Cohesive elements are inserted on layer at half height, along x direction, and h is defined as distance between nearest nodes of cohesive element; (a) h=50μm; (b) h=25μm; (c) h=16.7μm; (d) h=12.5μm; (e) h=8.33μm; (f) h=6.25μm; (f) h=5.56μm.

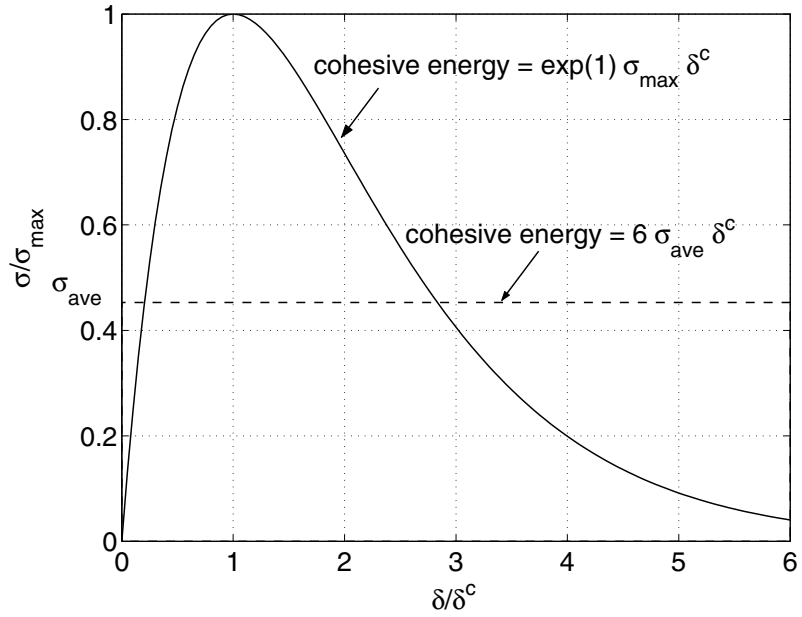

Figure 5.3: Determination of average cohesive strength σ_{ave} by equating cohesive energy of exponential cohesive law (area under exponential curve) with rectangular cohesive law (rectangle area). Complete decohesion is considered to occur at $\delta = 6\delta^c$.

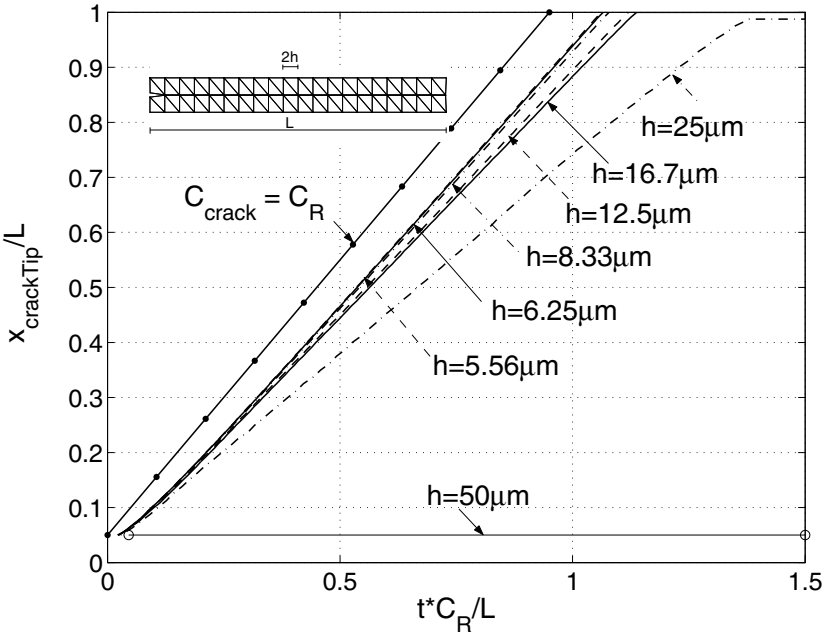

Figure 5.4: Normalized crack tip location versus normalized time for various levels mesh refinement. C_R denotes Rayleigh wave speed, initial stretch $\epsilon_0 = 0.035$.

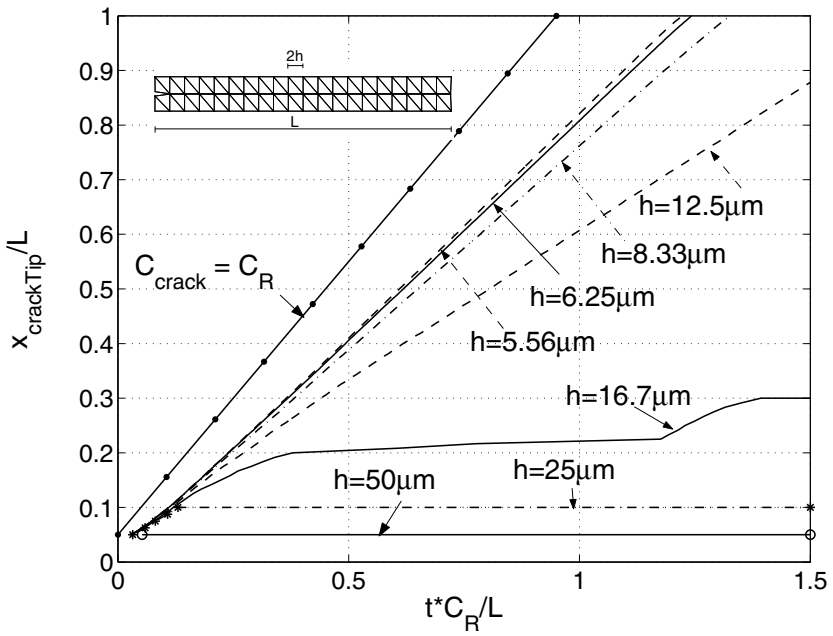

Figure 5.5: Normalized crack tip location versus normalized time for various levels of mesh refinement. C_R denotes Rayleigh wave speed, initial stretch $\epsilon_0 = 0.032$.

through the whole strip. For $\epsilon_0 = 0.035$ case, these three meshes produce very close results in terms of simulation time for the crack to propagate through the strip: $h = 5.56\mu m$, $h = 6.25\mu m$ and $h = 8.33\mu m$, and these two meshes also give good results: $h = 12.5\mu m$, $h = 16.7\mu m$, which differ from the result given by mesh of $h = 5.56\mu m$ only by 5% and 7%, respectively. However, for slightly lower value of initial stretch, $\epsilon_0 = 0.032$, only results from these two meshes are close: $h = 5.56\mu m$, $h = 6.25\mu m$, mesh size $h = 8.33\mu m$ produces 8.5% difference compared to the $h = 5.56\mu m$ result, and mesh size $h = 12.5\mu m$ gives over 30% difference, while $h = 16.7\mu m$ gives completely misleading result–crack arrests.

The results thus suggests that the characteristic element size should be chosen two or three times smaller than cohesive zone size to ensure convergence. For example, for this strip problem, when $h \leq 8.33\mu m$, which is around one third of the estimated cohesive zone size, the result is acceptable. This is consistent with suggestions made by other researchers ([12, 28]). Moreover, this requirement can be relaxed for some particular cases, *e.g.*, for this strip problem, at high initial stretch, larger cohesive element size can produce pretty accurate result, but it is difficult to generalize this observation to other problems.

A similar test is performed to model crack arrest under dynamic conditions, as depicted in Figure 5.6, which shows the effect of initial stretching of the elastic strip on the crack propagation. When a sufficient amount of energy is stored initially in the system, the crack speed quickly approaches the Rayleigh wave speed C_R. *e.g.*, for $\epsilon_0 = 0.5$, the crack tip curve

is almost parallel to that of the ideal case where crack tip speed equals Rayleigh wave speed ($C_{crack} = C_R$ curve). However, for initial stretch $\epsilon_0 < 0.031$, the crack arrests.

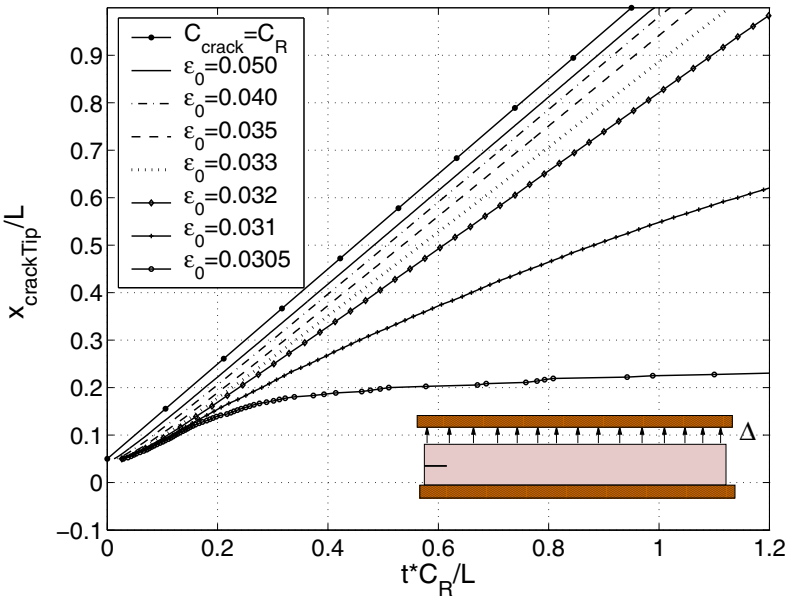

Figure 5.6: Normalized crack tip location versus normalized time for various initial stretching parameter ϵ_0. C_R denotes Rayleigh wave speed.

5.1.3 Mesh Orientation

Results presented in Figure 5.4, 5.5 and 5.6 are obtained for meshes shown in Figure 5.2, which has certain mesh orientation bias, *i.e.* the diagonal lines that bisect the quads into T6 elements are all aligned in -45 degree direction, with respect to x coordinate. With the concern whether a specific orientation influences computational results in current problem, two more mesh orientations are employed to simulate the same problem, which are plotted in Figure 5.7, for diagonal lines in 45 degree direction with respect to x coordinate (Figure 5.7(b)), and 'Union Jack' mesh (Figure 5.7(c)).

For visual clarity, the mesh shown in Figure 5.7 are for characteristic mesh size $h = 25\mu m$, while numerical simulations are performed using a further refined mesh of $h = 5.56\mu m$. Since the cohesive elements are along a predefined straight line and are of the same characteristic size in all three meshes, we expect the results to be similar. This is proved by the results shown in Figure 5.8, which compares the crack tip location of three meshes, for an initial stretch $\epsilon_0 = 0.035$. Apparently, results of the two 'biased' meshes, in the sense that the elements are not symmetric with respect to x coordinates, coincide with each other within plotting accuracy, while the 'Union Jack' mesh result is slightly different.

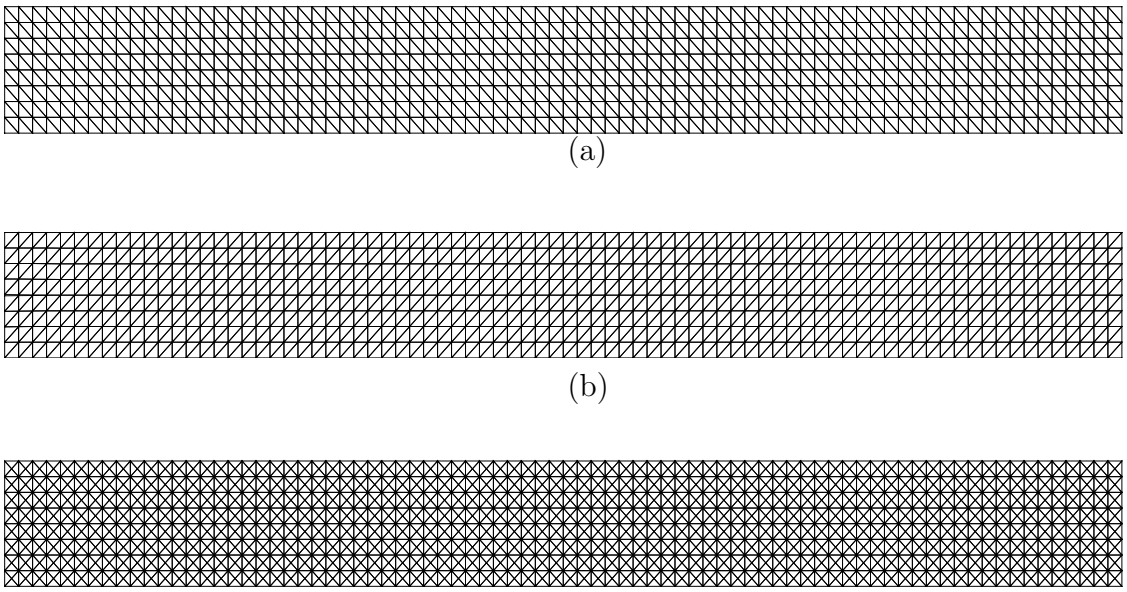

(a)

(b)

(c)

Figure 5.7: Three Mesh orientations, characteristic mesh size is $h = 25\mu m$; (a) Diagonal lines in -45 degree direction measured from x coordinate; (b) Diagonal lines in 45 degree direction measured from x coordinate; (c) Union Jack mesh.

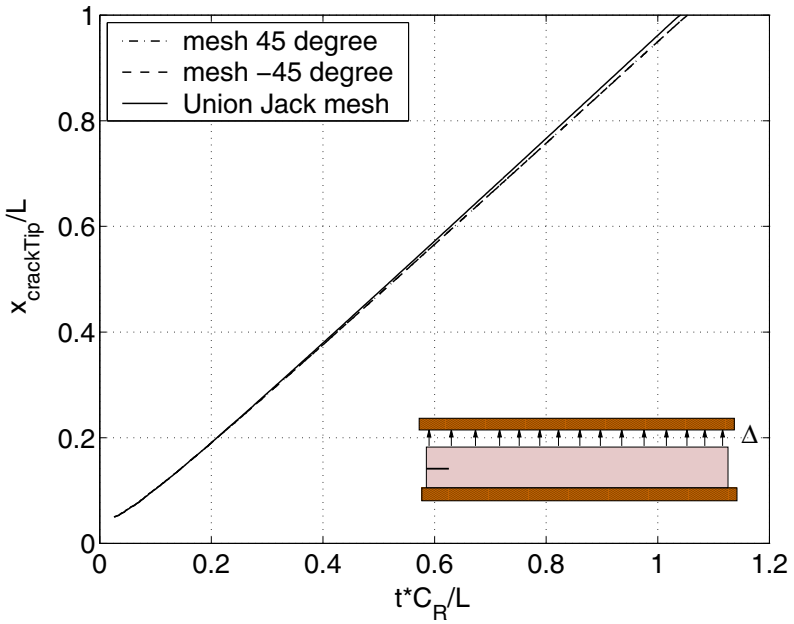

Figure 5.8: Normalized crack tip location versus time for three different mesh orientations (Figure 5.7). Initial stretch $\epsilon_0 = 0.035$, characteristic cohesive element size $h = 5.56\mu m$.

5.1.4 Energy Balance and Validation of Results

This elastic strip problem presents an appropriate example for us to examine the conversion among energies associated with different energetics during dynamic fracture process. There are two analytical solutions available that allow us to validate the computational results. First, the initial boundary condition is such that an analytical evaluation of the initial strain energy is easily obtained. Second, the cohesive elements are prescribed along a defined path, hence the total fracture energy required for crack to propagate through the entire strip can be computed readily. Moreover, the dissipated fracture energy presents a large portion of the total initial energy, thus the conversion between the stored strain energy and dissipated fracture energy is evident.

Energy balance expression. As described in Section 3.4, there are totally six energy components of interest. *i.e.*,

- External work E_{ext}
- Kinetic energy K
- Strain energy due to elastic deformation of the bulk elements U_{bulk}
- deformation energy due to elastic deformation of the cohesive elements U_{coh}
- Total cohesive energy E_{coh}
- Fracture energy E_{frac}

For the current problem under discussion, external work is kept constant, with value equal to the initial strain energy due to deformation. At any time instant, the total energy in the system is

$$E_{tot} = U + K + E_{frac} = const \tag{5.3}$$

where

$$U = U_{bulk} + U_{coh} \tag{5.4}$$

represents the total recoverable elastic energy of the system.

Initial strain energy. For the above described initial condition, *i.e.* uniform stretch in y direction at $t = 0$, the strain energy stored in the strip can be obtained analytically as:

$$U_{bulk} = w \times A = \frac{1}{2}\sigma_{ij}\epsilon_{ij} \times A = \frac{1}{2}\sigma_{yy}\epsilon_{yy} \times A = \frac{1}{2}\frac{E}{1-\nu^2}{\epsilon_{yy}}^2 \times A \tag{5.5}$$

where w denotes strain energy density and A is the strip area. Since the initial stretch is only in y direction, all stress and strain components vanish except for σ_{yy} and ϵ_{yy}. When initial stretch $\epsilon_0 = 0.032$, strain energy density is

$$w = \frac{1}{2}\frac{3.24 \times 10^9}{1 - 0.35^2}0.032^2 = 1.8905 \times 10^6 N \cdot m/m^2$$

and the total strain energy stored in the system ($w \times A$) is

$$U_{bulk} = 0.756184615 N \cdot m$$

while the initial strain energy calculated from finite element method is

$$U_{bulk} = 0.75618464211 N \cdot m$$

which is the same as the analytical solution up to seven digits.

Energy evolution. The evolution of various energy components for the spontaneous crack propagation simulation in the elastic strip with $\epsilon_0 = 0.032$ is shown in Figure 5.9, 5.10 and 5.11.

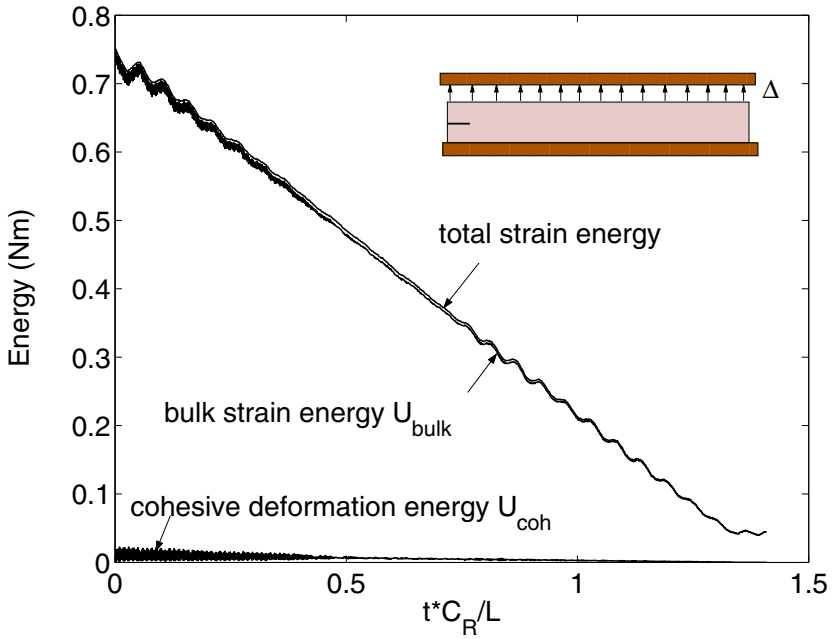

Figure 5.9: Total strain energy consists of contribution from bulk elements and cohesive elements. Cohesive element contribution only represents a small fraction of the total energy in the strip fracture problem. Applied strain $\epsilon_0 = 0.032$, characteristic cohesive element size $h = 6.25\mu m$.

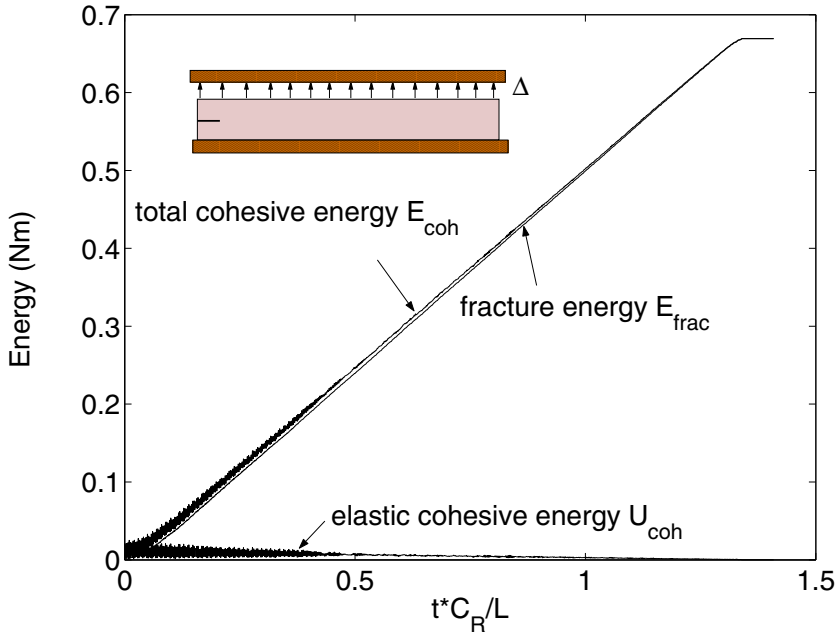

Figure 5.10: Total cohesive energy E_{coh} can be decomposed into recoverable elastic deformation energy U_{coh} and dissipated fracture energy E_{frac}. Applied strain $\epsilon_0 = 0.032$, characteristic cohesive element size $h = 6.25\mu m$.

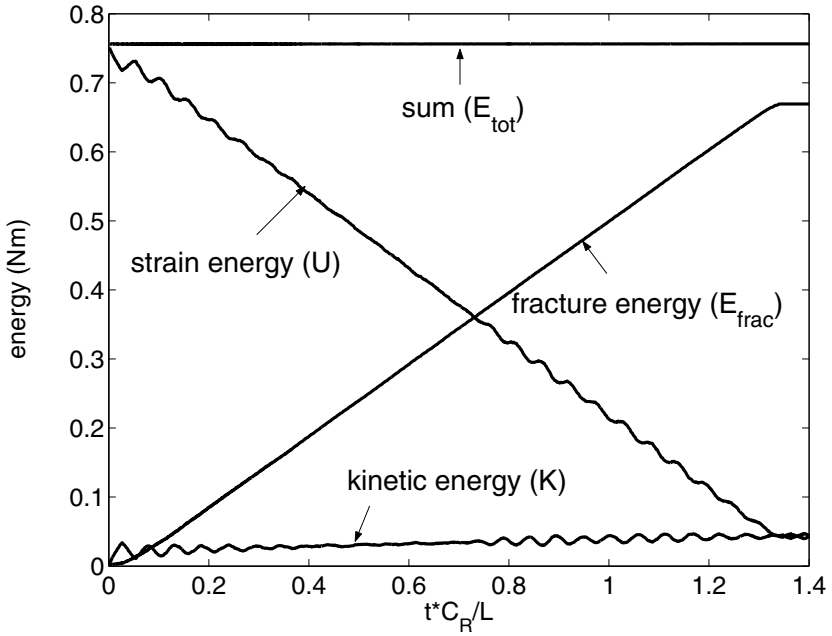

Figure 5.11: Evolution of various energy components for the strip fracture problem with applied strain $\epsilon_0 = 0.032$, characteristic cohesive element size $h = 6.25\mu m$.

As explained earlier in Section 3.4, some elastic energy is stored in the cohesive elements. As shown in Figure 5.9, the cohesive deformation energy denoted by the bottom curve only represents a small fraction of the total elastic energy. There is a constant dynamic exchange between these two types of elastic energies and their sum is a relatively smooth curve, as shown in Figure 5.9.

Total cohesive energy E_{coh} can be decomposed into recoverable elastic part U_{coh} and dissipated fracture energy E_{frac}, as shown in Figure 5.10. The curves representing total cohesive energy and elastic cohesive energy oscillates, while the dissipated fracture curve is rather smooth.

Figure 5.11 shows the total strain energy, kinetic energy, energy dissipated by fracture and the sum of these terms. Energy conservation is obtained as required. Apparently, the strain energy initially stored in the system gradually converts to fracture energy and drives the crack to propagate. A small portion of strain energy is converted to kinetic energy, which oscillates in equilibrium with the strain energy.

Fracture energy required for crack propagating through strip. Since the cohesive elements are prescribed along a predefined path and at the end of simulation they are all debonded, the energy required for the entire fracture process can be evaluated analytically:

$$E_{frac} = G_I A = 352.3N \cdot m/m^2 \times (1.9mm \times 1m) = 0.66935N \cdot m$$

while the finite element result is

$$E_{frac} = 0.66944N \cdot m$$

This is a positive indication that the numerical implementation of cohesive elements is successful.

The minimum initial stretch needed for the crack to propagate through the entire strip length can also be estimated. If kinetic energy K and elastic cohesive energy U_{coh} are neglected, *i.e.* assume all initial strain energy U_{bulk} can be converted into fracture energy E_{frac}, by equating Eq. 5.5 and the above value

$$U_{bulk} = \frac{1}{2}\frac{E}{1-\nu^2}{\epsilon_0}^2 \times A = E_{frac}, \tag{5.6}$$

the initial stretch needed for crack propagating through strip is obtained as $\epsilon_0 = 0.0301$. However, part of initial strain energy is converted to kinetic energy K and elastic cohesive energy U_{coh}. Elastic cohesive energy is nominal as shown in Figure 5.9, and we just estimate

the kinetic energy. When the strip is stretched only in y direction at $t = 0$, the left and right boundaries of the strip are kept straight. Afterwards, these two boundaries tend to deform in a curved shape due to Poisson effect. The kinetic energy can be estimated as the difference in strain energy from initial deformation shape to this curved deformation shape. Analytical solution is not sought, rather we estimate it from Figure 5.11 as $K = 0.05N \cdot m$. Hence, the initial stretch needed for crack propagating through entire strip is $\epsilon_0 = 0.0312$. This is consistent with the result shown in Figure 5.6.

5.1.5 Crack Propagation in FGM Strip

Now we consider that an FGM strip with an initial crack and linear material variation in x direction is subjected to initial stretch as described in the homogeneous case. The detailed material properties are tabulated in Table 5.2. Young's modulus is three times as high at left side ($4.86GPa$) as the right side ($1.62GPa$), and the average Young's modulus is kept the same as the homogeneous PMMA strip. Poisson's ratio and material density are assumed to remain constant. The cohesive strength is kept as $E/10$ and thus varies linearly along the x direction. The critical interface separation remains $0.4\mu m$. The cohesive elements are again prescribed along the ligament on the half height plane ($a < x < L$, $y = H$). For the current problem, mode I fracture dominates, and the two FGM cohesive zone models discussed in Chapter 3 will produce the same results. The effective quantity model (described in Section 3.1) is used with the parameters chosen as:

$$\beta_1 = \beta_2 = 1\,, \qquad \eta = \sqrt{2}$$

The stored strain energy drives the crack to propagate, and the numerical simulation results of crack tip location versus time for various ϵ_0 values are illustrated in Figure 5.14.

Table 5.2: Material properties for FGM strip subjected to initial stretch

	E (GPa)	ν	ρ (kg/m^3)	G_{Ic} (N/m)	$\sigma_{\max}$ (MPa)	δ_c (μm)
$x = 0$	4.86	0.35	1190	528.4	486	0.4
$x = L$	1.62	0.35	1190	176.1	162	0.4
average	3.24	0.35	1190	352.3	324	0.4

Notice that the crack tip velocity is no longer constant, as in the previous example. This is due to the nonhomogeneous material property. When input energy is sufficiently large, the crack tip velocity approaches the Rayleigh wave speed, which also depends on material location. One observes that as input energy increases, the crack tip velocity approaches the

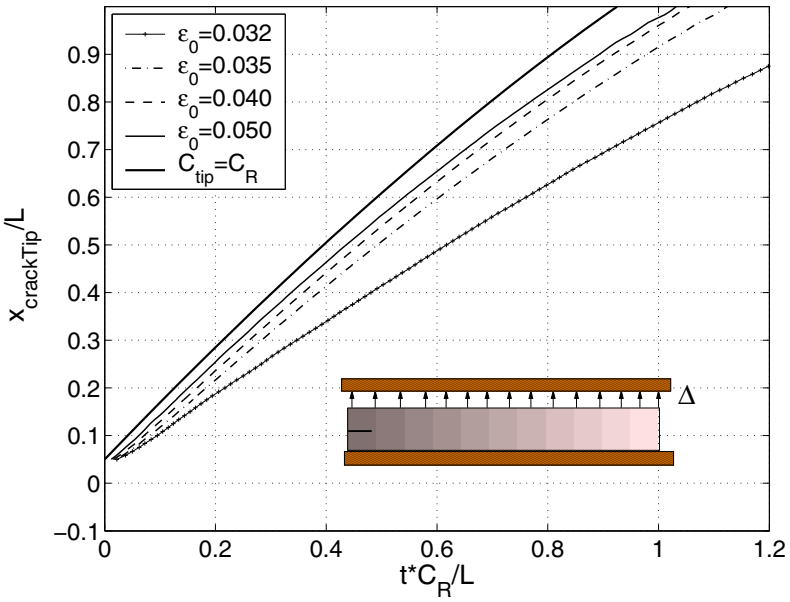

Figure 5.12: Normalized crack tip location versus normalized time for FGM strip subjected to various initial stretching parameter ϵ_0. Notice that the Rayleigh wave speed varies along the x direction.

theoretical Rayleigh wave speed.

Again, energy balance is obtained, as illustrated in Figure 5.13 for the initial stretch $\epsilon_0 = 0.032$. The fracture energy curve also exhibits nonlinear curvature. Obviously, the fracture energy required for the cohesive elements to lose cohesion is larger at left side than at right side, as indicated by the material property (Table 5.2).

First the numerical result of initial strain energy is checked with the theoretical value, which is computed as

$$U_{bulk} = \frac{1}{2}\frac{3.24 \times 10^9}{1 - 0.35^2} 0.032^2 \times (4 \times 10^{-7}) = 0.756184615 N \cdot m$$

The numerical result is $U_{bulk} = 0.756184642 N \cdot m$, which is the same as the theoretical value up to seven digits. Note that the uniform stretch results in non-uniform stress field, hence the strain energy density also varies linearly along the x-direction, and the above formulation uses the average value of Young's modulus for simplicity.

The energy required for the crack to propagate through is

$$E_{frac} = G_I A = 343.4 \times (1.9 \times 10^{-3}) = 0.65246 N \cdot m$$

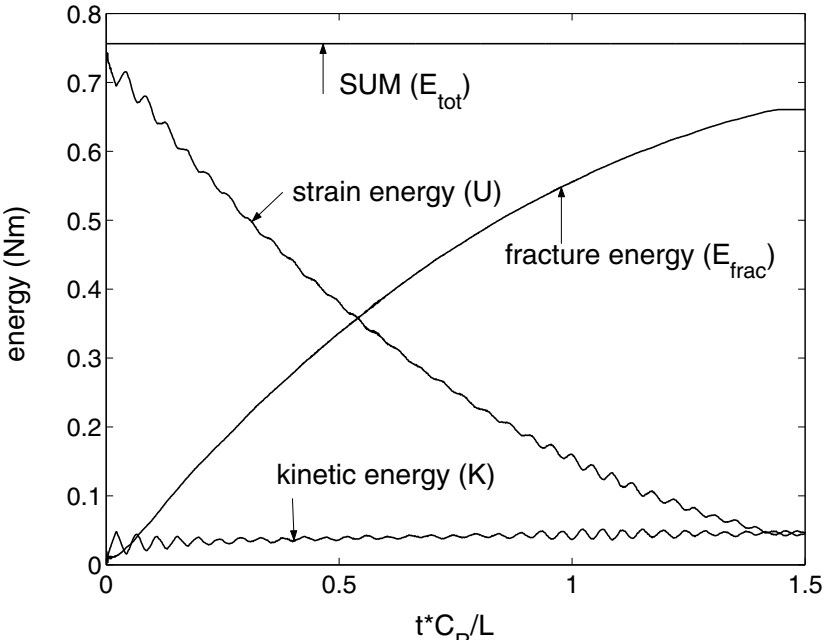

Figure 5.13: Evolution of various energy components for the FGM strip fracture problem with applied strain $\epsilon_0 = 0.032$, considering characteristic cohesive element size $h = 6.25\mu m$.

and the numerical result is

$$E_{frac} = 0.65262N \cdot m$$

the same as analytical value up to 3 digits. The energy release rate G_I in the above expression is the average value of G_I along $a < x < L$.

5.1.6 Spontaneous Crack Initiation in FGM Strip

So far, the discussion in this section has been restricted in strips with prescribed crack. For homogeneous material, a pre-crack was necessary for crack propagation to start. Without the initial crack, the uniform stretch incurs uniform stress in the entire domain, and crack cannot initiate spontaneously even though cohesive elements are prescribed, unless the stretch applied is very high. For instance, to have a uniform stress inside strip to reach cohesive strength $\sigma_{max} = E/10$, initial stretch ϵ_0 needs to reach roughly 0.1. Under such condition, the entire weak interface will debond simultaneously, therefore there is virtually no crack initiation and propagation involved. On the other hand, for FGM, since the material property is graded, uniform stretch results in nonuniform stress field, thus crack may nucleate at region of relatively high stress and low cohesive strength, and crack can initiate spontaneously.

Assume an FGM strip with linear material variation in x direction is subjected to uniform stretch, with detailed material properties tabulated in Table 5.3. Young's modulus is three times as high at one side ($4.86GPa$) as the other ($1.62GPa$), and the average Young's modulus is the same as the homogeneous PMMA strip. The Poisson's ratio and material density remain constant. The critical interface separation remains $0.4\mu m$. Notice that multiple cohesive strength values (σ^1_{max}– σ^4_{max}) are provided in Table 5.3. The reason will be discussed shortly. The cohesive elements are prescribed along the ligament on the half height plane ($0 < x < L$, $y = H$), but without initial crack.

Table 5.3: Material properties for FGM strip without pre-crack subjected to initial stretch

	E (GPa)	ν	ρ (kg/m^3)	δ_c (μm)	$\sigma^1_{\max}$ (MPa)	$\sigma^2_{\max}$ (MPa)	$\sigma^3_{\max}$ (MPa)	$\sigma^4_{\max}$ (MPa)
$x = 0$	4.86	0.35	1190	0.4	297	267	237	208
$x = L$	1.62	0.35	1190	0.4	297	267	237	208
average	3.24	0.35	1190	0.4	297	267	237	208

To nucleate a crack, the local stiffness, cohesive strength and stretch need to satisfy certain conditions, and the Poisson's ratio effect also plays a role. These issues are discussed next.

Critical stretch. In order to nucleate a crack with the CZM approach, local stress value must attain the level of the cohesive strength σ_{max} to allow one or several nodes to experience debonding. Therefore, the material properties and the range of stretch values employed in previous sections cannot induce crack nucleation. For instance, provided the cohesive strength is $E/10$, then applied $\epsilon_0 = 0.05$ cannot induce high enough stress locally to form a crack. The relationship between local stiffness E, σ_{max} and ϵ_0 must attain a level of roughly $\epsilon_0 \sim E/\sigma_{max}$. After carrying out simulations for various σ_{max} and ϵ_0 values, we conclude that at critical value

$$\epsilon_0 \approx 0.82\frac{E}{\sigma_{max}} \tag{5.7}$$

crack nucleation will occur, for the material system described in Table 5.3. Therefore, the cohesive strength σ^1_{max}– σ^4_{max} listed in Table 5.3 correspond to the following critical applied stretch: $\epsilon_0 = 0.05$, 0.045, 0.04 and 0.035, where E is taken as the value at the left side ($4.86GPa$). The numerical simulation result of crack tip location versus time is illustrated in Figure 5.14 for these four cases.

For the above described material system, as the FGM strip is stiffer at the left side ($E = 4.86GPa$), and stress is proportional to material stiffness, thus stress is higher at the

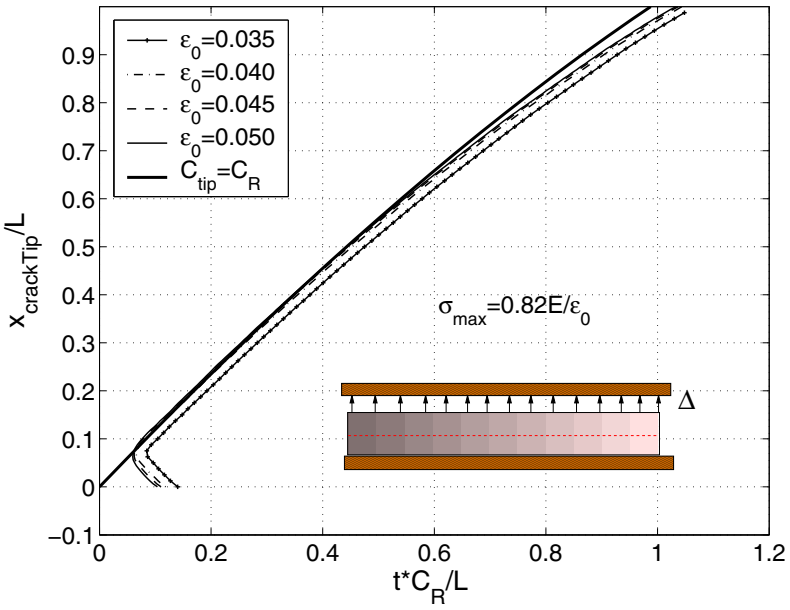

Figure 5.14: Normalized crack tip location versus normalized time for FGM strip subjected to various initial stretching parameter ϵ_0 and σ_{max}. C_R denotes Rayleigh wave speed, which varies along x direction.

$x = 0$ vicinity, and crack initiates if Eq. (5.7) is satisfied. One observes from Figure 5.14 that the crack initiation does not take place immediately. A short while after the simulation starts, the first nodal debonding occurs at $x = 0.07L$, *i.e.* not a boundary node. This is due to the Poisson's ratio effect, as will be discussed soon. After this node is debonded, it serves as a crack nucleation location and the crack quickly runs in both directions, as shown by the turning of the curves in Figure 5.14 at beginning stages. The crack tip location curve is not straight as in the homogeneous strip problem, because due to material inhomogeneity, the wave speed is varying along x direction. The ideal case where the crack begins to propagate at $t = 0$ from the left edge with the Rayleigh wave speed is also plotted for reference. For the four cases discussed above, the crack tip velocities, *i.e.* the slope of the curves, differ marginally, and they are approaching the Rayleigh wave speed. By studying Figure 5.14, we conclude that for the material system described in Table 5.3, once the critical strain is applied, crack propagation speed is only determined by the bulk material property, which is characterized by the Rayleigh wave speed C_R.

The energy evolution during the fracture process is investigated, and the result for $\epsilon_0 = 0.35$ case is plotted in Figure 5.15. First the numerical result of initial strain energy is

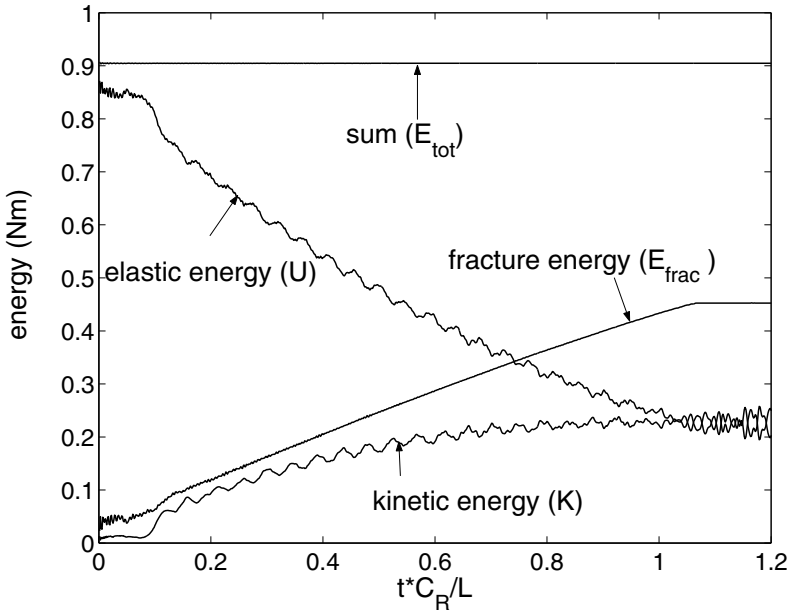

Figure 5.15: Evolution of various energy components for the FGM strip fracture problem with applied strain $\epsilon_0 = 0.035$, characteristic cohesive element size $h = 6.25\mu m$.

checked with the theoretical value, which is computed as

$$U_{bulk} = \frac{1}{2}\frac{3.24 \times 10^9}{1 - 0.35^2} 0.035^2 \times (4 \times 10^{-7}) = 0.904615385 N \cdot m$$

The numerical result is

$$U_{bulk} = 0.904615338 N \cdot m$$

the same as theoretical value up to seven digits. The above formulation uses the average value of Young's modulus for simplicity. Note that the uniform stretch results in non-uniform stress field, hence the strain density also varies linearly along x direction.

The energy required for the crack to propagate through is

$$E_{frac} = G_I A = exp(1)\sigma_{max}\delta_c \times (2 \times 10^{-3}) = 0.452322 N \cdot m$$

while the FEM result is

$$E_{frac} = 0.452342 N \cdot m$$

which is same to theoretical prediction up to 4 digits, and energy conservation is again obtained. The curve denoting fracture energy evolution is almost a straight line, because the cohesive strength is constant along x in this simulation, and the slight curvature is only introduced by the nonlinear crack tip speed.

Poisson's ratio effect. For a one dimensional problem, the coefficient in Eq. (5.7) would be 1 instead of 0.82. The reduction of critical stretch required for crack to nucleate in this problem is due to the Poisson's ratio effect. The initial condition dictates a uniform elongation in y direction while all nodes are kept stationary in x direction. When the dynamic simulation starts, the nodes at left and right edges tend to vibrate along x direction due to the Poisson's ratio effect. This movement presses the nodes adjacent to them to move inside, yet those nodes are under more constraint and cannot move freely. Therefore, the inside nodes that are close to the edge suffers larger stresses, and hence one of them debond first. Since this effect is caused by the Poisson's ratio effect, a test was performed to check if it vanishes with $\nu = 0$. Assume an FGM strip is subjected to initial stretch $\epsilon_0 = 0.035$, with the same material properties as described in Table 5.3, except for the Poisson's ratio, which is set to be $\nu = 0$. The boundary conditions are the same as in the previous example problem. The cohesive strength corresponding to the critical stretch is calculated as $\sigma_{max} = E \times \epsilon_0 = 170MPa$. The numerical simulation result of crack tip location versus time is illustrated in Figure 5.16. As expected, the first debonded node is the boundary node, and crack quickly propagates through the strip. Notice that the average Rayleigh wave speed is $C_R = 1020m/s$ when $\nu = 0$.

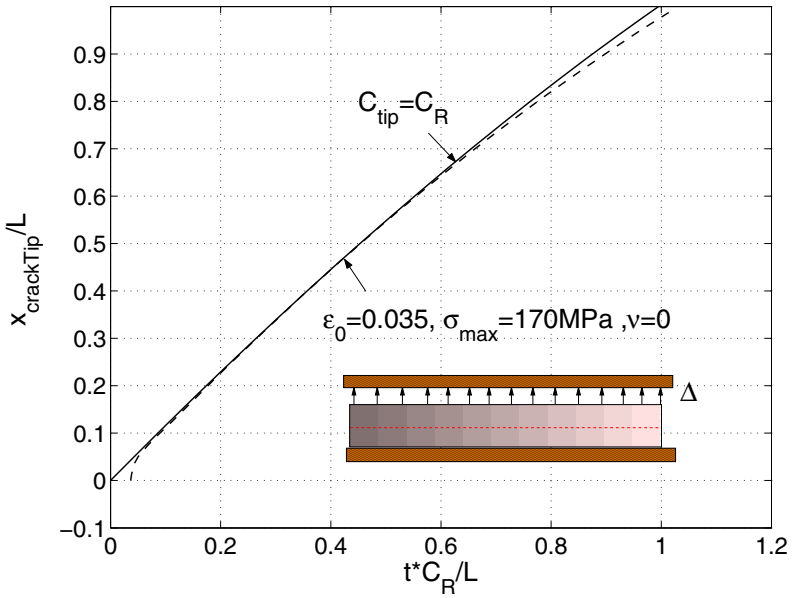

Figure 5.16: Normalized crack tip location versus normalized time for FGM strip subjected to initial stretching ϵ_0. The Poisson ratio is set to $\nu = 0$. Notice that the Rayleigh wave speed varies along x direction.

5.2 Dynamic Fracture of FGM Beam Under Impact Loading

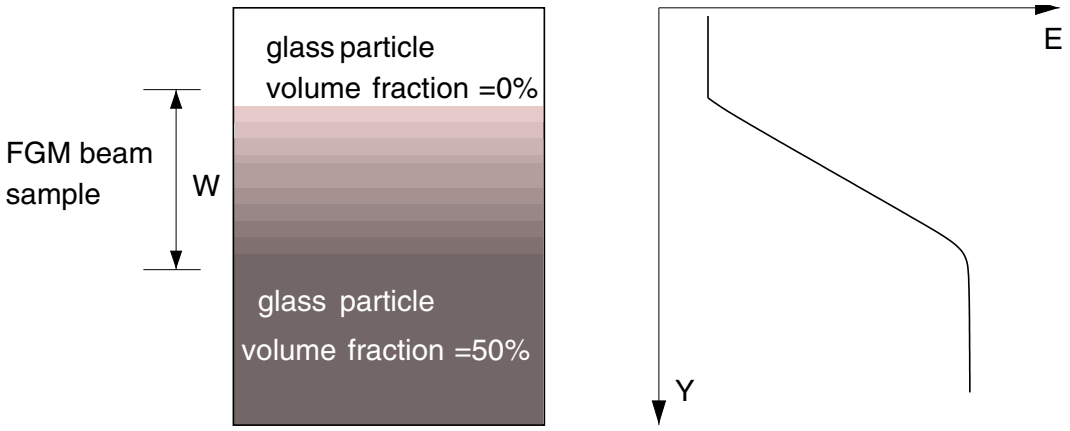

(a)

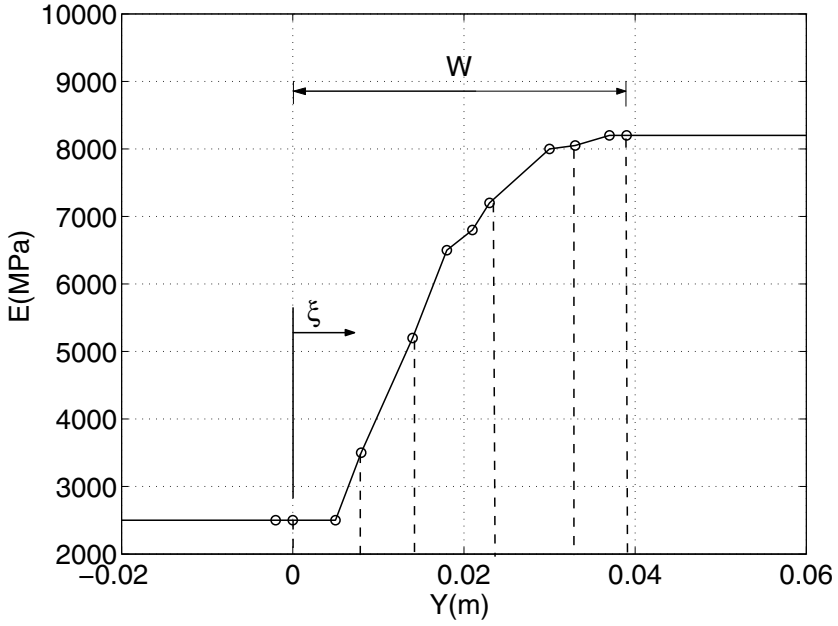

(b)

Figure 5.17: Material gradation of glass/epoxy FGM and Young's modulus variation in FGM plates under static test. (a) Glass particles volume fraction distribution in FGM plate with continuous variation of material property in Y direction. (b) Experimental data of Young's modulus variation in FGM beam. Origin of Y coordinate is set at the cutting position of the original plate for FGM specimen with glass volume fraction = 0. Vertical lines correspond respectively to $\xi = 0$, 0.17, 0.33, 0.58, 0.83 and 1. Parameter $\xi = Y/W$ is defined as the normalized length Y, where W is the height of FGM beam cut from the original plate. Figure obtained from Rousseau and Tippur [40] Fig.1.

Wherever possible, simulations should be performed based on real material properties and compared to experimental results. However, to date experimental data of real FGMs subjected to dynamic loading are rare. Rousseau and Tippur have done pioneering work on dynamic experiments of FGMs and reported results in a series of papers [40, 41, 42, 43].

The FGMs under test were epoxy/glass materials, with epoxy as matrix and glass particles dispersed in the matrix. In the manufacturing process, glass particles of mean diameter $42\mu m$ were cast into melting epoxy matrix, and due to higher mass density ($\rho_{glass} = 2470kg/m^3$, $\rho_{epoxy} = 1150kg/m^3$), glass particles sank gradually into the slowly curing matrix, and finally a smooth distribution of monotonically increasing (from top to bottom) volume fraction of glass spheres was formed.(Figure 5.17(a)). Experiments on both homogenous (with uniform volume fraction of particle inclusion in the material) and FGM specimens under dynamic loading were carried out. Rousseau and Tippur reported material property change under dynamic load, investigated stress fringe patterns and stress intensity factors at crack tip for both crack along and perpendicular to material gradation cases. Standard finite element simulation was carried out using ABAQUS to predict crack initiation time, and conclusion was drawn that crack initiates earlier for beam softer at cracked side than beam stiffer at cracked side [42]. In this section, numerical simulations of the same problems from Rousseau and Tippur [42] are performed, and results turn out to be consistent with the prediction in [42].

5.2.1 Problem Description

The geometry and boundary conditions are depicted in Figure 5.18. An FGM beam is subjected to low velocity ($5m/s$) impact loading, which is applied at the center point of top surface. Material gradation is along y direction, and the an initial crack of length $a = 0.2W = 7.4mm$ is predefined at the center of bottom side edge.

The epoxy/glass FGM is manufactured such that it possesses a smooth transition profile of V_f (volume fraction of glass spheres) varying from 0 percent at one side to 50 percent at the other, and in between V_f variation is roughly linear. The material properties at two sides with volume fraction $V_f = 0$ and $V_f = 0.5$ are listed in Table 5.4.

Table 5.4: Material properties of three-point bending FGM specimen, obtained from Rousseau and Tippur [40]

	$E(GPa)$	ν	$\rho(kg/m^3)$
$V_f = 0$	4.74	0.35	1150
$V_f = 0.5$	10.74	0.30	1810

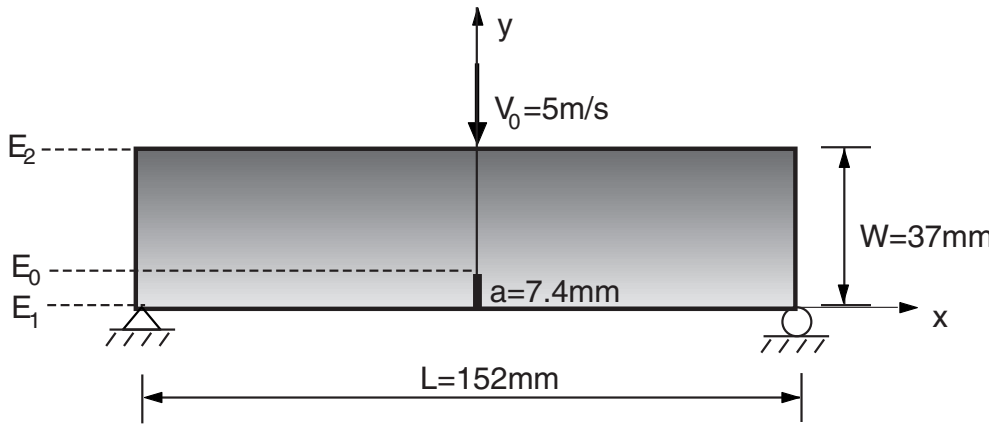

Figure 5.18: Geometry, load and boundary conditions for epoxy/glass beam under low velocity impact loading. The parameters E_0, E_1 and E_2 denotes Young's modulus at crack tip, bottom surface and top surface, respectively.

The cohesive energy is nonlinear with respect to glass inclusion volume fraction, and is plotted in Figure 5.19. The energy release rate data were obtained by conducting 3-point-bending test on monolithic glass/epoxy specimen of different volume fraction of glass inclusions.

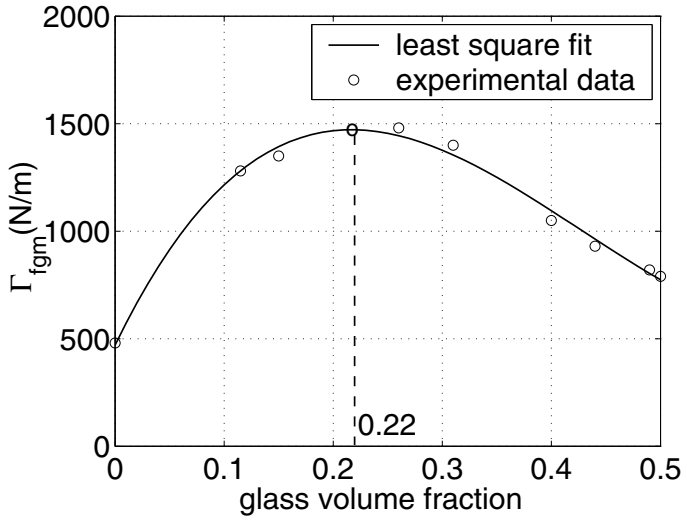

Figure 5.19: Cohesive energy of epoxy/glass FGM versus volume fraction of glass particle inclusion. Experimental data are retrieved from paper by Rousseau and Tippur [40], and the smooth curve is obtained by least square fitting of experimental data.

To investigate the influence of material variation on crack initiation and propagation features, five sets of material properties of different gradation profiles were used in the simulation:

- FGM, crack is located at the compliant side, *i.e.* if we designate subscript 1 to indicate bottom surface and 2 top surface, then $E_2 > E_1$, and the specimen is impacted on the stiffer side.
- FGM, $E_2 < E_1$, crack is located at the stiffer side, and impacted at the more compliant side.
- Homogeneous, $V_f = 0.1$, *i.e.*, $E_1 = E_2 =$ Young's modulus E_0 at crack tip in case 1.
- Homogeneous, $V_f = 0.4$, *i.e.*, $E_1 = E_2 =$ Young's modulus E_0 at crack tip in case 2.
- Homogeneous, $V_f = 0.25$, *i.e.*, $E_1 = E_2 =$ median value of Young's modulus in case 1 and 2.

Cohesive energy versus V_f of glass particles is given in Figure 5.19. This is one of the most influential factors that influence crack evolution, and notice that the peak cohesive energy occurs at around $V_f = 0.22$.

5.2.2 Effective Material Property

Under dynamic load, material behaves stiffer than in static case. Rousseau and Tippur gave the experimental data for FGM properties under quasi-static and dynamic load in paper [41] and [42], respectively. Under static load Young's modulus variation is between range $E = 2.6GPa$ to $E = 8GPa$ (the numbers are read from paper [41] Fig.1), while under dynamic load, Young's modulus varies from $E = 4.5GPa$ at $V_f = 0$ to $E = 11GPa$ at $V_f = 0.5$ (the numbers are read from paper [42] Fig. 5). Variation in Poisson ratio was not reported, and presumably the variation of Poisson ratio would be within a moderate range that it does not affect results noticeably, thus ν is assumed to be the same as static case. As for the mass density ρ, we can safely regard it as constant whether under static or dynamic loading. In this study, since the simulation is dynamic, material property under dynamic load is used.

Multiple theories exist to estimate effective property of the typical epoxy/glass composite. In this study, Mori-Tanaka method is employed. Rousseau and Tippur [41] have reported good agreement between this estimation and experimental results for static case, and here we assume that this method also gives good estimation on material properties under dynamic load.

As explained previously, graded element formulation approach is adopted in this study, and material properties should be computed at nodal points and interpolated to gauss points of elements. This also holds for cohesive elements.

To obtain the effective property at nodal points, first V_f of glass phase is calculated at each node. Second, the bulk modulus κ and the shear modulus μ of the composite are computed:

$$\kappa = \kappa_m \left[1 + \frac{V_f}{\dfrac{3(1-V_f)}{3\kappa_m + 4\mu_m} + \dfrac{\kappa_m}{\kappa_i - \kappa_m}} \right] \tag{5.8}$$

$$\mu = \mu_m \left[1 + \frac{V_f}{\dfrac{6(1-V_f)\left(\kappa_m + 2\mu_m\right)}{5\left(3\kappa_m + 4\mu_m\right)} + \dfrac{\mu_m}{\mu_i - \mu_m}} \right] \tag{5.9}$$

where the subscripts m and i denotes the matrix and the inclusions, respectively, and

$$\begin{aligned} \kappa_m &= \frac{E_m}{3(1-2\nu_m)}, \quad \mu_m = \frac{E_m}{2(1+\nu_m)} \\ \kappa_i &= \frac{E_i}{3(1-2\nu_i)}, \quad \mu_i = \frac{E_i}{2(1+\nu_i)} \end{aligned} \tag{5.10}$$

The Effective Young's modulus and Poisson ratio is thus given by

$$E_{eff} = \frac{9\mu \times \kappa}{\mu + 3\kappa}, \quad \nu_{eff} = \frac{1.5\kappa - \mu}{\mu + 3\kappa} \tag{5.11}$$

Effective material properties versus volume fraction of glass sphere inclusion V_f is plotted in Figure 5.20. In the current computation, V_f is assumed to vary linearly in FGM gradation direction, so Figure 5.20 effectively shows the material property gradation profile in the FGM beam in y direction.

5.2.3 Discontinuity Issues

T6 elements are used in the bulk discretization, and the mesh is illustrated in Figure 5.21. Cohesive elements are prescribed along the path at $x = 0$ (the symmetry line), so that crack will propagate along the defined path.

Based on the discussion in the previous Chapter, the choice of cohesive element size should take into account the cohesive zone size R (Eq. 5.2) as well as maximum cohesive strength σ_{max} and critical opening displacement δ_c. A high cohesive strength, *e.g.*, $E/\sigma_{max} = 10$ would result in a shorter cohesive zone size, and thus put a more stringent element size constraint. In this problem, $E/\sigma_{max} = 10$ gives cohesive zone size of approximately $15.5\mu m$.

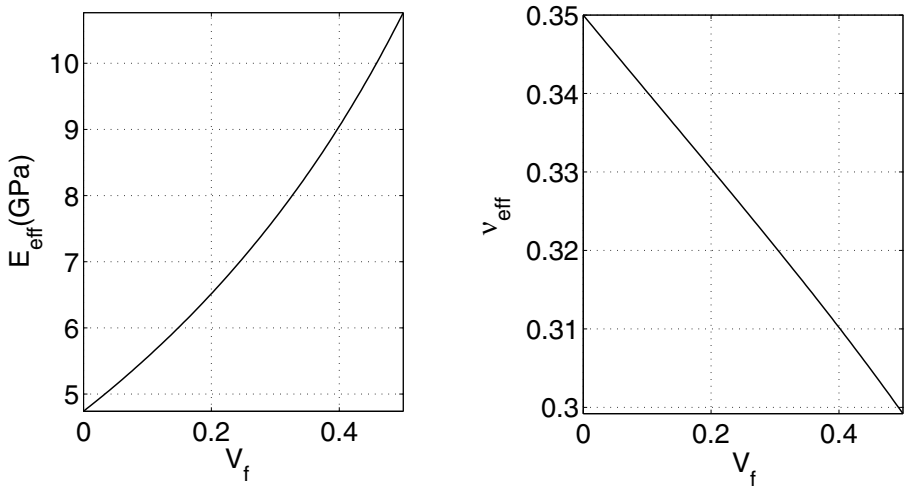

Figure 5.20: Effective Young's modulus and Poisson ratio versus volume fraction of glass sphere inclusion.

Notice that due to inhomogeneous material property, the determination of R is based on sampling at a number of points of different V_f of glass inclusion, and then the smallest R is chosen, which occurs at $V_f = 0.50$, the stiffest edge. According to the convergence requirement [12, 28], element size should be at most 1/2 to 1/3 of the cohesive zone size, so this estimation gives element size of at most $8\mu m$, which leads to a very large number of nodes and elements, hence heavy computation load. However, since cohesive elements are inserted only along a defined line, we can assume that using a lower σ_{max} value would not add too much compliance to the structure. Therefore, $E/\sigma_{max} = 50$ is used, which results in $R = 387\mu m$. The mesh size shown in Figure 5.21 is $h = 92.5\mu m$, so the cohesive zone spans over at least 2 cohesive elements, which is roughly within the convergence requirement.

It is of interest to point out that in this problem, the insufficiently refined mesh, which violates the convergence rule, results in a crack appearing way ahead of the main crack front. For example, when the $E/\sigma_{max} = 10$ ratio is used, and the mesh size held at h=$92.5\mu m$, which is much larger than cohesive zone size R=$26.6\mu m$, the crack pattern is illustrated in Figure 5.22. As can be seen in this plot, before the crack tip node experiences complete decohesion, some other nodes ahead of it have been cracked. This effect is undesirable, however, it can be circumvented by careful control of the cohesive element size.

5.2.4 Results

First, results for the three homogeneous beams are presented. Table 5.5 gives the material properties and crack initiation time for these three cases. Dilatational wave speed C_d is

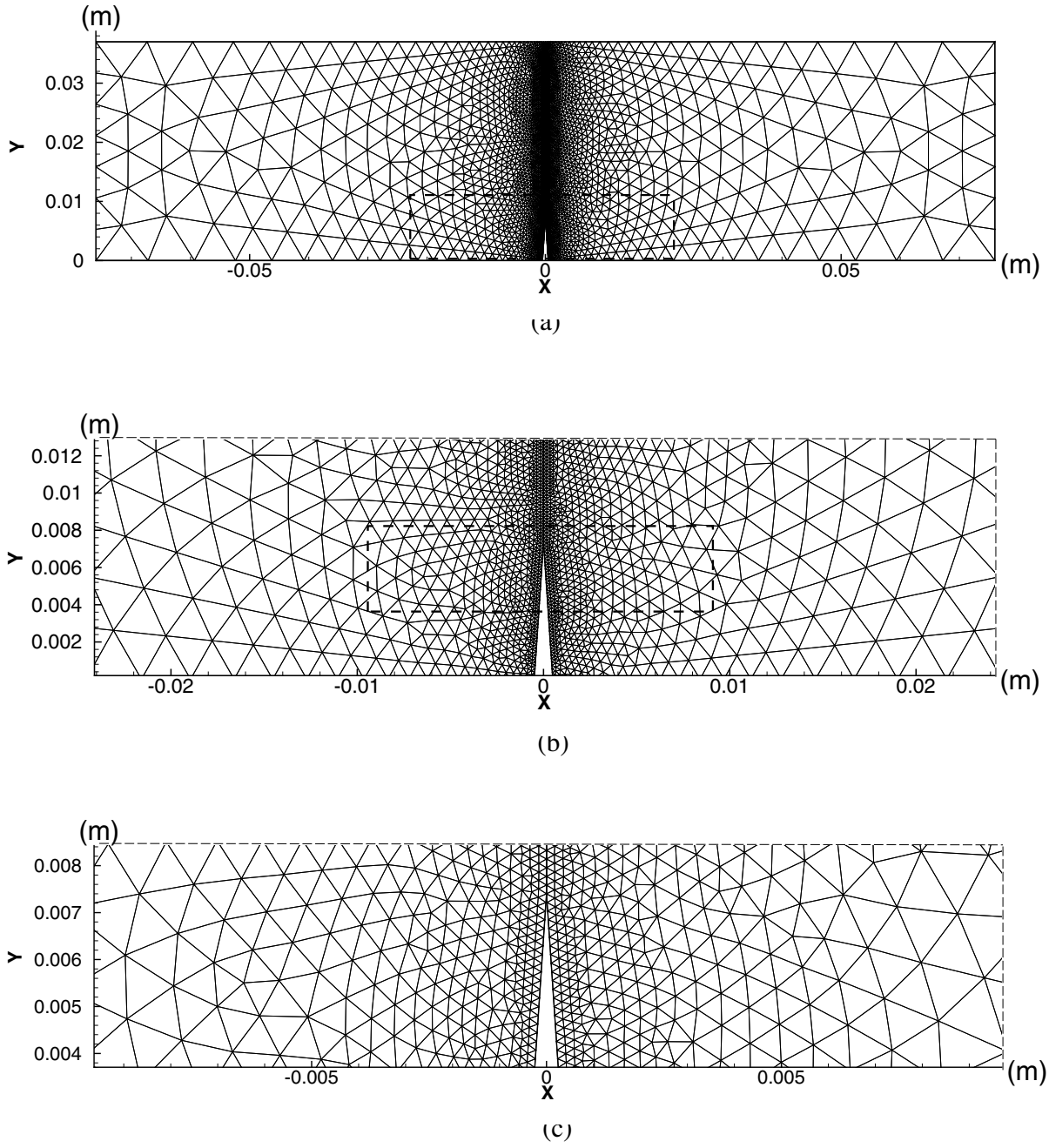

Figure 5.21: Mesh for three-point bending beam subjected to impact loading. Mesh contains 14991 nodes before cohesive elements are generated, 15312 nodes after cohesive elements are generated, 7388 T6 elements and 160 cohesive elements. Uniform cohesive element size equals $2h = 185\mu m$; (a) global mesh; (b) zoom of block region in (a); (c) zoom of block region in (b).

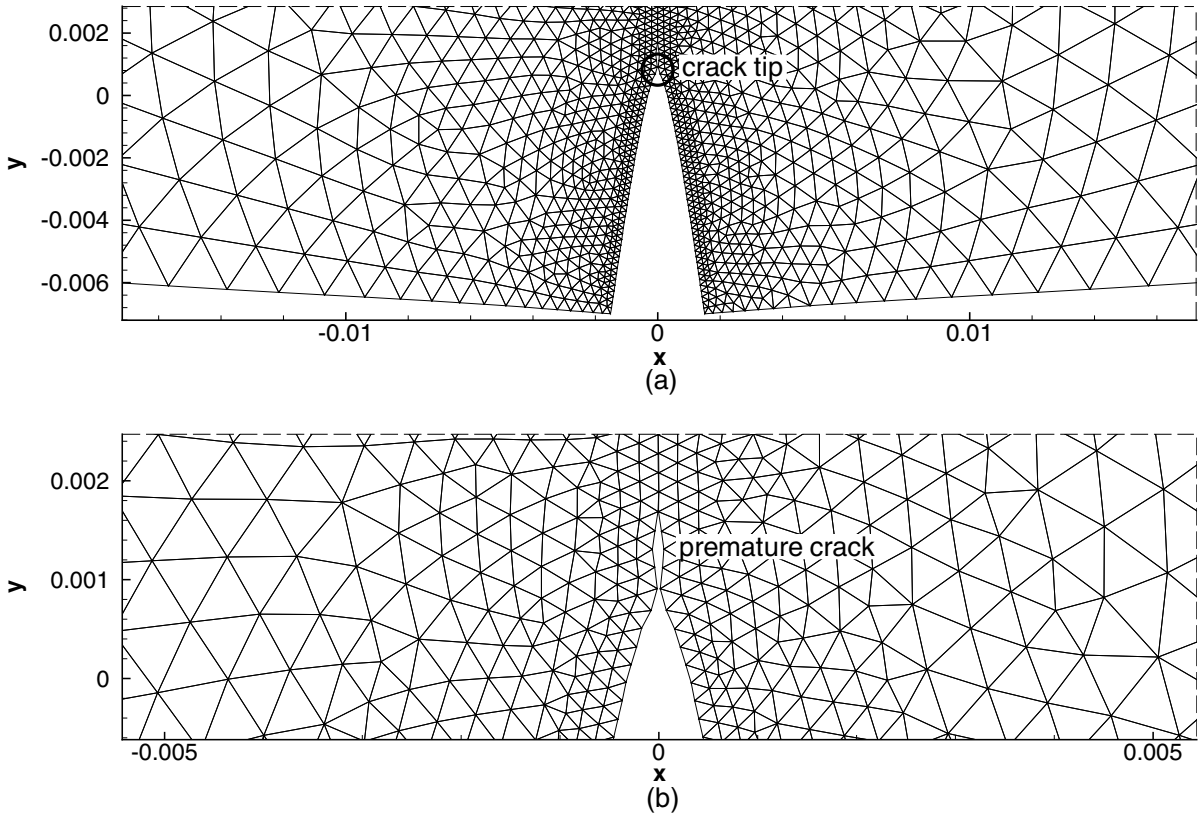

Figure 5.22: Premature crack front for FGM beam under dynamic load (Figure 5.18).

defined by

$$C_d = \sqrt{\frac{E}{(1+\nu)(1-\nu)\rho}} \tag{5.12}$$

for plane stress case and t_i, t_i^1 denote crack initiation time in absolute scale (seconds) and normalized scale ($t_i * C_d/W$ where W is the height of the beam), respectively.

Table 5.5: Material properties and crack initiation time for three-point bending homogeneous beam

V_f	E (GPa)	ν	ρ (kg/m^3)	C_d (m/s)	G_{Ic} (N/m)	$\sigma_{\max}$ (MPa)	δ_c (μm)	R (μm)	h (μm)	t_i (μs)	t_i^1
0.10	5.517	0.3406	1282	2218	1175.3	110.3	3.92	1166	92.5	120	7.2
0.25	7.020	0.3257	1480	2327	1459.6	140.4	3.82	1136	92.5	117	7.4
0.40	9.010	0.3103	1678	2476	1101.8	180.2	2.25	666	92.5	92	6.2

The crack tip location with respect to time is plotted in Figure 5.23.

Some interesting features can be noticed in the plot. On an absolute time scale, the stiffer the material, the earlier crack starts to propagate ($t_i^{V_f=0.4} < t_i^{V_f=0.25} < t_i^{V_f=0.1}$, Table 5.5).

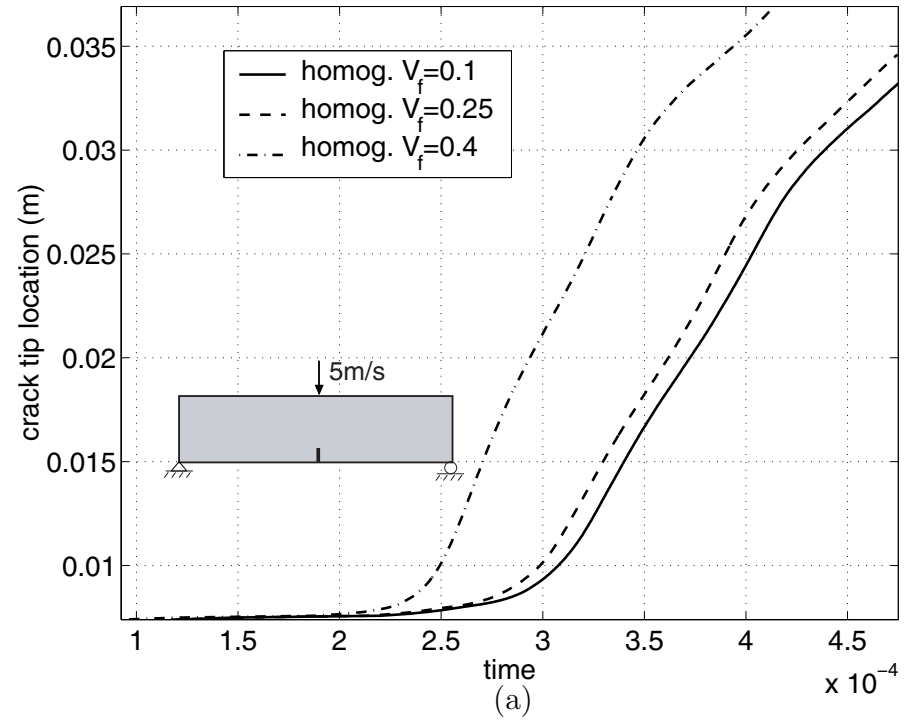

(a)

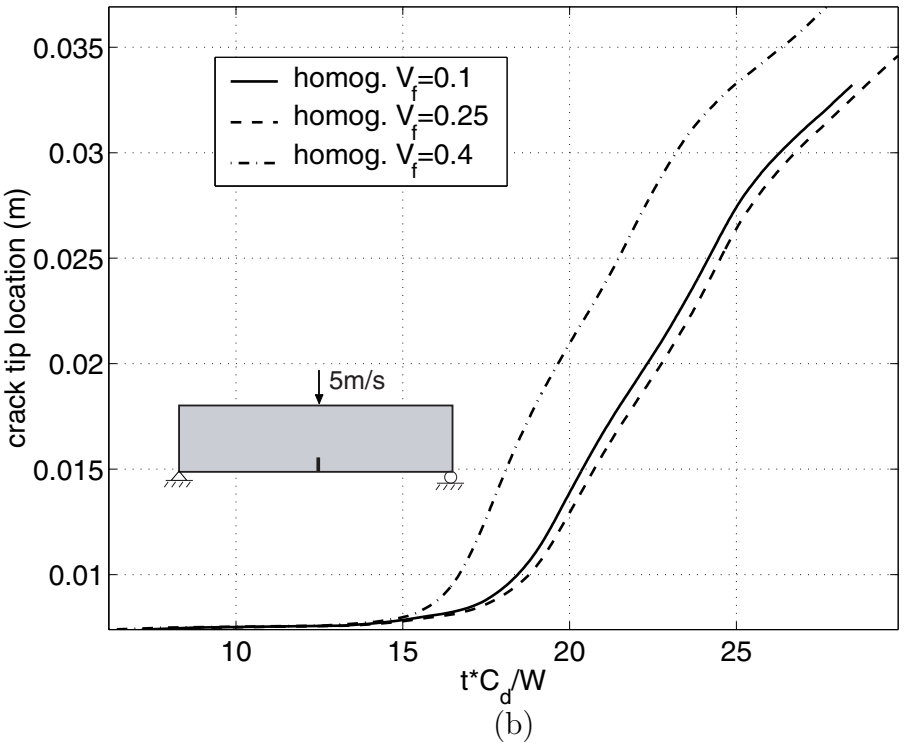

(b)

Figure 5.23: Crack tip location versus time for homogeneous beams with V_f=0.1, 0.25 and 0.4. (a) crack tip versus absolute time; (b) crack tip versus normalized time. Dilatational wave speed $C_d = 2218m/s$, $2317m/s$ and $2476m/s$ for $V_f = 0.1$, $V_f = 0.25$ and $V_f = 0.4$ beams respectively.

Two factors attribute to this phenomenon. First, in a stiffer media, wave propagates faster, and stress concentration accumulates at a higher speed, so that crack starts to propagate earlier than in softer media. This partly explains the difference between Figure 5.23 (a) and (b). Figure 5.23(b) uses normalized time, so the influence of different wave speed is partly excluded, and apparently the three curves in Figure 5.23(b) get closer than in (a). Second, Values of δ_c, critical displacements, of the three cases, are noticeably different. Since the local maximum cohesive strength σ_{max} is assumed to be proportional to local Young's modulus ($E/\sigma_{max} = 50$), stiffer material gives higher σ_{max} value. Although this seems to enhance the resistance of local material against crack initiation, it also causes the critical displacement δ_c to decrease, since the cohesive law states cohesive energy $\Gamma = e\sigma_{max}\delta_c$. The reduced δ_c turns out to affect the crack initiation more significantly than the increased strength σ_{max} in this case.

After crack initiation, crack tip appears to remain at a 'plateau' status for around $130\mu m$, during which crack front advanced very little. After careful examination of the deformation shape of the beam, we can explain the 'plateau stage' as follows: when impact load is applied on the top surface of the beam, first a compressive stress wave propagate downwards, then bounce back at the bottom surface, and propagate upward as tensile wave. During the same time, since the velocity load is continuously applied, the subsequent waves also propagate downwards and bounce back. After a short while, the combined effect of superimposing waves that propagate back and forth became rather complicated, and at the crack tip, the σ_x stress, which is the primary cause of crack extension, does not necessarily increase monotonically. In fact, it can be observed that the crack tip opening first increases, then decreases, and increase again. At the early stage, when the stress at initial crack tip attains critical value, one pair of nodes break up, then it takes another time interval for the stress to arrive at a equally high level to break up the next pair of nodes. This is the 'plateau' stage. However, in the long run, the bending effect overwhelms the wave effect and the local deformation at crack tip monotonically increases, and crack propagate at a much faster velocity.

When the crack speeds up, it propagates smoothly till the top surface. The trends of the three curves share a similar pattern (they are kind of 'parallel' in propagation stage). Curiously, however, the curve for $V_f = 0.25$ is not half way in between of the other two, as we might have assumed, but rather much closer to the V_f case, and in normalized scale it is the one that initiates last and propagates slowest! The reason is explained as follows: Although most mechanical properties (E, ν, ρ, etc.) of this $V_f = 0.25$ specimen are just the average values of that for the $V_f = 0.10$ and $V_f = 0.40$ cases, there is one important parameter, the cohesive energy, which is different. The cohesive energy is higher at $V_f = 0.25$ than both of the others ($1459.6N/m$ vs. $1175.3N/m$ for $V_f = 0.10$ and $1101.8N/m$ for $V_f = 0.40$),

and results in a critical displacement value δ_c just slightly smaller than the $V_f = 0.10$ case ($3.82\mu m$ vs. $3.92\mu m$), With this observation, we suggest that for this example, the local critical displacement δ_c is a more critical index than maximum strength σ_{max} for the prediction of crack propagation.

The crack tip velocity is also plotted for the three homogeneous beams (Figure 5.24), and again, plots with both absolute time and normalized time are given so as to differentiate the influence of wave speed. Notice that the time coordinate is shifted by $(t - t_i)$, where t_i is the crack initiation time for each individual case. By doing so the results are presented in a more comparable scale, and on this normalized basis, the velocity curve of $V_f = 0.25$ follows that of $V_f = 0.10$ closely, both in magnitude and shape. The stiffer material with V_f exhibits faster crack propagation speed.

Next we proceed to investigate the influence of material gradation. The relevant material properties and crack initiation time are listed in Table 5.2.4. Notice that for the FGM beam, the properties used are the effective quantities.

Table 5.6: Material properties and crack initiation time, for three-point bending homogeneous and FGM beams

	E (GPa)	ν	ρ (kg/m^3)	C_d (m/s)	G_{Ic} (N/m)	$\sigma_{\max}$ (MPa)	δ_c (μm)	R (μm)	h (μm)	t_i (μs)	t_i^1
$V_f = 0.10$	5.517	0.3406	1282	2218	1175.3	110.3	3.92	1166	92.5	120	7.2
$V_f = 0.25$	7.020	0.3257	1480	2327	1459.6	140.4	3.82	1136	92.5	117	7.4
$V_f = 0.40$	9.010	0.3103	1678	2476	1101.8	180.2	2.25	666	92.5	92	6.2
$E_2 > E_1$	7.292	0.3252	1480	2308	1166.2	145.8	2.94	666	92.5	101.5	6.3
$E_2 < E_1$	7.292	0.3252	1480	2308	1166.2	145.8	2.94	666	92.5	113.4	7.1

The crack tip location with respect to time is plotted in Figure 5.25 and the following observations can be made:

- In the absolute time scale, the crack tip location profile of the FGM beams are bounded between results for the two homogeneous cases. In the normalized time scale, this still holds true for most of the propagation time, except for the initiation stage.

- For $E_2 > E_1$ case for which the beam is more compliant at bottom, crack initiates at t=101.5μs; for $E_2 < E_1$ case for which the beam is stiffer at bottom, crack initiates at t=113.4μs. This trend is consistent with the prediction made by Rousseau and Tippur [41]. However, this is opposite to the homogeneous cases, for which crack initiates earlier in the stiffer material.

- After the first node experience decohesion, both cases experience a time interval during which the crack extends slowly. It is relatively longer for $E_2 > E_1$ case, with a 'plateau'

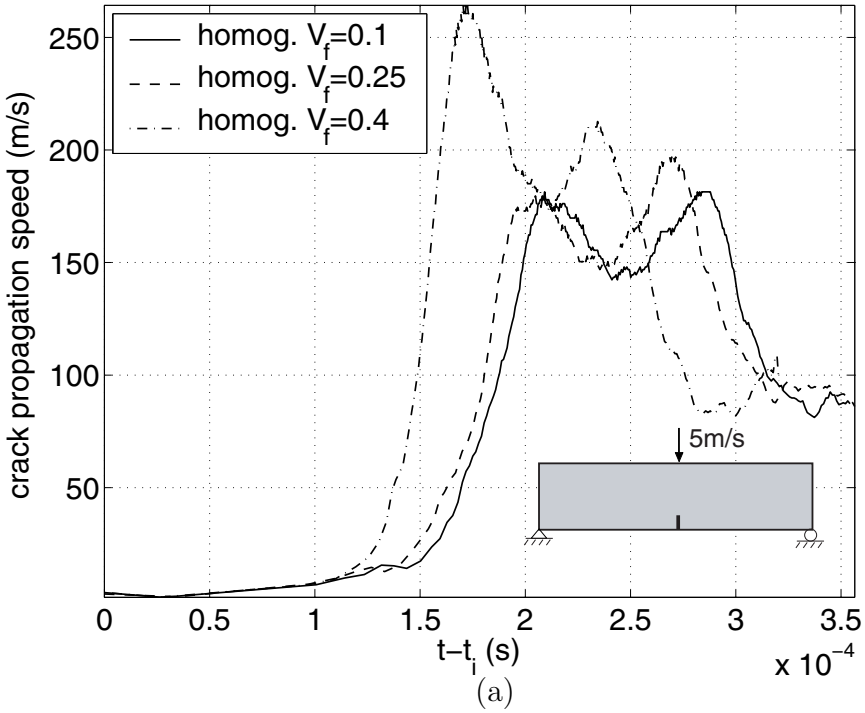

(a)

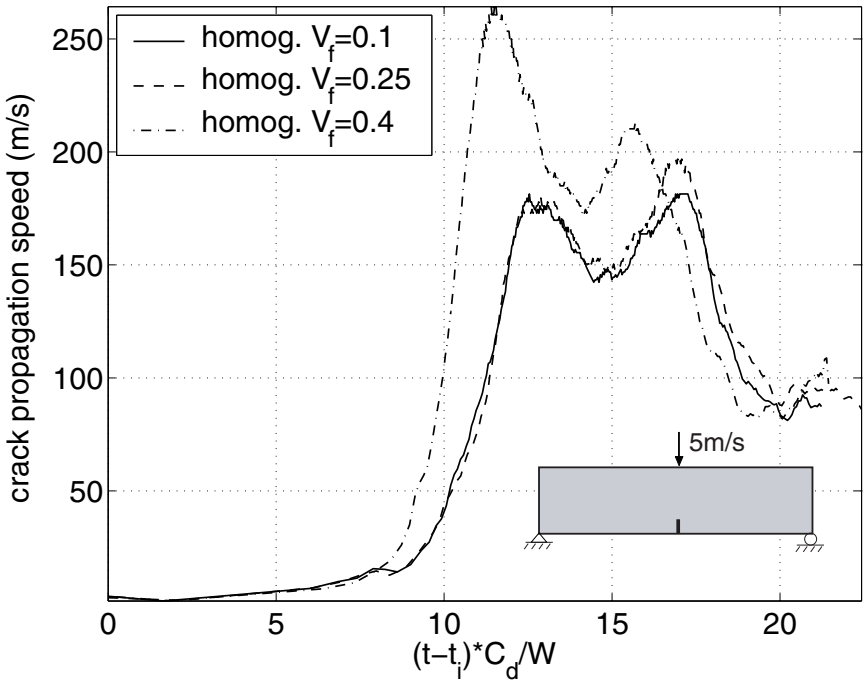

(b)

Figure 5.24: Crack tip velocity versus $t - t_i$ for homogeneous beams with V_f=0.1, 0.25 and 0.4, where t_i stands for crack initiation time. (a) crack tip velocity versus absolute time; (b) crack tip versus normalized time. Dilatational wave speed $C_d = 2218m/s$, $2317m/s$ and $2476m/s$ for $V_f = 0.1$, $V_f = 0.25$ and $V_f = 0.4$ beams respectively.

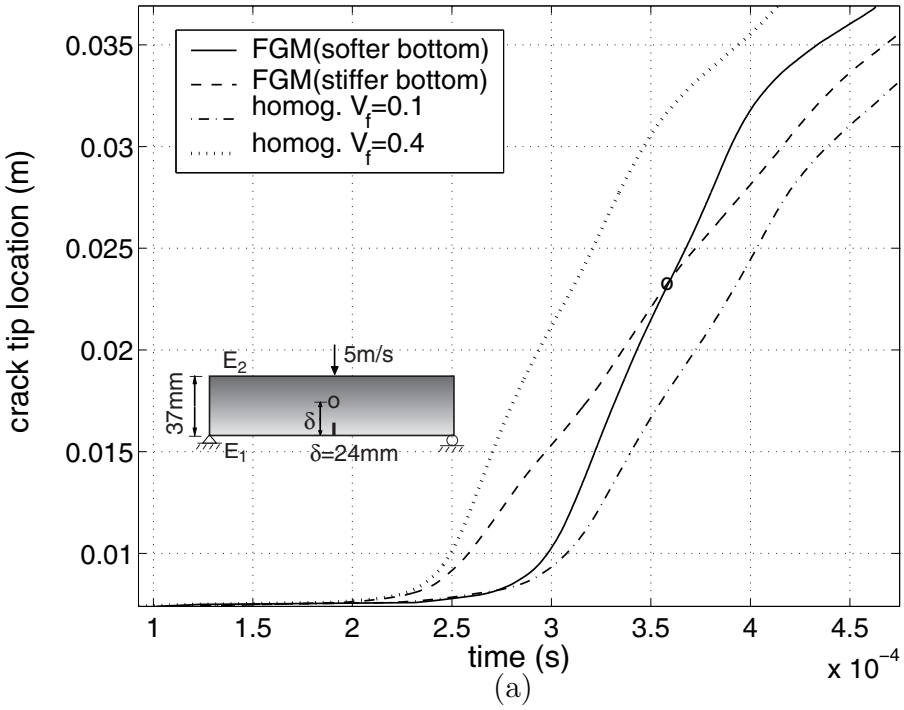

(a)

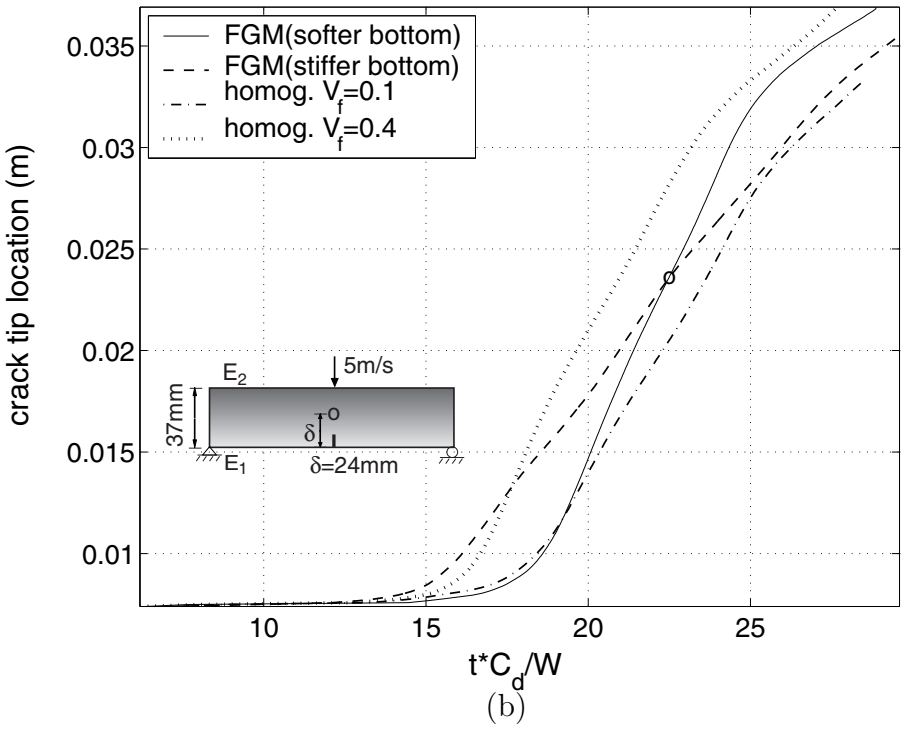

(b)

Figure 5.25: Crack tip location versus time for two FGM beams and two homogeneous beams with V_f=0.1 and 0.4. (a) crack tip versus absolute time; (b) crack tip versus normalized time. V_f denotes volume fraction of glass inclusion in specimen material. The intersection point of the two curves for FGM beams is indicated with a circle on the curves and also on the insert geometry figure.

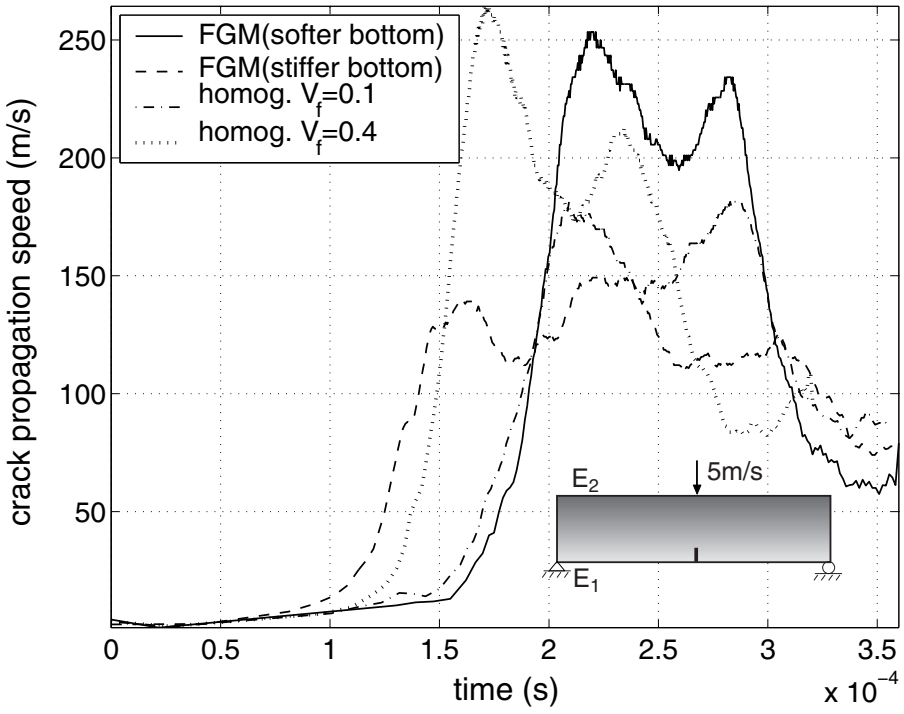

(a)

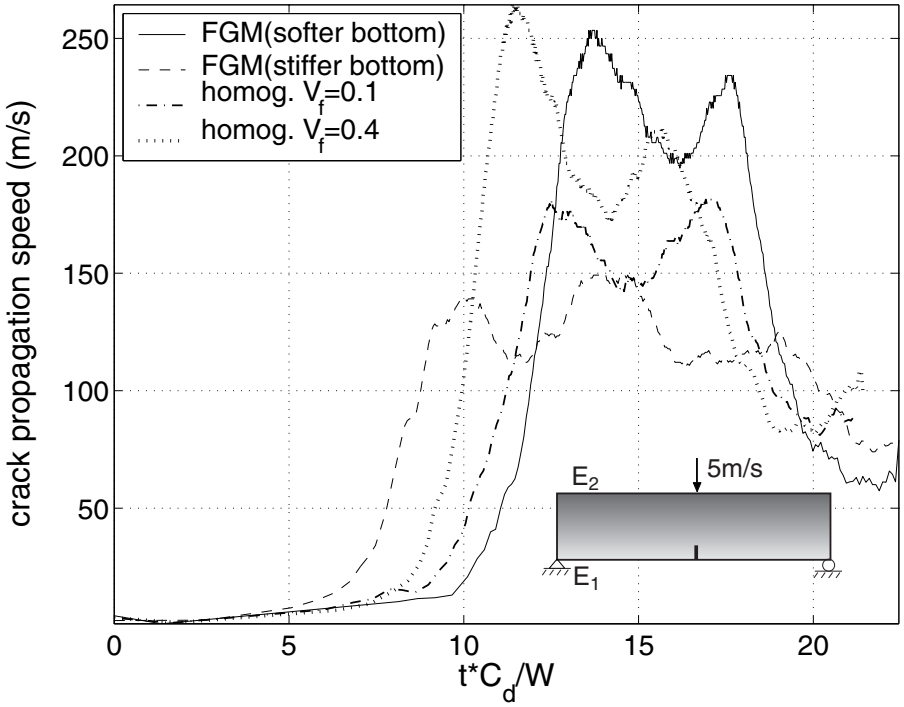

(b)

Figure 5.26: Crack tip velocity versus $t - t_i$ for for two FGM beams and two homogeneous beams with $V_f = 0.1$ and 0.4. where t_i denotes crack initiation time. (a) crack tip velocity versus absolute time; (b) crack tip versus normalized time.

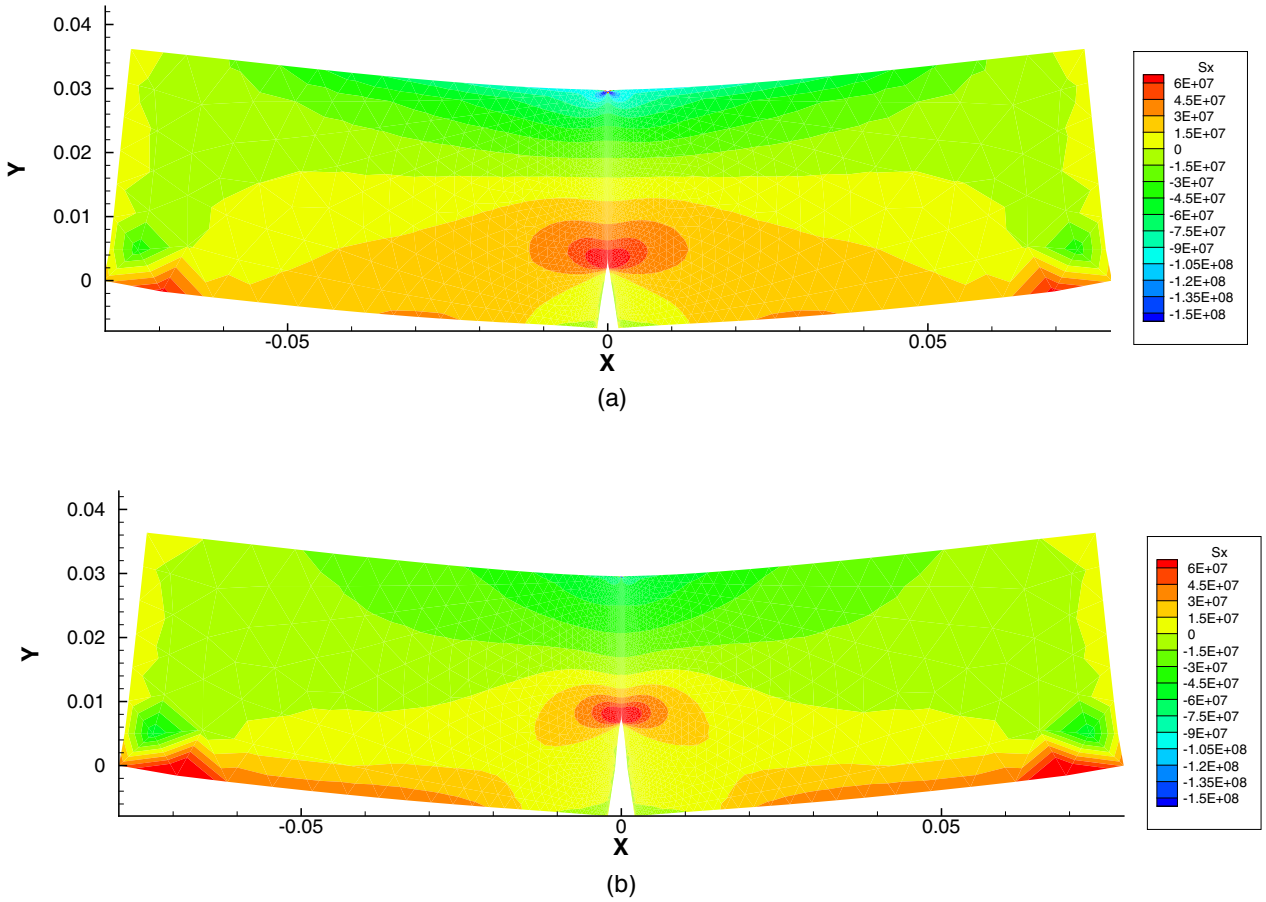

Figure 5.27: Comparison of stress field σ_x (units:Pa) at $t = 300\mu s$ for FGM beam soft at bottom and stiffer at bottom, beam subjected to three-point bending; (a) beam softer at bottom; (b) beam stiffer at bottom.

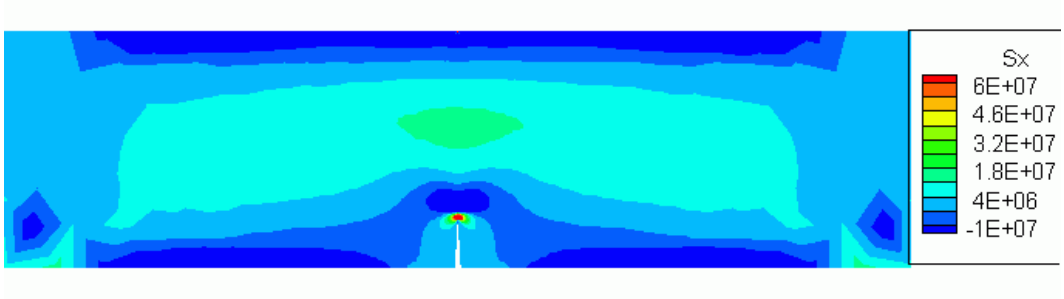

(a)

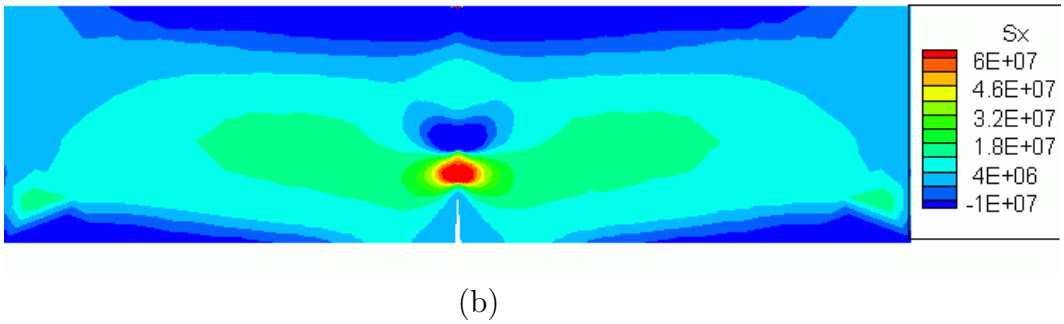

(b)

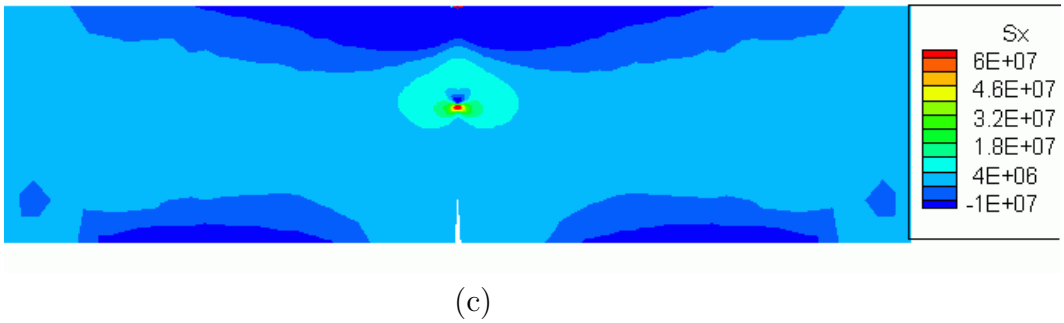

(c)

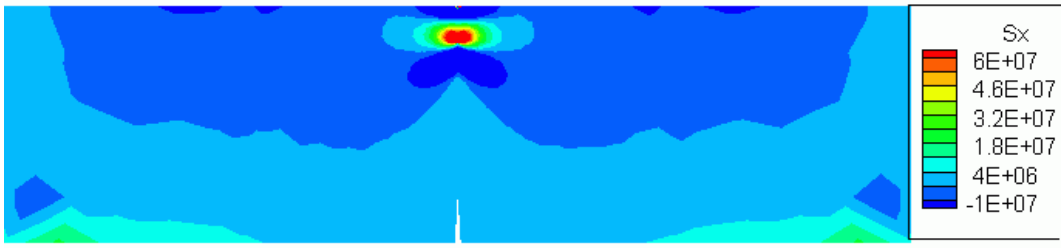

(d)

Figure 5.28: Difference in value of stress field $\sigma_x^{\text{soft bottom}} - \sigma_x^{\text{stiff bottom}}$ (units:Pa) for three-point bending FGM beam at different time; (a) $t = 250\mu s$, crack tip of the stiffer-bottom beam begins to take speed; (b) $t = 300\mu s$, both cracks speed up, crack tip of softer-bottom beam is lower than that of stiffer-bottom beam; (c) $t = 350\mu s$, crack tip of softer-bottom beam catches up with that of the stiffer-bottom beam; (d) $t = 400\mu s$, crack tip of softer-bottom beam overtakes that of the stiffer-bottom beam.

time of around 170μs, and shorter for $E_2 > E_1$ case, with a 'plateau' time of around 110μs.

- After the crack propagation takes speed, at first the crack tip of beam with $E_2 > E_1$ is ahead of that of the beam with opposite material gradation ($E_2 < E_1$, as illustrated in the stress field σ_x plot in Figure 5.27. However, the $E_2 < E_1$ case accelerates faster than the other, and at time around 360μs, the two cases reach the same crack tip location, and afterwards the $E_2 < E_1$ case keeps advancing ahead of the other one. Notice that in Figure 5.25, the curves of the two FGM results cross each other.

To further illustrate the difference of crack evolution pattern in the two FGM beams, the difference of stress field σ_x for the two FGM specimens is plotted in Figure 5.28, in undeformed configuration. By Comparing the stress field figure with crack tip location plotted in Figure 5.25, the characteristics listed above can be clearly observed. The difference is taken as $\sigma_x^{\text{softer bottom}} - \sigma_x^{\text{stiffer bottom}}$, so the red color indicates region where the stress of softer-bottom beam is larger, hence the red blob shows the crack tip location of softer-bottom beam; for the same reason, the blue blob shows the crack tip location of stiffer-bottom beam. Apparently, at first crack tip of stiffer-bottom beam advances ahead of softer-bottom beam, but is taken over by the latter at around $t = 360\mu s$ and height $24mm$.

The comparison of velocities of both FGM and homogeneous beams can be clearly observed in Figure 5.26, which shows the crack extension speed versus time. Again for clarity, the time axis is shifted by $t - t_i$. The crack propagates consistently faster in the softer bottom beam than the stiffer bottom beam except for a small time interval at the end of the crack extension, and the peak value of crack propagation speed in the softer bottom beam reaches 1.67 times as large as that in stiffer bottom beam. The reason for this simulation result is again attributed to the variation of critical displacement δ_c. For the soft-bottom beam, the crack is propagating towards the stiffer side, the δ_c in which region is constantly decreasing, thus crack is easier to form. For the stiff-bottom beam, the crack is propagating towards the compliant side, where δ_c is increasing, thus crack speed is deterred compared to the opposite case.

5.3 Dynamic Crack Branching

Observations of fast crack growth in brittle materials reveal complex patterns of crack branching [46]. The crack branch patterns are influenced by many factors, including material gradation profile, boundary conditions, applied impact velocity, etc. In this section, dynamic

crack branching phenomenon is explored with a plane strain plate containing an initial central crack subjected to tensile velocity loading. Qualitative behaviors of dynamic crack branching are investigated for both homogeneous materials and FGMs, as well as the for various impact loading velocities.

5.3.1 Problem Description

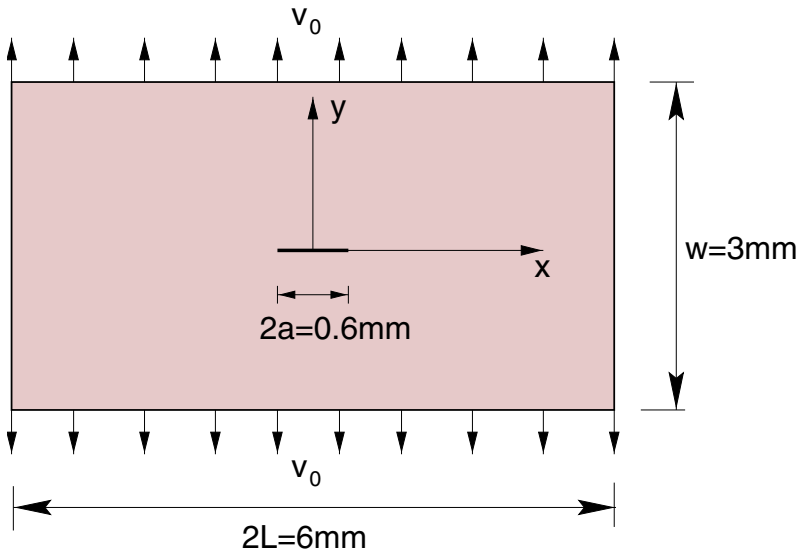

Figure 5.29: Geometry and boundary conditions of a plate containing a central crack subjected to velocity loading.

The computation is carried out for a center cracked rectangular plate as shown in Figure 5.29. Symmetric velocity loading v_0 is applied at the upper and bottom surfaces. Two classes of problems are investigated. First, to explore the influence of material gradation on crack branching patterns, three material cases are studied:

- case 1: both the bulk and cohesive properties are considered for homogeneous materials, as tabulated in Table 5.7.

Table 5.7: Material properties for plate containing central crack and subjected to velocity loading, case 1: homogeneous material (PMMA)

E (GPa)	ν	ρ (kg/m^3)	G_{Ic} (N/m)	$\sigma_{\max}$ (MPa)	δ_c (μm)
3.24	0.35	1190	352.3	324	0.4

- case 2: hypothetical "FGM", as tabulated in Table 5.8. The bulk material is considered as homogeneous, while the cohesive properties are linearly graded in y direction, as

the cohesive strength decreases from $486MPa$ at the upper surface to $162MPa$ at the bottom surface.

Table 5.8: Material properties for plate containing central crack and subjected to velocity loading, case 2: homogeneous bulk material property and graded cohesive property

	E (GPa)	ν	ρ (kg/m^3)	G_{Ic} (N/m)	$\sigma_{\max}$ (MPa)	δ_c (μm)
$y = 1/2W$	3.24	0.35	1190	528.4	486	0.4
$y = -1/2W$	3.24	0.35	1190	176.1	162	0.4
average	3.24	0.35	1190	352.3	324	0.4

- case 3: FGM with both the bulk and cohesive properties linearly graded in y direction as tabulated in Table 5.9.

Table 5.9: Material properties for plate containing central crack and subjected to velocity loading, case 3: graded bulk and cohesive properties

	E (GPa)	ν	ρ (kg/m^3)	G_{Ic} (N/m)	$\sigma_{\max}$ (MPa)	δ_c (μm)
$y = 1/2W$	4.86	0.35	1190	528.4	486	0.4
$y = -1/2W$	1.62	0.35	1190	176.1	162	0.4
average	3.24	0.35	1190	352.3	324	0.4

Second, the influence of impact velocity is investigated by applying different impact velocity v_0. The homogeneous material tabulated in Table 5.7 is considered. Three cases are studied: $v_0 = 1m/s$, $5m/s$ and $15m/s$.

5.3.2 FEM Model

Due to symmetry of the geometry, material gradation and loading condition with respect to y axis, only the right half of the geometry is modelled for the numerical simulation, along with proper boundary condition to account for the symmetry at $x = 0$. The domain is discretized with 40 by 40 quads each divided into 4 T3 elements, as depicted in Figure 5.30. In order to allow crack branching to occur, cohesive elements are inserted inside a rectangular region right to the initial crack, as shown with the thicker lines. Due to accuracy and computation cost considerations (as discussed in Chapter 4), the dimension of the cohesive region is preferably confined to the minimum potential crack propagation region. Therefore, the cohesive region depicted in Figure 5.30 is shown as an example, while in the simulations the size of the cohesive elements region may vary from case to case. However, for consistency reason, the results presented in this section are all obtained with the mesh shown in Figure 5.30.

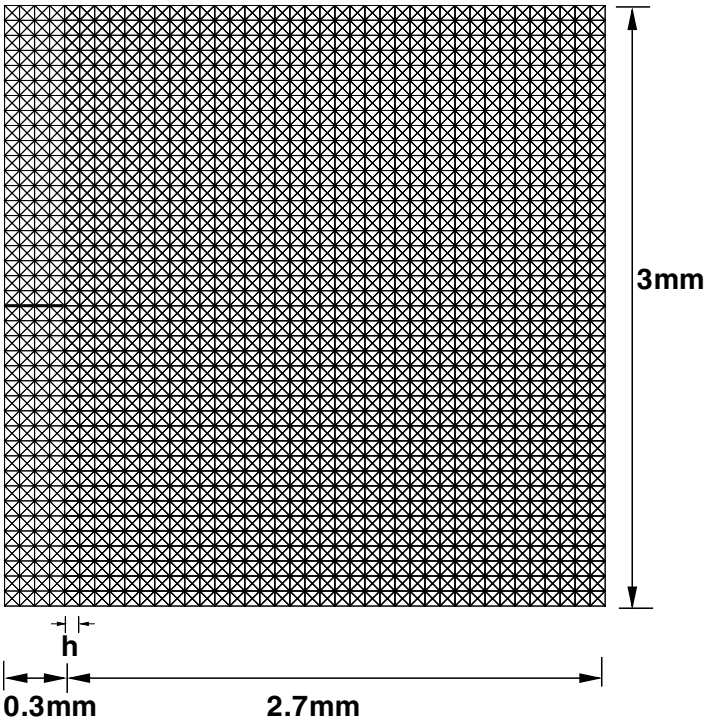

Figure 5.30: Mesh descretization of the dynamic branching problem with half of the original geometry modelled due to symmetry. Characteristic element size $h = 75\mu m$, and the rectangular region plotted with thicker lines indicates the region where cohesive elements are inserted. There are 6400 T3 elements, 8244 cohesive elements and 17650 nodes.

For the problems discussed in Sections 5.1 and 5.2, small deformation assumption was used because the nature of those problems does not incur large local rotation, for which case the large deformation formulation must be employed. However, when crack branching takes place, large rotation often occurs for elements around crack tips. Therefore, finite deformation formulation is used for the results presented in this section. Moreover, due to the expensive computation induced by large number of cohesive elements, the bulk elements are chosen as T3 instead of T6 elements, so as to save the computation cost.

Notice that the cohesive element size $h = 75\mu m$ with current mesh discretization does not satisfy the required criterion $h = (1/2 - 1/3)R$ where R is the cohesive zone size. For instance, $R = 23.6\mu m$ for the homogeneous case, as discussed in Section 5.1.1. Therefore the element size ought to be reduced significantly to satisfy the above requirement. However, the computation cost would be tremendous to resolve this problem, since the computation increases approximately cubically with the decease of the element size. For the time being, the mesh in Figure 5.30 is used. Clearly, the results can not resolve the accurate stress

distribution, hence nor the actual crack propagation behavior. Therefore, the examples presented *qualitatively* describe the fracture patterns for each case. Further investigations using refined meshes are under way, but not reported in the thesis.

5.3.3 Results for Various Material Gradation Profiles

Case 1: homogeneous PMMA material. Symmetric branch pattern is obtained, as shown in Figure 5.31. The crack begins to branch at $a_{branch} = 1.05mm$, after propagating along straight plane for a length of $0.75mm$. When the crack approaches the edge, the cracks further branch. Note that although crack branching can only take place either parallel to the coordinate axes or at $\pm 45°$, the overall branching angle is less than $45°$ from the x axis. In the example, the overall branching angle is about $29°$, calculated by approximating the main branch as a straight line. Due to the healing effect of the actual quantities model employed, when crack branching occurs along several paths in the simulation, continued growth takes place on one or more of these branches and the others heal. For instance, at the stage shown in Figure 5.31 (a), totally four crack branches form at the regions indicated by the two circles. Afterwards, two of them dominate and grow further while the other two close, as shown in the final crack branch pattern shown in Figure 5.31 (b). Observations of this example, as well as some similar simulations with different loading velocities reveal that, for most cases, the remaining branches are those leading in similar directions of the main cracks that they emanate from.

Case 2: Variation of cohesive strength. In this example, bulk material is considered to be homogeneous while cohesive strength varies linearly along y direction. The cohesive strength σ_{max} is lower at bottom surface ($\sigma_{max} = 162MPa$) and higher at top surface ($\sigma_{max} = 486MPa$), which implies weaker fracture resistance at the lower region. Therefore, the crack branching is expected to be more significant at the lower part of the plate, as shown in Figure 5.32(d). The crack branching initiation location is roughly the same as the homogeneous case, as indicated by Figure 5.32(a). However, this branching disappears in the final figure (Figure 5.32(d)). Because the lower region of the plate is weaker in resisting fracture, the crack branch towards the lower region dominates, and due to the healing effect, the initial upward branch becomes insignificant compared to the downward branch and finally heals, as shown in the series of Figures 5.32(b), (c) and (d). Further branches emanated from the main downward branch at a later stage, and again the lower one is more significant. More branches occur when the cracks approach the right surface.

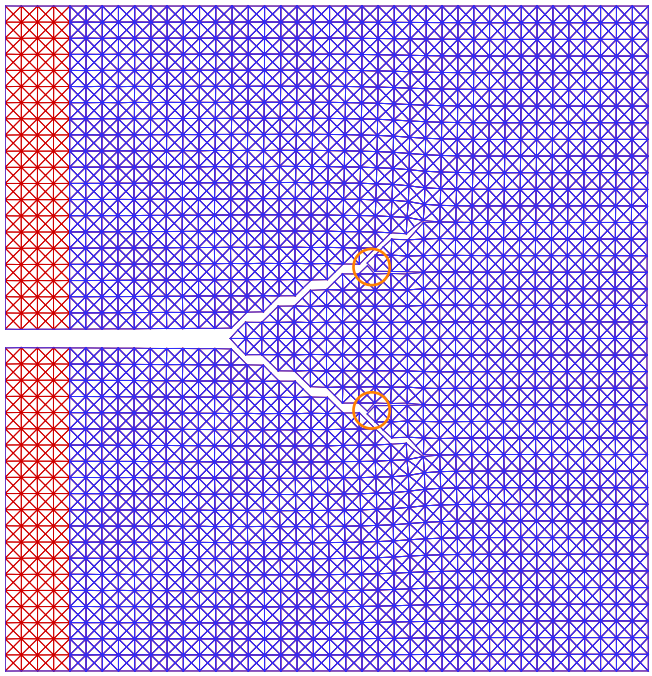

(a) $t = 9\mu s$

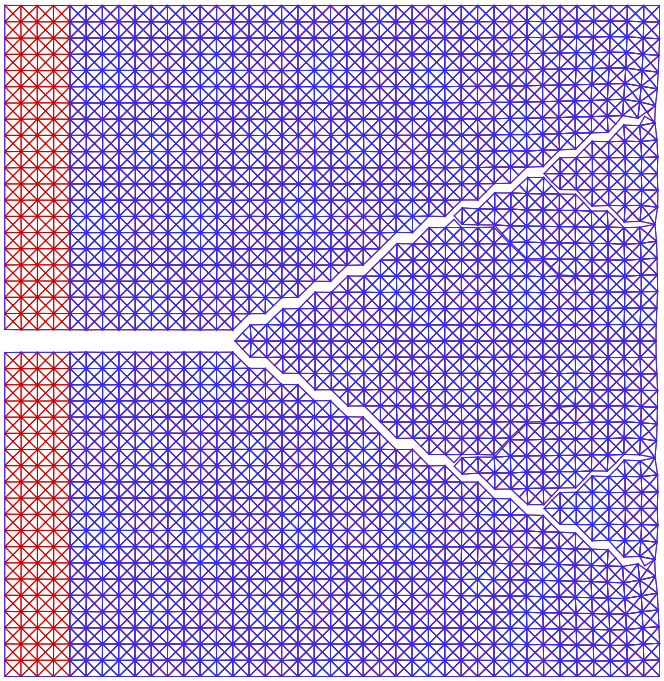

(b) $t = 10.6\mu s$

Figure 5.31: Crack branch pattern for homogeneous material PMMA subjected to $v_0 = 5m/s$ velocity loading; (a) local crack branches at $t = 9\mu s$ indicated with circles, among which two of them close at latter stage; (b) final crack pattern at $t = 10.6\mu s$.

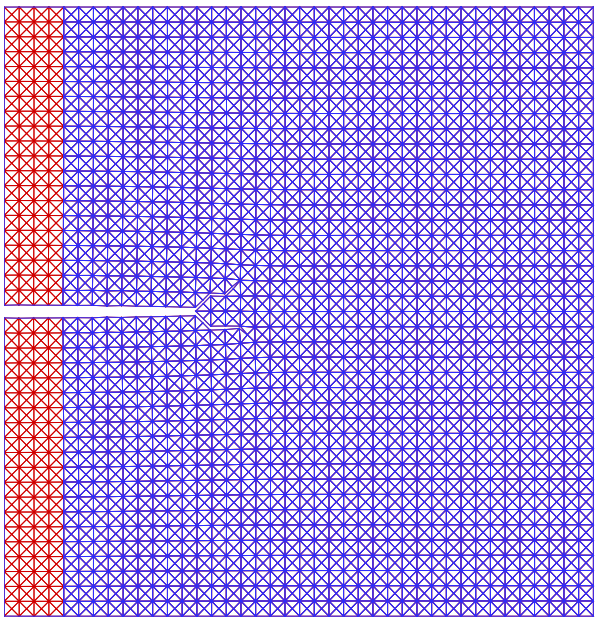

(a) $t = 7.5\mu s$

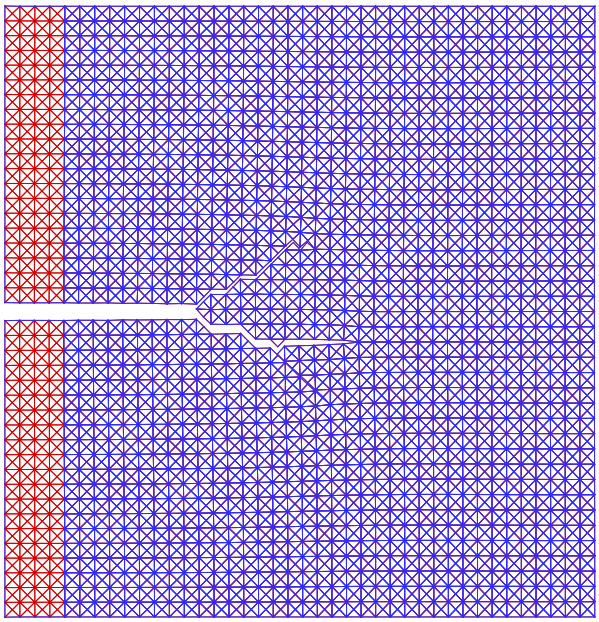

(b) $t = 8.25\mu s$

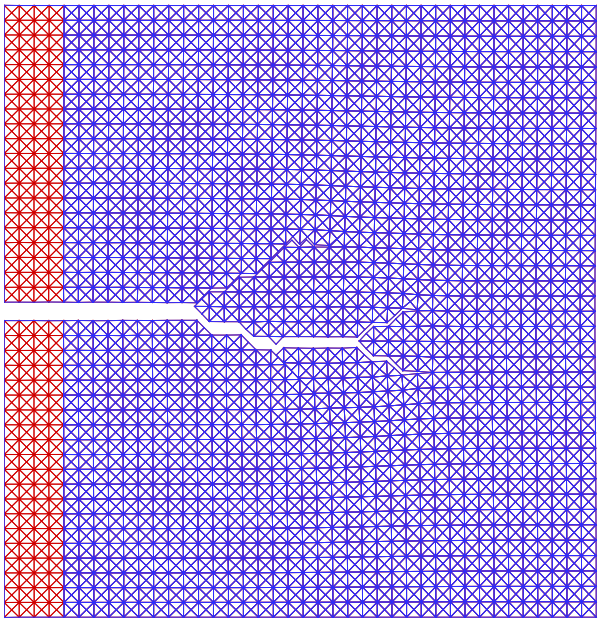

(c) $t = 8.85\mu s$

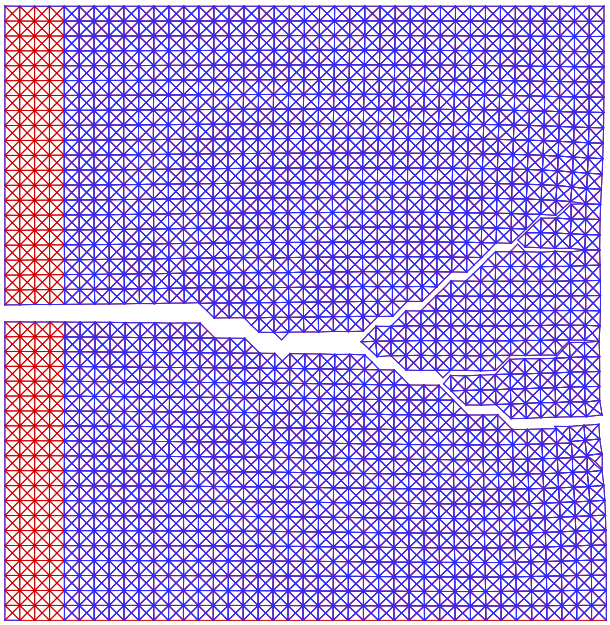

(d) $t = 10\mu s$

Figure 5.32: Crack branch patterns for "FGM" plate with bulk property following homogeneous PMMA material, while cohesive strength is graded linearly in y direction from $\sigma_{max} = 486MPa$ at upper surface to $\sigma_{max} = 162MPa$ at lower surface. The plate is subjected to $v_0 = 5m/s$ velocity loading. (a) branch pattern at $t = 7.5\mu s$; (b) branch pattern at $t = 8.25\mu s$; (c) branch pattern at $t = 8.85\mu s$; (d) branch pattern at $t = 10\mu s$.

Case 3: Graded bulk and cohesive properties. In this example, both bulk and cohesive properties vary linearly in y direction. The top surface is stiffer ($E_{top} = 4.86GPa$) and with higher cohesive strength ($\sigma_{top} = 486MPa$), while the bottom surface is more compliant ($E_{bot} = 1.26GPa$) and with lower cohesive strength ($\sigma_{bot} = 126MPa$). More issues come to concern than case 2 when predicting the crack branch pattern, due to the variation of bulk material property. On one hand, the weaker cohesive resistance favors the crack branching into the $y < 0$ region. On the other hand, two effects may promote the crack branching into the stiffer $y > 0$ region. First, displacement loading condition is employed, and the stress developed in the stiffer region is higher than that at the compliant region. Second, the stress waves generated from the loading at top surface propagates faster than its counterpart emanating from the bottom surface, due to higher dilatational wave speed, and thus reaches the crack plane earlier. These two mechanisms compete with each other in influencing crack branching pattern.

The final crack pattern for plate with material properties given in Table 5.9 is plotted in Figure 5.33. The initiation location of crack branching is the same as in case 2. Evidently, the influence of cohesive strength is dominant among the factors discussed above, as indicated by dominant crack branching towards the lower region. However, the main upward branch does not heal, but propagates almost horizontally.

The crack initiation time, branching time and first branching location for the three cases are compared in Table 5.10. One notices that the crack initiation times are very close for the homogeneous and 'cohesive strength σ_{max} gradation' cases, while for the plate with graded stiffness E and cohesive strength σ_{max}, crack initiation takes place slightly later. This can be explained by the variation of Young's modulus. For case 3, the material is more compliant at the lower region, thus the average wave propagation speed is also lower, and it takes longer time for the stress to accrue to the critical value for crack to propagate. The branching initiation occur at roughly the same time, and since the branching takes place earlier for the graded material cases, the branching initiation time is also less ($t_{branch} = 7.0210\mu s$ for case 2 and $t_{branch} = 7.4755\mu s$ for case 3, as compared to $t_{branch} = 7.5280\mu s$ for the homogeneous case 1). Crack branching locations are roughly the same for all cases, and only differs by one element length ($a_{branch} = 1.05mm$ for homogeneous case, and $a_{branch} = 0.975mm$ for the other two).

The crack tip location, as defined by the right-most crack tip location when multiple cracks exist, is plotted in Figure 5.34 with respect to time. The slope of the each curve indicate the speed of the crack. One observes that for each case, the crack tip runs at a roughly steady speed. The crack tip speeds are similar for the two graded plates, with $v_{tip} = 700m/s \approx 0.745C_R$ for case 2 and $v_{tip} = 667m/s \approx 0.710C_R$ for case 3, where $C_R = 939m/s$

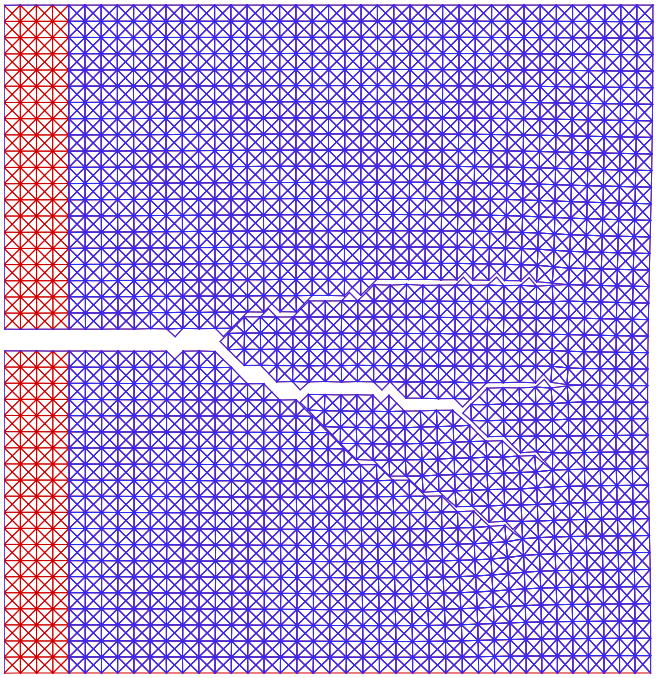

Figure 5.33: Crack branch pattern at $t = 10\mu s$ for FGM plate with both bulk and cohesive properties linearly graded in y direction. Cohesive strength is graded from $\sigma_{max} = 486MPa$ at upper surface to $\sigma_{max} = 162MPa$ at bottom surface. Young's modulus is $E = 4.86GPa$ at upper surface and $E = 1.26GPa$ at bottom surface. The plate is subjected to $v_0 = 5m/s$ velocity loading.

Table 5.10: Crack branch initiation time and location for different material gradation.

Gradation	Properties	t_{init} (μs)	t_{branch} (μs)	a_{branch} (mm)
Homogeneous	Table 5.7	6.1055	7.5280	1.050
Graded σ_{max}	Table 5.8	6.1235	7.2010	0.975
Graded E & σ_{max}	Table 5.9	6.4955	7.4755	0.975

denotes the average Rayleigh wave speed. The average crack tip speed is slowest for the homogeneous case, with $v_{tip} = 597m/s \approx 0.636C_R$.

5.3.4 Results for Different Velocities

The impact velocity has significant influence on the crack pattern. Consider a mode-I fracture induced by very low velocity impact, which can be regarded as a quasi-static problem. In this case, the crack will assumably propagate along a straight plane without branching. On the other hand, high velocity impact will induce more significant branching and fragmentation. Simulations are carried out for the homogeneous PMMA plate under various impact loading $v_0 = 1m/s$, $5m/s$ and $15m/s$, respectively, and the final crack branch patterns for $v_0 =$

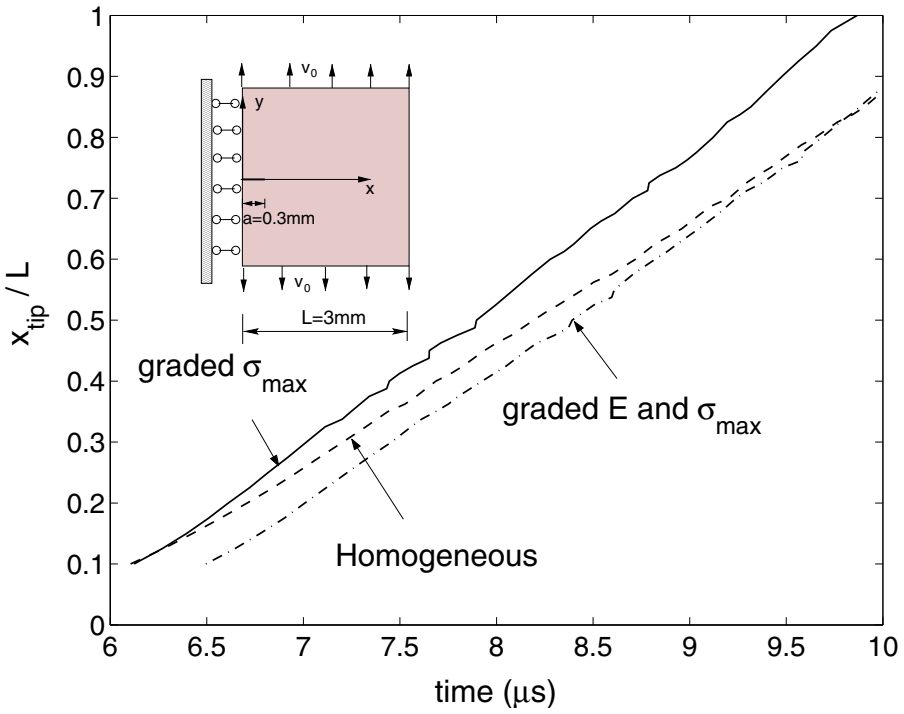

Figure 5.34: Crack tip location versus time for different material gradation cases.

$1m/s$ and $v_0 = 15m/s$ cases are plotted in Figure 5.35(a) and (b). The branch pattern for $v_0 = 5m/s$ case was plotted in Figure 5.31 in Section 5.3.3.

Branching occurs after the crack runs along the original plane for certain distance a_1. Clearly, this distance is significantly shorter for the plate subjected to higher impact loading. For $v_0 = 1m/s$, branch occurs at $a_{branch} = 1.8mm$, while for $v_0 = 15m/s$, branch occurs at $a_{branch} = 0.975mm$. In other words, the initial crack begins to branch after propagating along original plane for $a_1 = 1.5mm = 5a_0$ for the former, and $a_1 = 0.675mm \approx 2a_0$ for the latter, where a_0 denotes the initial crack length. The difference is significant. The stress carried by the wave propagating in the plate becomes very complicated due to the presence of the running crack, and the crack branching occurrence is also influenced. Therefore, higher velocity does not necessarily always induce earlier branching if the velocities under comparison are not far different. However, for significantly different impact velocity, the trend is consistent with the above observation. Another important observation is that at lower impact velocity, the crack branching pattern is 'cleaner', with only main branches present. At higher impact velocity, more sub-branches occur.

The crack initiation time, branching time and branching locations for the three impact velocity cases are compared in Table 5.11. Obviously, for lower impact velocity case, it takes longer time for the crack tip stress to accumulate to the critical value required for the

crack to propagate. After crack initiation, branching follows, and the gaps between these two characteristic time are $t_{gap} = 2.765\mu s$, $1.423\mu s$ and $1.260\mu s$, respectively. This time gap mainly depends on the horizontal distance a_1 on which the crack runs before branching. The crack speed is roughly the same for the three cases, as indicated by Figure 5.36.

Table 5.11: Crack branch initiation time and location for different applied impact velocity

impact velocity v_0	Properties	t_{init} (μs)	t_{branch} (μs)	a_{branch} (mm)	$a_1 = a_{branch} - a_0$ (mm)
$1m/s$	Table 5.7	27.2175	30.0125	1.80	1.50
$5m/s$	Table 5.7	6.1055	7.5280	1.05	0.75
$15m/s$	Table 5.7	1.7560	3.0155	0.975	0.675

The relationship between crack tip location and time is plotted in Figure 5.36 for each impact velocity. The crack tip speed is indicated by the slope of each curve. Due to the large difference in the crack initiation time, the three curves are far apart in Figure 5.36(a). To provide a more meaningful comparison, the crack initiation time is deducted from the time axis and the results are plotted in Figure 5.36(b). One observes that the crack propagates at almost constant speed, with slight acceleration for the $v_0 = 15m/s$ case. The average crack tip speeds are calculated as $v_{tip} = 566m/s \approx 0.603C_R$, $v_{tip} = 597m/s \approx 0.636C_R$ and $v_{tip} = 656m/s \approx 0.700C_R$ for $v_0 = 1m/s$, $v_0 = 5m/s$ and $v_0 = 15m/s$ cases, respectively. As expected, at higher impact velocity, crack runs at higher speed, yet the difference is not significant for the examples analyzed here.

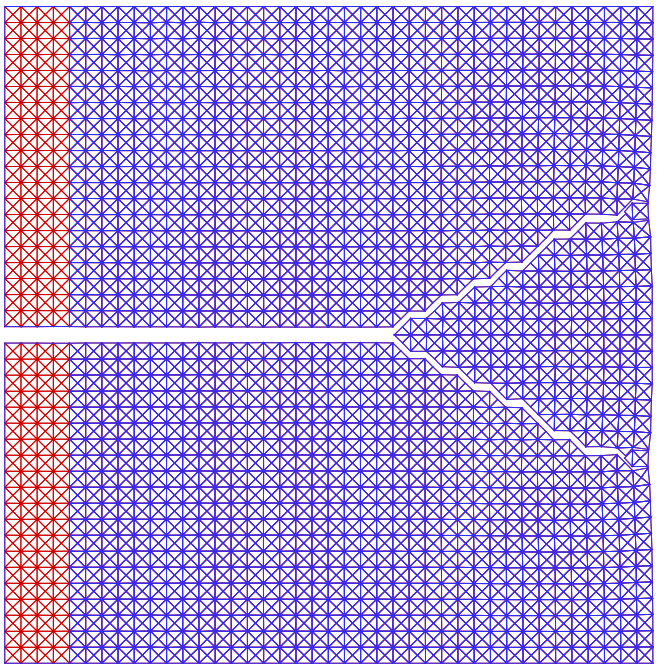

(a) $t = 32\mu s$, $v_0 = 1m/s$

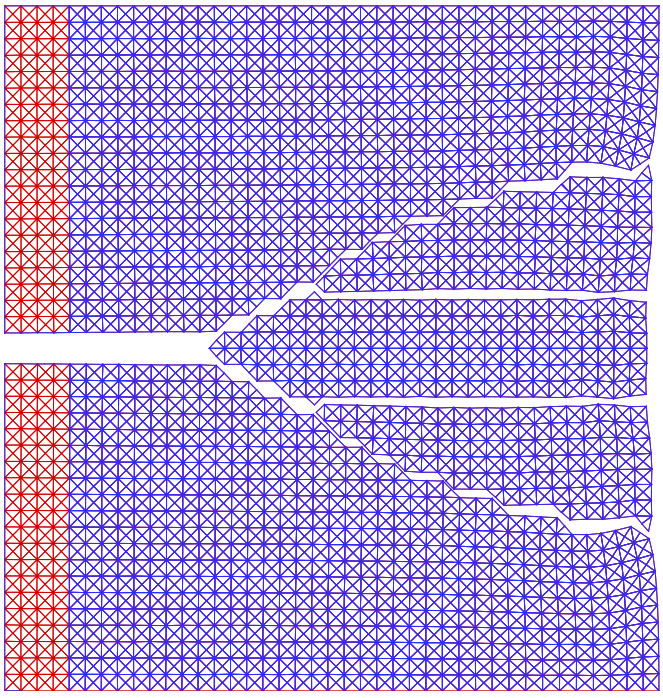

(b) $t = 6\mu s$, $v_0 = 15m/s$

Figure 5.35: Crack branch pattern for different impact velocity applied on homogeneous PMMA plate. (a) final crack pattern at $t = 32\mu s$ for applied impact $v_0 = 1m/s$; (b) final crack pattern at $t = 6\mu s$ for applied impact $v_0 = 15m/s$.

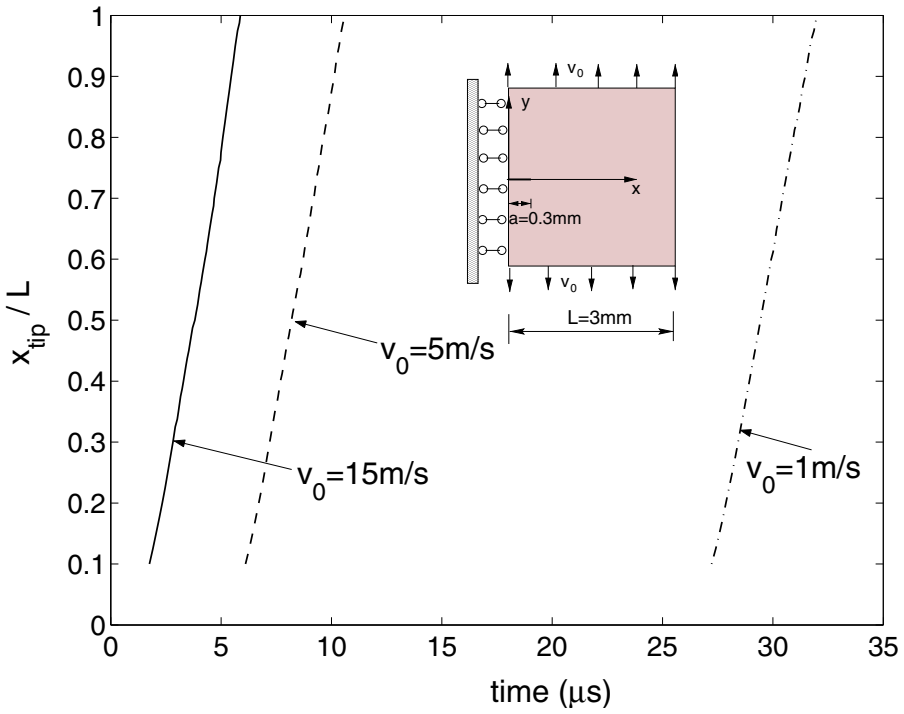

(a)

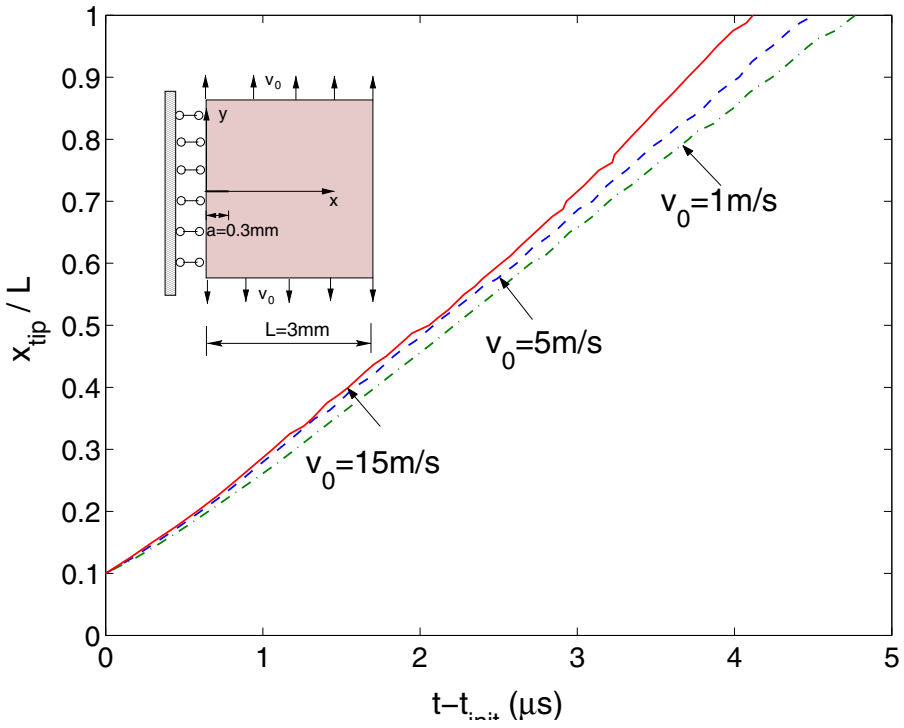

(b)

Figure 5.36: Crack tip location versus time for various impact loading velocity $v_0 = 1m/s$, $v_0 = 5m/s$ and $v_0 = 15m/s$. (a) crack tip versus absolute time; (b) crack tip versus $t - t_{init}$, where t_{init} denotes the branch initiation time for each case.

Chapter 6

Conclusions and Future Work

In this study, the dynamic behavior of homogeneous and functionally graded materials under dynamic loading is investigated, which include problems both with and without cracks. The research code **I-CD** (Illinois-Cohesive Dynamic) is developed using *explicit* dynamic scheme, with *graded* elements in the bulk material, and *graded cohesive* elements to model fracture. The graded elements are associated with nonhomogeneous elastic constitutive relationships of the bulk material, and the graded cohesive elements are associated with traction-separation relationships to describe the physical status at the crack tip (actual and fictitious) and the fracture evolution. As illustrated in the study, the cohesive approach, which is based on a cohesive view of material fracture, is promising for modeling generalized fracture without predefined fracture criteria. It proves to be an attractive alternative approach for investigating a broad range of fracture phenomena, especially for dynamic fracture propagation problems involving branching and fragmentation, which are not handled properly by other models.

In this Chapter, a brief summary of the content and contribution of the study is presented, followed by a number of suggestions for the future work.

6.1 Concluding Remarks

This work first provides some background information, including an overview of the numerical approach adopted in the study, explanation of the cohesive zone modeling concept, and how this model is implemented in the numerical scheme. A number of existing CZMs are critically reviewed to show the general capability of CZMs, as well as the advantages and potential caveats of each model. After that, dynamic behavior of homogeneous and graded materials *without* cracks are investigated. The explicit scheme is used in this study, with adaptation of the time step control due to varying wave speed in FGMs. Graded elements are introduced

by means of a generalized isoparametric formulation including material gradation at the element level. Examples are presented to validate the code and assess the bulk behavior under dynamic loading for homogeneous and functionally graded materials. A careful study of 3-point-bending homogeneous and FGM beams reveals the effect of material gradient on stress evolution in time. This investigation also provides some insight to predict the order of crack initiation time for different material gradient cases, which was confirmed by simulations with cracks.

Based on the understanding of CZMs for homogeneous materials, further discussion was carried out for a CZM developed for FGMs, which is a potential-based surface network approach. The main drawbacks of this approach include the artificial compliance introduced with the embedded cohesive elements, the attenuation of crack tip stress singularity due to cohesive surface separation, and the crude approximation of mode mixity by using effective quantities. As an alternative, Xu and Needleman's [46] model was extended to treat FGMs, which eliminates the dependence upon effective quantities, and may provide certain advantages when investigating crack branching. During the numerical implementation stage, detailed discussion was made on the stability, accuracy, and mesh convergence issues.

With the numerical scheme described above, a number of numerical simulations are carried out, for both homogenous and graded materials under dynamic loading, and considering crack propagation in predefined and non-predefined paths. Comparison of results of numerical simulation with those from experiments indicates that the cohesive zone approach is capable of qualitatively capturing the fracture evolution characteristics in homogeneous and graded materials, however, the quantitative match of results requires extensive calibration of cohesive zone model parameters.

The primary contributions in this study are briefly summarized as follows:

- Extension of the generalized isoparametric element formulation using graded elements to dynamic problems, which include both *bulk* and *cohesive* elements.
- Extension of the FGM CZM by Jin *et al.* [30] to the dynamic case.
- Extension of Xu and Needleman's [46] CZM to FGMs.
- Implementation of compositionally varying cohesive energy, which is obtained from actual experiments, rather than hypothetical assumptions.
- Investigation of difference between CZMs using effective quantities for traction-separation relationship (*e.g.* [30]) and those using separate laws for normal and tangential quantities (*e.g.* [46]).

- Investigation of spontaneous crack *nucleation* capacity of CZMs.
- Investigation of crack propagation in FGMs under impact loading using *real* material properties, and comparison of simulation results to that from experiments.

6.2 Suggestions for Future Work

To better explore fracture phenomena using the CZM approach, some fundamental issues need to be addressed, which include development of physics-based FGM CZMs. The future work on cohesive zone modeling should focus on a better understanding of the numerical caveats introduced, the limitations of different forms of model, and the impact of cohesive parameters entering the model. Based on such extended knowledge, a better CZM needs to be developed that incorporates fracture mechanisms at the FGM microstructural level. Specifically, the Camacho and Ortiz' [6] model and the Virtual Internal Bond model [27] should be scrutinized for their appealing features that have not been investigated in this study.

Some open problems that call for closer attention and careful treatment for the CZM approach are discussed below. The topic are listed from a more specific to a more general computational perspective.

Investigation and comparison of intrinsic versus extrinsic CZMs. As an innate characteristic of the *intrinsic* model, the artificial compliance is unavoidable. This mechanism has been elaborated upon in Chapter 3. An alternative approach is to adopt an *extrinsic* model for which the cohesive elements are inserted adaptively as in Camacho and Ortiz's [6] model. However, the adaptive modification of the mesh and the numerical model during the actual computation poses additional complications, which need to be further investigated.

Mesh dependence. Xu and Needleman [46] have reported that distinctively different crack propagation profiles are generated with different mesh orientation patterns. In reference [28], similar results have been presented, and the reason for this phenomenon was ascribed to mesh size. To ensure that the crack propagates in a continuum way rather than in a discrete manner, certain upper limit for mesh size needs to be prescribed. However this limit requires the mesh size to be of the same scale of the material characteristic length, for which the computation overhead is enormous. No results have yet been reported to demonstrate that violation of this condition is indeed responsible for mesh dependence. Thus a

systematic study need to be conducted to address mesh dependence in CZMs, including recommendation for practical simulation frameworks.

Time discontinuity. Papoulia and Vavasis [33] pointed out that in numerical applications, "initial rigid" models result in time discontinuous behavior if no special provision is made. This time discontinuity gives rise to oscillatory, non-convergent results in time, as well as dependence of results on nonphysical parameters. Though certain remedy was proposed to cure this problem, it is argued that the measure taken entails another pathology called "traction locking". Thus a mechanics-based treatment of "time-discontinuity" is needed.

Mode mixity effect. In some models, the normal and tangential traction-separation relations are coupled, as in Xu and Needleman's model [46], while in some others they are not, as in Camacho and Ortiz's model [6]. How to properly choose parameters to account for the effect of mode mixity in CZM formulation remains unclear and should be further investigated.

Physics-based model with microstructural considerations. A phenomenological model proposed for FGMs tries to capture the fracture property at a scale where the influence of discrete microstructure can be neglected. However, this proves to be problematic, as manifested by the discrepancy between the cohesive energy variation curve predicted by the proposed CZM and the experimental data for the glass/epoxy FGM beam (See Section 3.2). The discussion on the actual energy variation curve reveals the importance of local structure and interaction of material phases. Hence, a better model should ideally consider the microstructure of the FGMs, and may differ considerably in form for different FGMs systems.

Three-dimensional dynamic fracture simulations of advanced composites and FGMs. Certain fracture phenomena, *e.g.* crack front tunneling effect, complex loading conditions, and surface crack propagation, cannot be modelled by 2D simulation. Therefore, 3D simulation provides a richer field for fracture investigation, and models the fracture more realistically. A practical simulation framework for 3D analysis need to be developed further.

Parallel Computing. Parallelization of program code is mandatory for large scale simulation, particularly for 3D dynamic fracture simulation. In 3D simulation, the number of degrees of freedom (DOF) is usually high, and CZM parameters also dictates an upper limit of mesh size. Thus large number of DOFs in bulk area is generated. Moreover, the presence of cohesive elements again increases the number of DOFs of the finite element model by

introducing multiple nodes at the same location, and requires smaller time step to obtain stable results. All these factors lead to huge computation overhead, hence parallel computing must be employed.

Optimization of the code structure. Various element types (bulk and cohesive) are present in the CZM approach. They are associated with different constitutive laws and require different treatment during computation. Various complexities are introduced by the cohesive models, *e.g.* the adaptive insertion of cohesive elements and updating of mesh information using extrinsic model, and extinction of cohesive elements after complete decohesion. In light of these factors, advanced techniques need to be employed, including a more organized data structure, which would facilitate the management of data input/output, updating of array data with dynamic bounds, and specific item selection and reporting. Alternative programming languages may be considered, *e.g.* C++.

Scientific Visualization. Rich fracture fracture phenomena, *e.g.* crack tunneling, branching and fragmentation, can be captured with CZM approach. This also adds to the complexity in understanding and explanation of the results, especially in 3D simulations. To help understand the mechanical phenomena at various scales and regions of the body under investigation, scientific visualization tools need to be employed, including virtual reality. Various means involving visual and audio effects can be pursued. This further requires development of the finite element code to accomodate these features, *e.g.* real-time data retrieving, data postprocessing.

Appendix A

Nonlinear Finite Element Formulation

The explicit updating scheme employed in this study is a central difference method, and Eqs. (1.39-1.41) for updating nodal displacements, accelerations and velocities from time step (n) to $(n+1)$ are re-written here for convenience:

$$\mathbf{u}_{n+1} = \mathbf{u}_n + \Delta t \dot{\mathbf{u}}_n + \frac{1}{2}\Delta t \ddot{\mathbf{u}}_n \tag{A.1}$$

$$\ddot{\mathbf{u}}_{n+1} = \mathbf{M}^{-1}(\mathbf{F} + \mathbf{R}_{int_{n+1}} - \mathbf{R}_{coh_{n+1}}) \tag{A.2}$$

$$\dot{\mathbf{u}}_{n+1} = \dot{\mathbf{u}}_n + \frac{\Delta t}{2}(\ddot{\mathbf{u}}_n + \ddot{\mathbf{u}}_{n+1}) \tag{A.3}$$

where Δt denotes the time step, $\mathbf{M}$ is the mass matrix, $\mathbf{F}$ is the external force vector, $\mathbf{R}_{int}$ and $\mathbf{R}_{coh}$ are the global internal and cohesive force vectors, which are obtained from the contribution of *bulk* and *cohesive* elements, respectively. The appendix focuses on the methodology used to determine the internal force vector and the cohesive force vector.

A.1 Internal force vector

The global internal force vector $\mathbf{R}_{int}$ is assembled from the element internal force vector $\mathbf{R}^e_{int}$, which is defined as

$$\mathbf{R}^e_{int} = \int_{V_e} [\mathbf{k}^e]\{\mathbf{u}\} dV_e \tag{A.4}$$

with small deformation formulation, or

$$\mathbf{R}^e_{int} = \int_{V_e} [\mathbf{B}^{NL}]^T \{\mathbf{S}\} dV_e \tag{A.5}$$

with large deformation formulation, which is derived from the first term of Eq. (1.38). The matrix $\mathbf{B}^{NL}$ relates a virtual displacement to the virtual Lagrangian strain.

For small deformation formulation, the stiffness matrix $\mathbf{k}$ is constructed once and assumed to remain unchanged throughout the computation. Thus the calculation of (A.4) is straightforward, and the details are not repeated here. On the other hand, for large deformation, the stiffness matrix is dependent upon the deformation at each time step, and the detailed formulation is presented below. The derivation refers to $T6$ elements, however, analogous steps also apply to $T3$ elements. Both elements are employed in this work.

The displacement field $\mathbf{u}$ inside one element can be interpolated from nodal values using shape functions:

$$\mathbf{u} = \sum \mathbf{N}_i \mathbf{d}_i \tag{A.6}$$

where

$$\mathbf{u} = [u \ v]^T \tag{A.7}$$

$$\mathbf{N} = \begin{bmatrix} N_1 & 0 & N_2 & 0 & N_3 & 0 & N_4 & 0 & N_5 & 0 & N_6 & 0 \\ 0 & N_1 & 0 & N_2 & 0 & N_3 & 0 & N_4 & 0 & N_5 & 0 & N_6 \end{bmatrix} \tag{A.8}$$

$$\mathbf{d} = [u_1 \ v_1 \ u_2 \ v_2 \ u_3 \ v_3 \ u_4 \ v_4 \ u_5 \ v_5 \ u_6 \ v_6]^T \tag{A.9}$$

Green's strain tensor is constructed considering high order term:

$$\mathbf{E} = \frac{1}{2}\left(\nabla \mathbf{u} + \nabla^T \mathbf{u} + \nabla \mathbf{u} \nabla^T \mathbf{u}\right) \tag{A.10}$$

The following expression, which takes advantage of the symmetry properties of the tensors $\mathbf{S}$ and $\mathbf{E}$, is obtained after some algebra:

$$\begin{aligned} \mathbf{S} : \delta\mathbf{E} &= \mathrm{S}_{11}\delta\mathrm{E}_{11} + \mathrm{S}_{12}\delta\mathrm{E}_{21} + \mathrm{S}_{21}\delta\mathrm{E}_{12} + \mathrm{S}_{22}\delta\mathrm{E}_{22} \\ &= \mathrm{S}_{11}\delta\mathrm{E}_{11} + \mathrm{S}_{12}(\delta\mathrm{E}_{21} + \delta\mathrm{E}_{12}) + \mathrm{S}_{22}\delta\mathrm{E}_{22} \\ &= [\mathbf{B}^{NL}]^T\{\mathbf{S}\} \cdot \delta\mathbf{d} \end{aligned} \tag{A.11}$$

where the stress vector $\{\mathbf{S}\}$ is defined as

$$\{\mathbf{S}\} = \begin{Bmatrix} S_{11} \\ S_{22} \\ S_{12} \end{Bmatrix} \tag{A.12}$$

and

$$[\mathbf{B}^{NL}] = \begin{bmatrix} \dfrac{\partial N_1}{\partial x}\left(1+\dfrac{\partial u}{\partial x}\right) & \dfrac{\partial N_1}{\partial x}\dfrac{\partial v}{\partial x} & \cdots \\ \dfrac{\partial N_1}{\partial y}\dfrac{\partial u}{\partial y} & \dfrac{\partial N_1}{\partial y}\left(1+\dfrac{\partial v}{\partial y}\right) & \cdots \\ \dfrac{\partial N_1}{\partial y}\left(1+\dfrac{\partial u}{\partial x}\right)+\dfrac{\partial N_1}{\partial x}\dfrac{\partial u}{\partial y} & \dfrac{\partial N_1}{\partial x}\left(1+\dfrac{\partial v}{\partial y}\right)+\dfrac{\partial N_1}{\partial y}\dfrac{\partial v}{\partial x} & \cdots \end{bmatrix} \tag{A.13}$$

where the shape function derivatives $N_{i,x}$, $N_{i,y}$ and displacement derivatives $u_{,x}$, $u_{,y}$, etc. are constructed with the isoparametric formulation, *i.e.* using the Jacobian matrix and derivative of shape functions in parametric space. The above expression only illustrates the first two columns of the 3×12 fully populated matrix for a 6-noded triangular elements in 2D space.

The second Piola-Kirchhoff stress $\mathbf{S}$ is related to Green's strain tensor $\mathbf{E}$ as

$$\mathbf{S} = \mathbf{C}\mathbf{E} \tag{A.14}$$

where $\mathbf{C}$ denotes a fourth-order elastic stiffness matrix. In contracted form, the tensor $\mathbf{E}$ comprises 3 components for the 2D problem:

$$\mathbf{E} = \begin{Bmatrix} E_{11} \\ E_{22} \\ E_{12} \end{Bmatrix} = \frac{1}{2}\begin{Bmatrix} \mathrm{F}_{11}^2 + \mathrm{F}_{21}^2 - 1 \\ \mathrm{F}_{12}^2 + \mathrm{F}_{22}^2 - 1 \\ \mathrm{F}_{11}\mathrm{F}_{12} + \mathrm{F}_{21}\mathrm{F}_{22} \end{Bmatrix} \tag{A.15}$$

and the components form of deformation gradient tensor $\mathbf{F}$ can be written as

$$\mathbf{F} = \begin{bmatrix} 1+\dfrac{\partial u}{\partial x} & \dfrac{\partial u}{\partial y} \\ \dfrac{\partial v}{\partial x} & 1+\dfrac{\partial v}{\partial y} \end{bmatrix} \tag{A.16}$$

The relationship (A.14) can be expressed as

$$\begin{Bmatrix} S_{11} \\ S_{22} \\ S_{12} \end{Bmatrix} = E \begin{bmatrix} 1 & -\nu & 0 \\ -\nu & 1 & 0 \\ 0 & 0 & \dfrac{1}{2(1-\nu)} \end{bmatrix} \begin{Bmatrix} E_{11} \\ E_{22} \\ E_{12} \end{Bmatrix} \tag{A.17}$$

Once the $\mathbf{B}^{NL}$ matrix and the $\mathbf{S}$ vector are constructed, the internal force can be com-

puted accordingly using Gauss quadrature:

$$\mathbf{R}^e_{int} = \frac{1}{2}\sum_{i=1}^{n} w_i J_i [\mathbf{B}^{NL}]^T_i \left\{ \begin{array}{c} S_{11} \\ S_{22} \\ S_{12} \end{array} \right\}_i \tag{A.18}$$

where w_i and J_i denote the weight and Jacobian values evaluated at Gauss point i, respectively.

A.2 Cohesive Force Vector

The global cohesive force vector $\mathbf{R}_{coh}$ is assembled from the element cohesive force vector $\mathbf{R}^e_{coh}$, which is defined as

$$\mathbf{R}^e_{coh} = \int_{\Gamma_e} [\mathbf{N}]^T \{\mathbf{T}\} d\Gamma \tag{A.19}$$

where $\mathbf{N}$ is the shape function matrix and $\mathbf{T}$ is the traction vector. For 2D problems, the cohesive elements are line elements, and the shape functions are

$$N_1 = \frac{\xi}{2}(\xi - 1), \quad N_2 = \frac{\xi}{2}(\xi + 1), \quad N_3 = 1 - \xi^2 \tag{A.20}$$

for quadratic line elements (when $T6$ bulk elements are used) and

$$N_1 = -\frac{1}{2}(\xi - 1), \quad N_2 = \frac{1}{2}(\xi + 1) \tag{A.21}$$

for linear line elements (when $T3$ bulk elements are used). Expression (A.19) is evaluated numerically by integrating the tractions along the cohesive element surface using Gauss quadrature

$$R_{coh\,j} = \frac{L}{2}\sum_{i=1}^{n} w_i N_j(\xi_i) T(\xi_i) \tag{A.22}$$

and a three point quadrature rule was used with the Gauss points ξ and weights w listed in Table A.1.

Table A.1: Three point Gauss quadrature rule for cohesive line element integration

ξ_1	ξ_2	ξ_3	w_1	w_2	w_3
$-\sqrt{0.6}$	$\sqrt{0.6}$	0	5/9	5/9	8/9

Notice that the cohesive force vector $\mathbf{R}^e_{coh}$ is constructed with respect to the global co-

ordinate system, while the traction $\mathbf{T}$ is determined in a local coordinate system depending on the interface separation. Therefore, transformations between the local and global coordinate systems need to be carried out for the interface separations in normal and tangential directions

$$\begin{Bmatrix} \delta_t \\ \delta_n \end{Bmatrix} = \begin{bmatrix} \cos\alpha & \sin\alpha \\ -\sin\alpha & \cos\alpha \end{bmatrix} \begin{Bmatrix} \delta_x \\ \delta_y \end{Bmatrix} \tag{A.23}$$

and for interface tractions back to global coordinate system

$$\begin{Bmatrix} T_x \\ T_y \end{Bmatrix} = \begin{bmatrix} \cos\alpha & -\sin\alpha \\ \sin\alpha & \cos\alpha \end{bmatrix} \begin{Bmatrix} T_t \\ T_n \end{Bmatrix} \tag{A.24}$$

where α is the angle of the cohesive element interface measured in the global coordinate system. During computation, the α value needs to be updated to obtain accurate cohesive force because the elements around the crack tip can experience large rotations.

References

[1] Barenblatt, G. I. 1959. The formation of equilibrium cracks during brittle fracture: General ideas and hypothesis, axially symmetric cracks. *Applied Mathematics and Mechanics (PMM)*, **23**, 622-636.

[2] Barenblatt, G. I. 1962. Mathematical theory of equilibrium cracks in brittle fracture. In: Dryden, H. L., von Karman, T. (Eds.), *Advances in Applied Mechanics*, **7**, 55-125.

[3] Bathe, K.-J. 1996. *Finite Element Procedures*. Prentice-Hall, New Jersey.

[4] Baylor J, 1998. *A Numerical Simulation of Impact-induced Damage of Composite Materials*. Master Thesis, University of Illinois at Urbana-Champaign.

[5] Belytschko, T., Chiapetta, R. L. and Bartel, H. D. 1976. Efficient large scale non-linear transient analysis by finite elements. *International Journal for Numerical Methods in Engineering*, **10**, 579-596.

[6] Camacho, G. T. and Ortiz, M. 1996. Computational modeling of impact damage in brittle materials. *International Journal of Solids and Structures*, **33**, 2899-2938.

[7] Chin, E.S. C. 1999. Army focused research team on functionally graded armor composites. *Materials Science and Engienering*, **A259**, 155-161.

[8] Chopra, A.K. 1995. *Dynamics of Structures*, Prentic-Hall, New Jersey.

[9] Costanzo, F. and Walton, J.R. 1997. A study of dynamic crack growth in elastic materials using a cohesive zone model, *International Journal of Engineering Science*, **35**, 1085-1114.

[10] Dugdale, D.S. 1960. Yielding of steel sheets containing cracks. *J. Mech. Phys. Solids*, **8**, 100-104.

[11] Erdogan, F. 1995. Fracture mechanics of functionally graded materials. *Composites Engineering*, **5**, 753-770.

[12] Geubelle, P.H., Baylor, J. 1998. Impact-induced delamination of laminated composites: a 2D simulation. *Composites Part B Engineering*, **29** 589-602.

[13] Gooch, W.A., Chen, B.H., Burkins, M.S., Palicka, R., Rubin, J. and Ravichandran, R. 1999. Development and ballistic testing of functionally gradient ceramic/metal applique. *Mater. Sci. Forum*, **308-311**, 614-621.

[14] Gurson, A.L. 1977. Continuum theory of ductile rupture by void nucleation and growth: Part I–yield criteria and flow rules for porous ductile media, *Journal of Engineering Materials and Technology*, **99**, 2-15.

[15] Guinea, G.V., Elices, M. and Planas, J. 1997. On the initial shape of the softening function of cohesive materials, *International Journal of Fracture*, **87**, 139-149.

[16] Hill, R. 1962. Acceleration waves in solids, *Journal of the Mechanics and Physics of Solids*, **10**, 1-16.

[17] Hutchinson, J.W. 1968. Singular behavior at the end of tensile crack tip in a hardening material, *Journal of the Mechanics and Physics of Solids*, **16**, 13-31.

[18] Kim, J.-H. and Paulino, G. H. 2002. Isoparametric graded finite elements for nonhomogeneous isotropic and orthotropic materials, *ASME Journal of Applied Mechanics*, **69**, 502-514.

[19] Kim, J.-H. and Paulino, G. H. 2003. The interaction integral for fracture of orthotropic functionally graded materials: evaluation of stress intensity factors, *International Journal of Solids and Structures* (in press)

[20] Kim, J.-H. and Paulino, G. H. 2003. An accurate scheme for mixed-mode fracture analysis of functionally graded materials using the interaction integral and micromechanics models, *International Journal for Numerical Methods in Engineering* (in press)

[21] Kim, J.-H. and Paulino, G. H. 2003. T-Stress, mixed-mode stress intensity factors, and crack initiation angles in functionally graded materials: a unified approach using the interaction integral method, *Computer Methods in Applied Mechanics and Engineering*, **192**, 1463-1494.

[22] Kim, J.-H. and Paulino, G. H. 2003. Mixed-mode J-intergral formularation and implementation using graded elements for fracture analysis of nonhomogeneous orthotropic material, *Mechanics of Materials*, **35**, 107-128.

[23] Kim, J.-H. and Paulino, G. H. 2002. Mixed-mode fracture of orthotropic functionally graded materials using the finite element method and the modified crack closure method *Engineering Fracture Mechanics*, **14-16**, 1557-1586.

[24] Kim, J.-H. and Paulino, G. H. 2002. Isoparametric graded finite elements for nonhomogeneous isotropic and orthotropic materials, Jeong-Ho Kim and G. H. Paulino. *ASME Journal of Applied Mechanics*, **69**, 502-514.

[25] Paulino, G. H. and Kim, J.-H. 2003. Poisson's ratio effect on mixed-mode stress intensity factors and T-stress in functionally graded materials. *International Journal of Computational Engineering Science* (in press)

[26] Knauss, W.G. and Losi, G.U. 1993. Crack propagation in a nonlinearly viscoelastic solid with relevance to adhesive bond failure, *ASME Journal of Applied Mechanics*, **60**, 793-801.

[27] Klein, P. and Gao. H. 1998. Crack nucleation and growth as strain localization in a virtual-bond continuum, *Engineering Fracture Mechanics*, **61**, 21-48.

[28] Klein, P.A, Foulk, J.W., Chen, E.P., Wimmer, S.A. and Gao, H. 2000. Physics-based modeling of brittle fracture: Cohesive formulations and the application of meshfree methods, *Sandia National Laboratory, Technical Report, SAND2001-8099*

[29] Lee, Y. and Prakash, V. 1999. Dynamic brittle fracture of high strength structural steels under conditions of plane strain, *International Journal of Solids and Structures*, **36**, 3293-3337.

[30] Jin, Z.-H., Paulino, G. H. and Dodds, R. H. Jr. 2002. Finite element investigation of quasi-static crack growth in functionally graded materials using a novel cohesive zone fracture model, *ASME Journal of Applied Mechanics*, **69**, 370-379.

[31] Meirovitch, L. 1967. *Analytical Methods in Vibrations*. the Macmillan Company, New York.

[32] Orowan, E. 1948. Fracture and strength of solids, *Reports on Progress in Physics* **XII**, 185.

[33] Papoulia, K.D. Sam, C.H. and Vavasis, S.A. 2003, Time continuity in cohesive finite element modeling, *International Journal for Numerical Methods in Engineering*, **58**, 679-701.

[34] Paulino, G.H., Jin, Z.-H. and Dodds Jr., R.H., 2003, *Failure of Functionally Graded Materials*, In: Karihaloo, B. et al. (Editors), Encyclopedia of Comprehensive Structural Integrity, Vol.2, Chapter 13, Elsevier, Amsterdam.

[35] Prandtl, L., 1933, Ein Gedankenmodell für den Zerreibvorgang spröder Körper, *Zeitschrift für angewandte Mathematik und Mechanik*, **13**, 129-133. (as reported in [28])

[36] Rice, J.R. 1968. Mathematical analysis in the mechanics of fracture. *Fracture, an advanced treatise. Ed Liebowitz, Academic Press, New York*, **2**, 191-311.

[37] Rice, J.R. and Rosengren, G. F. 1968. Plane strain deformation near a crack tip in a power-law hardening material. *Journal of the Mechanics and Physics of Solids*, **16**, 1-12.

[38] Suresh, S. and Mortensen, A, 1998. *Functionally Graded Materials*, The Institute of Materials, IOM Communications Ltd., London.

[39] Rydholm, G., Fredriksson, B., and Nilsson, F. 1978. Numerical investigation of rapid crack propagation, *Numerical Methods in Fracture Mechanics*, Luxmoore. A.R. and Owen. D.J.R, (eds.), Pineridge Press, 660-672.

[40] Rousseau, C.-E. and Tippur, H. V. 2001. Dynamic fracture of compositionally graded materials with cracks along the elastic gradient: experiments and analysis, *Mechanics of Materials*, **33**, 403-421.

[41] Rousseau, C.-E. and Tippur, H. V. 2000. Compositionally graded materials with cracks normal to the elastic gradient, *Acta Materialia*, **48**, 4021-4033.

[42] Rousseau, C.-E. and Tippur, H. V. 2001. Influence of elastic gradient profiles on dynamically loaded functionally graded materials: cracks along the gradient, *International Journal of Solids and Structures*, **38**, 7839-7856.

[43] Rousseau, C.-E. and Tippur, H. V. 2002. Evaluation of crack tip fields and stress intensity factors in functionally graded elastic materials: cracks parallel to elastic gradient, *International Journal of Fracture*, **114**, 87-111.

[44] Rousseau, C.-E. and Tippur, H. V. 2002. Influence of elastic variations on crack initiation in functionally graded glass-filled epoxy, *Engineering Fracture Mechanics*, **69**, 1679-1693.

[45] Tvergaard, V. and Hutchinson, J. W. 1992. The relation between crack growth resistance and fracture process parameters in elastic-plastic solids, *Journal of the Mechanics and Physics of Solids*, **40**, 1377-1392.

[46] Xu, X. and Needleman, A. 1995. Numerical simulations of dynamic crack growth along an interface., *International Journal of Fracture*, **74**, 289-324.

[47] Warburton, G. B. 1976. *The Dynamical Behaviour of Structures*. Pergamon Press, Oxford.

[48] Yoon, C. and Allen, D.H. 1999. Damage dependent constitutive behavior and energy release rate for a cohesive zone in a thermoviscoelastic solid, *International Journal of Fracture*, **96**, 55-74.